

**PET detector technologies for next-generation molecular imaging
From single-positron counting to single-photoelectron counting**

Venialgo Araujo, Esteban

DOI

[10.4233/uuid:427e3ce3-2b01-4fa0-9e80-bf0e9c033213](https://doi.org/10.4233/uuid:427e3ce3-2b01-4fa0-9e80-bf0e9c033213)

Publication date

2019

Document Version

Final published version

Citation (APA)

Venialgo Araujo, E. (2019). *PET detector technologies for next-generation molecular imaging: From single-positron counting to single-photoelectron counting*. [Dissertation (TU Delft), Delft University of Technology]. <https://doi.org/10.4233/uuid:427e3ce3-2b01-4fa0-9e80-bf0e9c033213>

Important note

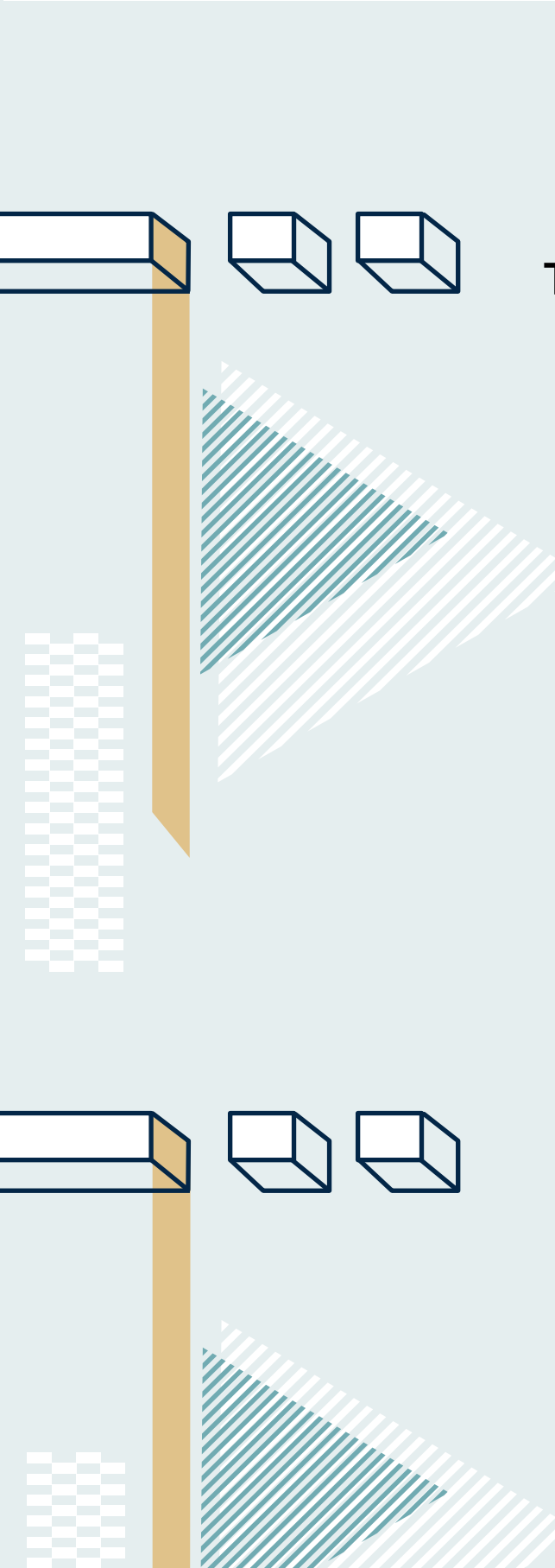
To cite this publication, please use the final published version (if applicable).
Please check the document version above.

Copyright

Other than for strictly personal use, it is not permitted to download, forward or distribute the text or part of it, without the consent of the author(s) and/or copyright holder(s), unless the work is under an open content license such as Creative Commons.

Takedown policy

Please contact us and provide details if you believe this document breaches copyrights.
We will remove access to the work immediately and investigate your claim.



PET DETECTOR TECHNOLOGIES FOR NEXT-GENERATION MOLECULAR IMAGING

From Single-positron Counting to
Single-photoelectron Counting

Esteban VENIALGO ARAUJO

PET detector technologies for next-generation molecular imaging

FROM SINGLE-POSITRON COUNTING TO
SINGLE-PHOTOELECTRON COUNTING

Proefschrift

ter verkrijging van de graad van doctor
aan de Technische Universiteit Delft,
op gezag van de Rector Magnificus prof.dr.ir. T.H.J.J. van der Hagen,
voorzitter van het College voor Promoties,
in het openbaar te verdedigen op woensdag 10 april 2019 om 10:00 uur

door

Esteban VENIALGO ARAUJO

Ingeniero en Electrónica,
Universidad Tecnológica Nacional, Ciudad Autónoma de Buenos Aires, Argentina.
geboren te Caseros, Buenos Aires, Argentinië.

Dit proefschrift is goedgekeurd door de

promotor: Prof. dr. ir. E. Charbon

Samenstelling promotiecommissie:

Rector Magnificus	voorzitter
Prof. dr. ir. E. Charbon	Technische Universiteit Delft
	promotor

Onafhankelijke leden:

Prof. dr. ir. A. J. van der Veen	Technische Universiteit Delft
Prof. dr. K. Ziemons	FH Aachen University of Applied Sciences, Germany
Dr. E. Auffray Hillemanns	Dept EP-CMX, European Organization for Nuclear Research, Switzerland
Prof. dr. S. Ziegler	University Hospital of Ludwig-Maximilians-Universität München, Germany
Dr. ir. D. R. Schaart	Technische Universiteit Delft
Assoc. prof. C. Verrastró	Universidad Tecnológica Nacional, Argentina Comisión Nacional de Energía Atómica, Argentina
Prof. dr. ir. S. Hamdioui	Technische Universiteit Delft reservelid



Printed by:

Front & Back: Art cover designed by Wenhan Hu.

Copyright © 2019 by Esteban Venialgo Araujo

All rights reserved. No part of the material protected by this copyright notice may be reproduced or utilized in any form or by any means, electronic or mechanical, including photocopying, recording or by any information storage and retrieval system, without written permission of the author.

ISBN 978-94-6323-595-2

An electronic version of this dissertation is available at
<http://repository.tudelft.nl/>.

To 文涵

El único héroe válido, es el héroe en grupo, nunca el héroe individual, el héroe solo.

Héctor German Oesterheld

SUMMARY

Positron Emission Tomography (PET) is one of the most relevant medical imaging techniques utilized for cancer detection and tumor staging. The success of PET relies on the high sensitivity and accuracy to detect and quantify molecular probe concentrations, in the order of pmolL^{-1} . Although there are several positron-emitting molecular probes available, the ^{18}F -fludeoxyglucose (^{18}F -FDG) contributes remarkably to the high PET specificity and sensitivity. Since the success of PET imaging is strongly connected to the ^{18}F -FDG, this imaging technique is also known as FDG-PET.

In FDG-PET imaging three elements are key:

- the molecular probe,
- a PET scanner,
- and an image reconstruction algorithm.

The molecular probe is the contrast enhancement agent, which is administrated to the patient and absorbed by the target volumes. The emitted radiation produced by electron-positron annihilation is detected by the PET scanner, and the detection information is utilized to reconstruct a volumetric probe distribution.

In essence, a PET scanner is a large acquisition system composed of thousands of channels that detect coincident γ -photons generated during electron-positron annihilations. Typically, a single detection channel is composed of a scintillation material and a photodetector. The scintillation material absorbs the γ -energy and emits light photons that produce digital or analog signals in the photodetectors. Nowadays, novel silicon-based photodetectors known as silicon photomultipliers (SiPMs) have been adopted as the next-generation photodetectors for PET applications.

In order to further improve the FDG-PET molecular sensitivity and specificity, next-generation instrumentation requires a more accurate time estimation of the detected γ -photon. Since in time-of-flight (TOF) PET the reconstructed images have an improved signal-to-noise ratio (SNR), which depends on the γ -photon timemark precision. Additionally, increasing the detection sensitivity improves the statistical quality of information utilized during the image reconstruction process.

This thesis introduces the basic concepts of molecular imaging and the key elements of FDG-PET in chapters 1 and 2. A comprehensive theoretical analysis on the utilization of the scintillation light information for γ -photon timemark estimation is presented in chapter 3. Several estimation methods, such as maximum-likelihood estimation (MLE) and best linear unbiased estimation (BLUE) are presented, as well as a performance comparison with respect to the Cramér-Rao lower bound. Additionally, a detailed study is performed to determine the conditions that allow to reach the Cramér-Rao lower bound.

Currently, FDG-PET imaging equipment is not equally available worldwide and one of the reasons is the high costs involved. Often, the design and implementation of TOF-PET instrumentation requires application specific integrated circuit (ASIC) designs, which

increases the complexity of the design and required long prototyping phases. Chapter 4 describes the design, implementation, and characterization of TOF-PET instrumentation based on off-the-shelf components, configurable time-to-digital converters (TDCs) implemented on field-programmable gate arrays (FPGAs), and analog SiPMs (A-SiPMs). The proposed solution achieves TOF precision with a full-flexible, fast-prototyping, and ASIC-less designs.

Recently, digital SiPMs (D-SiPMs) emerged as a next-generation photodetector for PET applications. In particular, the multichannel digital SiPM (MD-SiPM) architecture integrates single-photon avalanche diodes (SPADs), TDCs, and a readout logic into a monolithic CMOS photodetector. This type of photodetector confines all the measurement devices and circuits within an integrated solution. Therefore, it allows a direct system integration of a large number of channels since only digital signals are required for its operation. However, D-SiPM research and development requires long development and integration cycles due to the high complexity involved. Chapter 5 describes an individual building block and full-system comprehensive analysis of a monolithic array of 18×9 MD-SiPMs. Additionally, it describes in detail the methods developed for multiple TDC systems. In chapter 6, the system integration of MD-SiPMs for building PET detector modules is explained. The challenges of utilizing complex photodetectors for building PET modules, attachment of scintillator matrices, and digital readout strategies are described in a comprehensive manner.

Finally, a conclusion of the PET technologies investigated throughout this thesis is given. In addition, an outlook of newer detection methods based on Cherenkov-PET and the corresponding requirements and eventual advantages is discussed.

CONTENTS

Summary	vii
1 Introduction	1
1.1 Medical imaging	2
1.1.1 Structural and functional imaging	2
1.1.2 Molecular imaging	4
1.2 Positron emission tomography	7
1.2.1 ^{18}F -fludeoxyglucose	10
1.2.2 PET scanner basics	11
1.2.3 PET detector challenges	12
1.3 PET scanner modalities	13
1.3.1 Whole-body multimodal PET/CT systems	13
1.3.2 Brain PET insert (PET/MRI)	14
1.3.3 Endoscopic PET instrumentation (PET/US)	15
1.4 Research motivation and objectives	16
1.5 Thesis contributions	17
1.5.1 Theory of timing estimation with MD-SiPMs	17
1.5.2 Metrology and γ -photon detection with MD-SiPMs	17
1.5.3 Endoscopic and small-animal PET detector modules	17
1.5.4 ASIC-less TOF-PET based on A-SiPMs	18
1.6 Thesis organization	18
References	18
2 From a PET scanner to a SPAD	23
2.1 PET scanner relevant parameters	24
2.1.1 Basics of γ -photon transport	25
2.1.2 Energy resolution	26
2.1.3 Timing resolution	27
2.1.4 Spatial resolution	29
2.1.5 Effective counting	29
2.1.6 Basics of image reconstruction	31
2.1.7 Time-of-flight PET	37
2.2 PET detector module	38
2.2.1 Inorganic scintillators for PET	40
2.2.2 Photodetectors for PET	40
2.2.3 The multichannel digital SiPM	46
2.3 Single-photon avalanche diodes	46
2.3.1 SPAD basics	46
2.3.2 Relevant PET parameters	48

References	49
3 Theory of timing estimation with multiple timestamps	57
3.1 Timing estimation model evolution	58
3.2 The Cramér-Rao lower bound.	59
3.3 Maximum Likelihood Estimation	62
3.4 Weighted average timemark estimators	63
3.5 Skipping effect	65
3.6 Dark count rate filtering.	68
3.7 Overall performance	72
3.8 Summary	74
References	77
4 ASIC-less TOF-PET based on TDCs on FPGAs and A-SiPMs	81
4.1 ASIC-less TOF-PET module	82
4.1.1 Single count rate and channel multiplexing	83
4.1.2 Time-to-digital converters on FPGAs.	85
4.1.3 A-SiPMs models	88
4.1.4 Channel multiplexing and timing performance	92
4.1.5 Timing signal waveforms	99
4.1.6 LYSO pixel encoding	101
4.1.7 Energy resolution	101
4.2 Outlook	102
4.3 Summary	104
References	107
5 MD-SiPM metrology and measurement methods	111
5.1 Architecture.	112
5.1.1 SPAD cell array.	112
5.1.2 433-TDC array	114
5.1.3 Readout	120
5.2 Methods and characterization	123
5.2.1 SPAD-cell array	123
5.2.2 Characterization of the 433-TDC array.	127
5.2.3 Characterization of the SR logic	134
5.3 Characterization summary	137
References	138
6 MD-SiPM PET system integration	139
6.1 Small animal PET detector	141
6.1.1 Detailed firmware description	143
6.1.2 Radiation characterization	146
6.1.3 γ -energy characterization	146
6.1.4 CRT characterization.	146
6.2 Endoscopic PET detector design	155
6.3 Summary	155
References	155

7	Conclusions and outlook	157
7.1	Future work	159
	References	160
	Appendices	163
A	Pure standard CMOS P+/NWELL single-photon avalanche diodes	165
A.1	SPADs in a pure CMOS 140 nm process.	166
A.1.1	SPAD test structure	166
A.1.2	TCAD simulation.	167
A.1.3	Light-emission test.	168
A.1.4	Photon detection probability	169
A.1.5	Dark count rate	169
A.2	summary	169
	References	171
	Acknowledgements	173
	List of Publications	177

1

INTRODUCTION

Health care systems count on high-quality medical devices as essential tools for diagnosis and treatment of patients. Innovation in medical technologies improves health quality by providing more accurate systems, enabling new features and modalities. For example, in the recent past new hybrid imaging techniques such as *positron emission tomography / X-ray computed tomography* (PET/ X-ray CT), which is widely utilized for cancer diagnosis and treatment follow-up, emerged as an essential medical device utilized in oncology [1].

However, advanced medical devices are not equally available worldwide. According to a survey performed by the world health organization (WHO), only 10% of the countries have at least one *positron emission tomography* (PET) scanner unit. Although many countries did not provide data, this survey showed a high correlation between income level of a country and the availability of high-technology medical equipment [2].

Ideally, scientific research cannot only lead to innovation and technology transfer to industrial partners. Also, it can drive the medical technologies to cost-effective solutions that are available to a wider public, in addition to a broad dissemination of the latest achievements in the field.

1.1. MEDICAL IMAGING

Medical imaging techniques are a set of tools that allow medical doctors to study the human body in a *noninvasive way*. In other words, medical imaging acts as “the eyes of the medical professionals” that observe structures inside the human body, as well as functional and *molecular behavior* [3].

Examples of medical imaging modalities are X-ray CT, magnetic resonance imaging (MRI), PET, and ultrasound imaging (UI). There is not a superior or a universal medical imaging modality. Depending on the type of diagnosis or disease under study, one modality performs superiorly over the other ones. Nowadays, modern medical imaging systems combine several modalities into a single device in order to realize multimodal imaging systems, such as PET/CT.

1.1.1. STRUCTURAL AND FUNCTIONAL IMAGING

Structural imaging techniques allows to obtain medical images in terms of anatomical composition of tissues and skeletal information of the patient’s body. On the contrary, functional imaging techniques enables the observation of physiological processes in the patient’s body, such as cardiac pump function, organ flood flow, etc. [4, 5]. Nowadays, it is difficult to strictly classify medical imaging modalities into either structural or functional. Since the imaging technique of a single modality can potentially work as functional or structural depending of on type of medical study [6–8].

The first medical imaging modality was X-ray planar imaging [9]. As in any imaging systems, there must be one-to-one correspondence between a point in the object to be estimated and a point on the image sensor (see Figure 1.1). In clinical X-ray planar imaging this correspondence is achieved by utilizing a point-like X-ray source. This image modality operates in transmission mode because the X-ray penetrating power allows to image the inner structure of the body (see Figure 1.1).

Later, tomographic studies emerged as a powerful tool in order to obtain three di-

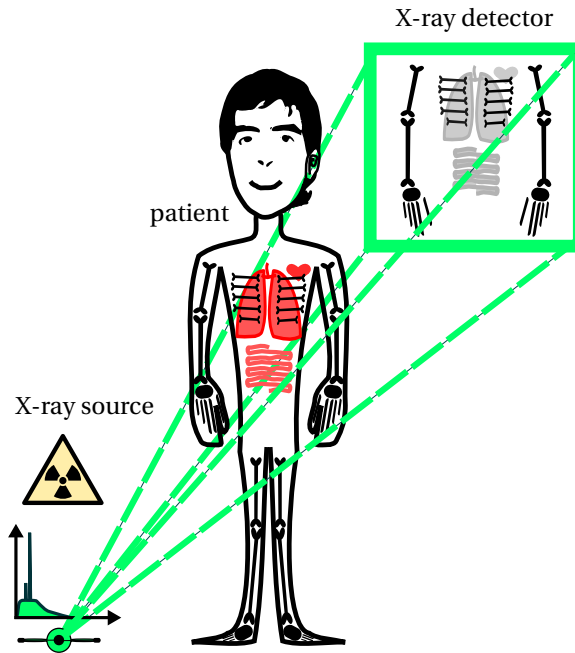


Figure 1.1: Forming process of a planar X-ray image.

dimensional (3D) information of the patient's body. For instance, in clinical X-ray CT the patient's body is placed between a rotating pair formed by a collimated X-ray source and an array of radiation detectors (see Figure 1.2). Since the radiation passes through the patient's body, a full 3D inner image can be reconstructed from the projection data [3]. A *fan-beam* of X-rays is generated by the source and directed towards the detectors. Subsequently, axial scanning is also required in the case of a whole-body study, which is realized by moving the scanning bed, in order to obtain volumetric data (see Figure 1.2). In helical X-ray CT acquisition mode, the scanning bed's movement is continuous [3].

In clinical X-ray CT, image contrast is limited by the X-ray linear attenuation of the different types of tissues of the patient's body. In the case of soft tissues, it is difficult to observe large contrasts, since the X-rays' attenuation difference between several types of soft tissues is not substantial. Typically, X-ray CT is utilized to observe structural changes in the patient's body, such as lesion assessment and trauma evaluation [9]. In addition, the utilization of X-ray CT in cardiology as a functional modality, particularly to determine cardiac infarct size, was already verified [6, 7].

Another relevant tomographic modality is MRI. This modality relies on a physical principle called nuclear magnetic resonance (NMR). In MRI, a net body magnetization is produced by placing the patient's body into a strong magnetic field, which is typically 1.5 T to 3 T [10]. It is possible to image the body by exciting regions selectively utilizing gradient coils and measuring the response signals with receiving coils [3]. Since MRI offers a better image contrast of soft tissues, it is widely utilized for musculoskeletal studies

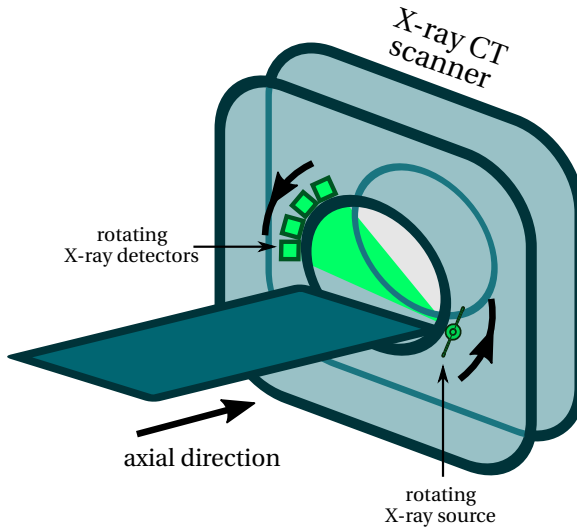


Figure 1.2: Schematic of an X-ray computed-tomography rotation system.

[11]. However, functional brain imaging in MRI was demonstrated few decades ago and nowadays it is widely utilized [8, 12].

1.1.2. MOLECULAR IMAGING

Since the mid-90s, molecular imaging has evolved as a set of tools and techniques that allow to visualize and quantify *in vivo* biological process at *cellular and molecular level* by utilizing specific *molecular probes*.

Molecular imaging enables temporal and spatial visualizations of molecular probes' distributions, which has been engineered in order to target specific cellular processes [4, 13, 14]. Functional and molecular imaging are linked to each other because of the relation between physiology and cellular processes. However, the main difference lies in the objective of molecular imaging that is the observation of cellular processes at a required *molecular sensitivity*.

Molecular probes are the image contrast enhancement agents utilized in molecular imaging. Any molecular probe must fulfill some requirements that:

- are biocompatible,
- reach the target and accumulate with enough concentration,
- and stay in the target during the imaging study without significant concentration reduction.

Nuclear medicine and in particular small-animal PET imaging have played a substantial role in the development of new molecular probes [5].

The main requirement of any imaging modality that is enabled to perform molecular imaging is to have enough molecular sensitivity. In order to qualitatively understand the trade-offs involved in the molecular sensitivity of a given image modality, a generic example of a molecular medical study is explained as follows:

- Firstly, a molecular probe is delivered to a patient and awaited until enough probe is accumulated into a target lesion.
- Later, an X-ray CT scan of the patient is performed and a structural image is obtained. Figure 1.3 shows an axial slice of the whole structural tomographic study.
- Lastly, the patient is exposed to a molecular imaging modality that measures and estimates the spatial and/or temporal distributions of the delivered molecular probe (see Figure 1.3, which depicts an axial slice of the molecular tomographic study).

This example would correspond to a PET/X-ray CT study, in which the structural information is estimated by a CT scanner and the molecular probe distribution is measured by a PET scanner.

Some of the delivered molecular probe reaches the target lesion; however, some probe, which adds undesired background counts, is absorbed by the tissues A and B (see Figure 1.3). In addition to the aspecific probe background, the imaging system itself adds noise counts that may also increase depending on the aspecific probe distribution.

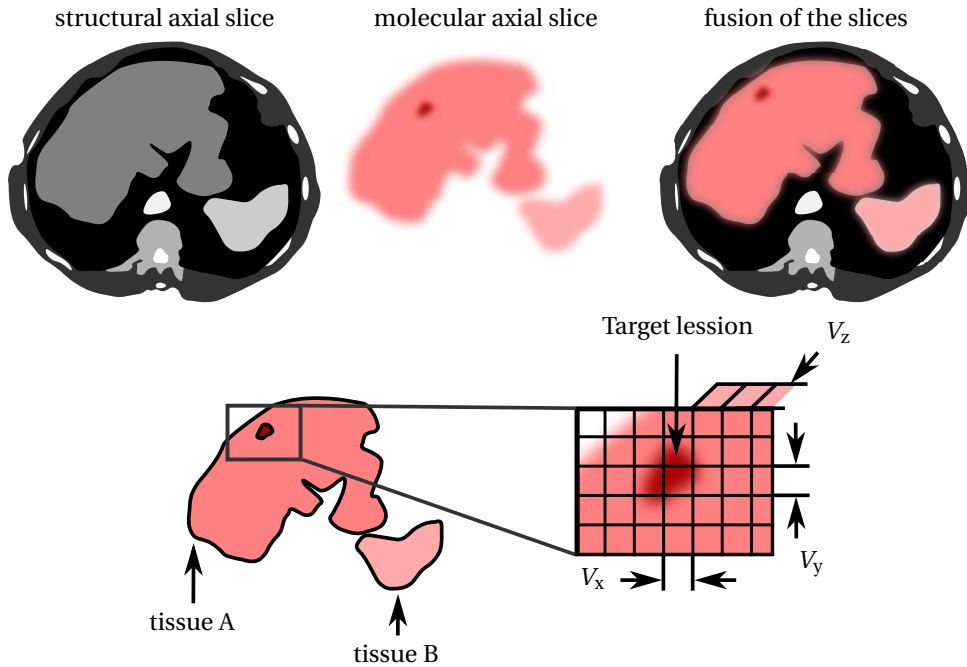


Figure 1.3: Representation of the molecular-imaging study example.

Under the previously defined conditions (see Figure 1.3, where V_x , V_y , and V_z represent the voxel dimensions), we can integrate the measured counts of the voxels that contain the target lesion as C_l . The counts in the lesion voxels accumulate specific and aspecific probe distributions' counts, as well as the corresponding noise counts of the molecular imaging modality. Also, we can estimate measured counts on a same size of voxel area but outside that target lesion, which is enclosed by the aspecific molecular

probe distribution, as C_{bg} . Additionally, we can consider C_{tl} and C_{bg} as random variables that follow Poisson statistics:

$$C_{tl} \sim P(\lambda_{ctl}) \quad (1.1a)$$

$$C_{bg} \sim P(\lambda_{cbg}), \quad (1.1b)$$

where $P(\lambda)$ is a Poisson distribution with mean value λ .

In order to obtain a more accurate estimation of the molecular probe concentration, a volume-of-interest (VOI) estimation method can be utilized instead of a voxel-based method [13, 15]. Here, we chose a voxel-base method in order to preserve the simplicity of the qualitative explanation. Molecular sensitivity is defined as the minimum amount of probe, which is detectable when background signal is present, per unit volume [5, 13, 14]. In order to define molecular sensitivity, we define the C_{diff} as

$$C_{diff} = C_{tl} - C_{bg}, \quad (1.2)$$

and propose to test the following hypothesis:

$$\begin{cases} H_0 : E(C_{diff}) = 0 \\ H_a : E(C_{diff}) > 0 \end{cases}, \quad (1.3)$$

with a significance level α . Since we are testing the detectability of the imaging modality scanner, H_0 is defined as the absence of signal. The minimum value that it is considered as signal is the $(1 - \alpha)^{th}$ percentile of the C_{diff} 's cumulative density function (CDF) in a voxel area of aspecific probe distribution (see Figure 1.4). And it is expressed as follows:

$$C_{min} = C_{diff} | [CDF(C_{diff}) = 1 - \alpha \wedge \lambda_{ctl-cbg} = 0]. \quad (1.4)$$

And finally, molecular sensitivity S , which is typically expressed in moles per liter, is given by

$$S = \frac{C_{min}}{N_A V_{vox}}, \quad (1.5)$$

where V_{vox} is the total volume of the voxels that enclose the target lesion expressed in liters, and N_A is the Avogadro's constant.

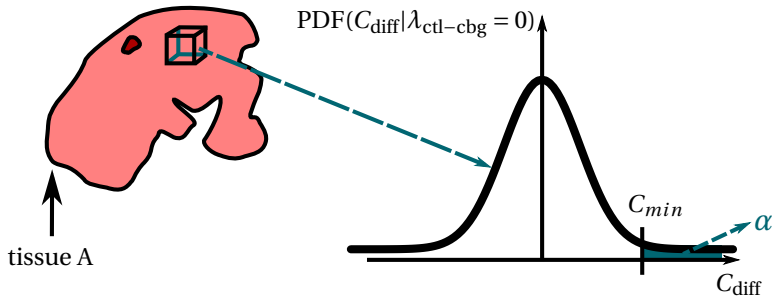


Figure 1.4: Hypothesis-testing representation of the molecular sensitivity example.

The background counts C_{bg} limits the minimum amount of detectable signal and they depend on the following aspects:

- The properties of the molecular probe and type, such as small molecules, nanoparticles, engineered proteins, etc. [14].
- aspecific probe distribution on the subject under study.
- Background noise specific to the imaging modality, which depends on the *instrumentation performance*.

By analyzing the qualitative example, the trade-offs involved in the minimization of C_{min} in terms of instrumentation performance, which is the scope of the thesis, can be determined. For example, in the case of small lesions the spatial resolution of the scanner influences directly on the partial volume effect that decreases C_{diff} and increases C_{bg} because of the lack of resolution. However, small resolution scanners require to collect more counts in order to keep the same uncertainty in the counts per voxel, which follow Poisson statistics [13, 16].

Estimating the molecular sensitivity quantitatively requires a more complex analysis that depends on many conditions related to the scanner hardware settings, image-reconstruction parameters, VOI delineation method, amount of delivered molecular probe, result observation of clinicians, type of medical or preclinical study, etc. [15, 17]. Therefore, for a given imaging modality the molecular sensitivity is expressed in a wide range of values (see Table 1.1, which is a comparisons summary of molecular imaging modalities) [5, 13, 14].

Several medical imaging techniques are qualified for molecular imaging, such as MRI, PET, single-photon emission computed tomography (SPECT), UI, and optical imaging (OI). However, PET is the most relevant molecular imaging technique because of its $\sim\text{pmolL}^{-1}$ molecular sensitivity range and large tissue penetration (see Table 1.1) [4, 5, 13, 14, 18, 19].

Furthermore, another central feature of a molecular imaging system is the quantitative accuracy in estimating the molecular probe concentration. Because in medical applications such as treatment monitoring in oncology, which requires accurate comparison between current and previous studies, accurate molecular probe quantification is mandatory.

1.2. POSITRON EMISSION TOMOGRAPHY

PET is an *emission-mode* tomography modality meaning that the patient is emitting the signals that are detected by the PET scanner, instead of being placed between the source and the detector system (see Figures 1.1 and 1.5). Another essential aspect of PET is *electronic collimation*, which is a detection method of electron-positron annihilations (see Figure 1.5)[20].

In PET, the patient is delivered with a molecular probe that is labeled with a positron-emitting radioisotope, such as ^{18}F -fludeoxyglucose, ^{18}F -FDG, or ^{62}Cu -labeled copper(II) pyruvaldehyde bis(N^4 -methylthiosemicarbazone), Cu(PTSM) (see Figure 1.5) [19, 21]. In the case of a PET study performed within the scope of oncology, the delivered molecular probe, which typically is ^{18}F -FDG, is utilized to detect cancer cells since they absorb abnormal quantities of ^{18}F -FDG. The high molecular sensitivity of PET makes this imaging modality unique in tumor detection and cannot be replaced by any other imaging modality in this field (see Table 1.1) [1].

Table 1.1: Comparison Table of molecular imaging modalities.

Imaging modality	detected signal type	signal penetrating depth (mm) ^a	molecular probe quantity (g) ^b	spatial resolution (mm) ^c	medical temporal resolution ^c	molecular sensitivity (molL ⁻¹) ^d	modality safety
SPECT	low-energy gamma-photons	>300	≈ 1n	1-2 ^e 8-10 ^f	minutes	10p-100p	ionizing radiation
PET	coincidence gamma photons	>300	≈ 1n	1-2 ^e 5-7 ^f	second-minutes	1p-10p	ionizing radiation
optical fluorescence imaging	near-infrared and visible light	<10	≈ 1μ-1m	2-3	second-minutes	≈ 1p-1n	-
Optical bioluminescence imaging	near-infrared and visible light	10-20	≈ 1μ-1m	3-5	second-minutes	≈ 0.01f-1f	-
MRI	radio-frequency waves	>300	≈ 1μ-1m	0.025-0.1 ^e 0.2-1 ^f	minutes-hours	10μ-1m	-
X-ray CT	X-rays	>300	not determined	0.050-0.2 ^e 0.5-1 ^f	minutes	not determined	ionizing radiation
UI	ultrasound waves	1-200	≈ 1μ-1m	0.01-0.1 ^g 1-2 ^h	second-minutes	not determined	-

^aValues according to [13] except for optical fluorescence imaging and optical bioluminescence imaging that are according to [14].

^bValues according to [5].

^cValues according to [14].

^dValues according to [14] except for US imaging that is according to [13].

^eThis value corresponds to preclinical systems.

^fThis value corresponds to clinical systems.

^gThis value corresponds to few mm depth imaging.

^hThis value corresponds to few cm depth imaging.

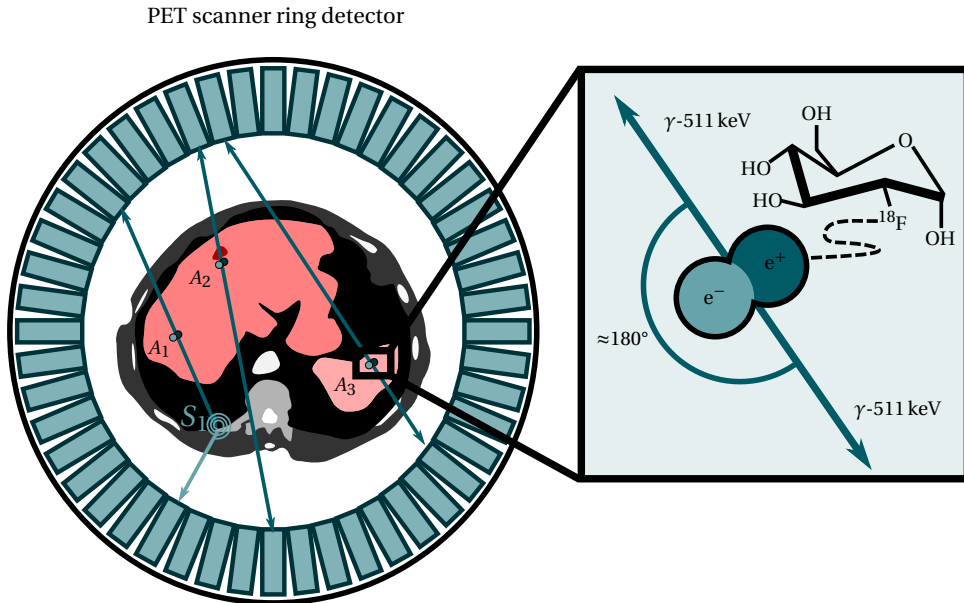


Figure 1.5: Diagram of the basic principle of PET.

When the ^{18}F radioisotope of the ^{18}F -FDG molecule emits a positron by means of β^+ decay. The positron travels a relatively short distance, which is known as *positron range*, before it encounters an electron where they combine to form a positronium (see Figure 1.5) [20]. This state lasts about hundreds of picoseconds before the electron-positron annihilation takes place. The result of the electron-positron annihilation is the emission of two γ -photons, which are emitted back-to-back (see Figure 1.5) [20].

The detection of the back-to-back simultaneous emission is known as electronic collimation, and this property is utilized to obtain image projections without the need of a physical collimator. In the case of single-photon emission computed tomography (SPECT) noncollinear low-energy γ -photons are detected. Therefore, a physical collimator, which is made of a high-density material, is required. In SPECT, the presence of the collimator significantly reduces the molecular sensitivity in comparison to PET (see Table 1.1) [20].

In PET, as well as in SPECT and X-ray CT, the volumetric spatial information is estimated from the projection data by an image-reconstruction algorithm. In the case of CT, the voxel information corresponds to X-ray attenuation level. In the case of PET or SPECT, the voxel information corresponds to molecular-probe concentration.

Another important aspect of the electron-positron annihilation is that the two γ -photons are emitted with the same energy, which is 511 keV, this is demonstrated by applying the conservation principles [1]. 511 keV γ -photons can be detected directly by a PET scanner ring, which is the case of the annihilations A_2 and A_3 (see Figure 1.5). However, in the annihilation A_1 there is a Compton interaction in the patient and one 511 keV γ -photon losses energy and deviate from its trajectory (see S_1 in Figure 1.5) [20].

PET image quality is intrinsically limited by the physics of electron-positron annihilation. This limitation lies on two main aspects:

- positron range
- and non-collinearity of 511 keV γ -photons.

The positron range depends on the kinetic energy that a positron has when it is emitted. This energy follows a continuous probability density function (PDF) with a parameters called the *energy endpoint* that depends on the positron-emitting radioisotope. For example, ^{18}F has an endpoint energy of 640 keV. The positron range also depends on the medium where the positron is emitted and the presence of a magnetic field, which is the case of PET/MRI.

The high detectability of the 511 keV γ -photons and the specificity of the ^{18}F -FDG are main reasons of the high molecular sensitivity of PET. Additionally, the accurate calculation of PET in detecting positron counts per voxel is reason of its excellent quantitative capabilities in molecular probe estimation.

In order to conclude the basic explanation of PET imaging, we invite the reader to consider a PET scanner as a single-positron counting machine. Because in principle with a given probability, it is capable of detecting single positrons. High timing resolution in the 511 keV γ -photons detection, which is known as coincidence resolving time (CRT), is required in order to estimate the position of the electron-positron annihilation by the direct time-of-flight (TOF) method. However, because of the limitations related to the molecular sensitivity and CRT, several counts must be detected in order to identify a significant change in the molecular probe concentration. Furthermore, the current status of TOF-PET scanner allows to estimate 511 keV γ -photon's timing difference a precision in the order of several hundreds of picoseconds. Subsequently, a TOF-PET scanner does not calculate the annihilation position by direct TOF, instead the timing information is utilized within the image-reconstruction algorithm [22].

1.2.1. ^{18}F -FLUDEOXYGLUCOSE

^{18}F -FDG is the most successful molecular probe utilized for in-vivo cancer detection because of its high accuracy [1] (see Figure 1.6). In addition, the success of PET, besides its poor spatial resolution compared to other imaging modalities (see Table 1.1), is related to its high intrinsic molecular sensitivity and the ^{18}F -FDG absorption accuracy as well [1].

The radioactive component of ^{18}F -FDG, which is ^{18}F , is a radioisotope that is synthesized utilizing single or dual particle cyclotrons. The half-life of ^{18}F -FDG, which is 109.7 minutes, allows for the distribution of ^{18}F -FDG to several medical centers from a centralized cyclotron production facility. In addition, it enables PET studies and the patient radioactivity decays within few hours. The most common cyclotron method to produce ^{18}F is the proton bombardment on an ^{18}O target [1, 19].

Depending on the cyclotron production method, the ^{18}F can be available in two different chemical species: electrophilic or nucleophilic. After producing the nucleophilic ^{18}F , the synthesis of the ^{18}F -FDG molecules is performed by combining the ^{18}F with precursors molecules following the nucleophilic substitution chemical procedure. The chemical process utilized with electrophilic ^{18}F is called electrophilic fluorination and

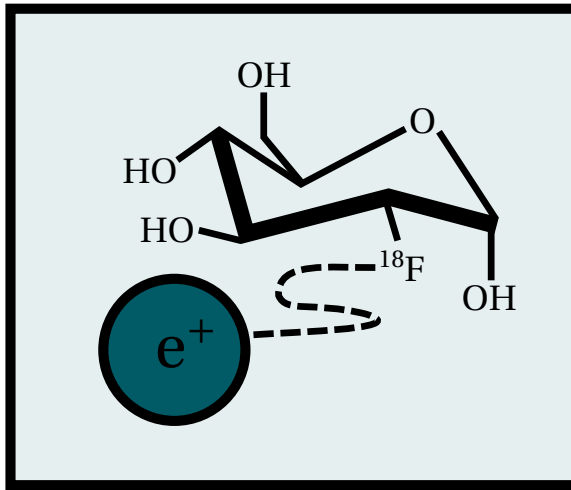


Figure 1.6: ^{18}F -FDG molecule structure

it was the first method utilized in the ^{18}F -FDG synthesis for PET. However, this method was replaced by nucleophilic substitution. The main reason is the resulting low specific activity in the production of electrophilic ^{18}F [1, 23].

1.2.2. PET SCANNER BASICS

A PET scanner acquisition detects millions of positrons and calculates a line-of-response (LOR) for each valid detected pair of γ -photons (see Figure 1.5). After collecting millions of LORs, an image-reconstruction algorithm estimates the molecular probe volumetric distribution by utilization the projection data as its input [1, 20].

In order to detect the two 511 keV back-to-back γ -photons that correspond to the same electron-positron annihilation and calculate their correct LOR (see Figure 1.7), individual PET detector modules of a PET ring estimate the following γ -photon characteristics:

- its deposited γ -energy,
- timemark,
- and the spatial coordinates of the point-of-interaction (POI).

γ -photons that lost energy by Compton interactions can be detected and discarded by measuring the energy that they deposited in the PET detector ring (see Figures 1.5 and 1.7). An energy-window filter is applied to discard and validate events, and the size of the window depends on the energy resolution of the PET detector modules. Typically, the energy window size is hundreds of keV wide [24].

A γ -photon's timemark is defined as its time-of-arrival (TOA) estimation with respect to a global clock of the PET scanner. In PET, the electronic collimation is realized by measuring timemark distances between detected 511 keV γ -photons. In other words, the validation that two simultaneous detections of 511 keV γ -photons belong to the same

annihilation process is performed by a time-window filter. There is a probability that two 511 keV γ -photons fall into the coincidence time window even though they belong to different annihilation processes. This probability depends on the 511 keV γ -photons rate, which is known as single count rate, and the size of the coincidence time window. These false detections are called the random coincidences [20].

Within the scope of this thesis, timemark is referred to a time-of-arrival estimation of a γ -photon. And, timestamp is referred to a time-of-arrival estimation of light photon, which is introduced in the following subsections and chapters.

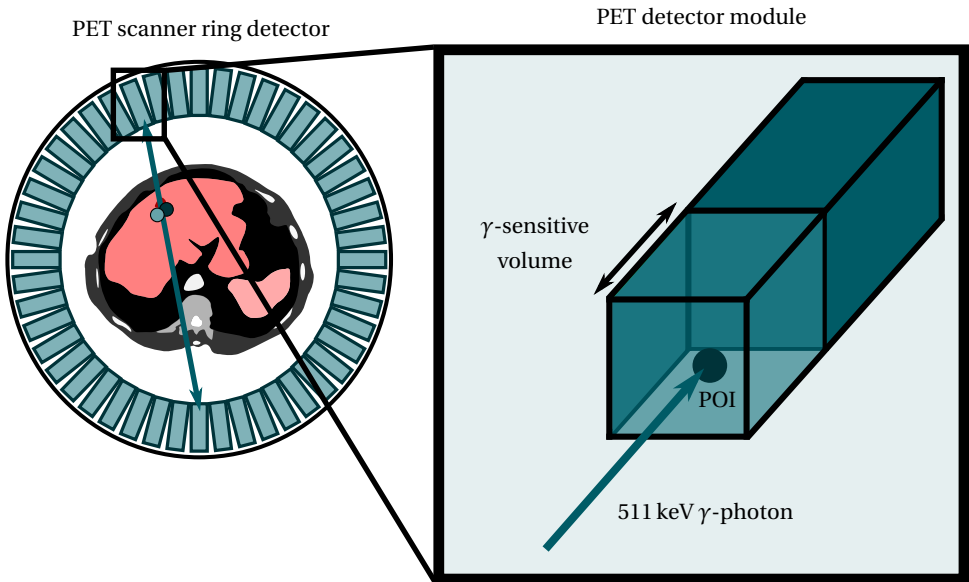


Figure 1.7: PET scanner ring and individual PET detector module representations.

Finally, a LOR is calculated utilizing the spatial coordinates of the two POIs of validated 511 keV γ -photons, which corresponds to the points where the two back-to-back γ -photons are detected within the γ -sensitive volumes of the individual PET detector modules (see Figure 1.7).

1.2.3. PET DETECTOR CHALLENGES

In any PET scanner, the detector parameters are designed in order to maximize the molecular sensitivity, which mainly depends on the PET scanner application.

For instance, in the case of small-animal PET imaging the VOI is smaller; subsequently, a higher POI precision is required with respect to whole-body PET imaging. In addition, TOF information improves the signal-to-noise (SNR) ratio of PET reconstructed images, because it limits the uncertainty of the positron's emission-point position within a single LOR [22]. However, this improvement is significant only for PET scanners with large diameters.

The main parameters to improve in a PET detector are the followings:

- γ -photon detection efficiency,
- POI spatial resolution,
- timemark resolution,
- and γ -energy resolution.

In any PET scanner applications, the γ -photon detection efficiency is the main parameter to maximize, since the precision and accuracy of the image-reconstruction algorithms relies on the statistical quality of the projection data. The improvement priority among the rest of the parameters depends on the specific PET scanner application.

Typically, PET detector modules are implemented coupling a high-density scintillation material to a photodetector. The γ -photon interacts with the scintillator, which is described as the γ -sensitive volume in Figure 1.7, and it produces a transient light pulse that is measured by a photodetector [20]. A comprehensive description of the technological aspects of PET scanners is explained in chapter 2.

1.3. PET SCANNER MODALITIES

As stated in the introduction of this thesis, there is not a superior imaging modality that would allow a full observation of all the aspects of a disease. Subsequently, the combination of imaging modalities into a single multimodal medical imaging system allows to investigate several aspects of a disease simultaneously. PET scanners are combined into multimodal medical imaging systems such as PET/CT or PET/MRI, which target a more comprehensive observation of specific medical or preclinical studies.

1.3.1. WHOLE-BODY MULTIMODAL PET/CT SYSTEMS

Nowadays, one can hardly find a PET-only scanner in any medical centers worldwide. The major PET vendors no longer offer new PET-only scanners, since PET/CT combines structural and molecular information by using a single machine [25].

In principle, a hospital that is equipped with a PET scanner and a CT scanner separately can combine CT and PET images, by utilizing software-based registration and fusion algorithms. This approach has several disadvantages, for example if several days had elapsed between the PET and CT scans, the disease progression could not be registered by the medical study that was performed first. In addition, from the hospital and patient logistical point of views, it is more convenient to perform the study in a single appointment and location [1].

A PET/CT scanner combines a CT and PET scanners into the same gantry (see Figure 1.8). In this way, the image registration becomes simpler and more accurate. In addition, the CT scan duration is much shorter than the PET scan duration; subsequently, simultaneous acquisition is not mandatory although desirable. Sequential acquisition has the advantage that two different detector systems, which are optimized for an specific function, can be integrated next to each other (see Figure 1.8). Furthermore, a physical separation allows almost no signal interference between integrated imaging system modalities [1].

Besides the increment in the scanner cost, one of the main disadvantages of PET/CT with respect to PET-only is the increase in the radiation dose of the patient. A typical PET scan dose is approximately 3-4 mSv and the CT dose range is about 1-20 mSv depending

on the CT scan purpose and quality. As a reference, natural radiation exposure accounts to about $3\text{--}5\ \mu\text{Svd}^{-1}$ in most locations in Europe. The patient dose becomes critical in pediatric medical applications [26]. Besides this main drawback, PET/CT has gained a central role in oncology imaging because of its high accuracy in cancer evaluation. The latest generation of PET/CT scanners are able to perform simultaneous PET and CT acquisitions by combining the PET and CT detectors within the same rotating gantry.

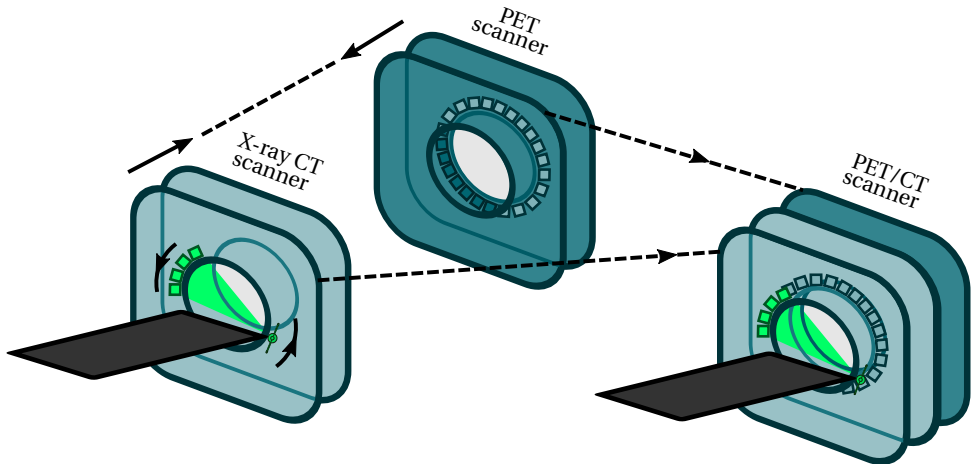


Figure 1.8: PET/CT scanner representation.

1.3.2. BRAIN PET INSERT (PET/MRI)

It is also possible to integrate PET and MRI scanners into a multimodal imaging system. However, the PET/MRI system integration is a challenging undertaking mainly because of technical limitations related to the interference between modalities. In addition, the clinical advantage of PET/MRI over PET/CT is limited only to soft-tissue imaging, such as brain and abdomen, where MRI performs superiorly over CT [10, 27, 28]. A clear advantage of PET/MRI over PET/CT is the elimination of the PET/CT radiation dose.

The first challenge related to PET/MRI is the unpractical sequential acquisition. The reason of this limitation is the long acquisition times required for both modalities, which are about 20–40 min each scan. Besides, the combination of both scanners in the axial direction would result into a long PET/MRI scanner that requires a larger hospital room (see Figures 1.8 and 1.9) [10].

PET/MRI is only practical with simultaneous acquisitions, which implies the integration of both modalities within the same gantry. This integration is performed by reducing the size of the PET detectors, in order to insert them into an MRI scanner (see Figure 1.9) [10, 27, 28]. In addition, the required high magnetic field, which is typically between 1.5–3 T in whole-body MRI scanners, imposes extra constraints in the design of the PET detectors. Conversely, inserting a compact PET subsystem inside an MRI superconducting magnet affects the required uniformity of the high magnetic field [10].

In order to achieve the PET/MRI integration, specialized PET detector that are

magnetic-field intensive are designed [10, 27, 28]. In addition, the PET detectors are also designed in order to minimize the interference against the MRI subsystem [28]. Furthermore, compact PET detector rings with smaller diameters, which are dedicated for brain-PET imaging, are implemented in order to insert them into standard MRI scanners [28]. Nowadays, PET/MRI scanners exist as commercially availability medical devices.

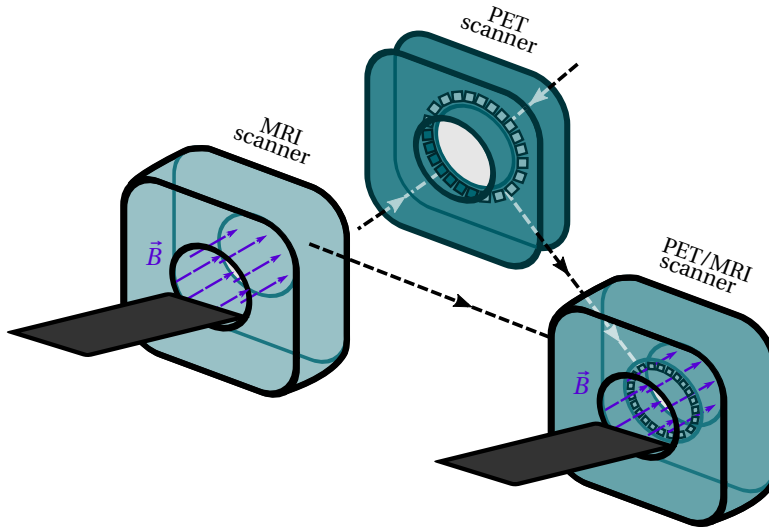


Figure 1.9: PET/MRI scanner representation.

1.3.3. ENDOSCOPIC PET INSTRUMENTATION (PET/US)

Endoscopic PET probes allow to place the detectors in the proximity of the VOI within the patient's body. The main advantage of this approach is the reduction of aspecific probe counts generated by organs that have a high normal absorption of molecular probe, such as the liver and the heart uptakes of ^{18}F -FDG [29].

The EndoTOFPET-US project main objective was to develop an asymmetric PET detector geometry composed of an external PET detector plate in combination with a PET/US probe system (see Figure 1.10) [29–31]. The target application of the EndoTOFPET-US was the development of new molecular probes for prostate and pancreatic cancers. This asymmetric PET scanner geometry faced several challenges:

- unfavorable solid angle coverage,
- incomplete projection information,
- required an effective random count rejection method,
- high integration/miniaturation of a PET detector into an endoscopic probe,
- and high spatial and timing resolution PET detector design.

The 511 keV back-to-back γ -photons emitted during an electron-positron annihilation have a uniform angular PDF. Subsequently, the positron detection efficiency, which is known as *PET sensitivity*, depends directly on the PET detector coverage of the positron

emitting volume. As observed in Figure 1.10, the detector coverage is unfavorable for the detection of 511 keV back-to-back γ -photons. However, the close proximity of the PET/US probe to the target volume mitigates the PET sensitivity reduction. Another disadvantage of the reduced solid-angle coverage is the incomplete projection information, which represents a challenge for the PET image-reconstruction algorithm.

Although the aspecific probe counts generated by high-uptake organs is reduced, the ratio between single count rate (amount of single 511 keV γ -photons detected per time unit) and the true count rate (amount of valid pairs of 511 keV γ -photons detected per time unit) is highly unfavorable. Mainly because of the incomplete detector coverage. In order to reject a high rate of random coincidence, the PET detectors were design with a sub-200 ps CRT. Therefore, the random coincidence rate is reduced by narrowing down the coincidence time window [29, 30].

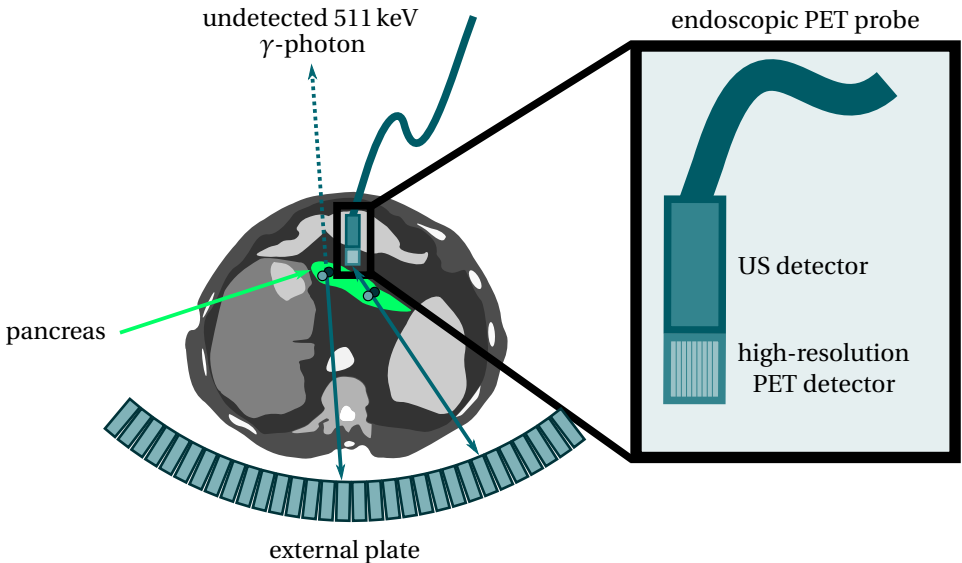


Figure 1.10: EndoTOPPET-US concept.

The miniaturization and integration of a compact PET detector module within a commercial US probe represented a major technical challenge [29–31]. In addition, in order to detect small lesions and effectively avoid random coincidences the PET/US probe was designed with demanding spatial and timing resolution constrains. The details about this implementation are discussed in chapter 6.

1.4. RESEARCH MOTIVATION AND OBJECTIVES

Molecular imaging enables early detection of diseases, such as cancer, before they produce structural lesions. Additionally, medical-treatment monitoring and development of new pharmaceuticals is guided by molecular imaging instrumentation. A more precise observation of molecular and cellular processes is only possible by increasing the molecular sensitivity of the current technologies. Furthermore, availability and open-

ness of molecular imaging technologies are essential for improving the health-care quality extensively.

The primary objective of this thesis is the comprehensive analysis, realization, and characterization of next-generation PET detector technologies that are capable of extending the molecular sensitivity and enabling new detection features [31, 32]. PET detector modules that are based on research technologies as building blocks demand a challenging level of complexity, in order to achieve successful results. Therefore, the investigation of PET detector modules that are based on standard components, which achieve state-of-the-art performance, is also a central objective of this work [33]. In this way, state-of-the-art performance is available to a wider academic or industrial audience. Additionally, the next-generation PET detector modules are fully described and characterized in order to successfully disseminate the presented technologies.

1.5. THESIS CONTRIBUTIONS

The thesis contributions are subdivided into theoretical disciplines, such as estimation theory, as well as technological ones such as the realization of next-generation detector modules. Both disciplines are strongly interconnected to each other; however, the theoretical aspects of the detection process predefine the technological specification of the physical detection systems.

1.5.1. THEORY OF TIMING ESTIMATION WITH MD-SiPMs

When a γ -photon interacts within the sensitive area of a PET detector module, it produces a signal that is timestamped in order to estimate the TOA. The timemark estimation precision rely on the amount of information that can be extracted from the PET detector module [34]. Before the beginning of this research work, this limit in precision, which is known as the Cramér–Rao lower bound (CRLB), in the timemark estimation was already established [34]. However, generalized estimation methods that achieve this limit were not described. In this thesis, a comprehensive and extensive analysis of timemark estimation methods is presented [32, 35].

1.5.2. METROLOGY AND γ -PHOTON DETECTION WITH MD-SiPMs

Next-generation photodetector technologies, which are a key-component of PET detector modules, such as multichannel digital silicon photomultipliers (MD-SiPMs) enables new features like multiple timestamping of light photons [36]. The MD-SiPMs were fully explored and characterized by performing a systematic analysis. For the first time, the measurement methods to extract the MD-SiPM metrics were developed and successfully implemented.

1.5.3. ENDOSCOPIC AND SMALL-ANIMAL PET DETECTOR MODULES

The integration of high spatial and timing resolution PET detectors into an endoscopic probe enables new multi-modal PET systems [29–31]. In addition, the development of small-animal PET modules with improved features is essential for building small-animal PET scanners that are utilized in preclinical applications. The system integration of MD-SiPMs into a PET detector module was investigated, implemented, and fully character-

ized [31, 37].

1.5.4. ASIC-LESS TOF-PET BASED ON A-SiPMs

As explained in the beginning of this work, medical technologies are only successful if they reach the majority of the population. In this regard, this thesis demonstrates that state-of-the-art PET performance is achieved by utilization technologies that are cost-effective and widely available, such as analog silicon photomultipliers (A-SiPMs) and field-programmable gate arrays (FPGAs) [33].

1.6. THESIS ORGANIZATION

In chapter 2, a full description of the main PET scanner parameters is introduced, in addition to technical details about the specific components of PET detector modules. Then, a thorough theoretical analysis of timemark estimation methods is presented in chapter 3. Further, in chapter 4, a detailed description of the design and characterization of PET detector modules based on standard components is given. Continuing, chapter 5 presents the measurement methods for the characterization of the metrics related to the MD-SiPMs. The realization and performance analysis of PET detector modules based on MD-SiPMs are addressed in chapter 6, as well as its radiation characterization. Last, chapter 7 summarizes the most relevant findings of this thesis within the scope of molecular imaging and it also gives an outlook regarding the technological directions of PET instrumentation.

REFERENCES

- [1] D. Bailey, D. Townsend, P. Valk, and M. Maisey, *Positron Emission Tomography: Basic Sciences* (Springer London, 2006).
- [2] World Health Organization, *Global atlas of medical devices* (World Health Organization, 2017).
- [3] J. Prince and J. Links, *Medical Imaging Signals and Systems* (Pearson, 2014).
- [4] W. Semmler and M. Schwaiger, *Molecular Imaging I*, Handbook of Experimental Pharmacology (Springer Berlin Heidelberg, 2008).
- [5] T. F. Massoud and S. S. Gambhir, *Molecular imaging in living subjects: seeing fundamental biological processes in a new light*. Genes & development 17 5, 545 (2003).
- [6] J.-F. Paul, M. Wartski, C. Caussin, A. Sigal-Cinqualbre, B. Lancelin, C. Angel, and G. Dambrin, *Late Defect on Delayed Contrast-enhanced Multi-Detector Row CT Scans in the Prediction of SPECT Infarct Size after Reperfused Acute Myocardial Infarction: Initial Experience*, Radiology 236, 485 (2005), PMID: 15972333, <https://doi.org/10.1148/radiol.2362040912>.
- [7] T. Kido, A. Kurata, H. Higashino, Y. Sugawara, H. Okayama, J. Higaki, H. Anno, K. Katada, S. Mori, S. Tanada, M. Endo, and T. Mochizuki, *Cardiac imaging using*

- 256-detector row four-dimensional CT: preliminary clinical report, *Radiation Medicine* 25, 38 (2007).
- [8] S. Ogawa, D. W. Tank, R. Menon, J. M. Ellermann, S. G. Kim, H. Merkle, and K. Ugurbil, *Intrinsic signal changes accompanying sensory stimulation: functional brain mapping with magnetic resonance imaging*, *Proceedings of the National Academy of Sciences* 89, 5951 (1992), <http://www.pnas.org/content/89/13/5951.full.pdf>.
- [9] C. Miller, J. Krasnow, and L. Schwartz, *Medical Imaging in Clinical Trials* (Springer London, 2014).
- [10] S. Vandenberghe and P. K. Marsden, *PET-MRI: a review of challenges and solutions in the development of integrated multimodality imaging*, *Physics in Medicine & Biology* 60, R115 (2015).
- [11] G. Liney, *MRI in Clinical Practice* (Springer London, 2007).
- [12] S. Faro and F. Mohamed, *Functional MRI: Basic Principles and Clinical Applications* (Springer New York, 2006).
- [13] C. S. Levin, *New Imaging Technologies to Enhance the Molecular Sensitivity of Positron Emission Tomography*, *Proceedings of the IEEE* 96, 439 (2008).
- [14] M. L. James and S. S. Gambhir, *A Molecular Imaging Primer: Modalities, Imaging Agents, and Applications*, *Physiological Reviews* 92, 897 (2012), pMID: 22535898, <https://doi.org/10.1152/physrev.00049.2010>.
- [15] J. Yan, J. Schaefferkoetter, M. Conti, and D. Townsend, *A method to assess image quality for Low-dose PET: analysis of SNR, CNR, bias and image noise*, *Cancer Imaging* 16, 26 (2016).
- [16] G. Knoll, *Radiation Detection and Measurement* (John Wiley & Sons, 2010).
- [17] S. Adler, J. Seidel, P. Choyke, M. V. Knopp, K. Binzel, J. Zhang, C. Barker, S. Conant, and R. Maass-Moreno, *Minimum lesion detectability as a measure of PET system performance*, *EJNMMI Physics* 4, 13 (2017).
- [18] W. Semmler and M. Schwaiger, *Molecular Imaging II*, *Handbook of Experimental Pharmacology* (Springer Berlin Heidelberg, 2008).
- [19] P. Schubiger, L. Lehmann, and M. Friebe, *PET Chemistry: The Driving Force in Molecular Imaging*, *Ernst Schering Foundation Symposium Proceedings* (Springer Berlin Heidelberg, 2007).
- [20] M. R. Phelps, *PET: Physics, Instrumentation, and Scanners* (Springer Science+Business Media, 2006).

- [21] H. Young, P. Carnochan, J. Zweit, J. Babich, S. Cherry, and R. Ott, *Evaluation of copper(II)-pyruvaldehyde bis (N-4-methylthiosemicarbazone) for tissue blood flow measurement using a trapped tracer model*, *European Journal of Nuclear Medicine* 21, 336 (1994).
- [22] W. a. Moses, *Time of flight in PET revisited*, *Nuclear Science, IEEE Transactions on* 50, 1325 (2003).
- [23] IAEA, *Introducing radioactive fluorine into glucose core structure* ((accessed May 31, 2018)).
- [24] G. Bolard, J. O. Prior, L. Modolo, A. Bischof Delaloye, M. Kosinski, C. Wastiel, J. Malterre, S. Bulling, F. Bochud, and F. R. Verdun, *Performance comparison of two commercial BGO-based PET/CT scanners using NEMA NU 2-2001*, *Medical physics* 34, 2708 (2007).
- [25] D. W. Townsend, *Combined positron emission tomography-computed tomography: the historical perspective*, in *Seminars in Ultrasound, CT and MRI*, Vol. 29 (Elsevier, 2008) pp. 232–235.
- [26] R. Boellaard, M. J. O’Doherty, W. A. Weber, F. M. Mottaghy, M. N. Lonsdale, S. G. Stroobants, W. J. G. Oyen, J. Kotzerke, O. S. Hoekstra, J. Pruim, P. K. Marsden, K. Tatsch, C. J. Hoekstra, E. P. Visser, B. Arends, F. J. Verzijlbergen, J. M. Zijlstra, E. F. I. Comans, A. A. Lammertsma, A. M. Paans, A. T. Willemsen, T. Beyer, A. Bockisch, C. Schaefer-Prokop, D. Delbeke, R. P. Baum, A. Chiti, and B. J. Krause, *FDG PET and PET/CT: EANM procedure guidelines for tumour PET imaging: version 1.0*, *European Journal of Nuclear Medicine and Molecular Imaging* 37, 181 (2009).
- [27] H.-P. W. Schlemmer, B. J. Pichler, M. Schmand, Z. Burbar, C. Michel, R. Ladebeck, K. Jattke, D. Townsend, C. Nahmias, P. K. Jacob, *et al.*, *Simultaneous MR/PET imaging of the human brain: feasibility study*, *Radiology* 248, 1028 (2008).
- [28] J. Wehner, B. Weissler, P. Dueppenbecker, P. Gebhardt, D. Schug, W. Ruetten, F. Kiessling, and V. Schulz, *PET/MRI insert using digital SiPMs: Investigation of MR-compatibility*, *Nuclear Instruments and Methods in Physics Research Section A: Accelerators, Spectrometers, Detectors and Associated Equipment* 734, 116 (2014), pSMR2013 - PET-MR and SPECT-MR: Current status of Instrumentation, Applications and Developments.
- [29] B. Frisch, E.-U. Collaboration, *et al.*, *Combining endoscopic ultrasound with time-of-flight PET: the EndoTOFPET-US project*, *Nuclear Instruments and Methods in Physics Research Section A: Accelerators, Spectrometers, Detectors and Associated Equipment* 732, 577 (2013).
- [30] N. Aubry, E. Auffray, F. Mimoun, N. Brillouet, R. Bugalho, E. Charbon, O. Charles, D. Cortinovis, P. Courday, A. Cserkaszy, *et al.*, *EndoTOFPET-US: a novel multimodal tool for endoscopy and positron emission tomography*, *Journal of Instrumentation* 8, C04002 (2013).

- [31] E. Venialgo, S. Sinha, T. Gong, S. Mandai, A. Carimatto, S. E. Brunner, D. R. Schaart, and E. Charbon, *Small-animal and endoscopic PET detector modules based on multichannel digital silicon photomultipliers*, in *Nuclear Science Symposium, Medical Imaging Conference and Room-Temperature Semiconductor Detector Workshop (NSS/MIC/RTSD), 2016* (IEEE, 2016) pp. 1–5.
- [32] E. Venialgo, S. Mandai, T. Gong, D. R. Schaart, and E. Charbon, *Time estimation with multichannel digital silicon photomultipliers*, *Physics in Medicine & Biology* 60, 2435 (2015).
- [33] E. Venialgo, N. Lusardi, A. Geraci, K. O’Neill, S. Gnecci, C. Jackson, S. E. Brunner, D. R. Schaart, and E. Charbon, *An order-statistics-inspired, fully-digital readout approach for analog SiPM arrays*, in *2016 IEEE Nuclear Science Symposium, Medical Imaging Conference and Room-Temperature Semiconductor Detector Workshop (NSS/MIC/RTSD)* (2016) pp. 1–5.
- [34] S. Seifert, H. van Dam, and D. Schaart, *The lower bound on the timing resolution of scintillation detectors*, *Phys. Med. Biol.* 57, 1797 (2012).
- [35] E. Venialgo, S. Mandai, and E. Charbon, *Time mark estimators for MD-SiPM and impact of system parameters*, in *Nuclear Science Symposium and Medical Imaging Conference (NSS/MIC), 2013 IEEE* (2013) pp. 1–2.
- [36] S. Mandai, V. Jain, and E. Charbon, *A fully-integrated 700x800 μm^2 multi-digital silicon photomultiplier with column-parallel time-to-digital converter*, in *ESSCIRC (ESSCIRC), 2012 Proceedings of the* (2012) pp. 89–92.
- [37] E. Venialgo, S. Mandai, and E. Charbon, *MD-SiPM PET detector module design*, in *Nuclear Science Symposium and Medical Imaging Conference (NSS/MIC), 2014 IEEE* (IEEE, 2014) pp. 1–4.

2

FROM A PET SCANNER TO A SPAD

The current chapter introduces the basics of γ -radiation detection, and describes the main parameters of a PET scanner by following a top-down approach. In the first section, introductory concepts of γ -radiation transport, PET scanner system-level features, and image-reconstruction are described. In the later section, the detector modules of a PET ring are explained by introducing their two main components: scintillation materials and photodetectors [1]. The most relevant and state-of-the-art photodetector utilized in molecular instrumentation is the silicon photomultiplier (SiPM). The building blocks of the SiPMs are the single-photon avalanche diodes (SPADs). These key elements set a limit in the performance of the SiPMs and they are the smallest granular unit of the detection system. The basic features of the SiPM-optimized SPADs are described at the end of this chapter.

2.1. PET SCANNER RELEVANT PARAMETERS

The precision and accuracy in estimating a molecular-probe concentration depends on the statistical quality of the projection data, which limits the performance of the image-reconstruction algorithm. Additionally, the quality of the projection data relies on the features of the PET scanner acquisition system (see Figure 2.1).

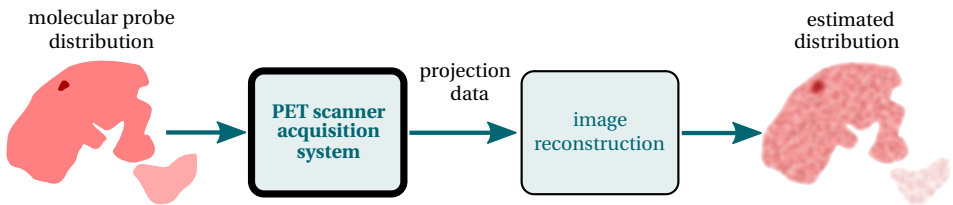


Figure 2.1: Block diagram of the data processing flow of PET.

The amount of detected valid γ -event pairs impacts on the statistical quality of the projection data, which can be modeled with Poisson statistics [1, 2]. This influences on the image-reconstruction accuracy because in Poisson statistics there is a direct relationship between mean-value estimation accuracy and the number of total valid counts [3]. Therefore, in any PET scanner modality one of the main parameter in consideration is the *effective sensitivity* [2].

The amount of false detections, such miscalculated LORs because of Compton scattered γ -photons or random coincidences, degrades the image quality [1]. Subsequently, the ability of a PET scanner to reject the false detections is directly related to its energy resolution and time-window size. Lastly, the spatial resolution restricts the capability to detect small lesion; therefore, the detection of molecular probe that is concentrated in small target volumes demands a finer spatial granularity.

In the following subsections these four main parameters:

- energy resolution,
- timing resolution,
- spatial resolution,
- and effective counting

are explained as well as image-reconstruction basics.

2.1.1. BASICS OF γ -PHOTON TRANSPORT

The main two process in which 511 keV γ -photons interact with matter are photoelectric effect and Compton scattering. Other types of interactions, such as pair-production or coherent scatter, are neglected since they do not occur at all or have a low interaction probability at 511 keV in comparison to photoelectric effect and Compton scattering [2, 4, 5].

These types of interactions are characterized at macroscopic level by a linear attenuation coefficient μ_t that depends on the energy of the interacting γ -photon and the composition of the medium. The total linear-interaction PDF is given by

$$i_t(t) = e^{-\mu_t t \|l\|_2}. \quad (2.1)$$

Where μ_t is the total linear attenuation coefficient, which includes the contribution of Compton scattering μ_c and photoelectric effect μ_p . The relationship between the linear attenuation coefficients is

$$\mu_t = \mu_c + \mu_p. \quad (2.2)$$

In equation (2.1), t represents a point in the segment L , which intersects the interacting material with the γ -photon trajectory (see Figure 2.2). L is given by

$$L = \{l_0 + t l \mid t \in [0, 1]\}. \quad (2.3)$$

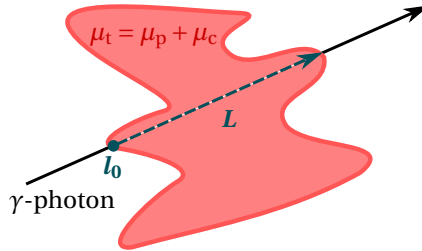


Figure 2.2: Geometrical description of the linear attenuation coefficient's setup.

When a Compton interaction occurs at t_c , the γ -photon partially loses energy and changes its direction. The absorbed energy is mainly transferred to a recoil electron (see Figure 2.3). The relationship between the initial γ -photon energy E , the scattered γ -photon energy E' , and the scattering angle θ_c is obtained by applying the momentum and energy conservation laws, and expressed by

$$E' = \frac{E}{1 + \frac{E}{m_e c^2} (1 - \cos \theta_c)}. \quad (2.4)$$

As result of the scattering collision, a cone of equally possible trajectories is defined by θ_c , which determines the new trajectory of the γ -photon' (see Figure 2.3). The θ_c PDF is described by the Klein-Nishida formula [1].

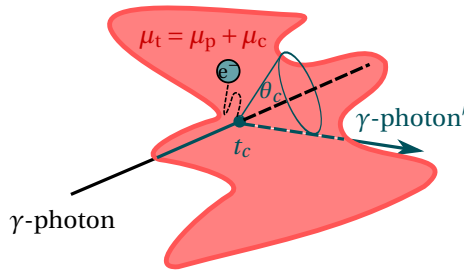


Figure 2.3: Representation of the Compton scatter process.

When a photoelectric interaction occurs, the γ -photon is completely stopped and most of its energy is transfer to a recoil electron. The difference between the recoil electron's kinetic energy and the initial γ -photon's energy is the electron's binding energy [2]. In practice, multiple interactions occur in the different materials where γ -photon are transported, such as the patient's body or PET detector rings. For example, in Figure 2.4 S_1 and S_2 represents subsequent Compton scattering interactions that are followed by a full photoelectric absorption P_1 . In reality, the radiation-transport process is more complex since the recoil electrons also generates more particles, when they interact with matter.

The γ -photon radiation transport is physical phenomenon that fits perfectly in the Monte Carlo simulation methods, because of the random nature and particle-type behavior of γ -photons. In PET medical imaging, several Monte Carlo simulation tools are available such as GATE/Geant4 [6, 7].

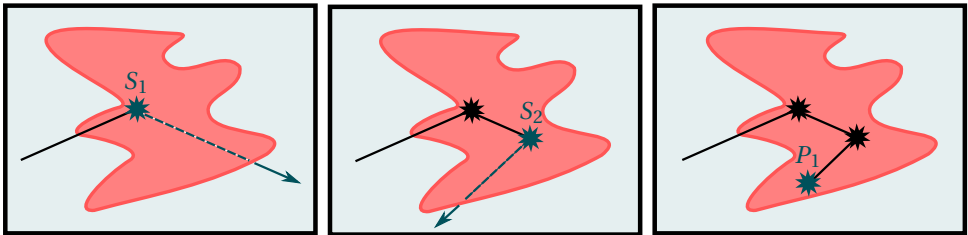


Figure 2.4: Representation of multiple interactions.

2.1.2. ENERGY RESOLUTION

In an energy-resolution experiment, a detector material is exposed to a γ -radioactive source and an energy histogram is built from the measured detection data (see Figure 2.5).

When the detector material is exposed to a γ -radioactive source that mainly emits mono-energetic radiation E_γ , some γ -photons deposit partial energy in a single Compton scattering interaction and escape. This type of interactions adds counts in the Compton spectrum of the histogram (see Figure 2.5). The maximum Compton-interaction de-

posited energy is lower than E_γ since it corresponds to a scattering angle θ_c of 180° (see Figure 2.5 and equation (2.4)). However, when more than one interaction occurs and the photon escapes, the deposited energy can be higher than $E_\gamma - E\gamma'(180^\circ)$. If a γ -photon is fully stopped by multiple or single interactions, it deposits its total energy E_γ and adds a count in the photopeak region of the histogram (see Figure 2.5) [5].

The energy resolution (ER) of the detector, which is specified at a particular E_γ , is calculated as follows:

$$\text{ER}|_{E_\gamma} = \frac{\text{FWHM}_\gamma}{E_\gamma} (\%). \quad (2.5)$$

In PET, the energy-window filter rejects Compton scattered events but also rejects 511 keV γ -photons that did not deposited the full energy into the detector material. Therefore, the detector's designer must maximize the counts within the photopeak region. This is achieved by choosing detector materials with a high μ_p and low μ_c if possible, and a suitable detector geometry. In addition, the sharpness of the photopeak region is blurred by the ER of the detector; therefore, the energy-window size is determined by the ER and it affects the efficiency of the Compton scattering rejection.

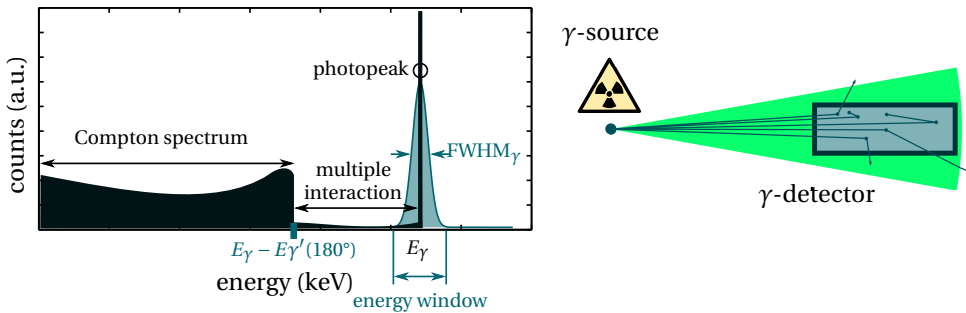


Figure 2.5: Representation of the detector energy resolution's setup.

When an object is placed between the detector and the radiative source, Compton scattering occurs in the object and γ -photons are deviated. These scattered γ -photons are detected with energies lower than E_γ ; however, if they enter into the energy window they are considered valid detections (see Figure 2.6). Narrow energy resolutions improves the Compton scattered event rejection. The upper threshold of the energy window reject piled-up events or residual γ -radiation emitted by the radioisotope. From the system level perspective, the overall energy resolution is degraded by individual detector non-uniformities.

2.1.3. TIMING RESOLUTION

The γ -photons that are validated by the energy-window filter are called the single events and the amount of detected single events per unit time is called the single count rate. In a coincidence experiment, two γ -detectors are placed in order to measure the back-to-back 511 keV γ -photons (see Figure 2.7).

A positron emitting radioactive source is placed between the detectors in a geometric arrangement that allows coincidence detections. Every single detected γ -photon

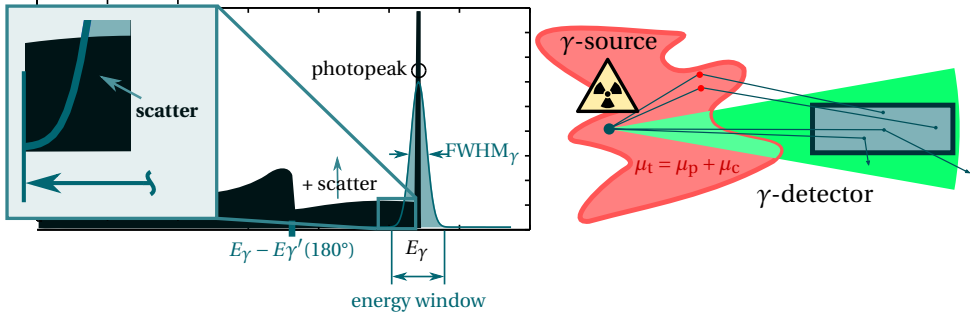


Figure 2.6: Representation of the detector energy resolution setup's including detected Compton scattered events.

is timemarked after the energy-window filter validates the detections. Typically, a histogram is built by measuring many timemark distances between coincident single events and the CRT is reported at FWHM and FWTM. In addition, the histogram offset is utilized for calibrating timing non-uniformities between detectors.

The time-window width is defined in order to capture most of the prompt events, which are detections validated by the energy-window and time-window filters. The CRT constrains the time-window width unless the PET scanner diameter in terms of time is larger than the CRT (see Figure 2.9). The timing and energy window must not cut off valid coincidences detections. Also, there is chance to detect more than two single events within the time window; and, typically this type of events, which are the called multiples, are discarded.

In the example setup of Figure 2.7, the detectors have similar characteristics and the arrangement is symmetric. Therefore, the single count rates S_{C1} and S_{C2} are the same in both detectors. In these conditions, the random count rate, which corresponds to the amount of false or uncorrelated coincidences per unit time, is given by

$$R_C = S_{C1}^2 \Delta_{TW}. \quad (2.6)$$

where Δ_{TW} is the time-window width. In addition, the true count rate T_C is defined as the total coincidence or prompt count rate P_C minus the random count rate R_C , since in these experiments there are not scattered counts.

Another important timing feature of the PET detector modules is the dead time, which limits its maximum achievable count rate. There are two dead time models, which are the paralyzable and nonparalyzable models [5]. In practice, modeling the full PET scanner dead time is a more complex task that depends on the acquisition system hierarchy. Since the overall dead time is a combination of several individual dead times into the instrumentation and acquisition chains [8]. At system level, the CRT is reported for the whole PET scanner; and it is affected by the CRT of the individual detectors, the timing jitter of PET clock synchronization, uncalibrated timing skews, etc [9, 10].

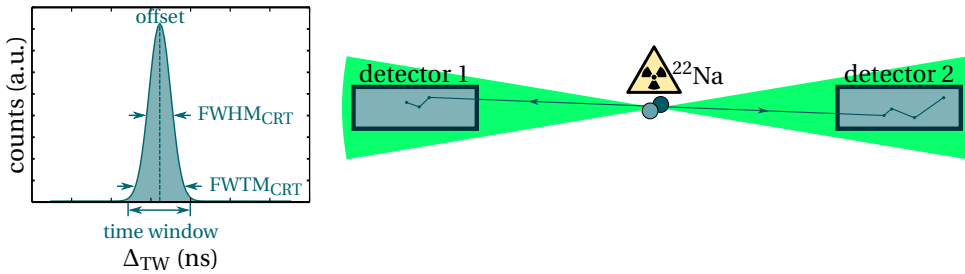


Figure 2.7: Representation of the coincidence measurement's setup.

2.1.4. SPATIAL RESOLUTION

The PET detector modules estimates the POI coordinates POI_x , POI_y , and POI_z . Often, the POI_z , which is known as depth-of-interaction (DOI), is not measurable by the module (see Figure 2.8). Subsequently, when a γ -photon impacts in a PET module with an incidence angle Φ_1 different from 0° the POI estimation has parallax error [2]. For example, annihilations A_1 and A_2 can produce the same POI_x, POI_y in the upper detector module, even though they are in different locations within the PET gantry (see Figure 2.8).

The parallax error causes a nonuniform spatial resolution within the PET scanner. For example, in the center of the scanner the parallax is negligible. However, events that are closer to the detector ring have a blurred spatial resolution. In addition, in a multiple ring PET system the parallax error occurs when a LOR is detected between different rings (see Figure 2.8). And, it is maximum if the two 511 keV γ -photon, which belong to the same LOR, hits the inner and outer rings. Typically, whole body PET scanner have the option to filter out LORs that are detected above a maximum acceptance axial angle.

Typically, a PET scanner spatial resolution is measured at several radial, axial, and tangential offsets within the scanner's gantry, and it is reported at FWHM and FWTM. Additionally, the ratio between the individual PET detector's intrinsic spatial resolution and PET system-level spatial resolution is reported [11].

2.1.5. EFFECTIVE COUNTING

In a PET study, increasing the total amount of prompt counts might not improve the molecular sensitivity. Since only the useful number of counts, which are calculated by removing the aspecific probe distribution and the PET instrumentation noise counts, enhances the molecular sensitivity and accuracy. Moreover, from the PET instrumentation perspective the effective number of counts is calculated without subtracting the aspecific molecular probe's counts. Because that is a property related to the intrinsic specificity of the molecular probe and not to the machinery of the PET scanner.

The maximization of the effective number of counts is directly linked to the *sensitivity* and the effective counting capability of the PET detector rings; in addition to the amount of injected molecular probe. The minimization of the amount of injected molecular probe benefits in reducing the radioactive dose received by the patient. Furthermore, an additional radioactive dose minimization extends PET imaging to new medical

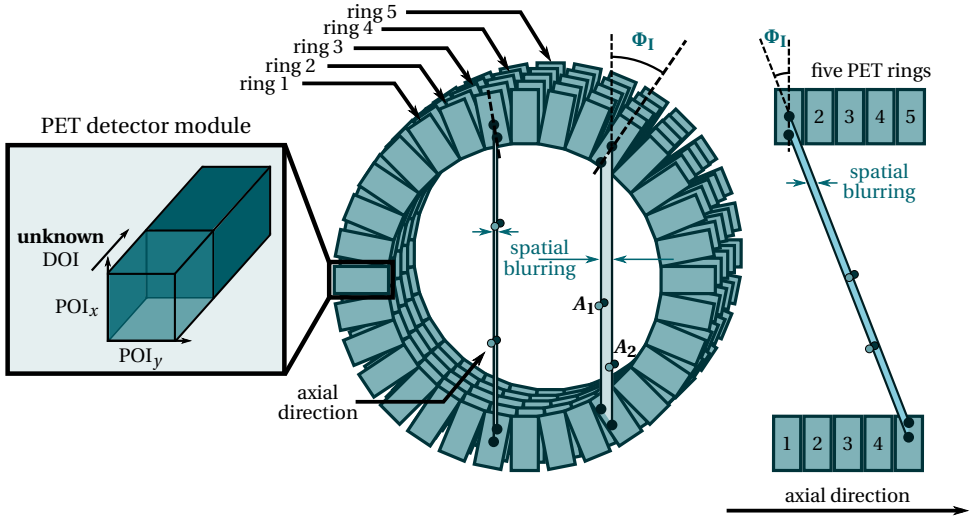


Figure 2.8: Descriptions of spatial resolution's blurring effects.

applications such as pediatric PET [12].

The sensitivity is the probability of detecting an electron-positron annihilation within the PET detector ring. The sensitivity of a PET scanner is measured at a lower radioactivity in order to eliminate the influence of random coincidences and detector dead times [1, 2]. It is important to notice that in PET at least two detectors are required in order to measure the back-to-back γ -photons, and in principle a rotating detector pair allows to measure a complete set of projection. However, the sensitivity is substantially increased when the positron emitting volume is surrounded by detectors (see Figure 2.9). Therefore, the detector coverage, which is known as field-of-view (FOV), of the positron-emitting volume determines the sensitivity. Additionally, the γ -sensitive thickness of the PET detector module sets the probability of detecting individual γ -photons, which also determines the sensitivity (see Figure 2.9) [1, 2]. In a cylindrical PET geometry, which is the typical PET arrangement, the axial length and diameter defines the scanner's FOV and their sizes are dependent of the specific PET application (see Figure 2.9).

In PET, the two types of false detections or noise counts are:

- random coincidences,
- and Compton scattered events.

As described in chapter 1, for every γ -photon detection a PET detector module calculates its deposited energy E_{ij} , its timemark T_{ij} , and its POI_{ij} (see Figure 2.10, where i represents the annihilation number and j represents the γ -photon pair index). In Figure 2.10, the LOR_1 , which is estimated from POI_{11} and POI_{12} , is miscalculated since one γ -photon is deviated by the Compton interaction S_1 and the POI_{12} is incorrect. E_{12} has a value that is higher than energy-window lower threshold, although the γ -photon lost energy in the Compton interaction S_1 ; subsequently, the PET scanner validated this detection.

In the annihilation A_2 , one γ -photon is fully absorbed within the patient's body by

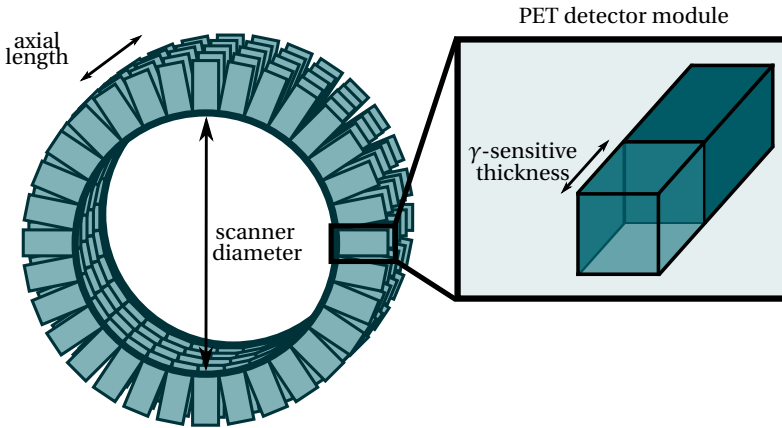


Figure 2.9: Geometrical dimensions of a PET gantry.

the photoelectric interaction P_2 , and in A_3 one γ -photon is undetected by the PET detector ring. Consequently, only two 511 keV γ -photons are detected instead of four (see Figure 2.10). Furthermore, these two detections happens very close in time; therefore, the coincidence detection system validates that T_{21} and T_{32} belongs to the same annihilation process. Then, LOR_{23} is a complete miscalculation based on two uncorrelated POIs. Finally, LOR_4 is a correctly calculated (see Figure 2.10). In summary, LOR_1 is a scatter count, LOR_{23} is a random count, and LOR_4 is a true count. The addition of these three types of counts is the prompt counts.

In a PET study, a mean molecular-probe concentration \bar{x}_j within the voxel j is estimated as \hat{x}_j (see Figure 2.11). Under specific measurement conditions, such as considering a cylindrical phantom as positron emitting volume and reconstructing the image with an analytic image-reconstruction algorithm the called filtered backprojection (see Figure 2.11); we can define the effective counting capability of the PET scanner. The noise equivalent count rate (NECR) is defined as the count rate that produces the same SNR on \hat{x}_j but from a set of projection data without false detections. This definition states that the \hat{x}_j SNR is proportional to the \sqrt{NECR} [13, 14]. After the introduction of iterative image-reconstruction algorithms, the linear relationship between the SNR and the \sqrt{NECR} is no longer valid [3, 15]. However, the NECR is included into the NEMA standards as a measure of effective count rate [11].

The NECR is given by

$$NECR = \frac{T_C^2}{T_C + S_C + R_C}, \quad (2.7)$$

where T_C is the true count rate, S_C is the Compton scattered event rate, and R_C is random count rate; all of them are evaluated within the PET scanner's FOV.

2.1.6. BASICS OF IMAGE RECONSTRUCTION

In the acquisition process of a PET study, a spatial molecular-probe concentration is estimated from 511 keV γ -photon pairs, which are represented as LORs or projection

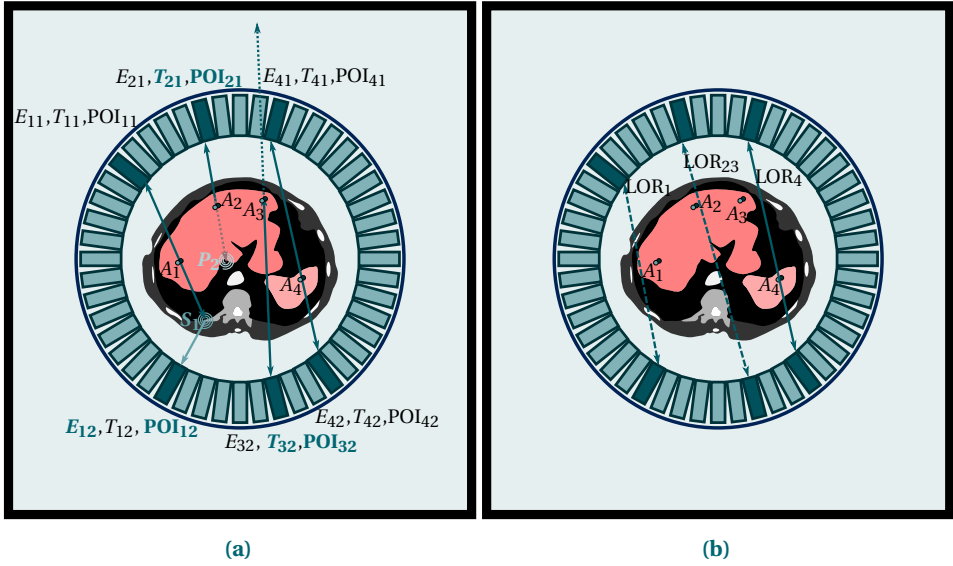


Figure 2.10: Representation of the false detection types in PET. (a) γ -photons' detection process. (b) LORs calculation process.

data (see Figure 2.1). Assuming a 2D planar molecular-probe distribution, a LOR can be represented by an orthogonal angle ϕ and a distance to the origin r , as shown in Figure 2.12a. The transformation of a planar molecular-probe distribution $f(x, y)$ into a LOR space $p(r, \phi)$ is known as the Radon transform, which analytically models the PET scanner's acquisition process (see Figure 2.1). The Radon transform is defined as the following line integral:

$$p(r, \phi) = \int_{S_{r, \phi}} f(x, y) ds, \quad (2.8)$$

where $S_{r, \phi}$ is a LOR within the PET detector ring. The LOR histogram is known as sinogram (see Figure 2.12b).

The objective of the image reconstruction algorithm is to convert back the sinogram into the planar molecular-probe distribution. An analytical approach to reconstruct $f(x, y)$ from the acquired sinogram is the backprojection algorithm. A simplified backprojection algorithm can be implemented based on overlapping all the LORs that generated that sinogram. During the overlapping process, the LOR counts are added to all the intersected pixels weighted by the intersection length [1].

However, this approach approximates the molecular probe distribution with a $\frac{1}{R}$ blurring effect [1, 16]. The $\frac{1}{R}$ blur is compensated by applying a filter to the sinogram [1, 16]. Figure 2.12b shows the reconstructed 2D image of Figure 2.12a with and without compensating the $\frac{1}{R}$ blur with a ramp filter [1]. In the case of a 3D-PET image reconstruction, it is possible to convert the 3D information into a series of stacked 2D sinograms by utilizing rebinning methods [16, 17].

Another way to obtain a molecular-probe distribution from the projection data is by

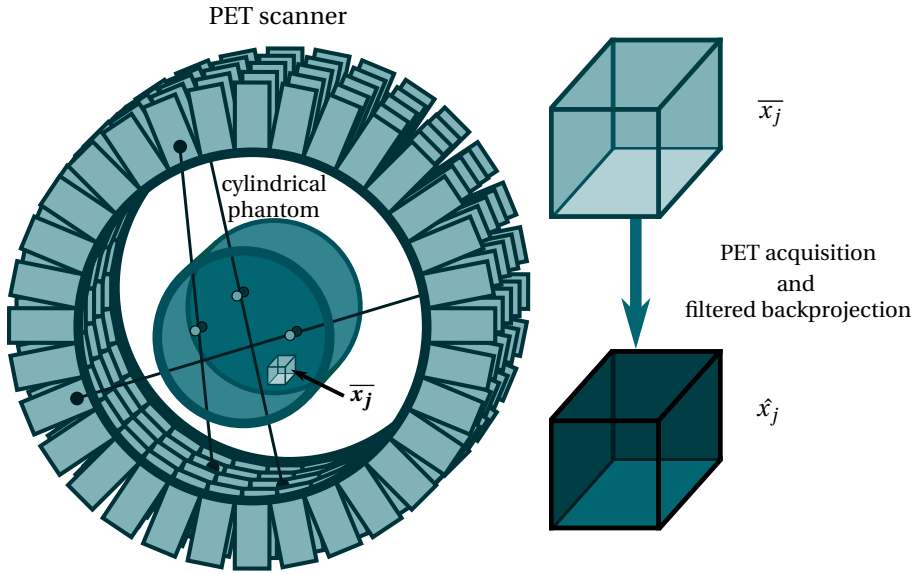


Figure 2.11: Representation of the NECR's measurement setup.

the utilization of *iterative* image-reconstruction algorithms [1–3, 16]. The reconstruction problem can be formulated as follows:

$$\bar{\mathbf{p}} = \mathbf{A}\bar{\mathbf{x}}, \quad (2.9)$$

where $\bar{\mathbf{x}}$ is a mean molecular-probe concentration per voxel represented as a column vector, $\bar{\mathbf{p}}$ is the mean counts per sinogram bin also represented as a column vector, and \mathbf{A} is the system matrix that relates voxel counts \bar{x}_j with sinogram bins \bar{p}_i .

In practice, a measured sinogram \mathbf{p} contains significant statistical fluctuations, due to the limited number of detected counts during the scanning time and the random nature of the β^+ decay process. The objective of the iterative image-reconstruction algorithm is to find the $\bar{\mathbf{x}}$ that generated \mathbf{p} ; by considering that the measured sinogram bins p_i are random variables, which are often modeled with a Poisson distribution $P(\mu)$.

The maximum-likelihood estimator (MLE) of the mean value μ of a Poisson distribution is a known unbiased and efficient estimator. Assuming a simplified single-voxel experiment, we can calculate the MLE \hat{x}_1 of the single-voxel mean detected counts \bar{x}_1 ; given the observation of a single-sinogram bin p_1 , as follows:

$$\hat{x}_1 = \frac{p_1}{a_{11}}. \quad (2.10)$$

Where a_{11} is the single element of \mathbf{A} , which represents the detection probability of an emission from the single voxel into the single-sinogram bin. The likelihood equation of this single-voxel experiment is given by

$$L(\bar{x}_1 | p_1) = \log\left(\frac{(a_{11}\bar{x}_1)^{p_1} e^{-\bar{x}_1 a_{11}}}{p_1!}\right). \quad (2.11)$$

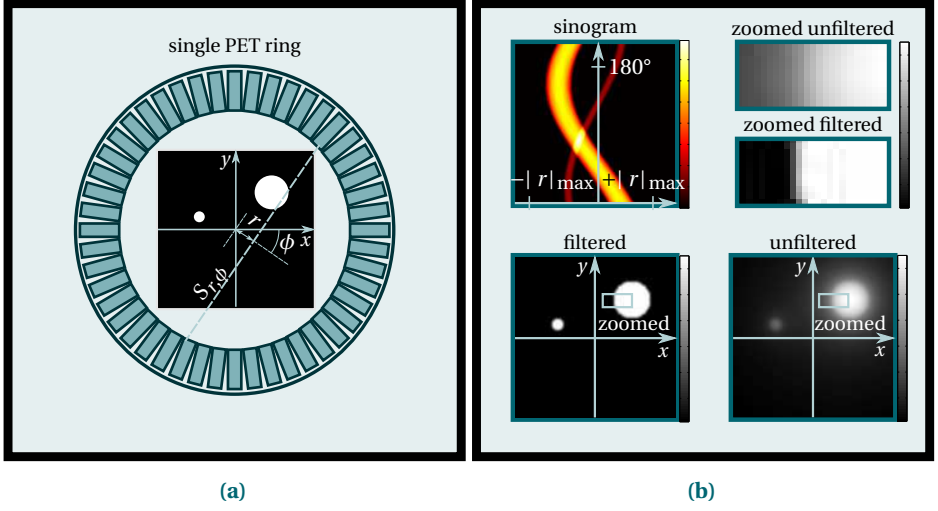


Figure 2.12: 2D PET image-reconstruction representation. (a) Single PET ring with two circular radioactive sources. (b) 2D sinogram space representation and 2D reconstructed images.

In the case of multiple bins p_i that belong to the sinogram vector \mathbf{p} and multiple voxels \bar{x}_j , the likelihood equation is defined as follows:

$$L(\bar{x}_j | \mathbf{p}) = \sum_i \log \left(\frac{(a_{ij} \bar{x}_j)^{p_i} e^{-\bar{x}_j a_{ij}}}{p_i!} \right), \quad (2.12)$$

in which its maximization results in a non-closed form solution.

However, the maximum-likelihood expectation maximization (ML-EM) algorithm can approximate the solution of the likelihood equation maximization in several k iterations [3]. The ML-EM algorithm equation is defined as follows:

$$\hat{x}_j^{k+1} = \frac{\hat{x}_j^k}{\sum_i a_{ij}} \sum_i \frac{a_{ij}}{\sum_d a_{id} \hat{x}_d^k} p_i. \quad (2.13)$$

We can identify several stages within equation (2.13). The first stage is called the forward projection and is given by

$$\hat{p}_i^k = \sum_d a_{id} \hat{x}_d^k. \quad (2.14)$$

The next stage is called the comparison and defined by

$$e_i = \frac{p_i}{\hat{p}_i^k}. \quad (2.15)$$

Later, the comparison backprojection is given by

$$u_j = \sum_i a_{ij} e_i. \quad (2.16)$$

And finally, the next-iteration estimated distribution is updated by following

$$\hat{x}_j^{k+1} = \frac{\hat{x}_j^k}{\sum_i a_{ij}} u_j. \quad (2.17)$$

The ML-EM procedure flow is described in algorithm 1 and Figure 2.13; where the initial guess or starting point of the algorithm is defined as a uniform molecular probe distribution \hat{x}^0 .

input : measured sinogram vector \mathbf{p} of size I
input : The system matrix A of size $I \times J$
input : maximum number of iterations K_MAX
output: estimated molecular-probe spatial distribution $\hat{\mathbf{x}}$ of size J

```

 $\hat{\mathbf{x}}^k = \text{uniform}(J)$ ;
 $k = 0$ ;
while  $k < K\_MAX$  do
     $\hat{\mathbf{p}}^k = \text{forward\_projection}(A, \hat{\mathbf{x}}^k)$ ;
     $\mathbf{e} = \text{comparison}(\hat{\mathbf{p}}^k, \mathbf{p})$ ;
     $\mathbf{u} = \text{back\_projection}(A, \mathbf{e})$ ;
     $\hat{\mathbf{x}}^k = \text{update}(A, \mathbf{u}, \hat{\mathbf{x}}^k)$ ;
     $k++$ ;
end

```

Algorithm 1: ML-EM image-reconstruction algorithmic procedure.

The main advantages of an iterative image-reconstruction algorithm over an analytic one are:

- full system modeling within A ,
- it is not limited to a cylindrical geometry by definition,
- and the consideration of the statistical nature of \mathbf{p} , within the optimization process.

The forward projection can be as complex as a full Monte Carlo simulation of the PET acquisition that includes detector non-idealities, full γ -radiation transport simulations, positron range modeling, etc. However, a very complex simulation would result into an impractical execution time. In practice, only the modeling of the effects that have a significant contribution to the image quality are included within the forward projection. In addition, a more accurate estimation is achieved by modeling A for the specific PET scanner under use.

During the image-reconstruction process, data correction techniques are essential steps in order to obtain an accurate quantitative estimation of the spatial molecular-probe concentration, which can be included within A or applied directly to the projection data. The data correction methods are the followings:

- attenuation correction,
- FOV sensitivity correction,

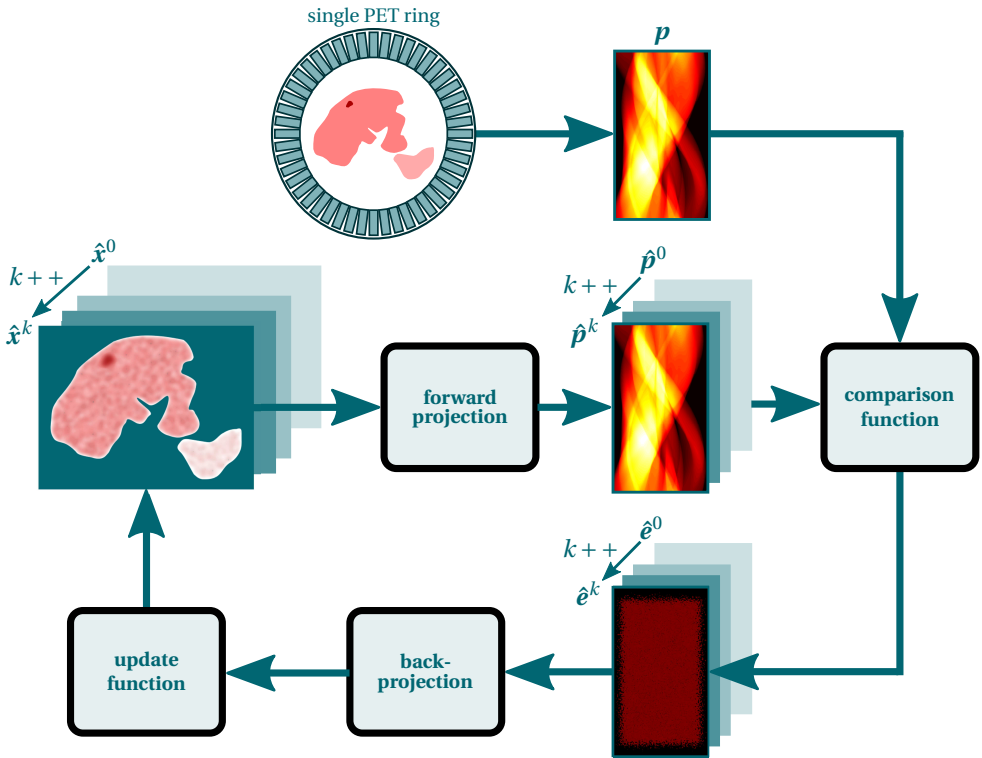


Figure 2.13: Block diagram of the ML-EM image-reconstruction algorithm.

- random coincidence correction,
- dead time correction,
- and Compton scattering correction.

The probability of detecting γ -photons depends on the media that surrounds the POEs. As explained in subsection 2.1.1.1, the emitted γ -photons interacts with matter, and have a probability to be stopped or scattered before reaching the PET detectors. In the case of a PET study, the surrounding media is the patient's body, which obviously changes scan to scan. Therefore, the volumetric attenuation data needs to be measured by performing a transmission scan, before reconstructing the emission image, in order to compensate for it. This compensation process is called attenuation correction, and typically in PET/X-ray CT scanners the attenuation data is measured by the X-ray CT and converted into the corresponding 511 keV attenuation values [2].

The FOV sensitivity correction is a technique that compensates the detection probability non-uniformity within the scanner's FOV. The amount of random coincidences can be estimated from the single count rate, as shown in equation (2.6) and corrected accordingly. Additionally, the amount of undetected counts due to dead time limitations can also be compensated by measuring the single count rate. Compton scattering noise counts are the most difficult to compensate for [1]. One example of a Compton scat-

tering correction method is performing a γ -photon transport Monte Carlo simulation that considers Compton scattering, within the forward projection of an iterative image-reconstruction algorithm. However, this approach is computationally intensive.

2.1.7. TIME-OF-FLIGHT PET

When the CRT of a PET scanner is considerably smaller than its FOV's diameter in terms of time, TOF information is potentially available for improving the PET image quality.

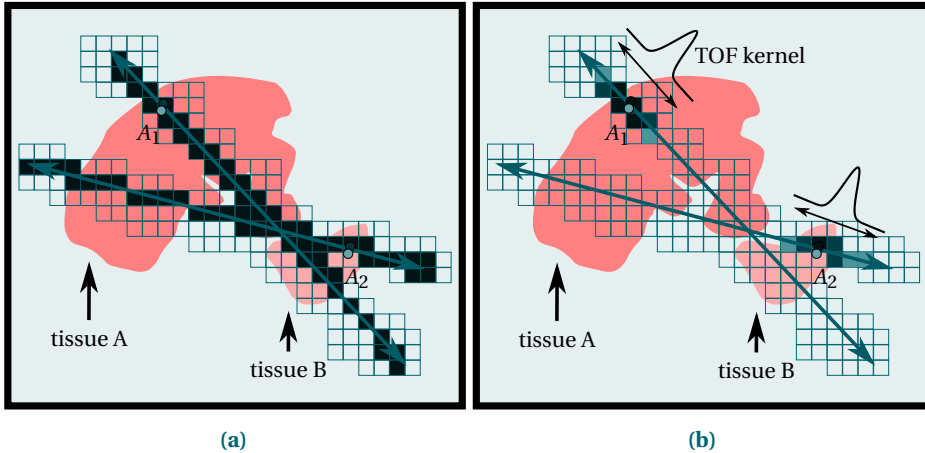


Figure 2.14: Representation of the TOF-PET concept. (a) Non TOF-PET LORs' representation. (b) TOF-PET LORs' representation.

In a non-TOF PET study, when a LOR is detected, the image-reconstruction algorithm considers that the POE is unknown over the whole LOR's segment. In other words, it considers a uniform POE probability along the LOR's segment (see Figure 2.14a). If we had a projection dataset with negligible statistical noise and without TOF information we could reconstruct an image with very high quality. However, in practice the datasets have a limited statistical quality with significant amount of noise. The efficacy of filtering noise injected from the tissue A into the tissue B and vice-versa, due to the unknown POE, is limited by the statistical quality of the projection dataset, among other factors (see Figure 2.14a).

By knowing the time distance between γ -photons with enough precision, the emission probability along the LOR's segment can be reduced by modeling it with a TOF kernel PDF. The timing response of the detectors determines the TOF kernel PDF (see Figure 2.14b).

Under specific PET study conditions, the relationship between the SNR gain of a non-TOF-PET and a TOF-PET study can be established. This relationship is calculated by following the NECR definition with a reduced and equivalent FOV diameter. Assuming a cylindrical phantom and a filtered-backprojection image-reconstruction algorithm, the

SNR_{TOF} is defined as follows:

$$\text{SNR}_{\text{TOF}} = \sqrt{\frac{D}{\Delta x}} \text{SNR}. \quad (2.18)$$

Where D represents the scanner diameter, SNR is measured without TOF, and the TOF-kernel has a width Δx given by

$$\Delta x = \frac{c\Delta T}{2}, \quad (2.19)$$

where ΔT is the CRT the scanner. Following the previous definitions the SNR improves 2.82 if we consider a PET scanner diameter of 60 cm and a timing resolution of 500 ps.

However, in practice the patient is not ideal cylinder and nowadays iterative image-reconstruction algorithms widely utilized instead of the filtered backprojection. However, the clinical benefits of TOF were verified and the SNR improvement is correlated to the patient size [18]. Additionally, TOF-PET scanners can obtain similar SNRs in comparison to non-TOF scans but at a lower number of detected counts. This benefit can be interpreted as patient-dose reduction at the same scanning time or a scanning-time reduction at the same patient dose [19, 20].

Intrinsically, the maximum TOF improvement is limited by the electron-positron annihilation physics, which are explained in section 1.2. However, the current PET technologies are not even close to that limit. Commercial clinical PET scanner achieve a TOF precision of few hundreds of picoseconds [20, 21]. Subsequently, PET detector technologies have a large room for improvement in order to reach the fundamental limits of PET in terms of TOF.

2.2. PET DETECTOR MODULE

γ -photon detection can be measured with solid-state detectors, ionization chambers, inorganic scintillator-based detectors, etc. The latter type of detectors are widely used in PET since they offer the best trade-off between energy, timing, and spatial resolutions as well as a high detection efficiency for 511 keV γ -photons.

The inorganic scintillator converts deposited γ -energy into light photons following a fast transient response. The scintillator's output light pulse is sensed by a photodetector, which is optically coupled to the scintillator, and transformed into an analog or digital signals. There several ways to arrange the a scintillator-based PET detector module (see Figure 2.15c).

For example, Figure 2.15a shows the traditional γ -camera approach, where a large-area continuous or monolithic scintillator is coupled to an array of photodetectors [22, 23]. The scintillator is covered with a reflective coating in order to maximize the photodetectors' light collection. The POI coordinates are estimated by utilizing the light spread over the photodetectors, which is intentionally widen by producing a refractive index mismatch with a light guide. The energy of the absorbed γ -photon is estimated by adding the partial energy that is individually collected by the photodetectors. The main disadvantage of this approach is that a large detector area is disabled during certain dead time, when a γ -photon detection occurs; as a result, the maximum-achievable single count rate is significantly limited.

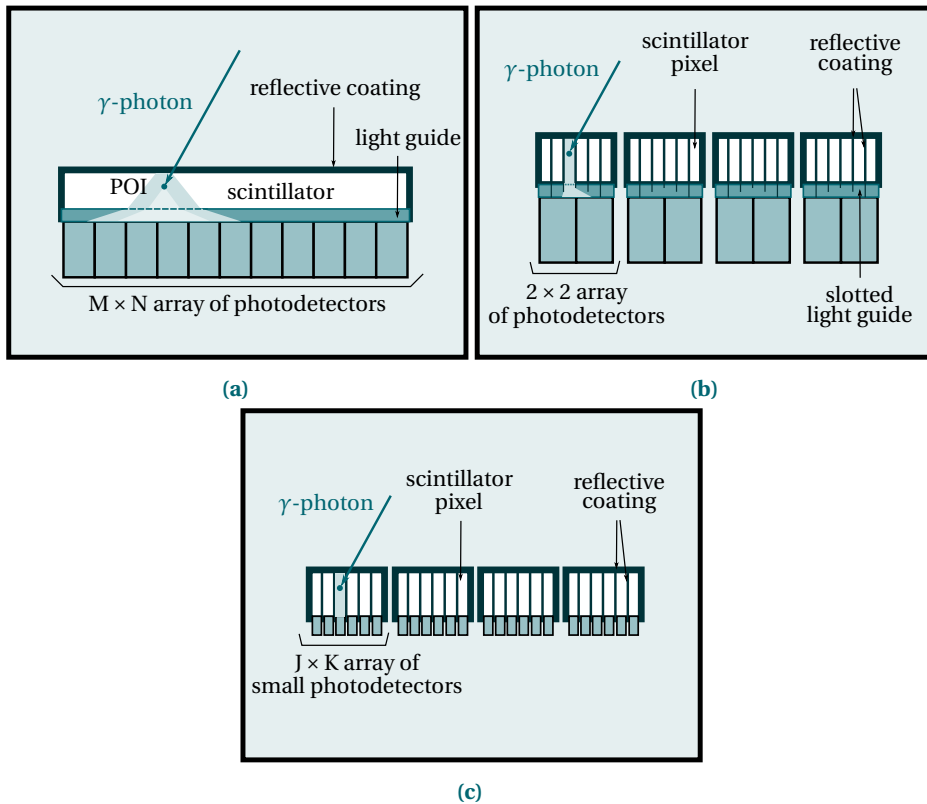


Figure 2.15: Representation of common types of PET module configurations. (a) γ -camera based detector type. (b) BGO block detector type. (c) one-to-one coupling detector type.

A more effective approach is to couple an array of pixellated scintillators, in which every pixel is covered by a reflective coating, to a 2×2 array of photodetectors through a slotted light guide (see Figure 2.15b). In this design, the scintillator pixel encoding is performed by controlling the light sharing between photodetectors with the slotted light guide. This approach allows to build large detection areas modularly and it outputs a higher single count rate at the same radioactive dose in comparison to the γ -camera approach [24].

By further partitioning the detection area, PET detector modules are designed by one-to-one optical coupling between the scintillator pixels and small photodetectors (see Figure 2.15c). This approach requires a higher level of integration and complexity for reading out the photodetectors' output signals [25]. In high spatial-resolution PET, such as small-animal PET imaging, a small scintillator pixel pitch is required when utilizing pixellated scintillators. Therefore, the packing fraction, which is the ratio between γ -sensitive and total detector areas, could be significantly reduced by the reflective coating thickness and the dead spaces between the photodetectors. In order to achieve a suitable packing fraction, the reflective coatings are designed with thin reflective films

[26]. Additionally, in small-pitch scintillator pixels the inter-crystal Compton scattering between scintillator pixels affects the detector performance.

Alternative designs implemented miniaturized versions of the γ -camera approach in order to achieve a high spatial resolution without a packing fraction reduction [27]. In addition, the DOI information is obtained by implementing nonlinear estimation methods based on the POI's light spreading. Besides, double-side readout has been proposed in order to estimate the DOI of the POI; however, this approach doubles the number of required photodetectors [28].

2.2.1. INORGANIC SCINTILLATORS FOR PET

Inorganic scintillators are transparent crystals that emit a flash of light as a response of an interaction with ionization radiation. Some scintillators, such as LYSO or LSO, have an addition of impurities in order to increase their light output or improve their timing performance. Their main parameters that are of relevance for PET are listed in Table 2.1.

Given a specified PET sensitivity, the required scintillator's thickness can be approximated by the integral of equation 2.1; utilizing the corresponding scintillation material's linear attenuation coefficient $\mu_t(511 \text{ keV})$, which is calculated for 511 keV of interacting γ -energy. Also, Monte Carlo simulations are utilized to obtain more accurate estimations of the required scintillator's thickness. Thicker scintillators are undesired since they increase the parallax error, decrease the light output, and degrades the CRT (see Figure 2.8) [29].

The precision of the γ -photon's timemark, the POI coordinates, and the energy resolution are related to the total amount of collected photons by the photodetector. The photodetector's light collection depends on the refractive index mismatch between the scintillator and the photodetector. Also, the light collection depends on the compatibility between the emission spectrum of the scintillator and the wavelength profile of the photodetector's photon detection efficiency (PDE). Obviously, high light-output scintillators are desired in order to increment the total amount of collected photons. And finally, the intrinsic CRT precision of a scintillation material is a function of the its light-output, rise time, and decay time [30, 31].

The very first γ -camera was built based on NaI(Tl) scintillators [22]. Later, few PET prototypes were also build with this scintillation material [23, 32, 33]. However, the main disadvantage of NaI(Tl) was its hygroscopic behavior that makes difficult to build scintillator pixels. Next, the very first PET block detector, which was based on BGO, was introduced (see Figure 2.15b) [24]. Nowadays, most of the cutting-edge technology and commercial PET scanners are built from LYSO or LSO. Since, LYSO has superior features in comparison to BGO and also allows to build block detectors (see Table 2.1).

Recently, LaBr₃(Ce) was introduced as a high light-output scintillator [34]. However, this scintillation material has not been commercially adopted in PET scanners because it is hygroscopic, costly, and has a lower stopping power in comparison to LYSO or LSO.

2.2.2. PHOTODETECTORS FOR PET

Traditionally in nuclear medicine, the photodetector of choice has been photomultiplier tubes (PMTs). These devices present a large signal gain as well as a precise single-photon timing resolution (SPTR) [11, 22, 23, 41].

Table 2.1: Comparison Table of common inorganic scintillators utilized in PET.

material	linear attenuation ^a (cm ⁻¹)	light output (ph keV ⁻¹)	refractive index	emission-peak wavelength (nm)	primary decay time (ns)	primary rise time (ps)
NaI(Tl) ^b	0.34	38	1.85	415	250	-
BGO ^c	0.96	8-10	2.15	480	300	-
LYSO ^d	0.83	27.6	1.81	420	45	90
LaBr ₃ (Ce) ^e	0.46	63	≈1.9	380	16	280

^aThe linear attenuation is specified at 511 keV.

^bValues according to [35] except for the linear attenuation that is according to [1].

^cValues according to [36] except for the linear attenuation that is according to [1].

^dValues according to [37] except for the rise time that is according to [38].

^eValues according to [39] except for the linear attenuation that is according to [40] and the rise time that is according to [30].

The PMTs have two stages in which the signal is generated. The first stage, which is called the photocathode, emits a single photoelectron by photoelectric emission when it absorbs a single light photon. The average number of emitted photoelectrons per absorbed light photons is called the quantum efficiency (QE) (see Figure 2.16) [41]. Typical photocathodes that are compatible with PET scintillators' emission spectrum features a QE peak of about 30 % [41].

The second stages is the electron multiplying stage that is composed by the focusing electrode, the dynodes, and the cathode (see Figure 2.16). The focusing electrode directs and accelerates the photoelectrons towards the first dynode, which multiplies the photoelectron by secondary emission with a multiplication ratio δ [41]. The following dynodes keeps on accelerating and multiplying electrons in order to realize a large total multiplication gain. The second stage's elements are biased with an increasing high voltage with steps of about hundreds of volts. Figure 2.16 shows an even bias voltage increase ΔV ; however, in practice the voltage steps are not necessarily uniform. Particularly, in applications that required excellent timing, the first elements are biased at higher voltage steps in order to reduce variations in the initial electron trajectories.

The PMTs feature a SPTR, which is also known as transit time spread (TTS), that is ranging from tens of picoseconds in the case of multichannel plate PMTs (MCP-PMTs), to few nanoseconds for PMT with standard dynode structures. MCP-PMTs are not commercially utilized in PET because of their high cost. The PMT's output capacitance is about tens of picofarads. The dark current is relative low in comparison to large-area silicon-based photodetectors. The main drawback of the PMTs is the high sensitivity to magnetic fields that prevents this technology from being utilized in PET/MRI systems.

The PDE of a PMT is defined as follows:

$$\text{PDE} = \text{QE} \cdot \text{CE}_1 \cdot \text{FF}, \quad (2.20)$$

where CE_1 is the collection efficiency between the photocathode and the first dynode (typically above 80 %), the geometrical fill factor (FF) is the ratio between the sensitive

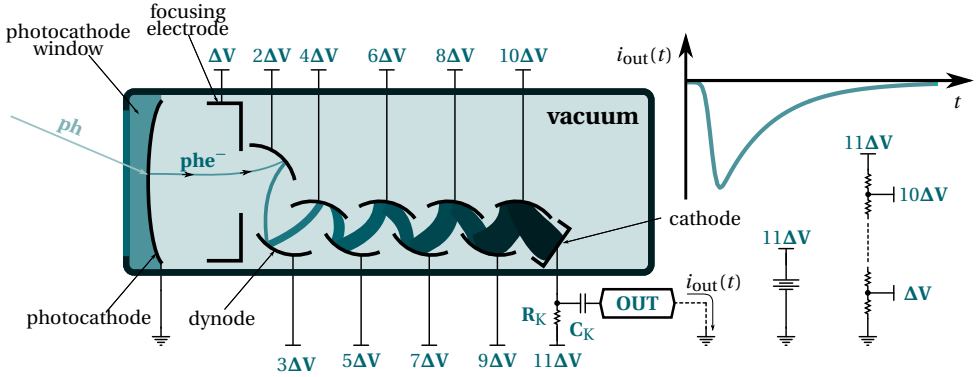


Figure 2.16: PMT schematic diagram.

area and total PMT's area, and the QE, which is measured with uniform incident light [41]. Typically in PMTs for PET applications, the FF is considered to be close to 100 %, since dead spaces are kept to a minimum inside the active area. The surrounding dead spaces, which are required for enclosing and packing the PMT, are not considered into the FF.

Recently, analog SiPMs (A-SiPMs) emerged as a silicon-based alternative to the PMTs [42]. Essentially, the A-SiPMs are a parallel connection of thousands of SPAD cells (see Figure 2.17). The SPAD cells are composed of a quenching resistor and a SPAD, which is a single light-photon detector [43, 44]. When a light photon is absorbed within the SPAD active area, there is a probability that a fast avalanche is produced and immediately quenched by an external circuit, which is a quenching resistor in the case of A-SiPMs (see Figure 2.17). This single light photon detection mechanism is similar to the way that traditional ionizing radiation detectors called the Geiger-Müller counters detect high-energy particles [44]. When a SPAD cell is fired, it is inactive to detect a subsequent light photon for a certain SPAD cell dead time. Therefore, the A-SiPM's output signal has a saturation behavior with respect to the amount of impinging light photons, when it is illuminated with fast scintillation light pulses.

In the case of A-SiPMs the PDE is defined as

$$\text{PDE} = \text{QE} \cdot \text{AP} \cdot \text{FF}, \quad (2.21)$$

where the avalanche probability (AP) considers the likelihood that an avalanche is triggered by a generated free carrier within the silicon [45, 46]. Typically the PDE is measured by utilizing a setup composed of a light source, a monochromator, an integrating sphere, and reference photodetector. Obviously, the dark counts, crosstalk, and after pulses must not be considered into the PDE [46]. The A-SiPMs have a discontinuous active area with a reduced FF in comparison to PMTs, since every SPAD cell has quenching and connection circuitries, spacing between cells, as well as a peripheral guard ring required by the SPADs in order to avoid premature edge breakdown [47].

The A-SiPMs are characterized by a higher PDE in comparison to PMTs that can reach a value of 50 % for 420 nm wavelength incident light [48], which is compatible with the

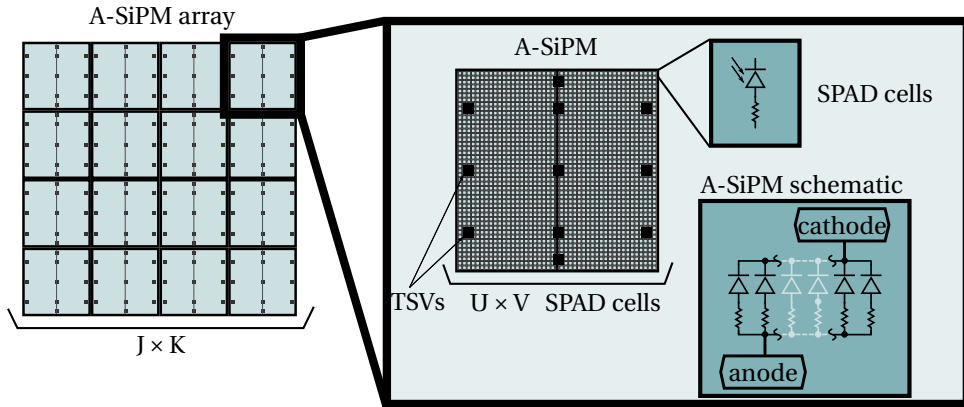


Figure 2.17: SiPM array and single SiPM description diagrams.

LYSO scintillators' emission spectrum (see Table 2.1). The A-SiPM suffers from higher after pulsing and crosstalk probabilities in addition to larger dark counts in comparison to PMTs. This is inherent to the SPAD physics and designs, in addition to the amount of current circulating during the avalanche, which defines the gain of the device. The SPTR performance of the A-SiPMs, which is about few hundreds of picoseconds, is superior in comparison to standard PMTs. Also, SPTR degrades as the A-SiPM active area increases [49]. PET detector modules that are based on A-SiPMs achieve a CRT performance that is compatible with TOF-PET [29, 30].

In order to cover a large detection area, which is required by a PET module, A-SiPM arrays are utilized (see Figures 2.15c and 2.17). Advanced SiPMs arrays connects the output terminals utilizing through-silicon vias (TSVs), in order to achieve a small dead space in the packing and enclosing supports. The output capacitance of A-SiPMs is in the range of hundreds of picofarads. There several approaches for the readout of SiPMs signals, which are addresses in chapter 4.

Initially, SPADs were implemented into custom semiconductor technologies and later the integration of SPADs into a CMOS process was demonstrated [50]. Subsequently, by integrating SPADs in CMOS it was possible to build complex systems-on-chip (SOCs). One of the first SPAD-based SOC implementations was a TOF CMOS image sensor [51]. Afterwards, the first implementation of a SPAD-based SOC named as D-SiPMs was introduced [52]. And later, several designs which included different levels of complexity and features were also introduced [53–55].

Unlike in A-SiPMs, the D-SiPM architectures feature large differences among their implementations [53–55]. Nevertheless, common structures can be identified in the different D-SiPMs implementations (see Figure 2.18a), which are:

- SPAD cell arrays,
- time-to-digital converters (TDCs),
- timing lines,
- as well as readout and discriminator circuits.

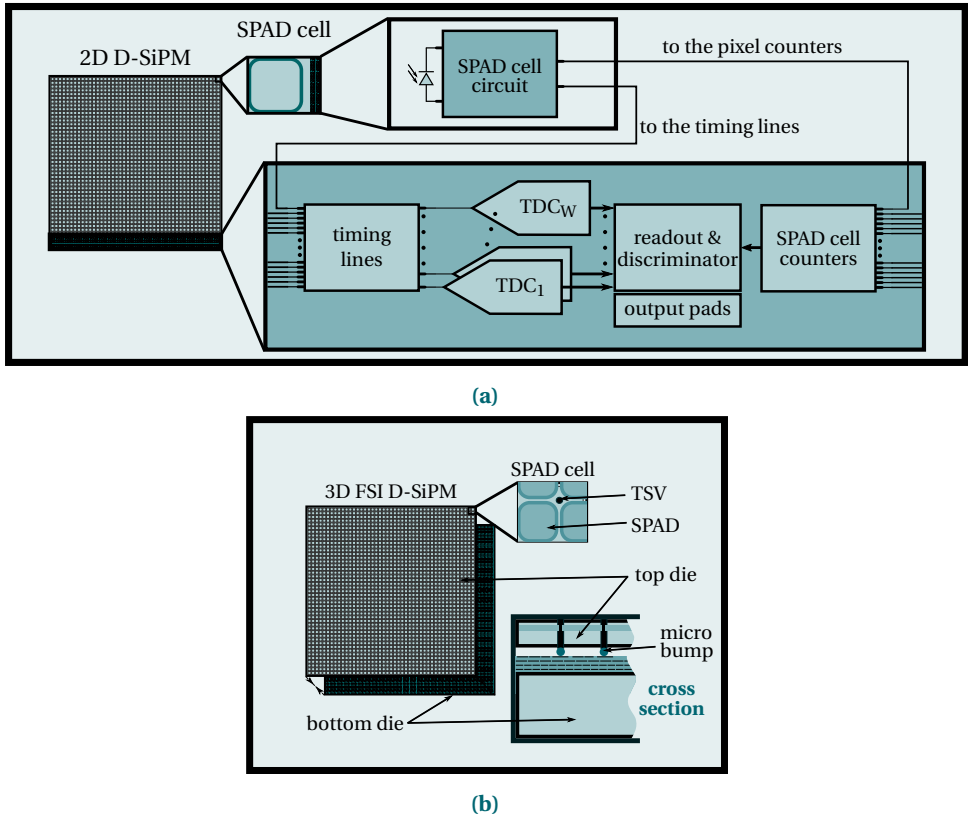


Figure 2.18: Representation diagrams of D-SiPMs. (a) 2D D-SiPM example diagram. (b) 3D FSI D-SiPM example diagram.

Typically the SPAD cells of D-SiPMs comprises a complex CMOS circuit in order to realize extra functionalities, such as masking, memory, etc. The masking circuit allows to disable a particular SPAD cell in order to deactivate the cells with high dark count rate (DCR). The memory stores the logical state of the SPAD cell before it is read out. Commonly, the SPAD cell array is arranged in a hierarchy of sets. For instance, the digital photon counter (DPC) single die is subdivided into four groups called pixels of 3200 SPADs [56]. Each pixel is also subdivided into four sub-pixels. In the case of the 18×9 array of MD-SiPMs, the SPAD cells are arranged in sets of 416 elements called clusters [57].

A common D-SiPM building block are the TDCs, which measure a time distance between two signals called start and stop. Usually in a PET system, one of these signals is a synchronization clock utilized as a reference signal. The second signal, which can be either stop or start, is a SPAD cell's output pulse. The TDC information is utilized to timestamp the TOA of the detected light photons [58].

Often, the total number of TDCs on chip is less than the total number of SPAD cells. For example, the 18×9 array of MD-SiPMs allocates 432 TDCs in total, whereas the total

number of SPAD cells is 67392. Therefore, several SPAD cells share a common TDC through the timing lines (see Figure 2.18a). For instance, the 18×9 array of MD-SiPMs interfaces SPAD cells to a TDC with a pull-down line that is sampled by a comparator, an inverter, or an amplifier, which is selected by a configuration memory [59].

Typically, there is a direct coupling of the D-SiPMs to the scintillators [60]; therefore, the extra space required by the readout circuitries and the TDCs, which is light insensitive, must be minimized (see Figure 2.18a). For example, the DPC allocates the TDCs, discriminator and readout logic within the peripheral areas of the sub-pixels [61].

The D-SiPMs send data to an external digital device, such as an FPGA, only after a validation process is performed. This readout scheme is known as event-driven, and its main purpose is to optimize the utilization of the data transfer bandwidth [59]. The discriminator circuit avoids sending events that only contain dark counts or low-energy γ -photon depositions depending on the implementation (see Figure 2.18a). For example, in the SPADNET sensor, the event discrimination is performed by continuous counting the total number of fired SPAD cells within a group [54]. The SPAD cell counters add the output values of the SPAD cell memories in order to perform the energy estimation of γ -photons, in the case of coupling the D-SiPM to a scintillator. Finally, the readout circuit sends the TDC information and counting values to an external device.

Alternatively, 3D-CMOS integration allows the maximization of the packing fraction since the light insensitive circuits can be allocated in a bottom die (see Figure 2.18b). The integration of CMOS circuits impacts the performance of the SPADs cells and vice-versa. Therefore, in a 3D-CMOS process, advanced CMOS technologies can be used in the bottom die in order to achieve lower power consumption, faster circuits, and more complex SOCs. Also, SPAD optimized technologies can be used in the top die (see Figure 2.18b) [55]. Furthermore, the SPAD cell FF can also be improved by allocating the SPAD cell circuits in the bottom die. Front-side illumination (FSI) is needed in 3D D-SiPMs, in order to detect the photons emitted by the commonly used scintillators, with wavelengths towards the violet and near-ultra violet (NUV) spectra.

There is a controversy about effectiveness of A-SiPMs over D-SiPMs and vice-versa for building PET scanner. Objectively speaking, both technologies have advantages and disadvantages, but A-SiPMs are more utilized in the construction of full PET scanners [61, 62]. Table 2.2 summarizes the parameters of importance, when building PET scanners, of A-SiPMs and D-SiPMs. A-SiPMs have a superior PDE in comparison to D-SiPMs since they are fabricated in custom technologies. However, D-SiPMs have a better timing performance than A-SiPMs because of the TDCs and timing lines integration [63].

A-SiPMs that have TSVs for connecting the anode and cathode to a surface mount device (SMD) package achieve a high packing fraction. Currently, there is only one D-SiPM array or tile of 4×4 elements that is commercially available. This D-SiPM array connects the signals through bonding wires that limit the array packing fraction to 78% (see Table 2.2). For the pixellated scintillator approach, the packing fraction reduces the PET scanner sensitivity. However, by utilizing continuous scintillator the packing fraction of the PET detector is increased [64].

Availability of components is a critical issue when building full PET systems. D-SiPMs have a very restricted availability due to the fact that only one manufacturer produces these devices commercially [65]. However, several companies produce and manufac-

Table 2.2: Comparison Table of A-SiPMs and D-SiPMs.

	maximum PDE (%) ^a	SPTR (ps)	DCR (kHzmm ⁻²)	packing fraction (%)	availability	system integration
A-SiPMs	≈50 ^b	125-250 ^c	50-150 ^b	94 ^d	high	indirect
D-SiPMs	≈30 ^e	101-113 ^f	96 ^g	78 ^h	low	direct

^aMaximum PDE measured at 420 nm photon wavelength.

^bValues according to [48].

^cValues measured for several A-SiPM sizes and according to [49].

^dValue calculated as the active area divided by the package dimensions and according to [48]

^eValues according to [61].

^fValues measured at pixel level and according to [56].

^gValue measured as average good SPAD DCR at 20 °C divided by the SPAD cell size and according to [52].

^hValue calculated as the pixel size of 12.48 mm² multiplied by 4 times (die size) and by 16 (tile size), and finally divided by the tile size of 1024 mm² [56].

tures A-SiPM. In terms of system integration, the D-SiPMs allow a direct integration requiring a minimum amount of digital readout devices, which are typically FPGAs [60]. On the contrary, A-SiPMs require specialized mixed-signal front-ends for energy and timemark estimation [25]. The system integration challenges are addressed in chapters 4 and 6.

2.2.3. THE MULTICHANNEL DIGITAL SiPM

The concept, design, and implementation of the MD-SiPMs was introduced few years ago [53]. The main objective of the MD-SiPM was to realize a D-SiPM with a relative high FF considering a large number of TDCs. This target was achieved by sharing the TDCs among the SPAD cells through pull-down lines in a column-wise arrangement (see Figure 2.19).

When building an array of MD-SiPMs, such as 4 × 4 or 18 × 9 elements, the column-wise arrangement is kept in order to obtain a high SPAD cell array FF and high MD-SiPM array packing fraction. For example, in an array composed of 18 × 9 MD-SiPMs every MD-SiPM element shares a common set of 48 TDCs (see Figure 2.20) [57]. This configuration increases the total number of SPAD cells connected into a single pull-down line. More details about system integration and characterization of MD-SiPMs is given in chapters 5 and 6.

2.3. SINGLE-PHOTON AVALANCHE DIODES

2.3.1. SPAD BASICS

As explained in the previous subsections, A-SiPMs and D-SiPMs are built from SPAD cells, among other extra circuits in the case of D-SiPMs. The SPADs sets the bound of the SPTR performance for the sensor. In addition, they also limit the maximum achievable PDE. And ultimately, the PDE and SPTR of the photodetector in combination with the scintillator's parameters and PET detector module architecture determine the PET scanner system performance. Subsequently, the SPAD is a key-element of the A-SiPM and

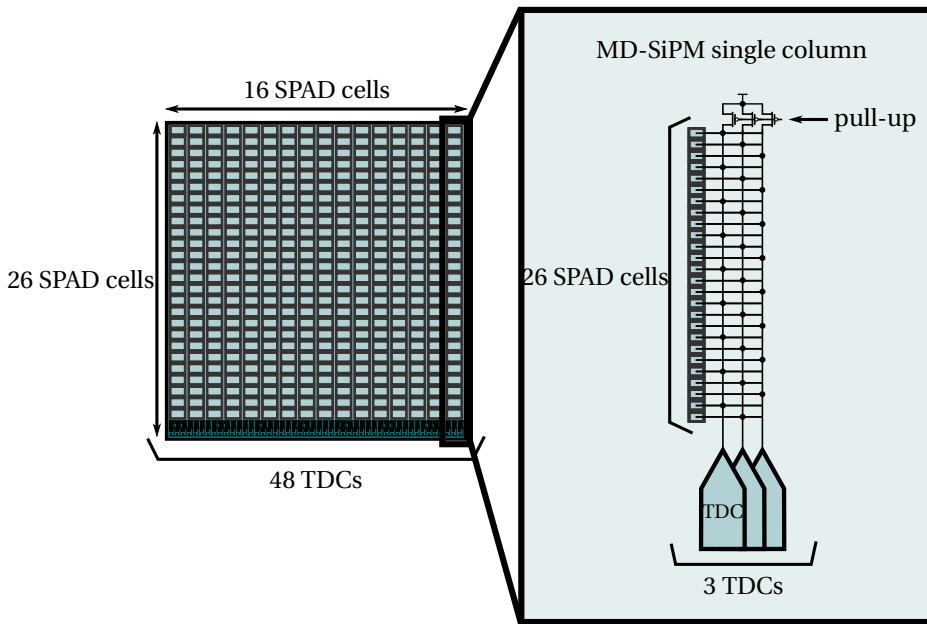


Figure 2.19: MD-SiPM concept diagram.

D-SiPM designs utilized in PET.

SPADs are biased at a reverse voltage higher than their breakdown voltage. This is possible, for example, by connecting a high resistance in series to the SPAD. In this way, when the avalanche is produced by injecting a carrier into a high electric field region, the SPAD output current produces a drop in the series resistor and reduces the applied voltage across to the SPAD; subsequently, the self-sustained avalanche is quenched [43]. This process cannot be understood from a typical I-V curve since the avalanche triggering and quenching are transient processes.

SPADs are characterized by having a high-electric field region called the multiplication region, in which a self-sustained avalanche is likely to be triggered (according to the AP) by the injection of a carrier that follows an impact ionization process. In order to realize an uniform and high enough electric field, which allows impact ionization, guard ring peripheral regions are implemented into the SPAD to avoid premature edge breakdown.

Figure 2.21 shows the structure of a SPAD implemented in a CMOS technology utilizing the CMOS available doping profiles, such as highly doped p-type (P+), highly doped n-type (N+), deep n-type well (DNW), n-type well (NW), and p-type well (PW) [47]. In this SPAD structure the cathode, which is composed by the NW, is connected to the top surface through the DNW region. The Anode is located within the P+ implantation region. Finally, the guard region is created by the PW implant, which prevents premature breakdown at the edges of the P+ region. The SPAD's active area is located within the high electric field region. This SPAD is implemented within the epitaxial layer of the CMOS

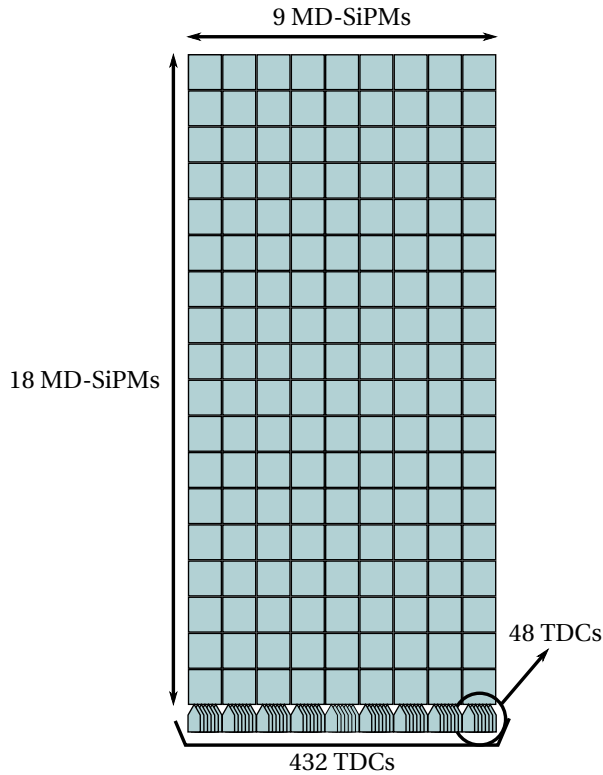


Figure 2.20: Description diagram of the monolithic array of 18 × 9 MD-SiPMs.

wafer. Another important aspect of SPAD design is the process optical stack, which is defined by the passivation layers required to place the top metal layers in the case of a CMOS process.

2.3.2. RELEVANT PET PARAMETERS

When building A-SiPMs or D-SiPMs for PET, the overall PDE, SPTR, and DCR are the main parameters of interest. They are related to the following SPADs characteristics:

- photon detection probability (PDP),
- device FF,
- dark count rate,
- afterpulsing probability,
- timing jitter,
- and breakdown and excess bias voltages.

The PDE of the photodetectors for PET are optimized to match the emission wavelength of the scintillators, which are toward the violet and NUV regions. Subsequently, the multiplication region of the SPADs for PET are designed to be as close as possible to the surface. In this way photons, with violet or NUV wavelengths can generate photo-

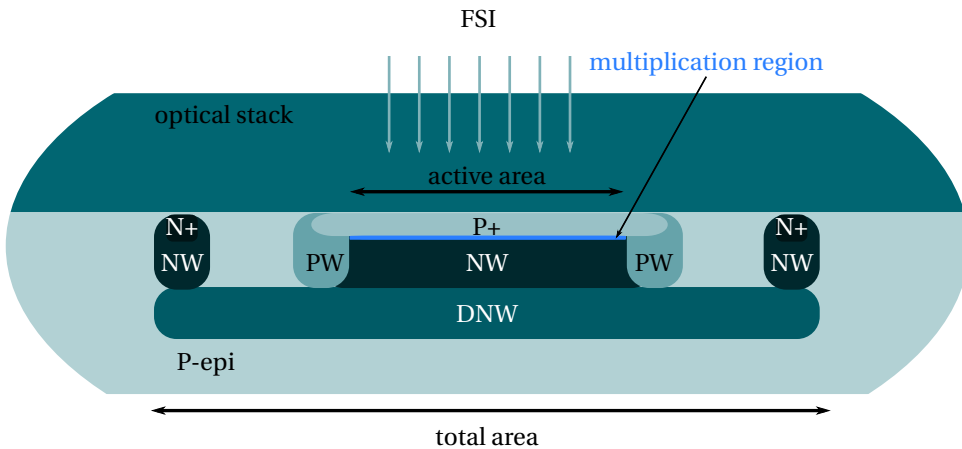


Figure 2.21: Representation of an FSI CMOS SPAD.

carries within the multiplication region. This is the reason why FSI devices are preferred for PET. Additionally, the device FF maximization is realized by minimizing the guard ring regions and sharing the DNW contacts among several SPADs [66].

The DCR depends on the process impurities, dopant concentration of the doping profile, and guard ring designs [67]. Specialized CMOS image sensor (CIS) designed for implementing SPADs provide specialized doping profiles with lower dopant concentrations, which allows a tunneling-generated DCR reduction.

The likelihood that a subsequent correlated avalanche is produced is quantified by the afterpulsing probability. In D-SiPMs, these undesired events are highly controllable since the SPAD cell can be recharged after an adjustable time [68]. Whereas in A-SiPMs, the afterpulsing probability is a consequence of the SPAD and passive quenching designs.

The SPAD timing jitter, which is also measured at single-photon level, sets a limit to the overall SPTR of the photodetector. Fast avalanche detection electronics minimizes the timing fluctuations due to the avalanche propagation statistics [69]. In D-SiPMs, these types of circuits can be integrated into D-SiPMs at SPAD cell level [70]. More details about SPAD implementations in CMOS are given in appendix A.

REFERENCES

- [1] M. R. Phelps, *PET: Physics, Instrumentation, and Scanners* (Springer Science+Business Media, 2006).
- [2] D. Bailey, D. Townsend, P. Valk, and M. Maisey, *Positron Emission Tomography: Basic Sciences* (Springer London, 2006).
- [3] L. A. Shepp and Y. Vardi, *Maximum Likelihood Reconstruction for Emission Tomography*, *IEEE Transactions on Medical Imaging* 1, 113 (1982).
- [4] NIST, *The Mass Attenuation Coefficient* ((accessed April 20, 2018)).

- [5] G. Knoll, *Radiation Detection and Measurement* (John Wiley & Sons, 2010).
- [6] S. Jan, D. Benoit, E. Becheva, T. Carlier, F. Cassol, P. Descourt, T. Frisson, L. Grevillot, L. Guigues, L. Maigne, *et al.*, *GATE V6: a major enhancement of the GATE simulation platform enabling modelling of CT and radiotherapy*, *Physics in Medicine & Biology* 56, 881 (2011).
- [7] J. Allison, K. Amako, J. Apostolakis, P. Arce, M. Asai, T. Aso, E. Bagli, A. Bagulya, S. Banerjee, G. Barrant, *et al.*, *Recent developments in Geant4*, *Nuclear Instruments and Methods in Physics Research Section A: Accelerators, Spectrometers, Detectors and Associated Equipment* 835, 186 (2016).
- [8] C. R. Schmidtlein, A. S. Kirov, S. A. Nehmeh, Y. E. Erdi, J. L. Humm, H. I. Amols, L. M. Bidaut, A. Ganin, C. W. Stearns, D. L. McDaniel, *et al.*, *Validation of GATE Monte Carlo simulations of the GE Advance/Discovery LS PET scanners*, *Medical physics* 33, 198 (2006).
- [9] R. J. Aliaga, J. M. Monzó, M. Spaggiari, N. Ferrando, R. Gadea, and R. J. Colom, *PET system synchronization and timing resolution using high-speed data links*, *IEEE Transactions on Nuclear Science* 58, 1596 (2011).
- [10] M. Bijwaard, C. Veerappan, C. Bruschini, and E. Charbon, *Fundamentals of a scalable network in SPADnet-based PET systems*, in *Nuclear Science Symposium and Medical Imaging Conference (NSS/MIC), 2015 IEEE* (IEEE, 2015) pp. 1–3.
- [11] A. L. Goertzen, Q. Bao, M. Bergeron, E. Blankemeyer, S. Blinder, M. Cañadas, A. F. Chatziioannou, K. Dinelle, E. Elhami, H.-S. Jans, *et al.*, *NEMA NU 4-2008 comparison of preclinical PET imaging systems*, *Journal of nuclear medicine: official publication, Society of Nuclear Medicine* 53, 1300 (2012).
- [12] S. R. Cherry, T. Jones, J. S. Karp, J. Qi, W. W. Moses, and R. D. Badawi, *Total-body PET: Maximizing sensitivity to create new opportunities for clinical research and patient care*, *J Nucl Med* 59, 3 (2018).
- [13] S. Strother, M. Casey, and E. Hoffman, *Measuring PET scanner sensitivity: relating countrates to image signal-to-noise ratios using noise equivalent counts*, *Ieee transactions on nuclear science* 37, 783 (1990).
- [14] T. F. Budinger, S. E. Derenzo, W. L. Greenberg, G. T. Gullberg, and R. H. Huesman, *Quantitative potentials of dynamic emission computed tomography*. *Journal of nuclear medicine: official publication, Society of Nuclear Medicine* 19, 309 (1978).
- [15] T. Chang, G. Chang, J. W. Clark, R. H. Diab, E. Rohren, and O. R. Mawlawi, *Reliability of predicting image signal-to-noise ratio using noise equivalent count rate in PET imaging*, *Medical physics* 39, 5891 (2012).
- [16] A. Alessio, P. Kinahan, *et al.*, *PET image reconstruction*, *Nuclear medicine* 1, 1 (2006).

- [17] B. Bendriem and D. W. Townsend, *The theory and practice of 3D PET*, Vol. 32 (Springer Science & Business Media, 2013).
- [18] J. S. Karp, S. Surti, M. E. Daube-Witherspoon, and G. Muehllehner, *The benefit of time-of-flight in PET imaging: Experimental and clinical results*, Journal of nuclear medicine: official publication, Society of Nuclear Medicine 49, 462 (2008).
- [19] S. Surti, *Update on time-of-flight PET imaging*, Journal of nuclear medicine: official publication, Society of Nuclear Medicine 56, 98 (2015).
- [20] S. C. Behr, E. Bahroos, R. A. Hawkins, L. Nardo, V. Ravanfar, E. V. Capbarat, and Y. Seo, *Quantitative and visual assessments toward potential Sub-mSv or ultrafast FDG PET using high-sensitivity TOF PET in PET/MRI*, Molecular Imaging and Biology 20, 492 (2018).
- [21] A. M. Grant, T. W. Deller, M. M. Khalighi, S. H. Maramraju, G. Delso, and C. S. Levin, *NEMA NU 2-2012 performance studies for the SiPM-based ToF-PET component of the GE SIGNA PET/MR system*, Medical physics 43, 2334 (2016).
- [22] H. O. Anger, *Scintillation camera*, Review of scientific instruments 29, 27 (1958).
- [23] E. Venialgo, C. Verrastro, D. Estryk, M. Belzunce, A. Carimatto, E. da Ponte, L. M. Garbino, and J. Alarcon, *PET calibration method of nonlinear position estimation algorithms for continuous NaI(Tl) crystals*, in *Nuclear Science Symposium and Medical Imaging Conference (NSS/MIC), 2011 IEEE* (IEEE, 2011) pp. 3359–3364.
- [24] M. E. Casey and R. Nutt, *A Multicrystal Two Dimensional BGO Detector System for Positron Emission Tomography*, IEEE Transactions on Nuclear Science 33, 460 (1986).
- [25] N. Aubry, E. Auffray, F. Mimoun, N. Brillouet, R. Bugalho, E. Charbon, O. Charles, D. Cortinovis, P. Courday, A. Cserkaszy, *et al.*, *EndoTOFPET-US: a novel multimodal tool for endoscopy and positron emission tomography*, Journal of Instrumentation 8, C04002 (2013).
- [26] G. Llosá, J. Barrio, C. Lacasta, M. Bisogni, A. Del Guerra, S. Marcatili, P. Barrillon, S. Bondil-Blin, C. de La Taille, and C. Piemonte, *Characterization of a PET detector head based on continuous LYSO crystals and monolithic, 64-pixel silicon photomultiplier matrices*, Physics in Medicine & Biology 55, 7299 (2010).
- [27] M. C. Maas, D. R. Schaart, D. J. van der Laan, P. Bruyndonckx, C. Lemaître, F. J. Beekman, and C. W. van Eijk, *Monolithic scintillator PET detectors with intrinsic depth-of-interaction correction*, Physics in Medicine & Biology 54, 1893 (2009).
- [28] S. Seifert and D. R. Schaart, *Improving the time resolution of TOF-PET detectors by double-sided readout*, IEEE Transactions on Nuclear Science 62, 3 (2015).
- [29] S. Dolinsky, G. Fu, and A. Ivan, *Timing resolution performance comparison of different SiPM devices*, Nuclear Instruments and Methods in Physics Research Section A: Accelerators, Spectrometers, Detectors and Associated Equipment 801, 11 (2015).

- [30] S. Seifert, H. van Dam, and D. Schaart, *The lower bound on the timing resolution of scintillation detectors*, Phys. Med. Biol. 57, 1797 (2012).
- [31] S. Gundacker, E. Auffray, B. Frisch, P. Jarron, A. Knapitsch, T. Meyer, M. Pizzichemi, and P. Lecoq, *Time of flight positron emission tomography towards 100ps resolution with $l(y)$ so: an experimental and theoretical analysis*, Journal of Instrumentation 8, P07014 (2013).
- [32] M. E. Phelps, E. J. Hoffman, N. A. Mullani, C. S. Higgins, and M. M. Ter Pogossian, *Design considerations for a positron emission transaxial tomograph (PETT III)*, IEEE Transactions on Nuclear Science, 516 (1976).
- [33] G. Muehllehner, M. Buchin, and J. Dudek, *Performance parameters of a positron imaging camera*, IEEE Transactions on Nuclear Science 23, 528 (1976).
- [34] E. Van Loef, P. Dorenbos, C. Van Eijk, K. Krämer, and H.-U. GÜdel, *Scintillation properties of LaBr₃: Ce³⁺ crystals: fast, efficient and high-energy-resolution scintillators*, Nuclear Instruments and Methods in Physics Research Section A: Accelerators, Spectrometers, Detectors and Associated Equipment 486, 254 (2002).
- [35] S.-G. Crystals, *NaI(Tl) and Polyscin® NaI(Tl) Sodium Iodide Scintillation Material* ((accessed April 20, 2018)).
- [36] S.-G. Crystals, *BGO Bismuth Germanate Scintillation Material* ((accessed April 20, 2018)).
- [37] S.-G. Crystals, *LYSO Scintillation Material* ((accessed April 20, 2018)).
- [38] S. Seifert, J. Steenbergen, H. Van Dam, and D. Schaart, *Accurate measurement of the rise and decay times of fast scintillators with solid state photon counters*, Journal of Instrumentation 7, P09004 (2012).
- [39] S.-G. Crystals, *Lanthanum Bromide and Enhanced Lanthanum Bromide* ((accessed April 20, 2018)).
- [40] C. W. Van Eijk, *Inorganic scintillators in medical imaging*, Physics in Medicine & Biology 47, R85 (2002).
- [41] H. P. K. K., *PHOTOMULTIPLIER TUBES Basics and Applications* ((accessed April 20, 2018)).
- [42] V. Saveliev and V. Golovin, *Silicon avalanche photodiodes on the base of metal-resistor-semiconductor (MRS) structures*, Nuclear Instruments and Methods in Physics Research Section A: Accelerators, Spectrometers, Detectors and Associated Equipment 442, 223 (2000).
- [43] M. Ghioni, S. Cova, A. Lacaita, and G. Ripamonti, *New silicon epitaxial avalanche diode for single-photon timing at room temperature*, Electronics letters 24, 1476 (1988).

- [44] M. W. Fishburn, *Fundamentals of CMOS single-photon avalanche diodes* (fishburn, 2012).
- [45] M. Stipcevic, D. Wang, and R. Ursin, *Characterization of a commercially available large area, high detection efficiency single-photon avalanche diode*, *Journal of lightwave technology* 31, 3591 (2013).
- [46] L. SensL Technologies, *Technical note: MPPC* ((accessed April 20, 2018)).
- [47] C. Veerappan and E. Charbon, *A substrate isolated CMOS SPAD enabling wide spectral response and low electrical crosstalk*, *IEEE Journal of Selected Topics in Quantum Electronics* 20, 299 (2014).
- [48] L. SensL Technologies, *High PDE and Timing Resolution SiPM Sensors in a TSV Package* ((accessed April 20, 2018)).
- [49] V. Puill, C. Bazin, D. Breton, L. Burmistrov, V. Chaumat, N. Dinu, J. Maalmi, J. Vagnucci, and A. Stocchi, *Single photoelectron timing resolution of SiPM as a function of the bias voltage, the wavelength and the temperature*, *Nuclear Instruments and Methods in Physics Research Section A: Accelerators, Spectrometers, Detectors and Associated Equipment* 695, 354 (2012).
- [50] A. Rochas, M. Gosch, A. Serov, P. Besse, R. Popovic, T. Lasser, and R. Rigler, *First fully integrated 2-D array of single-photon detectors in standard CMOS technology*, *IEEE Photonics Technology Letters* 15, 963 (2003).
- [51] C. Niclass, A. Rochas, P.-A. Besse, and E. Charbon, *Design and characterization of a CMOS 3-D image sensor based on single photon avalanche diodes*, *IEEE Journal of Solid-State Circuits* 40, 1847 (2005).
- [52] T. Frach, G. Prescher, C. Degenhardt, R. de Gruyter, A. Schmitz, and R. Ballizany, *The digital silicon photomultiplier-Principle of operation and intrinsic detector performance*, in *Nuclear Science Symposium Conference Record (NSS/MIC), 2009 IEEE*.
- [53] S. Mandai and E. Charbon, *Multi-channel digital SiPMs: concept, analysis and implementation*, in *2012 IEEE Nuclear Science Symposium and Medical Imaging Conference Record (NSS/MIC)* (IEEE, 2012) pp. 1840–1844.
- [54] L. H. C. Braga, L. Gasparini, L. Grant, R. K. Henderson, N. Massari, M. Perenzoni, D. Stoppa, and R. J. Walker, *A Fully Digital 8× 16 SiPM Array for PET Applications With Per-Pixel TDCs and Real-Time Energy Output*. *J. Solid-State Circuits* 49, 301 (2014).
- [55] B.-L. Bérubé, V.-P. Rhéaume, A. C. Therrien, S. Parent, L. Maurais, A. Boisvert, G. Carini, S. A. Charlebois, R. Fontaine, and J.-F. Pratte, *Development of a single photon avalanche diode (SPAD) array in high voltage CMOS 0.8 μm dedicated to a 3D integrated circuit (3DIC)*, in *Nuclear Science Symposium and Medical Imaging Conference (NSS/MIC), 2012 IEEE*.

- [56] S. Brunner, L. Gruber, A. Hirtl, K. Suzuki, J. Marton, and D. Schaart, *A comprehensive characterization of the time resolution of the Philips digital photon counter*, *Journal of Instrumentation* 11, P11004 (2016).
- [57] A. Carimatto, S. Mandai, E. Venialgo, T. Gong, G. Borghi, D. R. Schaart, and E. Charbon, *11.4 A 67,392-SPAD PVTB-compensated multi-channel digital SiPM with 432 column-parallel 48ps 17b TDCs for endoscopic time-of-flight PET*, in *Solid-State Circuits Conference (ISSCC), 2015 IEEE International*.
- [58] E. Venialgo, S. Mandai, T. Gong, D. R. Schaart, and E. Charbon, *Time estimation with multichannel digital silicon photomultipliers*, *Physics in Medicine & Biology* 60, 2435 (2015).
- [59] S. Mandai, *Multichannel Digital Silicon Photomultipliers for Time-of-Flight PET* (Delft University of Technology, 2014).
- [60] E. Venialgo, S. Sinha, T. Gong, S. Mandai, A. Carimatto, S. E. Brunner, D. R. Schaart, and E. Charbon, *Small-animal and endoscopic PET detector modules based on multichannel digital silicon photomultipliers*, in *Nuclear Science Symposium, Medical Imaging Conference and Room-Temperature Semiconductor Detector Workshop (NSS/MIC/RTSD), 2016 (IEEE, 2016)* pp. 1–5.
- [61] D. R. Schaart, E. Charbon, T. Frach, and V. Schulz, *Advances in digital SiPMs and their application in biomedical imaging*, *Nuclear Instruments and Methods in Physics Research Section A: Accelerators, Spectrometers, Detectors and Associated Equipment* 809, 31 (2016).
- [62] S. Vandenberghe and P. K. Marsden, *PET-MRI: a review of challenges and solutions in the development of integrated multimodality imaging*, *Physics in Medicine & Biology* 60, R115 (2015).
- [63] S. Mandai and E. Charbon, *Timing optimization of a H-tree based digital silicon photomultiplier*, *Journal of Instrumentation* 8, P09016 (2013).
- [64] H. T. Van Dam, G. Borghi, S. Seifert, and D. R. Schaart, *Sub-200 ps CRT in monolithic scintillator PET detectors using digital SiPM arrays and maximum likelihood interaction time estimation*, *Physics in Medicine & Biology* 58, 3243 (2013).
- [65] T. Frach, G. Prescher, C. Degenhardt, R. de Gruyter, A. Schmitz, and R. Ballizany, *The digital silicon photomultiplier - Principle of operation and intrinsic detector performance*, in *Nuclear Science Symposium Conference Record (NSS/MIC), 2009 IEEE (2009)* pp. 1959–1965.
- [66] S. Mandai and E. Charbon, *A 4 × 4 × 416 digital SiPM array with 192 TDCs for multiple high-resolution timestamp acquisition*, *Journal of Instrumentation* 8, P05024 (2013).
- [67] C. Veerappan, *Single-Photon Avalanche Diodes for Cancer Diagnosis* (Delft University of Technology, 2016).

- [68] C. Niclass and M. Soga, *A miniature actively recharged single-photon detector free of afterpulsing effects with 6ns dead time in a 0.18 μm CMOS technology*, in *Electron Devices Meeting (IEDM), 2010 IEEE International* (IEEE, 2010) pp. 14–3.
- [69] A. Gulinatti, P. Maccagnani, I. Rech, M. Ghioni, and S. Cova, *35 ps time resolution at room temperature with large area single photon avalanche diodes*, *Electronics Letters* 41, 272 (2005).
- [70] E. V. A. Sachdeva and E. Charbon, *In-pixel Low-Threshold Comparator for Improved Timing-Resolution Digital SiPM*, in *Nuclear Science Symposium and Medical Imaging Conference (NSS/MIC), 2018 IEEE* (IEEE, 2018) pp. 1–2.

3

THEORY OF TIMING ESTIMATION WITH MULTIPLE TIMESTAMPS

Part of this chapter has been published as “Esteban Venialgo, Shingo Mandai, Tim Gong, Dennis R Schaart, and Edoardo Charbon. Time estimation with multichannel digital silicon photomultipliers. *Physics in Medicine & Biology*, 60(6):2435, 2015”.

The timemark precision determines the TOF-PET gain in terms of image quality SNR [1]. In scintillator/photodetector-based PET modules, the timemark of the γ -photon is estimated from the photodetector's output signals [2–5]. D-SiPMs with multiple TDCs are capable of detecting multiple photoelectron timestamps per scintillation event, in order to reconstruct a precise timemark of the initial γ -photon [6–8]. This chapter describes the evolution of statistical models of scintillator/photodetector signal generation, timemark estimation methods based on single and multiple photoelectron timestamps, as well as an analysis and limitations of statistical lower bounds [8].

3

3.1. TIMING ESTIMATION MODEL EVOLUTION

In the early 1950s, a statistical model that described the decay process of a scintillator was introduced for the first time [2]. It was based on Poisson statistics, assumed a single-exponential decay model and did not include the SPTR of the photodetector. Consequently, it predicted that the best timing performance of the γ -photon's timemark estimation was obtained when utilizing the first photoelectron.

In 1966, a review paper was published that compared experimental and simulation results of coincidence measurements with scintillation detectors. This work demonstrated that the lowest variance is not necessarily obtained with the first photoelectron because of the influence of the SPTR and the finite rise time in scintillators [9].

Later, a broad theoretical background was established that allowed the use of any type of scintillation decay pulse shape or PDF [3]. According to this model, the PDF of the q^{th} photoelectron's timestamp, called p_q , is given by

$$p_q(t) = \frac{R!}{(q-1)!(R-q)!} [1 - F(t)]^{(R-q)} [F(t)]^{(q-1)} f(t), \quad (3.1)$$

where $f(t)$ represents the photoelectron time distribution PDF and $F(t)$ its corresponding CDF.

In 2010, the concept of order statistics was introduced to the scintillation decay process, in combination with a double-decay exponential model [4]. It is possible to obtain the same theoretical framework previously derived in [3] using order statistics. The double exponential decay model, where τ_r , τ_d are the rise and decay constants, respectively, while T_0 is the timemark of the γ -photon, can be expressed as

$$f_s(t) = \begin{cases} 0 & \text{for } t \leq T_0 \\ \frac{1}{\tau_d - \tau_r} [e^{-\frac{t-T_0}{\tau_d}} - e^{-\frac{t-T_0}{\tau_r}}] & \text{for } t > T_0 \end{cases}. \quad (3.2)$$

According to the model proposed in that work, the distribution of timestamps generated by a system composed of a scintillator and a photodetector follows the distribution defined by

$$f(t) = f_s(t) * \mathcal{N}(\mu_{\text{TJ}}, \sigma_{\text{TJ}}). \quad (3.3)$$

The Gaussian distribution $\mathcal{N}(\mu_{\text{TJ}}, \sigma_{\text{TJ}})$ models the total timing jitter of the instrumentation chain. In addition, the PDF of the resulting photoelectron time distribution is the convolution between $f_s(t)$ and $\mathcal{N}(\mu_{\text{TJ}}, \sigma_{\text{TJ}})$ since the total timing jitter is modeled as

additive noise. μ_{TJ} and σ_{TJ} model the total timing skew and jitter, respectively [4]. σ_{TJ} includes all of the sources of time uncertainty such as, TDC's timing jitter, SPTR, electronic noise, etc.

Next, the Cramer-Rao lower bound (CRLB) on the time resolution of scintillation detectors was derived [5]. Instead of the single bi-exponential function $f_s(t)$ given in equation (3.2), the analysis is based on a more accurate model of scintillation decay that is able to account for the multiple, simultaneous cascades of excitation and decay processes that occur in some scintillators, such as $\text{LaBr}_3(\text{Ce})$. This model can be used with a Gaussian function to describe the total timing jitter of the instrumentation chain, as in equation (3.3), or with a more complex PDF in cases where a Gaussian approximation is considered insufficiently accurate. Moreover, the possibility to utilize multiple photoelectron timestamps for γ -photon's timemark estimation was analyzed in some depth [5].

Given a set of multiple timestamps, the CRLB predicted the maximum efficiency that a γ -photon's timemark estimator could potentially reach. However, it does not define any particular estimator that could reach such a performance. Initially, multiple timestamp estimation methods were proposed; however, they degrade the performance as the number of timestamps increases unless the multiple timestamp set is complete [10, 11]. Next, a linear estimation method based on multiple timestamps that improves the estimation performance as the number of timestamp increases was introduced [6]. Later, the γ -photon's timemark MLE for multiple timestamps was described including an extended analysis of the CRLB [8].

3.2. THE CRAMÉR-RAO LOWER BOUND

The CRLB is a scalar value that establishes the lower bound on the variance of any unbiased estimator of the parameter of interest, and it is applicable to the particular case of order statistic [5, 12, 13]. However, regularity conditions are required in order to obtain a valid CRLB [14]. Common support is a condition for obtaining a valid Fischer information calculation. This regularity condition can be expressed as follows for the problem under consideration in this work:

$$\{t : f(t|T_0) > 0\} \text{ is the same } \forall T_0 \in \mathbb{R}. \quad (3.4)$$

In principle one might question if this condition is fulfilled since our model assumes zero probability of scintillation photon emission before T_0 [5, 15].

However, the condition is fulfilled when the scintillation decay function is convolved with the total Gaussian timing jitter of the system, as in equation (3.3). It is to be noted that this model in principle allows the (false-positive) registration of scintillation photons at times earlier than T_0 . Although this is not unphysical if the instrumentation chain indeed exhibits a white timing jitter spectrum or dark counts are timestamped, one might prefer to also truncate $\mathcal{N}(\mu_{\text{TJ}}, \sigma_{\text{TJ}})$ at T_0 in equation (3.3). Such truncation should be performed carefully in order to include a sufficiently large part of the left tail of $\mathcal{N}(\mu_{\text{TJ}}, \sigma_{\text{TJ}})$, so as to avoid significant breaching of regularity condition. Fortunately, this is easily achieved in practice because in a typical photodetector instrumentation chain, $\mu_{\text{TJ}} - T_0$ is many times larger than σ_{TJ} .

In general, it is not guaranteed that an unbiased estimator exists that is able to reach the CRLB for a given problem. To illustrate this, we investigate the simple case in which the registration time of only one of the scintillation photons is known and we compare the only possible unbiased estimator that exists in this case to the CRLB, as a function of several system parameters.

When estimating the γ -photon's timemark just utilizing the q^{th} photoelectron only, the only possible unbiased estimator is given by

$$\hat{T}_0 = t_q - A, \quad (3.5)$$

where A is expressed as

$$A = E[p_q | T_0 = 0]. \quad (3.6)$$

The precision of this estimator in terms of the root mean square error (root-MSE) is equal to the square root of the variance of the PDF of the timestamp of the q^{th} photoelectron.

$$\sqrt{MSE(\hat{T}_0)} = \sigma_q. \quad (3.7)$$

Equation (3.7) provide a simple means to compare the only possible unbiased estimator performance against the CRLB for several system design parameter configurations.

In the single-photoelectron T_0 estimation case, the Fisher information $I(T_0)$ is given by

$$\begin{aligned} I(T_0) &= \int_{-\infty}^{+\infty} \left[\frac{\partial}{\partial T_0} \log p_q(t|T_0) \right]^2 p_q(t|T_0) dt \\ &= \int_{-\infty}^{+\infty} \left[\frac{\partial}{\partial T_0} \log g_q(t - T_0) \right]^2 g_q(t - T_0) dt \\ &= \int_{-\infty}^{+\infty} \left[\frac{1}{g_q(t - T_0)} \frac{\partial}{\partial t} g_q(t - T_0)(-1) \right]^2 g_q(t - T_0) dt \\ &= \int_{-\infty}^{+\infty} \left[\frac{\partial}{\partial t} g_q(t - T_0) \right]^2 \frac{1}{g_q(t - T_0)} dt, \end{aligned} \quad (3.8)$$

where the chain rule was applied to rewrite $p_q(t|T_0)$ as follows:

$$p_q(t|T_0) = g_q(t - T_0). \quad (3.9)$$

We calculated the Fisher information with a time step of 1 ps, for different values of the essential scintillation properties and swept the system design parameters [5, 16–18]. Subsequently, we calculated the standard deviation of $p_q(t)$ with the same time step and compared the results.

Figure 3.1a shows the σ_q and root-CRLB as a function of the photoelectron order for different numbers of detected photoelectrons. Figures 3.1b and 3.1c depict similar comparisons for different scintillators and for different values of total timing jitter of the system respectively. In all of the plots the total timing jitter of the system is given at FWHM level. The number of photoelectrons was intentionally kept low in Figures 3.1b and 3.1c (i.e., corresponding to an overall PDE of about 6 %, since under these conditions the only possible unbiased estimator does not fully reach the CRLB, as in Figure 3.1a).

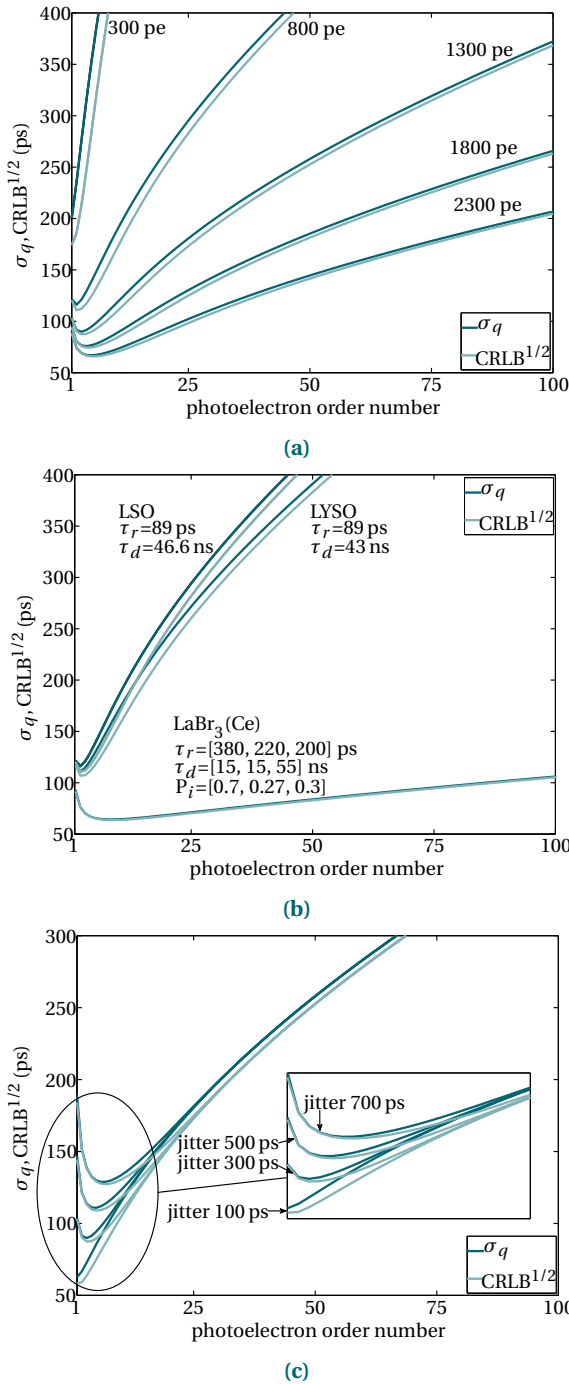


Figure 3.1: σ_q and root-CRLB as a function of the photoelectron order for different system design parameters. (a) τ_r was set to 89 ps and τ_d to 46.6 ns, the total timing jitter of the system was set to 300 ps (FWHM). (b) The number of detected photoelectrons was 1800 for LaBr₃(Ce) and 800 in all of the other scintillators; the total timing jitter of the system was 300 ps (FWHM). (c) τ_r and τ_d was set as in (a); the total number of detected photoelectrons was 1300.

3.3. MAXIMUM LIKELIHOOD ESTIMATION

As demonstrated in the previous section, the only possible unbiased estimator in the single-photoelectron timestamp case does not always reach the CRLB, for certain system design parameters. In the multiple-photoelectron time estimation case, there are many possible unbiased estimators, and it is computationally impractical to perform the previous analysis for all system design parameter combinations.

In the multiple photoelectron timestamp case, we therefore limited ourselves to the calculation of the MSE of the multiple-photoelectron MLE in two different conditions, which were defined based on the results obtained in the single-photoelectron time estimation case. We calculated the CRLB of the multiple-photoelectron estimation case for the same two conditions and compared it to the result obtained with the MLE.

The likelihood function defined for the $t_{1:Q}$ timestamps of the first Q photoelectrons, for the estimation of location parameter (T_0) is expressed by

$$L_{1:Q}(t_1, \dots, t_Q | T_0) = \frac{R!}{(R-Q)!} \prod_{q=1}^Q f(t_q | T_0) \{1 - F(t_Q | T_0)\}^{R-Q}. \quad (3.10)$$

This expression corresponds to a type II censored sample of order statistics [14]. The likelihood functions were calculated with a time step of 1 ps. Subsequently, the root-MSE of the multiple-photoelectron MLE was evaluated utilizing random timestamps generated with a Monte Carlo code, which follows the same model as $L_{1:Q}(t_1, \dots, t_Q | T_0)$.

As observed in Figures 3.1a, 3.1b and 3.1c, the only possible unbiased estimator in the single photoelectron timestamp case does not fully reach the CRLB when the timing jitter level is low and the number of detected photoelectrons is small. Thus, we generated two random timestamp datasets called I and II, the dataset I with 100 ps FWHM timing jitter and 300 photoelectrons; the dataset II with 700 ps FWHM timing jitter and 3800 photoelectrons. The scintillation decay constants were the same for both datasets, namely LSO with properties according to [5, 18]. The Fisher information of a set of order statistic random variables was already derived [13]. In addition, the corresponding Fisher information of the multiple-photoelectron timestamps, which is a set of order statistic random variables, is defined as follows:

$$I_{1:Q} = \int_{-\infty}^{+\infty} \left[\frac{\partial}{\partial T_0} \log h(t | T_0) \right]^2 \left[\sum_{q=1}^Q p_q(t | T_0) \right] dt, \quad (3.11)$$

$$h(t | T_0) = \frac{f(t | T_0)}{1 - F(t | T_0)}. \quad (3.12)$$

The performance of MLE for estimating the location parameter T_0 utilizing both datasets is depicted in Figure 3.2. The number of TDCs is equal to the number of sorted timestamps utilized for the estimation and varies from 1 to 30. The root-MSE of the MLE differs from the CRLB by about 67 ps in the case of the dataset I. However, for the dataset II (see Figure 3.2) the root-MSE of the MLE is very close to the CRLB. In conclusion, we observe that the MLE does not fully reach the CRLB if the number of detected photoelectrons is small and the total timing jitter of the system is low, similarly to what was observed for the only possible unbiased estimator in the single photoelectron timestamp case. The important difference between the single and multiple photoelectron

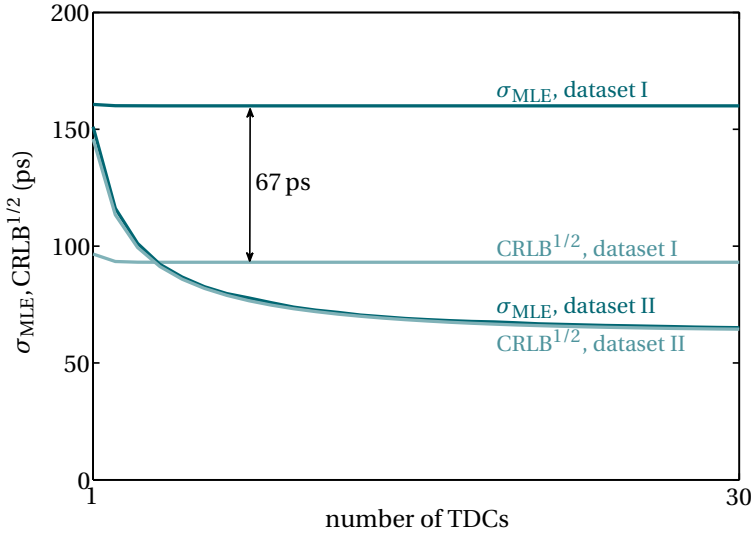


Figure 3.2: root-MSE of the multiple-timestamp MLE and root-CRLB vs. size of multiple timestamps set, when utilizing the datasets I and II.

timestamp cases is that in the latter many different estimators can be defined. The fact that the MLE does not reach the CRLB under some conditions in the multiple photoelectron timestamp case implies that it may be possible to find more efficient estimators than the MLE under such conditions. However, obtaining good timing resolution in scintillation detectors requires the use of scintillators with high light output in combination with photodetectors with high photoelectron detection efficiency (PDE) [5]. Under those conditions, the present results indicate that the MLE is an efficient estimator.

3.4. WEIGHTED AVERAGE TIMEMARK ESTIMATORS

In general, a linear function of a sorted set of random samples provides an efficient estimator of the location parameter [14]. We tested several weighted-average estimators such as the *simple mean*, the *variance weighted* and the *best linear unbiased estimator* (BLUE) by calculating the single detector root-MSE of the estimators using the Monte Carlo simulator.

The weighted-average timemark estimators are given by

$$\hat{T}_0^{(p)} = \sum_{q=1}^Q t_q w_q^{(p)}, \quad p = 1, 2, 3. \quad (3.13)$$

The first estimator calculates the average value of a group of ordered Q photoelectron timestamps. We call this estimator the simple mean estimator and the weights are given by ($p = 1$)

$$w_q^{(1)} = \frac{1}{Q}, \quad q = 1, \dots, Q. \quad (3.14)$$

The number of photoelectrons timestamps Q utilized to calculate the mean value was varied from 1 to 48, since the MD-SiPM that was designed in our laboratory has 48 TDCs per MD-SiPM [19, 20]. Furthermore, t_q corresponds to the timestamp of the q^{th} photoelectron.

The second method is a weighted-average estimator, in which the weights are calculated according to the variance of the corresponding t_q timestamp ($p = 2$)

$$w_q^{(2)} = \frac{\text{Var}(t_q)^{-1}}{\sum_{i=1}^Q \text{Var}(t_i)^{-1}}, \quad q = 1, \dots, Q. \quad (3.15)$$

Furthermore, the weights are normalized so the sum of the weights is equal to the unity, in order to preserve the linearity of the estimation. This method is called the variance weighted estimator. Experimentally, each weight can be estimated during a calibration procedure.

The third method is also a weighted-average estimator but we calculated the weights according to the covariance of the timestamps following ($p = 3$)

$$\Delta w_q^{(3)} = [w_1^{(3)}, w_2^{(3)}, \dots, w_Q^{(3)}]^T, \quad (3.16)$$

$$\Delta w_q^{(3)} = \frac{\Delta C^{-1} \Delta d}{\|\Delta C^{-1/2} \Delta d\|_2^2}, \quad (3.17)$$

where Δd is a column vector filled with ones and with a length equal to the number of utilized timestamps, and ΔC is the covariance matrix of the timestamps. This estimator follows the BLUE methodology in order to obtain a weighted-average estimation with minimum variance. The last step in the derivation of this estimator for the case of a single detector would be to compensate the bias in the estimation by subtracting the multiplication between $\Delta w_q^{(3)}$ and the mean vector of the timestamps. However, in a coincident setup such as a PET system this step is not required, since the biases of two equal, coincident detectors cancel against each other.

In order to test the estimators, we generated random timestamps with the Monte Carlo code based on the models explained in [5]. In addition, we included the influence of the energy resolution (ER) into the Monte Carlo code by sampling R (number of detected photoelectrons) randomly according to the selected ER.

Figure 3.3a shows the root-MSE of all estimators as a function of the number of TDCs under two timing jitter conditions. Figures 3.3b and 3.4a show the root-MSE as a function of the number of photoelectron timestamps for two different energy resolutions and for two different number of photoelectrons, respectively. Figure 3.4b shows the root-MSE of the estimators for two types of crystals scintillators.

In Figures 3.3a, 3.3b, 3.4a and 3.4b the LYSO decay constants were taken from [5] Table 1 entry 10. In Figure 3.4b, the LaBr₃(Ce) decay constants were taken from [16].

As observed, the accuracy of BLUE and MLE improves as more TDCs are included in the estimation. In contrast, the other estimators tend to degrade when increasing the number of TDCs. The MLE and BLUE estimators are observed to have practically equal efficiency under all the system conditions studied.

3.5. SKIPPING EFFECT

In the previous sections, we did not yet take into account the fact that the TDCs are shared. Subsequently, the number of available TDCs per SPAD is less than 1. This condition significantly modifies the time distribution of the ordered photoelectrons; therefore, the likelihood function must be readjusted in order to account for this effect.

In this implementation, each of the 3 TDCs in a column is shared by 8 or 9 SPADs through an OR gate (see Figure 2.19); therefore, as soon as a TDC detects the q^{th} photoelectron signal, it becomes unavailable and the overall probability that the next photoelectron is timestamped decreases. In other words, if a photoelectron generates an avalanche in a SPAD cell that is connected to an already-triggered TDC, then its time information is lost. We call this decrease in detection probability the skipping effect. Assuming that the photoelectron detection probability is equal and constant for every group composed by 8 or 9 SPADs and a TDC; then, the probability to detect a continuous set of timestamps without skipping can be straightforwardly calculated as follows:

$$P(1 : Q) = \prod_{i=1}^Q \frac{(N_{\text{TDCs}} - i + 1)}{N_{\text{TDCs}}}, \quad (3.18)$$

where N_{TDCs} represents the total number of TDCs of the MD-SiPM, and $1 : Q$ is referred to a set of sorted timestamps of size $Q < N_{\text{TDCs}}$.

From equation (3.18), $P(1 : Q)$ decreases significantly if the set size $1:Q$ is larger than 20 and N_{TDCs} is 48, for instance. Consequently, the resulting time distribution of the q^{th} photoelectron does not follow equation (3.1) anymore and the likelihood function of equation (3.10) is no longer valid. In order to obtain an accurate estimation with the MLE method, the likelihood function must account for this effect.

The photoelectron timestamp probability distribution including the skipping effect can be modeled as a two-stage order-statistics process if we assume that the photoelectron detection probability is equal for every TDC when all TDCs are in non-occupied state. We first model the time distribution of the unsorted timestamps measured by the TDCs using a modified version of the function $f(t)$ called f_k as follows:

$$R' = \frac{R}{N_{\text{TDCs}}}, \quad (3.19)$$

$$f_k(t) = R'[1 - F(t)]^{(R'-1)} f(t). \quad (3.20)$$

Thus, $f_k(t)$ represents the time distribution of the first photoelectron that is timestamped by any of the TDCs. In the second step, we model the sorting of the TDC's timestamps. The resulting $p_q(t)$ that accounts for the skipping effect is given by

$$p_q(t) = q \binom{N_{\text{TDCs}}}{q} [1 - F_k(t)]^{(N_{\text{TDCs}}-q)} [F_k(t)]^{(q-1)} f_k(t). \quad (3.21)$$

Figure 3.5a depicts the $p_q(t)$ for several ordered photoelectrons with and without skipping effect modeling. Figure 3.5b shows the PDFs calculated by equation (3.21) and the normalized histograms generated from a Monte Carlo simulation.

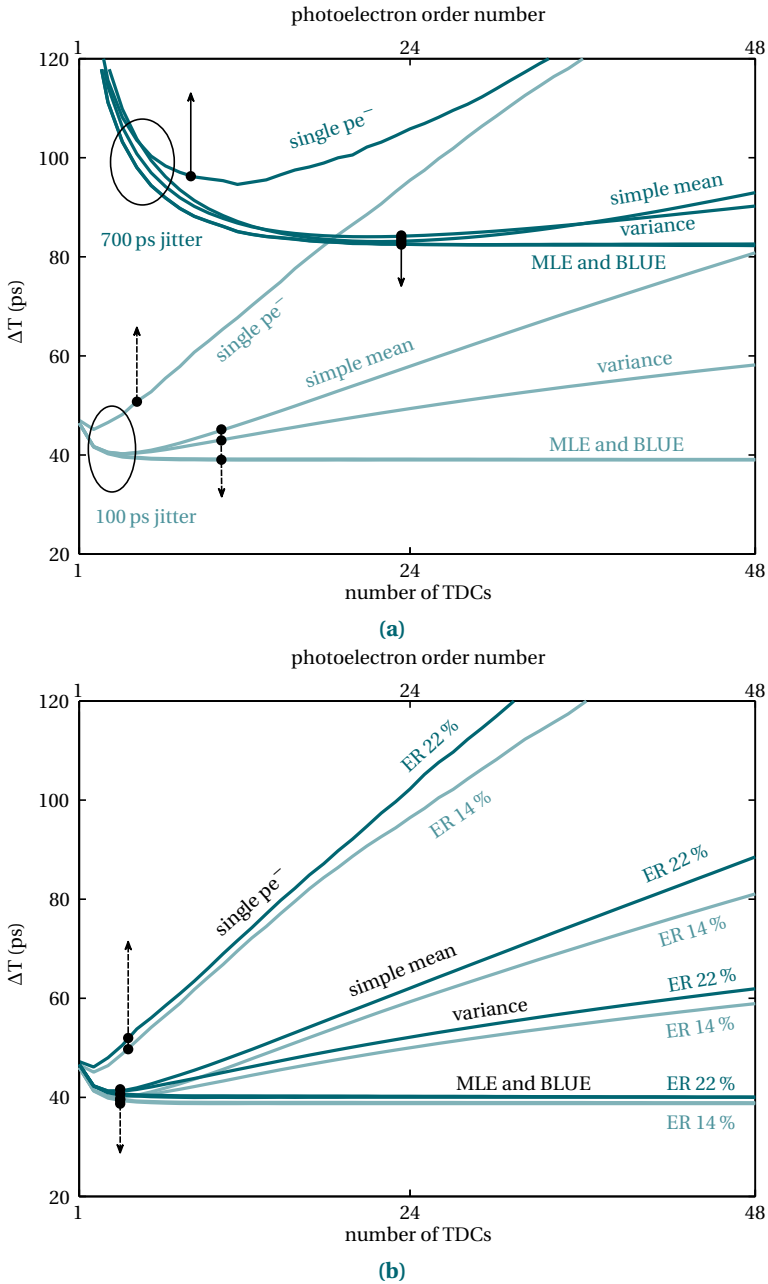
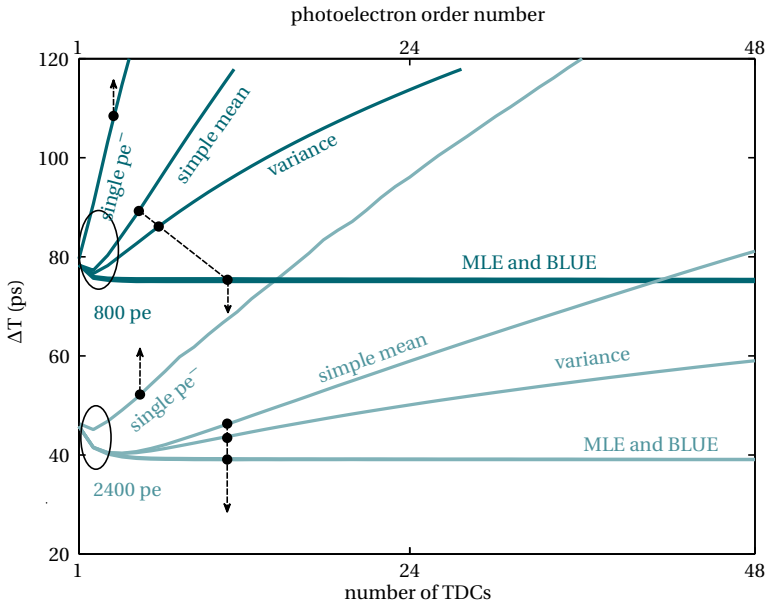
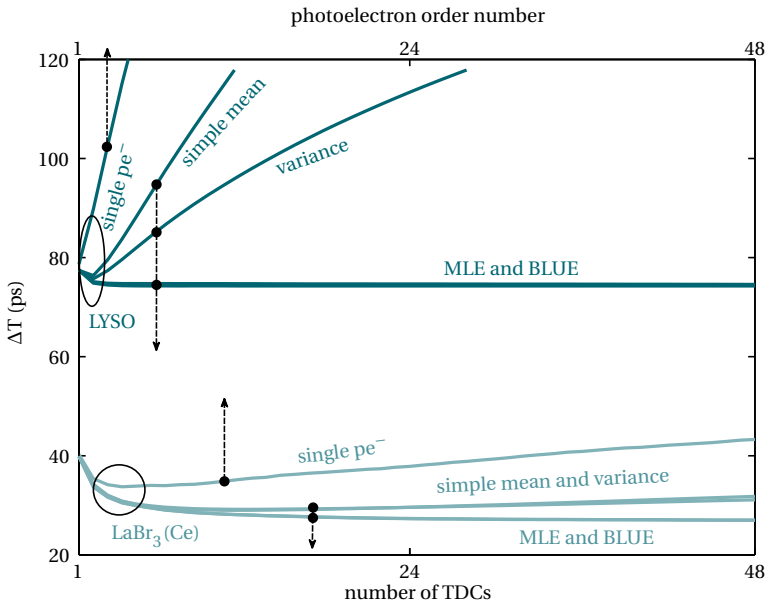


Figure 3.3: Single detector root-MSE (ΔT) for all of the estimators. (a) For two different timing-jitter levels, the ER was set to 14%, the number of detected photoelectrons was set to 2400 and the scintillator was set to LYSO. (b) For two different ERs, the number of detected photoelectrons was set to 2400, the scintillator was set to LYSO and the total timing jitter of the system was set to 100 ps (FWHM).



(a)



(b)

Figure 3.4: Single detector root-MSE (ΔT) for all of the estimators. (a) For two different number of photoelectrons, the ER was set to 14 %, the scintillator was set to LYSO and the total timing jitter of the system was set to 100 ps (FWHM). (b) For two scintillators, the number of detected photoelectrons was set to 2400 for the LYSO scintillator and 4800 for the $\text{LaBr}_3(\text{Ce})$ scintillator; the ER was set to 14 %, and the total timing jitter of the system was set to 100 ps (FWHM).

Table 3.1: System design parameters for condition I and II.

	Scintillator Size	MD-SiPMs	TDCs	SPAD Cells	Total DCR(max)
Condition I	$0.8 \times 0.8 \times h \text{ mm}^3$	1	48	416	125 Mcps
Condition II	$1.6 \times 1.6 \times h \text{ mm}^3$	4	96	1664	500 Mcps

The next step is to derive a likelihood function that models the skipping effect. Such a function is given by

$$L_{1:Q'}(T_0|t_1, \dots, t_{Q'}) = \frac{N_{\text{TDCs}}!}{(N_{\text{TDCs}} - Q')!} \prod_{q=1}^{Q'} f_k(t_q|T_0) \{1 - F_k(t_{Q'}|T_0)\}^{N_{\text{TDCs}} - Q'}, \quad (3.22)$$

where in this case, $1 : Q'$ represents a subset of the timestamps that were registered by a system that has skipping effect.

This equation shows that, if all of the timestamps are utilized, then the MLE does not require sorted timestamps. In addition, under this condition the assumption of equal detection probability for every TDC is no longer required; consequently, the $f_k(t)$ can be replaced by a specific TDC PDF [11].

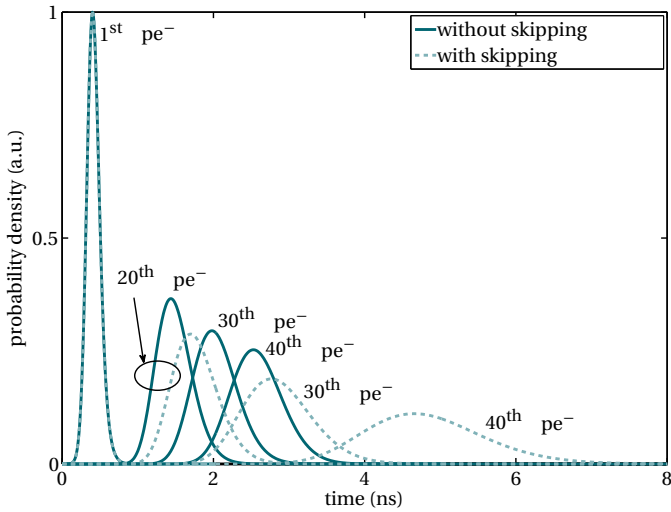
3.6. DARK COUNT RATE FILTERING

Dark counts can significantly affect the resolving time of a PET detector module composed by SiPMs. Several DCR filtering methods have been implemented in digital SiPMs [19–22]. In this section, we simulated the DCR rejection method described in [20], propose a new filtering method based on timestamps subtractions, and correct the likelihood function to account for DCR.

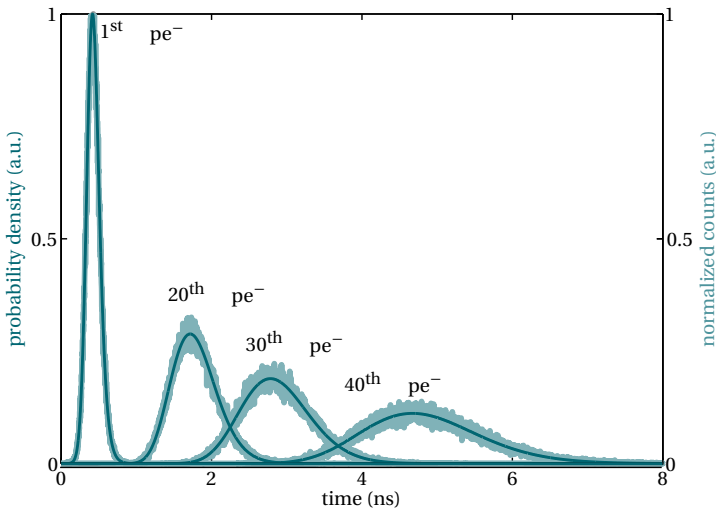
Additionally, we consider two scintillator/photodetector coupling conditions (see Figure 3.6). In condition I, a single pixel of LYSO is coupled directly to a single MD-SiPM. In condition II, we simulated a pixel of LYSO, with a four times larger footprint, coupled to a 2×2 MD-SiPM array. Consequently, in condition II the initial amount of available TDCs is twice as high as in condition I and the DCR is four times higher. The number of TDCs in condition II is not four times larger because of the way of sharing the TDCs in an array of MD-SiPMs [20]. The number of TDCs in condition II is twice as high as in condition I. The photoelectron dynamic range of condition II quadruples in condition I. Table 3.1 shows the system design parameters for condition I and II. Figures 3.6a and 3.6b show a representation of the coupling condition between the LYSO pixels and the MD-SiPMs.

In order to simplify the free parameters, we assume that the factor limiting the total amount of light detected is only the MD-SiPM dynamic range. That is, it is not limited by the crystal light output nor the MD-SiPM's PDE. Consequently, the mean number of detected photoelectrons was fixed to 800 for condition I and 3200 for condition II. The total timing jitter of the system (σ_{TJ}) was kept equal to 179 ps for both cases [19].

We included the DCR effect within the Monte Carlo simulation and simulated the smart-reset technique [19]. The γ -photon's timemark was randomly generated following a uniform distribution between 0 and 100 ns. The dark counts were generated fol-



(a)



(b)

Figure 3.5: $p_q(t)$ for several ordered q^{th} photoelectrons. (a) $p_q(t)$ was calculated with skipping effect from equation (3.21) and without skipping effect from equation (3.1). (b) $p_q(t)$ was obtained from a Monte Carlo simulation, as compared with the calculated values accounting for skipping effect. Note the near perfect match between the calculated and simulated values of $p_q(t)$

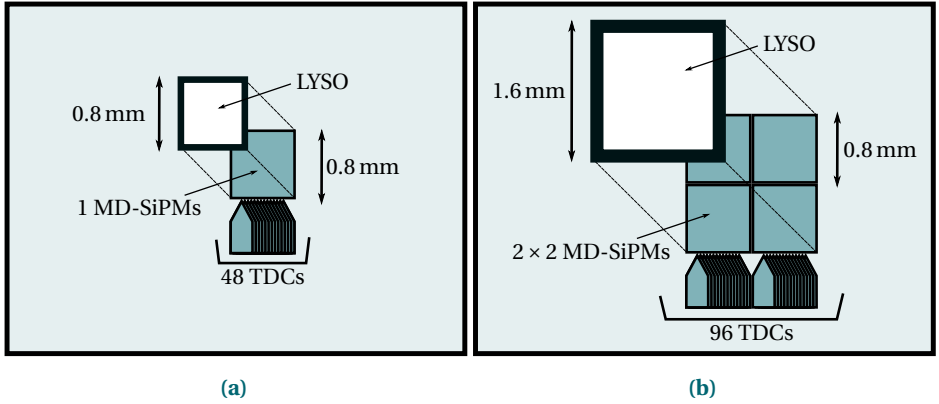


Figure 3.6: Condition I and II representation. In (a), the crystal pixel is attached to one MD-SiPM and in (b) the crystal pixel is attached to four MD-SiPMs.

lowing an exponential distribution with a given DCR, since the SPADs are reset in every new detection cycle. Afterpulsing was ignored. The DCR was kept identical for every group composed by a TDC and 8 or 9 SPADs. If the total DCR of the MD-SiPM is above 100 Mcps, then the probability that a dark count triggers a TDC within the detection cycle of 100 ns is considerable. Consequently, another filtering technique should be performed before the time estimation occurs. We propose to filter out the dark counts based on the time differences between sorted timestamps (see Figure 3.7, where $\Delta T_{q,q+1}$ and $\Delta T_{d,d+1}$ represents the time difference between two consecutive photoelectron timestamps and two dark counts timestamps, respectively).

For known system design parameters, such as crystal type, total number of TDCs, etc.; it is possible to calculate the distribution of the time difference between consecutive timestamps. Utilizing $f_k(t)$ from equation (3.20), the joint distribution of order statistics can be expressed as follows:

$$p_{q,q+1}(t_1, t_2) = \frac{N_{\text{TDCs}}!}{(q-1)!(N_{\text{TDCs}} - q - 1)!} [F_k(t_1)]^{q-1} [1 - F_k(t_2)]^{N_{\text{TDCs}} - q - 1} \times f_k(t_1) f_k(t_2), \quad (3.23)$$

where $t_1 < t_2$.

Using this result, the distribution of the time difference between two consecutive timestamps t_q and t_{q+1} is given by

$$f_{\Delta(q,q+1)}(t) = \int_{-\infty}^{+\infty} p_{q,q+1}(a, t+a) da. \quad (3.24)$$

It is important to mention that $f_k(t)$ and consequently $F_k(t)$ must be recalculated for each of the possible skipping effect conditions that may arise due to the presence of dark counts. DCR modifies the amount of available TDCs because of dark counts that accumulate after each reset. Consequently, for each $f_{\Delta(q,q+1)}(t)$ there are $N_{\text{TDCs}} - 1$ possible

PDFs (see Figures 3.8a and 3.8b). These PDFs are utilized to define a filtering time window for the time difference between subsequent photoelectron in every skipping effect condition. The time windows are defined as the time at which $f_{\Delta(q,q+1)}(t)$ is completely vanished. Figure 3.9 shows the normalized histograms of $\Delta(q, q+1)$ calculated from Monte Carlo simulations, which overlap the $f_{\Delta(q,q+1)}(t)$ using equation (3.24).

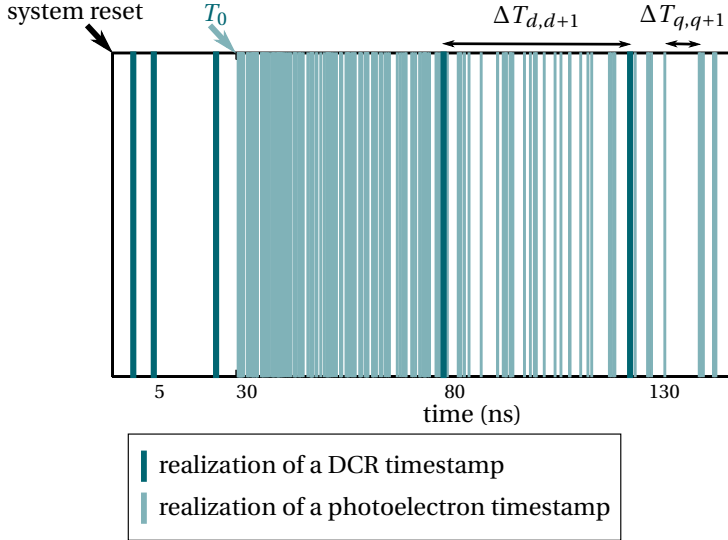


Figure 3.7: Realizations of photoelectron and DCR timestamps.

Before the arrival of the γ -photon, the TDCs are being fired with dark counts that follow a certain inter-avalanche time distribution. When the γ -photon triggers a scintillation event, light photons are emitted producing a higher avalanche rate in the photodetector (see Figure 3.7). Consequently, the proposed filter is designed to remove the dark counts that accumulated in the beginning of the measurement frame before the γ -photon's arrival, by measuring the distance between timestamps. After the γ -photon's arrival, it is not possible to discriminate dark counts from actual photoelectron detections.

The filtering procedure is shown in Algorithm 2, where the timestamps are calculated and compared to a time window. If the first N timestamp differences are not inside their corresponding time windows, the first timestamp is discarded and the procedure is repeated by utilizing new windows that correspond to the new skipping condition. The set size of the first N timestamps is defined by the parameter *length* in the Algorithm 2.

Some dark counts are not discriminated because they are randomly generated inside the time windows (see Figure 3.7). Particularly, among the first photoelectron timestamps there is more probability to register dark counts even after filtering, because of the dark count accumulation before γ -photon's detection. In order to account for this effect within the likelihood functions, we re-estimated $f_k(t)$ for several DCR levels by utilizing Monte Carlo simulations and a kernel density estimator based on the Epanechnikov kernel function. Figures 3.10a and 3.10b show the estimated $f_k(t)$ for condition I

input : A timestamp set $T_M(q)$ of N_{TDCs} size.
input : A set of time windows $W_N(\Delta q, \text{skipped})$ of size $(N_{\text{TDCs}} - 1) \times (N_{\text{TDCs}} - 1)$
input : Number of required first timestamps within their corresponding time windows, *length*
output: A filtered timestamp set $F_M(q)$ of $(N_{\text{TDCs}} - \text{skipped})$ size.
output: Amount of TDCs that are initially triggered by dark counts, *skipped*

```

skipped =  $N_{\text{TDCs}}$ ;
deltaT = diff( $T_M$ ) ;
for sweep = 1 : ( $N_{\text{TDCs}} - 1$ ) do
    current = deltaT (sweep:end);
    condition =  $W_N(:, \text{sweep}) - \text{current} > 0$ ;
    if all(condition (1 : length)) then
        skipped = sweep;
         $F_M = T_M(\text{sweep} : \text{end})$  ;
        break;
    end
end

```

Algorithm 2: DCR Filter Algorithm

and II. The magnified area shows an increase of probability in the beginning of the PDF that depends on DCR. This effect is produced by dark counts that are not discriminated among the first photoelectron timestamps, as explained before.

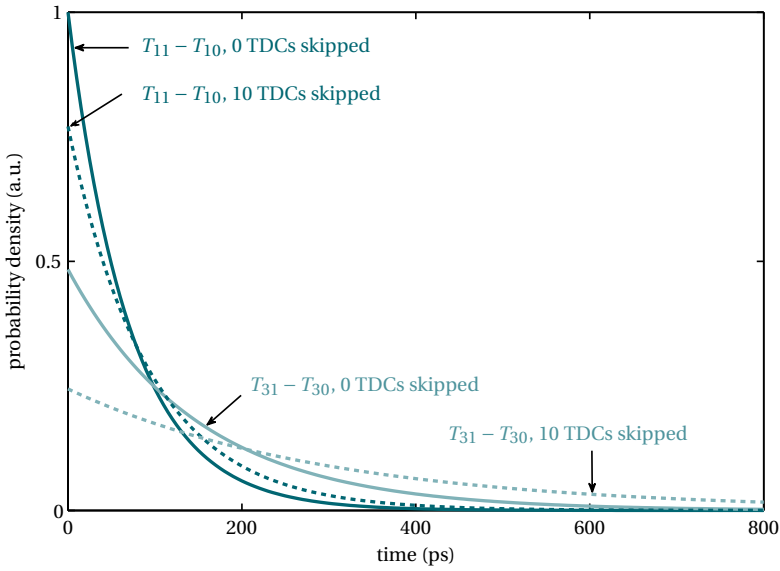
It is to be noted that we did not take into account the statistical Poisson variations of R' in equations (3.19) and (3.20). These fluctuations can potentially modify the likelihood equation significantly if the number of photoelectrons per TDC is low. Consequently, we included this effect within the Monte Carlo simulation that estimates $f_k(t)$. Therefore, the likelihood functions depicted in Figures 3.10a and 3.10b do take into account the statistical variations of R' . In addition, we calculated a $f_k(t)$ with a fixed value of R' for condition I and 250 kcps DCR. This $f_k(t)$ is depicted with a dashed line in 3.10a.

3.7. OVERALL PERFORMANCE

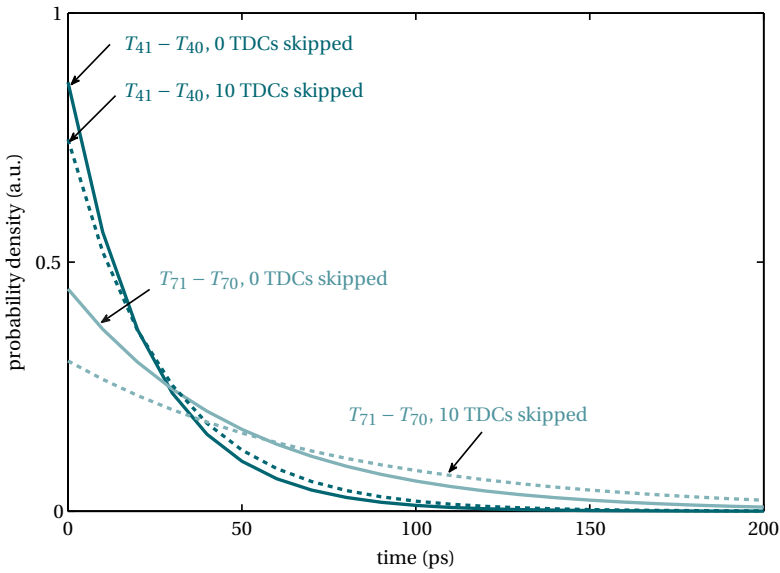
After including the DCR model in the Monte Carlo code, it appears that DCR filters and corrections of the likelihood function are required to account for the dark counts that are not discriminated. The last part of this study is focused on the performance of BLUE and MLE under DCR and skipping effect conditions. A new set of Monte Carlo simulations was run, which included the skipping effect, DCR, and the proposed rejection method.

Random timestamps were regenerated under condition I and II (see Table 3.1 and Figures 3.6a and 3.6b), taking into account the influences of DCR and skipping effect. The coefficients of BLUE were calculated utilizing a different realization of the Monte Carlo data; consequently, they include the influence of DCR and skipping effect. MLE utilizes the $f_k(t)$ functions depicted in Figures 3.10a and 3.10b in order to model the DCR influence.

In addition, the likelihood function was customized for each individual γ -photon,



(a)



(b)

Figure 3.8: (a) $f_{\Delta(q,q+1)}(t)$ calculated for condition I and several skipping cases. (b) $f_{\Delta(q,q+1)}(t)$ calculated for condition II and several skipping cases.

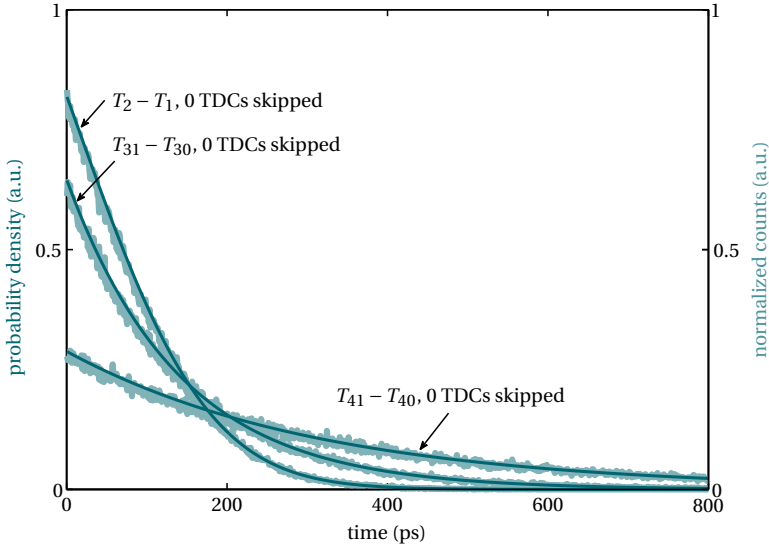


Figure 3.9: Normalized histograms obtained from a Monte Carlo simulation, as compared with the calculated $f_{\Delta(q,q+1)}(t)$ from equation (3.24).

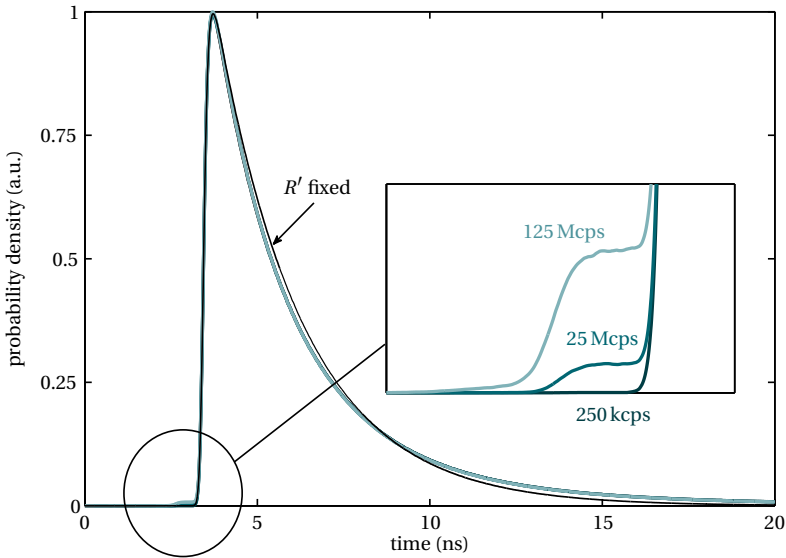
since the skipping effect changes depending on how many TDCs were occupied by dark counts, see equations (3.20) and (3.21). For instance, if 10 TDCs are triggered by dark counts, N_{TDCs} must be readjusted to 38. The number of TDCs that are initially triggered by dark counts are detected by the DCR filter for each individual γ -photon (see variable *skipped* in algorithm 2).

Figures 3.11a and 3.11b show the performance of several estimators for condition I and condition II respectively, when including DCR and skipping effect. It appears that MLE approximates a minimum root-MSE when increasing the size of the multiple-photoelectron timestamp set.

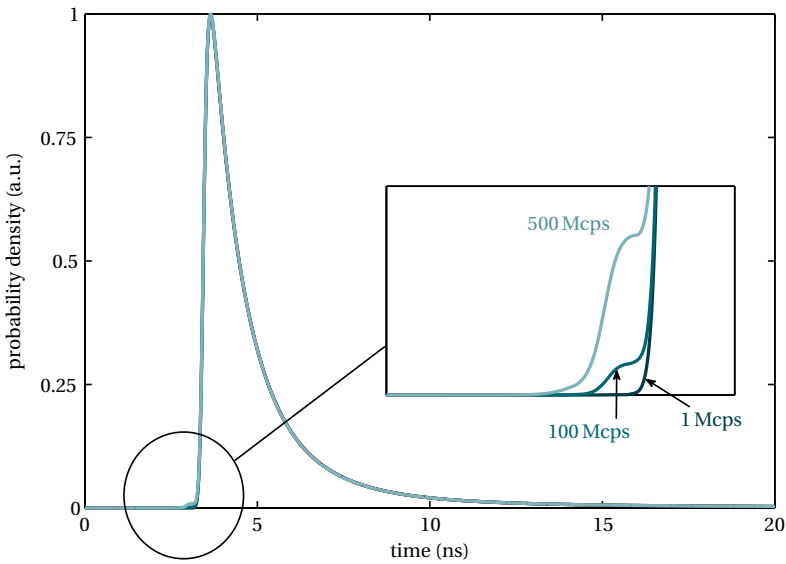
To investigate the efficiency of the estimators developed in this section, the CRLB that accounts for DCR and skipping effect was calculated using $f_k(t)$ that was estimated with Monte Carlo events. In equations (3.11) and (3.12), we replaced $f(t)$ by $f_k(t)$, the corresponding CDE, and Q by N_{TDCs} . $p_q(T|t_0)$ was calculated performing the same replacement in equation (3.1). Furthermore, in $p_q(T|t_0)$ we replaced R by N_{TDCs} . The CRLB calculated for the maximum number of available timestamps is depicted in Figures 3.11a and 3.11b.

3.8. SUMMARY

In section 3.2, we first analyzed the single-photoelectron estimation case. We concluded that with a single timestamp, the only possible unbiased estimator did not fully reach the CRLB under certain conditions, namely when the number of photoelectrons registered is low and the timing jitter of the complete instrumentation chain is small (see Figures 3.1a, 3.1b and 3.1c). In section 3.3, we tested the MLE in the multiple timestamp estima-

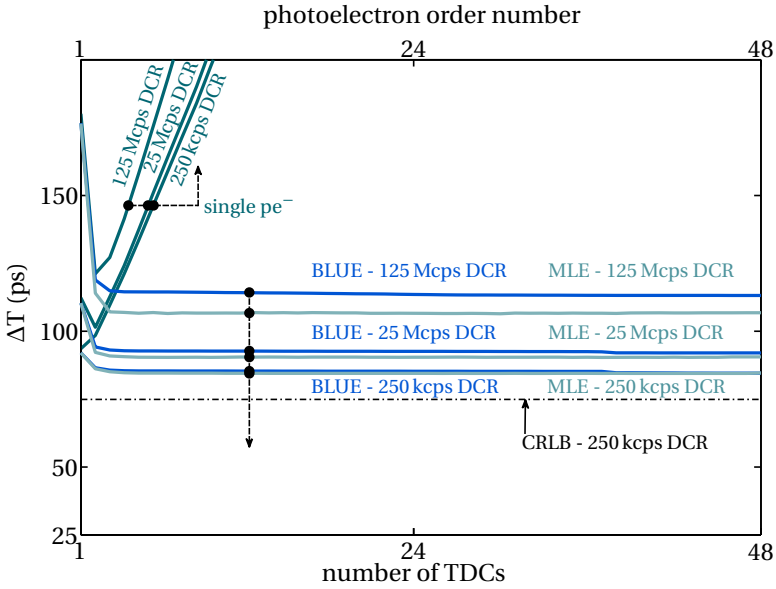


(a)

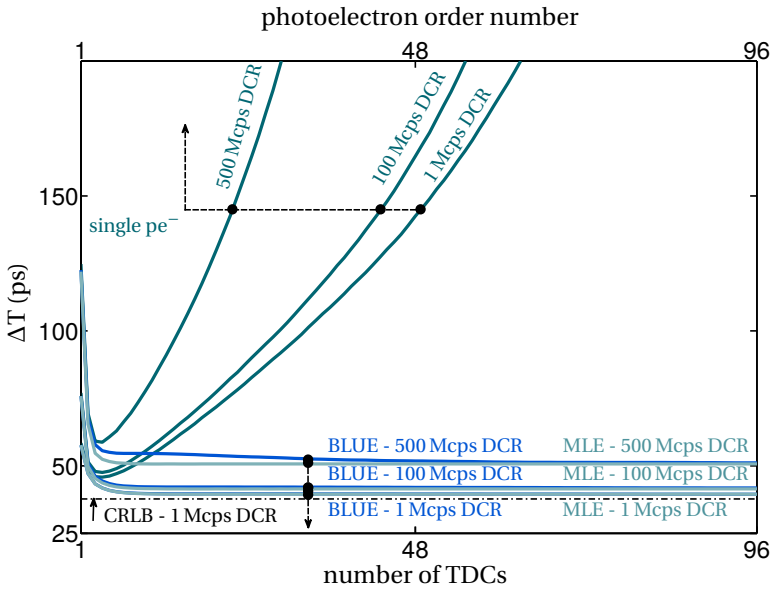


(b)

Figure 3.10: $f_k(t)$ estimated with Monte Carlo simulations: (a) with condition I, (b) with condition II. The DCR is the total amount of one MD-SiPM for condition I and of four MD-SiPMs for condition II. In (a), $f_k(t)$ is shown, estimated with a Monte Carlo simulation for condition I that fixed R' without any random samplings. The total DCR was 250 kcps.



(a)



(b)

Figure 3.11: Single detector root-MSE (ΔT) for several estimators for different DCR levels: (a) with condition I, (b) with condition II. The DCR is the total amount of one MD-SiPM for condition I and of four MD-SiPMs for condition II.

tion case and it did not fully reach the CRLB under similar conditions (see Figure 3.2). Nevertheless, under conditions that are typical for scintillation detectors intended for fast timing applications, i.e. detectors based on fast, bright scintillators and photodetectors with a high PDE, it appears that the MLE is an efficient estimator of the time of interaction of the γ -photon.

It was shown in section 3.4 that BLUE can reach the same performance as MLE in the multiple photoelectron timestamp case, under no-DCR conditions. In addition, both estimation methods are essentially insensitive to the energy resolution (see Figure 3.3b). Furthermore, the largest improvement in time resolution due to the use of multiple timestamps is obtained in systems with a high level of total timing jitter (see Figure 3.3a). It is important to notice that BLUE does not degrade the estimation performance as the timestamp set size increases in comparison to the other analyzed linear estimation methods. BLUE's coefficients are properly calculated since it considers the high correlation of the order statistic timestamp set.

In section 3.7, it was shown that a favorable performance under high-DCR conditions (see Figures 3.11a and 3.11a) can be achieved by a DCR filter. Thus, DCR robustness is a particular advantage of the MD-SiPM. Since this architecture is more DCR-tolerant, it can be implemented in a standard CMOS process instead of requiring a more expensive and less widely available image sensor CMOS process [20].

In section 3.7, it was furthermore shown that the performance of BLUE and MLE are essentially equal in the presence of DCR and skipping effect (with a DCR filter applied). Moreover, both estimators appear to be efficient (i.e., they closely approach the CRLB), when the amount of detected photoelectrons is high (i.e., under condition II).

However, BLUE is much simpler than MLE in terms of computing power or hardware implementation. BLUE requires just N_{TDCs} multiplication and accumulation operations (MACs). On the other hand, MLE requires several MACs per TDC, depending on the numerical resolution of $f_k(t_q|T_0)$ in addition to a maximum-value search algorithm. Hence, BLUE is considered the best of the different estimators tested for estimating the time of interaction of γ -photon in MD-SiPM based scintillation detectors.

In conclusion, a comprehensive theoretical analysis of multiple-photoelectron time estimation in MD-SiPM based scintillation detectors was performed, supported with realistic Monte Carlo simulations. The statistical models that are described within this work can be applied to any time estimation problem based on MD-SiPMs by substituting the appropriate function for $f_s(t)$.

REFERENCES

- [1] J. S. Karp, S. Surti, M. E. Daube-Witherspoon, and G. Muehllehner, *The benefit of time-of-flight in PET imaging: Experimental and clinical results*, Journal of nuclear medicine: official publication, Society of Nuclear Medicine 49, 462 (2008).
- [2] R. F. Post and L. I. Schiff, *Statistical Limitations on the Resolving Time of a Scintillation Counter*, Phys. Rev. 80, 1113 (1950).
- [3] R. Gioacchino, *Time statistics of the photoelectron emission process in scintillation counters*, Nuclear Instruments and Methods in Physics Research Section A: Accelerators, Spectrometers, Detectors and Associated Equipment 335, 121 (1993).

- [4] M. Fishburn and E. Charbon, *System Tradeoffs in Gamma-Ray Detection Utilizing SPAD Arrays and Scintillators*, Nuclear Science, IEEE Transactions on 57, 2549 (2010).
- [5] S. Seifert, H. van Dam, and D. Schaart, *The lower bound on the timing resolution of scintillation detectors*, Phys. Med. Biol. 57, 1797 (2012).
- [6] E. Venialgo, S. Mandai, and E. Charbon, *Time mark estimators for MD-SiPM and impact of system parameters*, in *Nuclear Science Symposium and Medical Imaging Conference (NSS/MIC), 2013 IEEE* (2013) pp. 1–2.
- [7] E. Venialgo, S. Mandai, T. Gong, D. Schaart, and E. Charbon, *Practical time mark estimators for multichannel digital silicon photomultipliers*, in *Nuclear Science Symposium and Medical Imaging Conference (NSS/MIC), 2015 IEEE* (IEEE, 2015) pp. 1–3.
- [8] E. Venialgo, S. Mandai, T. Gong, D. R. Schaart, and E. Charbon, *Time estimation with multichannel digital silicon photomultipliers*, Physics in Medicine & Biology 60, 2435 (2015).
- [9] E. Gatti and V. Svelto, *Review of theories and experiments of resolving time with scintillation counters*, Nuclear Instruments and Methods 43, 248 (1966), proceedings of the Tenth Summer Meeting of Nuclear Physicists.
- [10] L. H. Braga, L. Gasparini, and D. Stoppa, *A time of arrival estimator based on multiple timestamps for digital PET detectors*, in *Nuclear Science Symposium and Medical Imaging Conference (NSS/MIC), 2012 IEEE* (IEEE, 2012) pp. 1250–1252.
- [11] H. T. Van Dam, G. Borghi, S. Seifert, and D. R. Schaart, *Sub-200 ps CRT in monolithic scintillator PET detectors using digital SiPM arrays and maximum likelihood interaction time estimation*, Physics in Medicine & Biology 58, 3243 (2013).
- [12] S. Kay, *Fundamentals of Statistical Signal Processing, Volume III: Practical Algorithm Development*, Fundamentals of Statistical Signal Processing (Prentice-Hall PTR, 2013).
- [13] S. Park, *On the asymptotic Fisher information in order statistics*, METRIKA 57, 71 (2003).
- [14] B. Arnold, N. Balakrishnan, and H. Nagaraja, *A First Course in Order Statistics*, Classics in Applied Mathematics (Society for Industrial and Applied Mathematics, 1992).
- [15] D. Hanggi and P. Carr, *Errors in exponentially modified Gaussian equations in the literature*, Analytical Chemistry 57, 2394 (1985), <http://pubs.acs.org/doi/pdf/10.1021/ac00289a051> .

- [16] J. Glodo, W. Moses, W. Higgins, E. van Loef, P. Wong, S. Derenzo, M. Weber, and K. Shah, *Effects of Ce concentration on scintillation properties of LaBr3:Ce*, Nuclear Science, IEEE Transactions on 52, 1805 (2005).
- [17] T. Szczesniak, M. Moszynski, L. Swiderski, A. Nassalski, P. Lavoute, and M. Kapusta, *Fast Photomultipliers for TOF PET*, Nuclear Science, IEEE Transactions on 56, 173 (2009).
- [18] T. Ludziejewski, K. Moszynska, M. Moszynski, D. Wolski, W. Klamra, L.-O. Norlin, E. Devitsin, and V. Kozlov, *Advantages and limitations of LSO scintillator in nuclear physics experiments*, Nuclear Science, IEEE Transactions on 42, 328 (1995).
- [19] S. Mandai, V. Jain, and E. Charbon, *A fully-integrated 700x800 μm^2 multi-digital silicon photomultiplier with column-parallel time-to-digital converter*, in *ESSCIRC (ESSCIRC), 2012 Proceedings of the* (2012) pp. 89–92.
- [20] S. Mandai and E. Charbon, *A 4 x 4 x 416 digital SiPM array with 192 TDCs for multiple high-resolution timestamp acquisition*, Journal of Instrumentation 8, P05024 (2013).
- [21] T. Frach, G. Prescher, C. Degenhardt, R. de Gruyter, A. Schmitz, and R. Ballizany, *The digital silicon photomultiplier - Principle of operation and intrinsic detector performance*, in *Nuclear Science Symposium Conference Record (NSS/MIC), 2009 IEEE* (2009) pp. 1959–1965.
- [22] L. H. C. Braga, L. Gasparini, L. Grant, R. K. Henderson, N. Massari, M. Perenzoni, D. Stoppa, and R. J. Walker, *A Fully Digital 8x 16 SiPM Array for PET Applications With Per-Pixel TDCs and Real-Time Energy Output*. J. Solid-State Circuits 49, 301 (2014).

4

ASIC-LESS TOF-PET BASED ON TDCs ON FPGAs AND A-SiPMs

Part of this chapter has been published as “Esteban Venialgo, Nicola Lusardi, Fabio Garzetti, Angelo Geraci, Stefan E Brunner, Dennis R Schaart, and Edoardo Charbon. Towards a Full-Flexible and Fast-Prototyping TOF-PET Block Detector Based on TDC-on-FPGA. IEEE Transactions on Radiation and Plasma Medical Sciences, 2018”.

In the previous chapters, we explained the basics of molecular imaging, general aspects of PET instrumentation, and the theoretical limitations of scintillation detectors for TOF-PET. In this chapter, practical methods for designing and implementing TOF-PET modules based on scintillators and A-SiPMs are described. Moreover, in the beginning of this thesis, public availability of molecular imaging technologies was described as a concern of healthcare systems. In order to address this issue, the proposed TOF-PET solution is based on off-the-shelf components, full-flexible and fast prototyping designs, and it does not require application-specific integrated circuit (ASIC) implementations. Additionally, since it only utilizes standard and cost-effective elements, its availability is less restricted in comparison to solutions that require customized elements.

4.1. ASIC-LESS TOF-PET MODULE

Since the introduction of the PET block detector in the 1980s, it was possible to build PET scanners in a modular approach [1]. One advantage of breaking out the detection area into many independent block detectors was the drastic increase in the count rate capability of the PET scanner [2, 3].

With the advent of TOF-PET and PET/MRI imaging modalities, new technologies were introduced, e.g. A-SiPMs, in order to fulfill the new requirements, such as high timing resolution and magnetic field insensitivity. In addition to A-SiPMs, ASIC development appeared as a solution that integrates even more independent channels per PET block detector up to a single channel per scintillator pixel [4, 5]. This solution avoids utilizing scintillator pixel-encoding circuits, which are usually difficult to calibrate on the edge of the block detector, and allows to further increase the single count rate. However, the main disadvantages of the ASIC approach are the lack of flexibility and long development and testing cycles.

More recently, D-SiPMs appeared as an alternative photodetector utilized in combination with scintillators for γ -photon detection in PET [6–8]. This type of photodetector represents a further step into system integration and ASIC development, since they integrate SPAD cells along with a comprehensive readout circuit into the same chip. In addition, the analog readout is entirely removed by exploiting the intrinsic digital nature of SPADs when detecting light. Once the photodetector is developed, it allows a more direct system integration; however, its main drawbacks are the even longer development and testing cycles due to their high complexity.

In order to obtain accurate timing information from an A-SiPM, which features a relatively large output capacitance, specialized shaping circuits are required in order to keep a fast signal rise time. However, since the introduction of the fast terminal (FT) by SensL, a fast signal can be obtained without any specialized circuits [9]. Because the FT is integrated into the A-SiPM, the analog readout circuit can be simplified by removing entirely the timing shaping circuits and reducing it to few off-the-shelf components.

In PET instrumentation, time-to-digital converters (TDCs) replaced free-running fast sampling analog-to-digital converters (ADCs) for timemarking γ -photons [10]. FPGAs can allocate TDCs as well as digital readout and interfacing logic in order to build a PET detector module. As an added benefit, FPGAs can be reprogrammed at any point in time of the development cycle in order to add or fix PET detector functionalities [11, 12].

In this chapter, we describe a series of experiments in order to demonstrate that full-

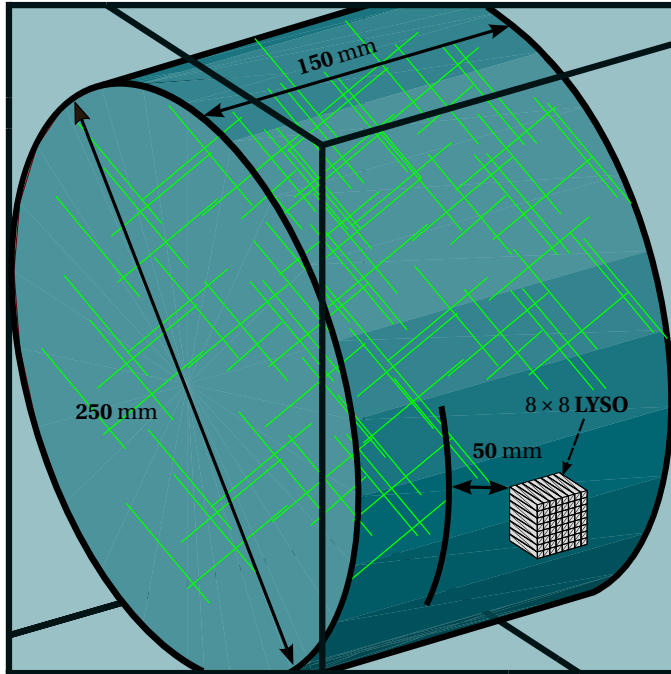


Figure 4.1: Setup description of the GATE/Geant4 Monte Carlo simulation.

flexible and fast-prototyping TOF-PET detector modules can be built directly from off-the-shelf components without ASIC development. The prototype circuits are based on TDC-on-FPGA, off-the-shelf components, and FT J-series A-SiPMs from SensL [13–15].

4.1.1. SINGLE COUNT RATE AND CHANNEL MULTIPLEXING

When designing a PET scanner, the noise equivalent count rate (NECR) and the sensitivity are among the most important parameters under consideration [2, 3]. The NECR is reduced mainly by three factors: detector dead time, unrejected scattered events, and random coincidences.

The amount of random coincidences depends on the single count rate and the coincidence-window width. If the system-level coincidence resolving time (CRT) is smaller than the field-of-view (FOV) diameter in terms of time distance, which is 833 ps for a 250 mm diameter, the coincidence-window width is limited by the FOV diameter. Additionally, the coincidence-window width is extended beyond the FOV in terms of time by a factor that depends on the scanner CRT, in order not to suppress valid events due to the timing measurement uncertainty.

The unrejected scattered events depend on energy resolution. Finally, the NECR sensitivity can be reduced significantly, depending on the injected radioactivity, which moreover depends on the specific PET application.

Incrementing the number of channels by subdividing the detector area into blocks

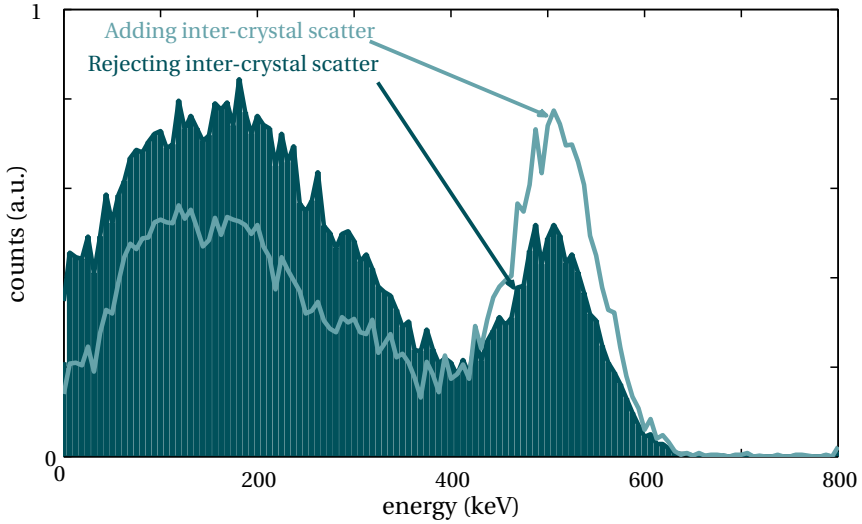


Figure 4.2: GATE/Geant4 simulated energy spectrum (the energy resolution was set to 17% at 511 keV).

drastically improves the NECR [2, 3]. However, implementing several channels within the same PET detector module might not increase the NECR significantly, because it also depends on the injected radioactive dose and scanner geometry.

We performed a GATE/Geant4 simulation in order to study the impact of the channel multiplexing on the single count rate of a PET detector module [16, 17]. We considered a brain-PET detector module case, which is described in Figure 4.1, because this application requires high NECR and sensitivity [18, 19].

For the simulation, a cylindrical phantom, which is 250 mm in diameter and 150 mm in length, was filled with ^{18}F and water. The phantom radioactivity was varied from 0.1 to 1000 MBq. A PET detector module composed of 8×8 LYSO pixels of 3 mm pitch and 20 mm depth was simulated. In order to simulate a scanner inner bore diameter of 350 mm, the inner face of the PET detector module was placed 50 mm away from the external side of the cylindrical phantom. The obtained energy spectrum is depicted in Figure 4.2. In all the simulations, an energy resolution of 17% at 511 keV was assumed based previous works [18].

For calculating the single count rate, all of the detected events were considered singles, as an example of extreme conditions for the instrumentation, without filtering events by an energy window.

In PET instrumentation, after detecting a γ -event, an energy discrimination is applied in order to immediately discard Compton scattered γ -photons. For instance, if we select the low threshold of the energy-window around 300 keV, γ -events that generate multiple hits from Compton scattering within the scintillators, in which their individual hit energy is lower than 300 keV, are rejected. As a consequence, about 14% of the events with inter-crystal scatter are rejected if the multiple hits are not combined as a single γ -event (see Figure 4.2). Therefore, in order to accept events with multiple hits, the PET

detector module must be capable of combine the individual hits as a single γ -event.

As mentioned, the detector was composed of 64 LYSO pixels and we analyzed the single count rate for several scintillator pixel multiplexing cases (see Figures 4.3a to 4.4b). In the following analysis, 64 channels refer to one independent measurement channel per LYSO pixel. Conversely, one channel means that the 64 LYSO pixels share a single measurement channel. We considered that the detector is composed of TDCs for γ -photon timestamping and energy estimation [10]. Additionally, we assumed that the dominant dead time of the system is the time-of-conversion of the TDCs, which can be modeled as non-paralyzable. Furthermore, we chose 1 μ s dead time as a reasonable time-of-conversion that can be achieved by a TDC on FPGA and 10 μ s as a worse-case comparison point [10].

Figures 4.3a and 4.3b show the absolute count rate of single events when sweeping the phantom activity for the 10 and 1 μ s channel dead time cases, respectively. In addition, we calculated the relative single count rate normalized with respect to the optimum case, which is 64 channels. Figures 4.4a and 4.4b depict the relative single count rate for the 10 and 1 μ s channel dead time cases, respectively.

In previously reported injected doses utilized in brain-PET imaging, which were around 400 MBq, we observed a relative count rate loss of about 55 % and 12 % for the 10 and 1 μ s channel dead time cases, respectively, in the case of 8 channels (see Figures 4.4a and 4.4b) [18]. Therefore, we concluded that a reasonable number of channels per PET detector module is 8, if the channel dead time is 1 μ s, since the decrease in efficiency of the single count rate is low with respect to having 64 independent channels. An additional argument to favor 8 channels is that a row-wise readout circuitry can be implemented when choosing a 8 \times 8 A-SiPM array, in order to achieve 8 independent measurement channels, as it is shown in the following sections.

4.1.2. TIME-TO-DIGITAL CONVERTERS ON FPGAS

The TDCs are essential elements for SiPMs' signal timestamping. FPGAs are equipped with thousands of look-up tables (LUTs), routing resources, flip-flops, etc., for implementing digital logic by preferably following a synchronous register-transfer level (RTL) methodology. In addition, they integrate specialized digital blocks that performs specific functions such as multiplication and accumulation (MAC) units, fast carry chains for adder implementation, etc. TDCs on FPGAs are built by implementing tapped delay lines (TDLs) utilizing the fast carry chains as delay elements (see Figure 4.5) [20, 21]. The least-significant bits (LSBs) are estimated by the TDLs and the TDC range is typically extended by the implementation of a course counter. Often, in PET instrumentation the stop signal is the reference clock of the PET scanner (see Figure 4.5).

The timestamping precision influences directly on the total timing jitter of the system, as it was analyzed in chapter 3. Subsequently, the main TDC parameter to be optimized in PET instrumentation is the single-shot resolution, which is determined by the TDC's LSB size, differential nonlinearity (DNL), and TDC's timing jitter. A TDC implemented on an FPGA can achieve a single-shot resolution of tens of picoseconds [15, 20].

In the experiments explained within this chapter, we utilized a version of a TDC-on-FPGA board that comprises an Artix7 system-on-module (SOM), digital-to-analog converters (DACs) for automatic threshold scanning, low-jitter comparator (ADCMP607),

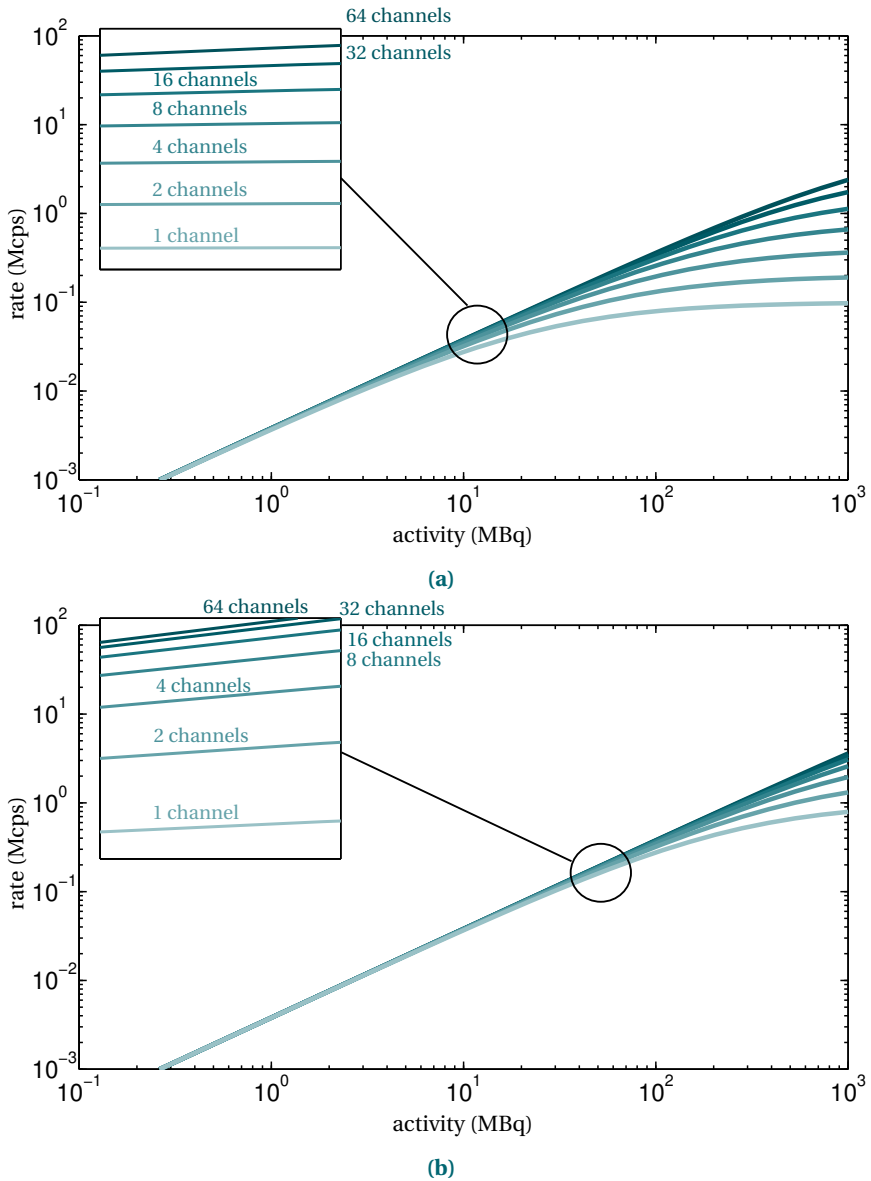


Figure 4.3: Absolute single count rate comparison for several channel multiplexing cases and channel dead times. (a) with a channel dead time of $10 \mu\text{s}$. (b) with a channel dead time of $1 \mu\text{s}$.

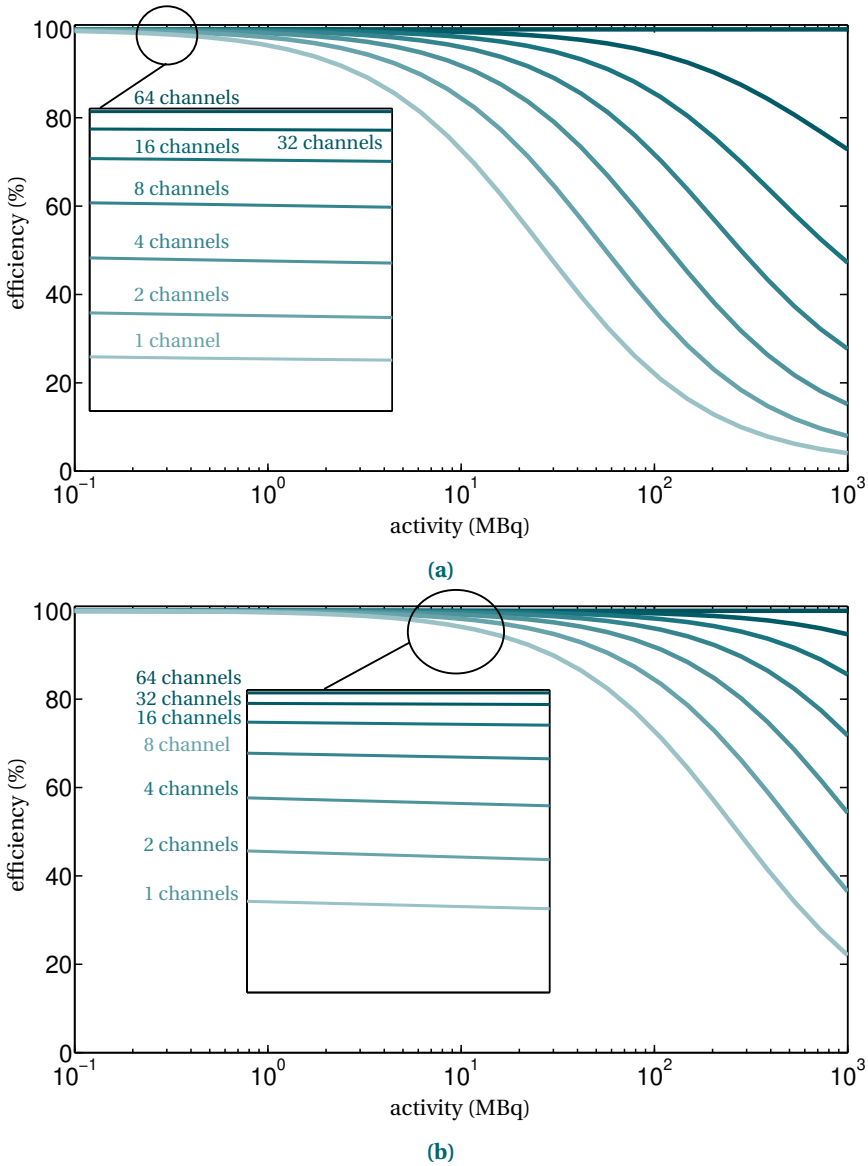


Figure 4.4: Normalized single count rate relative to the 64 channel case for several channel multiplexing cases and channel dead times. (a) with a channel dead time of $10 \mu\text{s}$. (b) with a channel dead time of $1 \mu\text{s}$.

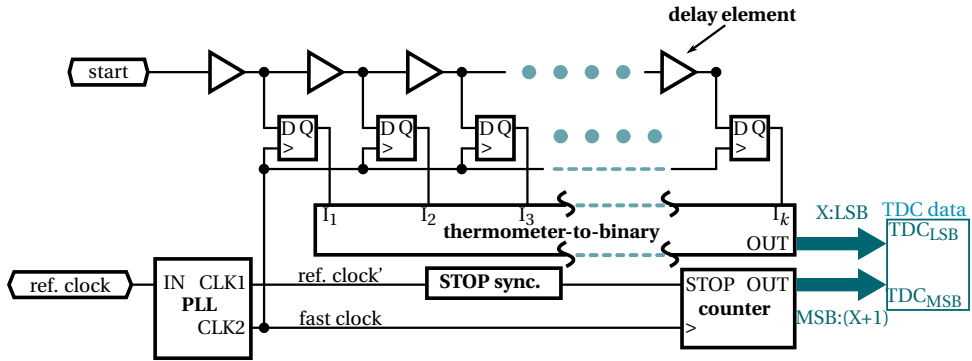


Figure 4.5: TDC-on-FPGA basic structure (simplified diagram).

Table 4.1: Panther board performance summary.

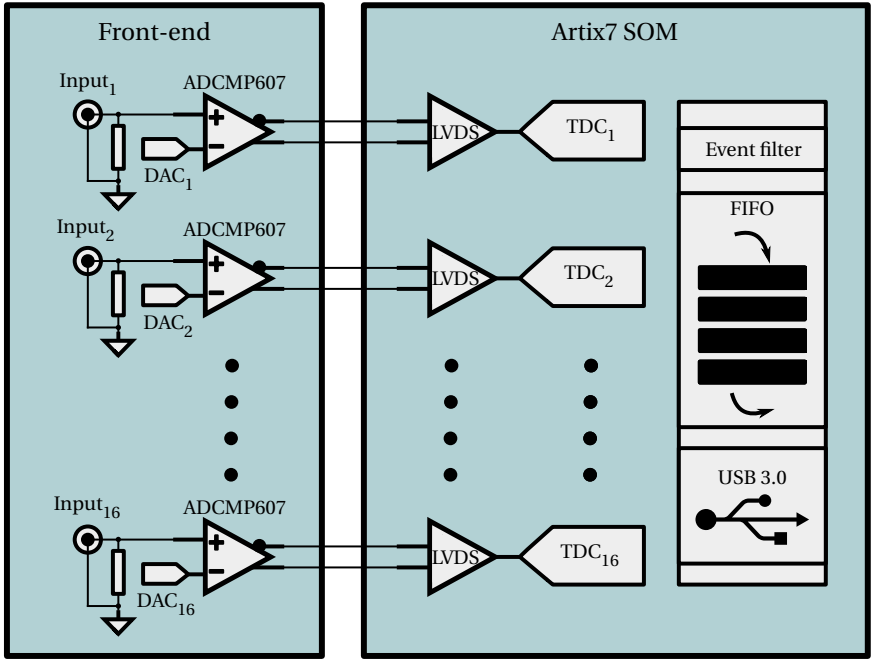
Feature	Value
Number of channels	16
Logic per channel	1200 Slices, 54 kbit BRAM, 1 DSP48E1s
Channel latency	110 ns
Maximum channel rate	20 MHz
System-on-module	Artix7 Trenez
Single shot resolution	12 ps (σ)
full scale range	2.4 μ s

and a high-speed USB 3.0 interface. This board, known as Panther, can allocate up to 16 TDC channels (see Figures 4.6a 4.6b) [13]. The TDCs are implemented based on a tapped-delayed line (TDL) architecture achieving an LSB of 4.7 ps and a single-shot resolution of 12 ps σ [14]. A full scale-range of 2.4 μ s is obtained utilizing the nutt technique [15]. The total FPGA occupation per channel is 1200 SLICES, 54 kbit BRAM, and 1 DSP48E1 (see Table 4.1). The 16 TDCs have a common stop signal connected to an internally generated clock, and the start signals are externally interfaced through the low-jitter comparators (see Figure 4.6a).

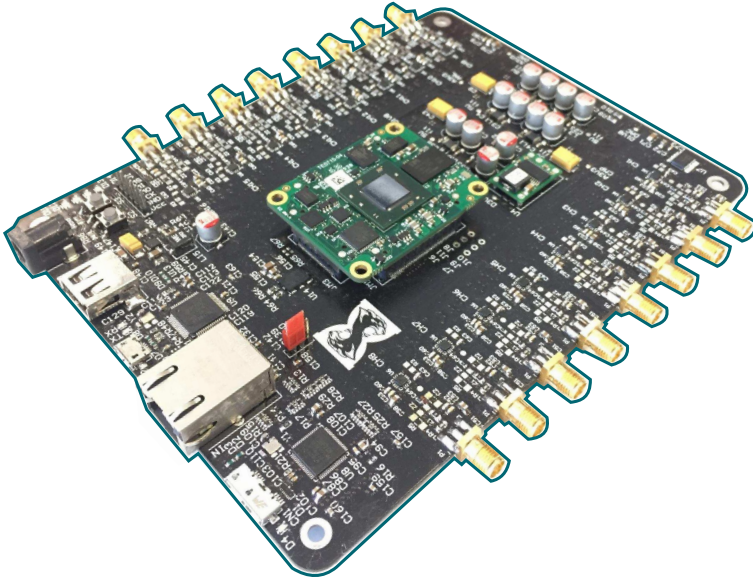
4.1.3. A-SiPMs MODELS

A SPAD avalanche can be modeled as a fast current discharge by means of a switch that closes when the avalanche is triggered [22]. Figure 4.7 depicts a SPAD circuit model, where C_{dp} includes the SPAD junction and parasitic capacitances, R_d models the space-charge resistance, and V_{bd} represents the breakdown voltage [22]. In passively quenched SPADs, which is the case of A-SiPMs, the series quenching resistor R_q has a value of about hundreds of kilo-ohms, which is significantly larger than R_d , in order to quench the avalanche properly [23]. Subsequently, the quenching phase is much shorter than the recharge phase (see Figure 4.7).

Conventional A-SiPMs feature two terminals (anode and cathode) in order to interface biasing and readout circuits (see Figure 4.8). A-SiPMs can be models as two sets of



(a)



(b)

Figure 4.6: Panther board. (a) Simplified system block diagram. (b) Panther board photograph.

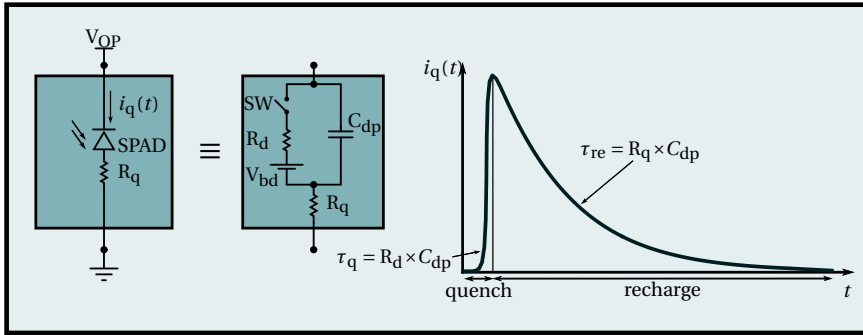


Figure 4.7: SPAD cell's simplified equivalent circuit.

4

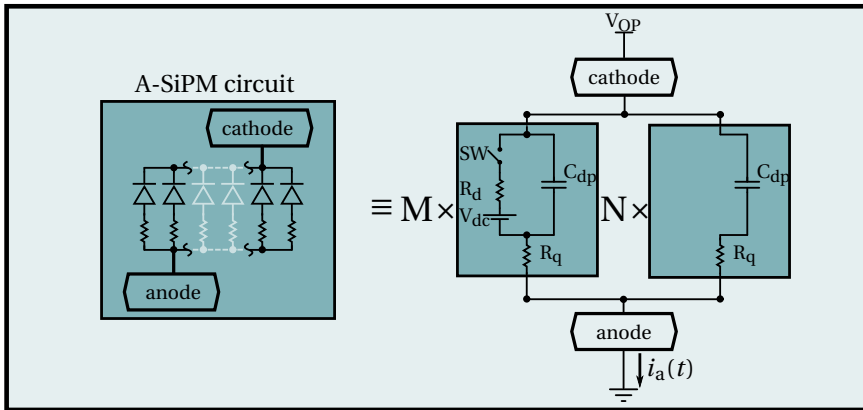


Figure 4.8: A-SiPM's simplified equivalent circuit.

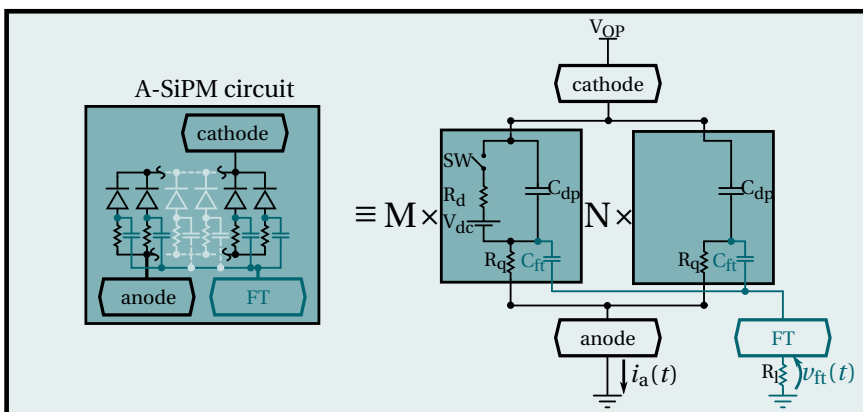


Figure 4.9: Simplified equivalent circuit of an A-SiPM equipped with FT.

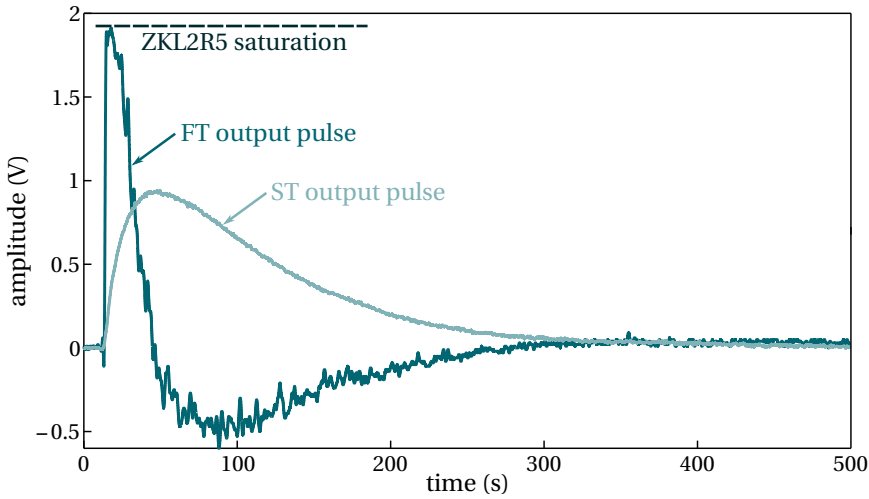


Figure 4.10: ST and FT output pulses of a J-Series A-SiPM coupled to a LYSO(Ce) scintillator. A ^{137}Cs radioactive source was placed close to the detector and the pulses that corresponds to the maximum amplitude were captured. A scope of 500 MHz bandwidth and with sample rate of 2.5 GS^{-1} was utilized. The ST terminal was terminated to a $50\ \Omega$ resistor and the FT was amplified with a Minicircuits's wideband amplifier ZKL2R5.

SPADs cells of M and N sizes in parallel connection. The set of M SPAD cells is composed by fired cells and the set of size N represents the passive cells (see Figure 4.8) [23]. Although this model considers simultaneous cell firing, which is not the case in scintillation detection, it highlights the switching behavior during the SiPM operation for non-simultaneous firing. This switching behavior produces a changing circuit conditions, which complicates the output-signal readout. Additionally, the relative low output impedance of the SPAD is largely increased by the series connection of R_q . Moreover, the total A-SiPMs' output capacitance features a large value of hundreds of picofarads due to the parallel connection of many SPAD cells. Subsequently, the A-SiPMs are preferably read out by low input impedance circuits, in order to overcome the previously explained circuit conditions [5, 24, 25].

Alternatively, A-SiPMs can be equipped with a FT, which is an extra connection formed by a series capacitor C_{ft} per SPAD cell connected directly to the SPAD anode (see Figure 4.9) [26]. The overall output capacitance of the FT is considerable lower than the ST output capacitance [26]. In addition, the FT forms a low-impedance terminal and its output voltage, measured over a resistive load $v_{ft}(t)$, has a boosted rise time because of the derivative effect of C_{ft} (see Figures 4.9 and 4.10). However, it was demonstrated that by utilizing a proper shaping circuit on the ST and performing a CRT experiment, the obtained performance is similar to utilize the FT directly[9]. However, the FT integration within the A-SiPM facilitates the design of analog front-end circuits, since the subdivision of signals, one path for timing and one path for energy, is provided directly.

4.1.4. CHANNEL MULTIPLEXING AND TIMING PERFORMANCE

Previously, we demonstrated that state-of-the-art CRT can be achieved by PET detectors composed of TDC-on-FPGA and A-SiPMs equipped with FTs [10]. The case of having one timing channel per LYSO pixel requires many TDCs integrated on the FPGA. Additionally, an extensive analog front-end, which consumes a significant amount of power, is needed. To achieve a full-flexible ASIC-less design channel multiplexing is necessary, in order to reduce power consumption and FPGA implementation complexity. We studied the timing impact of sharing the same measurement channel among several A-SiPM's FTs. In all of the experiments presented in this chapter, which were performed at room temperature, the bias voltage of the A-SiPMs was 30 V. The utilized J-series A-SiPMs are characterized by a minimum and maximum breakdown voltage of 24.2 V and 24.7 V at 21 °C, respectively [26].

Firstly, we calibrated our reference detector that was composed of a SensL single A-SiPM evaluation board of a J-Series 3 mm-pitch A-SiPM. We performed a coincidence measurement with two identical detectors in order to estimate the single detector resolution (SDR) (see Figure 4.11). $3 \times 3 \times 5$ mm³ LSO(Ce) scintillators from Agile were glued on top of the A-SiPMs.

We estimated the energy of the γ -event using the time-over-threshold (ToT) technique. For this reason, we connected two TDC channels per A-SiPM standard terminal (ST) in order to timestamp the falling and rising edges of the energy signal (see Figure 4.11). The γ -photon timemark estimation was performed by a single TDC connected to the FT after amplifying its signal with a metal-shielded case wideband amplifier of 30 dB gain and 2.5 GHz bandwidth (Minicircuits ZKL2R5).

As observed in Figure 4.12, we obtained a CRT of 122 ± 8.9 ps FWHM. In the latter measurements, we utilized one of these detectors as a reference with a SDR of 86.3 ps FWHM. The SDR is derived from the measured CRT of 122 ps and by considering the two detectors with identical SDR.

Secondly, we built A-SiPM array test circuits in order to evaluate the impact of sharing FTs on the same TDC channel. There were three test structures: single A-SiPM, row of A-SiPMs with Schottky diodes, and row of A-SiPMs without Schottky diodes (see Figure 4.13).

In the first test structure, the single A-SiPM's FT was connected to a surface-mount wideband amplifier (BGA2818) (see Figure 4.14). In addition, its ST was connected to a transimpedance amplifier (TIA) based on the OPA656 (see Figure 4.15). The single A-SiPM is the number 13 on the 4×4 A-SiPM array (see Figure 4.13). The hysteresis value ADCMP607 that connected the BGA2818 was kept as low as possible by removing its programming resistor, in order to achieve an accurate leading edge threshold.

In the second test structure, the FTs were connected in parallel through Schottky diodes in order to partially decouple their output capacitance (see Figure 4.16) [27, 28]. In addition, an external bias voltage was applied to the Schottky diodes to guarantee a faster signal transmission from the FTs to a second BGA2818 wideband amplifier [27, 28]. The STs were connected into a resistor divider chain, which is amplified by two additional TIAs, for scintillator pixel identification and energy estimation (see Figures 4.15 and 4.17). The TIAs are called left and right amplifiers (see Figure 4.17). This circuit connected the A-SiPMs 1, 2, 3, and 4 (see Figure 4.13 and 4.17).

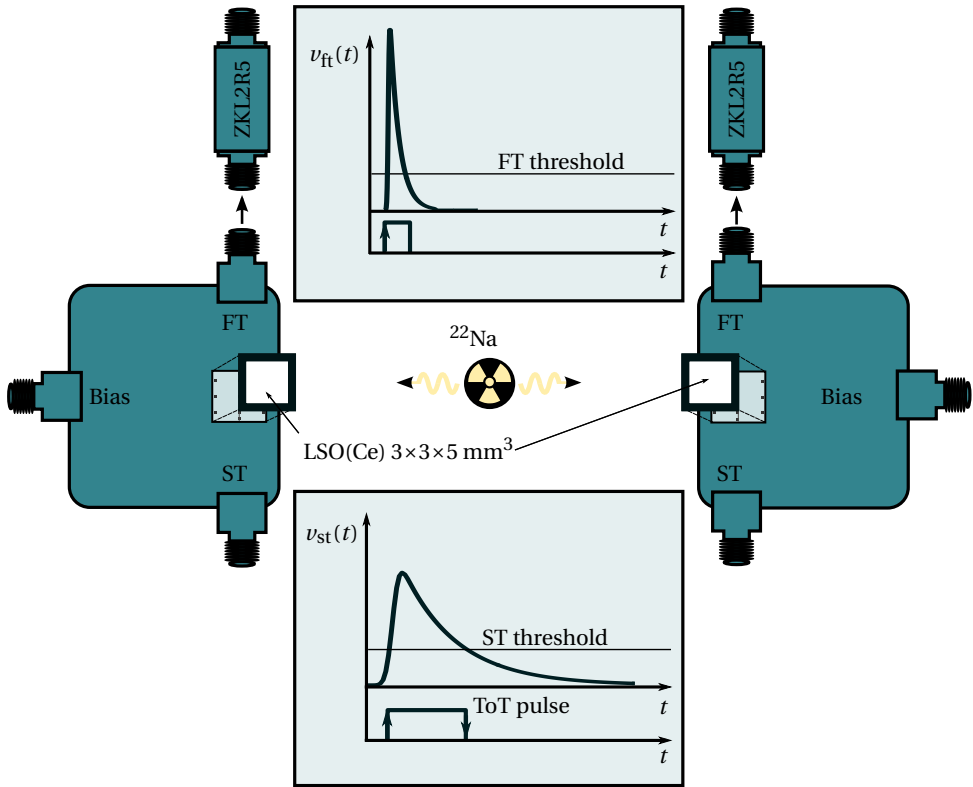


Figure 4.11: Block diagram of the reference detector measurement setup.

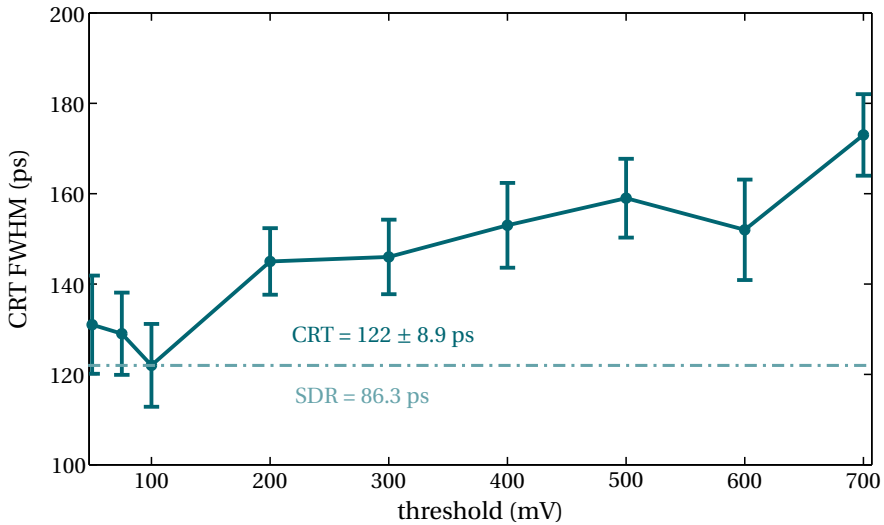


Figure 4.12: CRT threshold scan of the reference detectors.

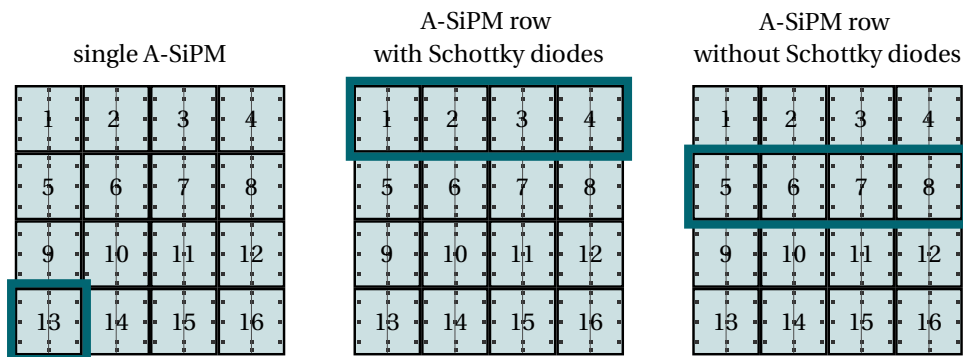


Figure 4.13: Location within the A-SiPM array of the test circuits.

4

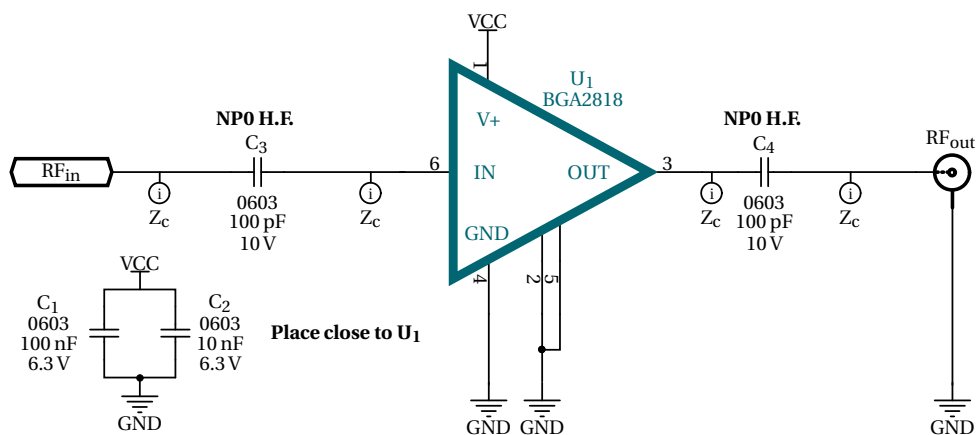


Figure 4.14: RF amplifier schematic.

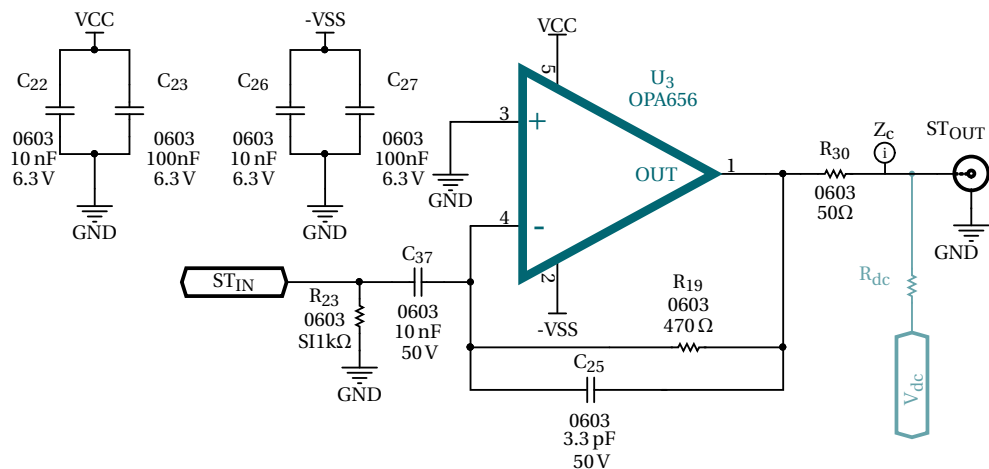


Figure 4.15: TIA schematic.

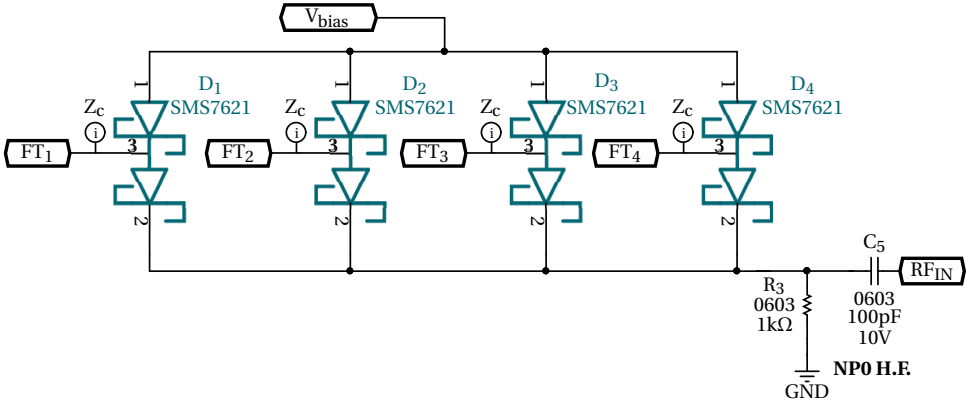


Figure 4.16: Schottky circuit schematic.

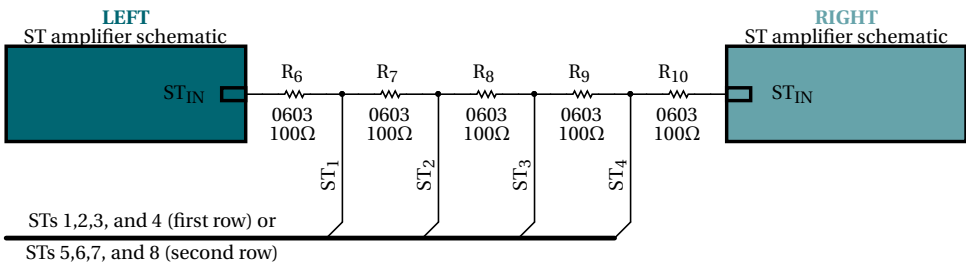


Figure 4.17: Scintillator pixel-encoding circuit schematic.

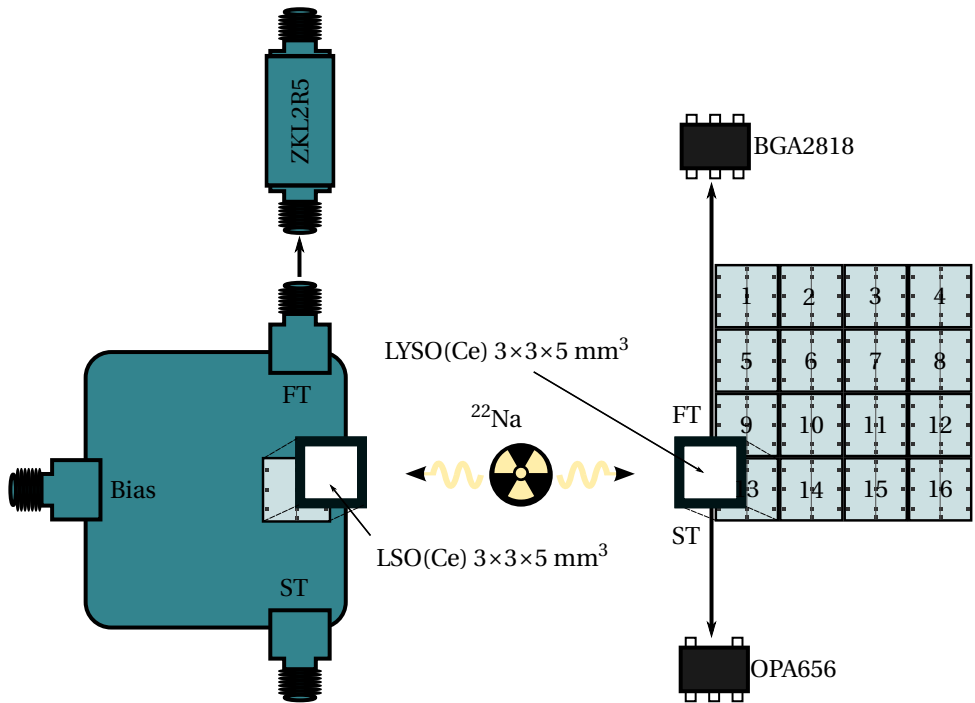


Figure 4.18: Measurement block diagram of the single A-SiPM setup

The third test structure is similar to the second but the FTs were connected directly to a third wideband amplifier without any Schottky diodes. Also, two additional TIAs were connected in a second scintillator pixel-encoding circuit (see Figures 4.15 and 4.17). This circuit connected the A-SiPMs 5, 6, 7, and 8 (see Figure 4.13 and 4.17).

In the actual hardware, the TDCs, comparators, and DAC references were located into the Panther board (see Figure 4.6). A custom A-SiPM array testing board, which allocated the rest of the circuits, was built with off-the-shelf surface-mount wideband amplifiers (BGA2818), Schottky diodes (SMS7621), and TIAs based on the OPA656. We chose small footprint SMD components in order to verify their performance and confirm that a compact PET readout circuit can be designed in this way.

Firstly, we verified the performance of the single A-SiPM circuit in terms of timing, which is based on the BGA2818 instead of the bulky Minicircuits ZKL2R5. We attached a $3 \times 3 \times 5 \text{ mm}^3$ scintillator of LYSO Gen3 from Saint-Gobain to the A-SiPM 13 (see Figure 4.13) and measured the CRT against the reference detector (see Figure 4.18) [29]. In this measurement, only the single A-SiPM test circuit and reference detector signals were connected to the Panther board. The CRT threshold scan is depicted in Figure 4.19 and no significant change was observed between the reference detector characterization and this measurement. We concluded that no timing degradation was detected between the timing channel based on the Minicircuits ZKL2R5 and that based on the BGA2818.

Next, we studied the timing resolution of the A-SiPM row that shares a single timing

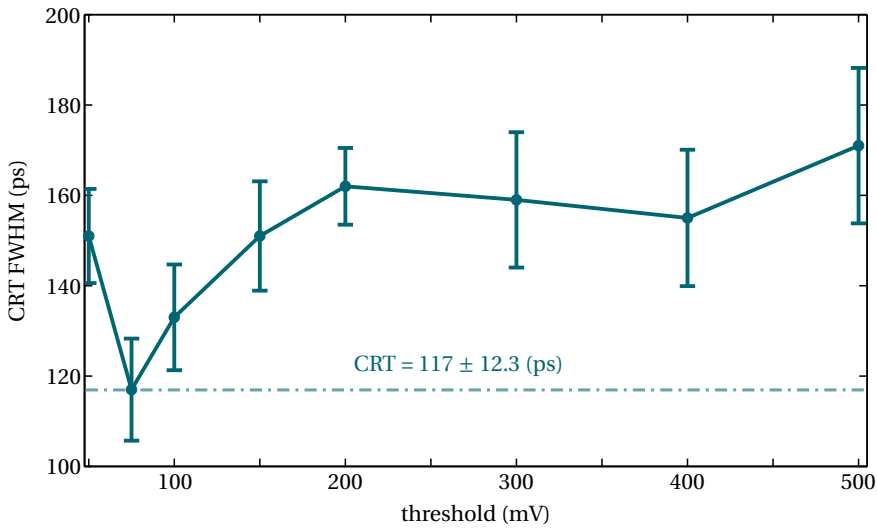


Figure 4.19: CRT threshold scan of the single A-SiPM within the 4×4 array.

channel through Schottky diodes. This coincidence measurement was also performed against the reference detector. We connected the circuits of the corresponding A-SiPM row and the reference detector to the Panther board (see Figure 4.13 and 4.6b). We attached the 3×3×5 mm³ scintillator of LYSO Gen3 to the A-SiPM 1 (see Figure 4.13), aligned the reference detector, and disconnected the single A-SiPM test circuit. Consequently, in this A-SiPM row one out of four A-SiPMs has a scintillator; however, the four A-SiPMs of the row were biased and had the FTs connected. If non-uniformities, such as breakdown voltage variation, become significant; they can be compensated for by implementing an individual overvoltage-adjustment circuit based on ultra-low power DACs such as DAC088S085.

The minimum measured CRT was 128 ± 7.8 ps (see Figure 4.20a) but at a lower threshold, which increases the sensitivity to threshold variations. The amplitude of the FT signal is slower in comparison to the single A-SiPM circuit because it is loaded with extra capacitance, which is partially decoupled by the Schottky diodes, added by the row FTs. After subtracting the SDR of the reference detector in quadrature and assuming two identical detectors, we extrapolated a CRT* of 138 ps FWHM. In addition, we performed a Schottky bias scan at a fixed comparator threshold, which was 10 mV. The best of CRT performance was achieved when the Schottky diodes were biased at 1.5 V, showing a current of 337 μA per diode (see Figure 4.20a).

Last, we re-glued the 3×3×5 mm³ scintillator of LYSO Gen3 from the A-SiPM row with Schottky diodes to the A-SiPM row without Schottky diodes (A-SiPM 5). And, we reconnected the Panther board to that A-SiPM row. The result of the CRT threshold scan of this case is shown in Figure 4.21. The measured CRT was 135 ± 10.3 ps and the extrapolated CRT* assuming identical detectors was 147 ps FWHM.

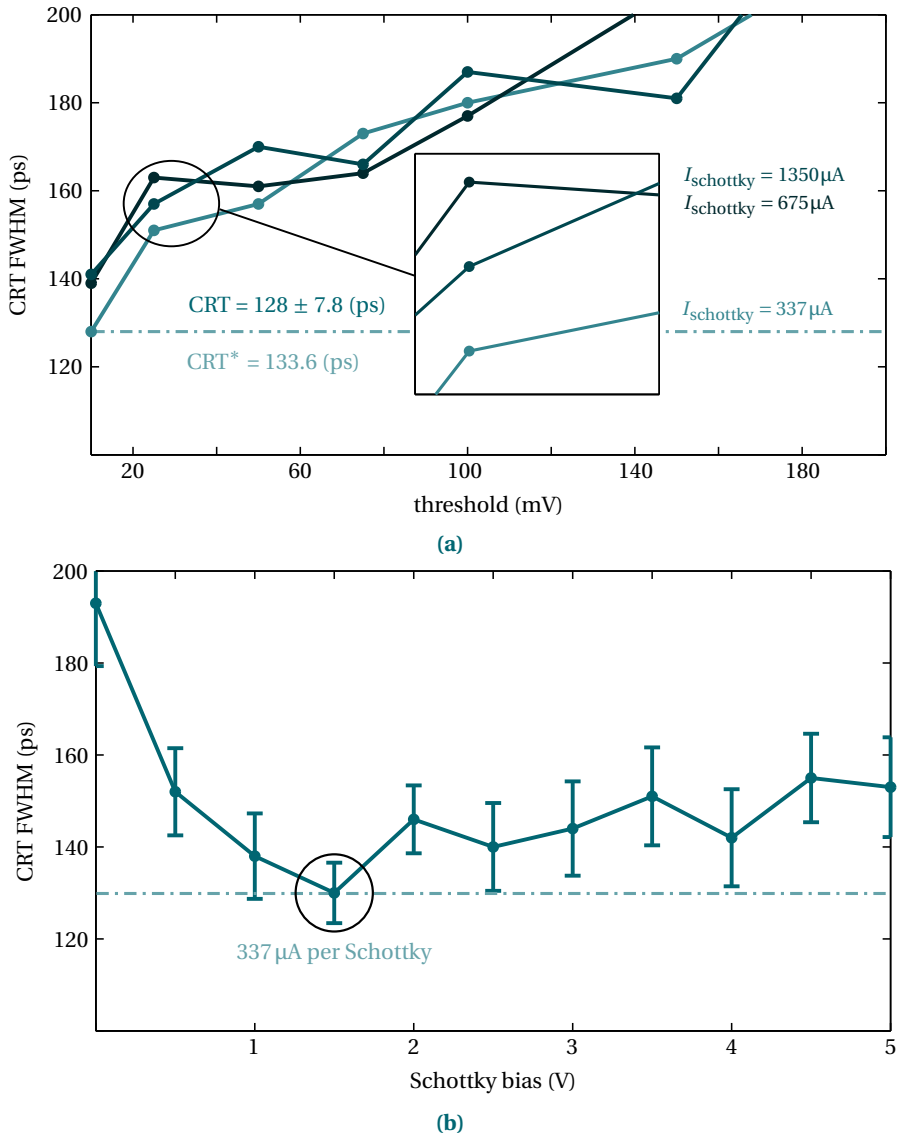


Figure 4.20: Coincidence measurement result of the A-SiPM within the Schottky row against the reference detector. (a) CRT threshold scan. (b) Schottky diode bias scan at a fixed comparator threshold.

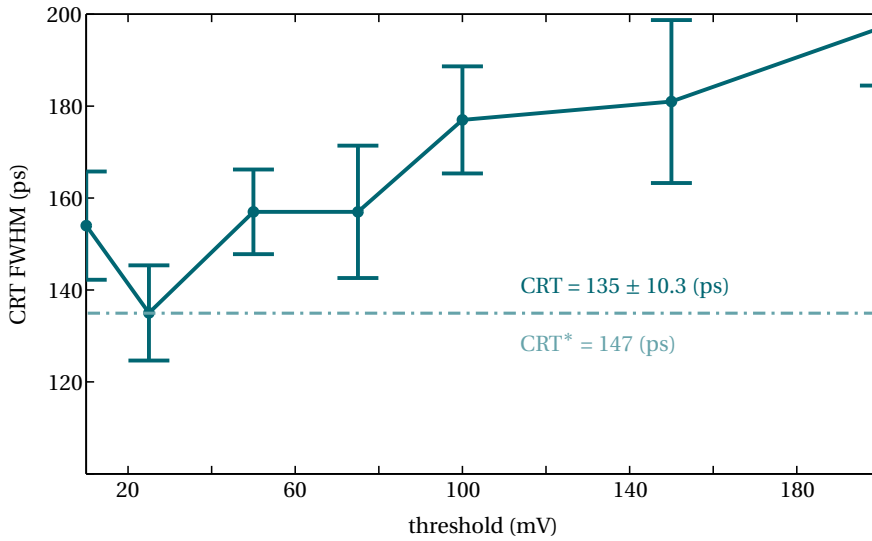


Figure 4.21: CRT threshold scan of the A-SiPM row without Schottky diodes.

4.1.5. TIMING SIGNAL WAVEFORMS

For comparing the output signals of the timing circuits, a source of ^{137}Cs was placed close to the detectors in order to obtain a maximum deposited energy of 662 keV, which is close to 511 keV. We re-glued the $3 \times 3 \times 5 \text{ mm}^3$ scintillator of LYSO onto the A-SiPMs 1, 5, and 13. An oscilloscope with 2.5 GSs^{-1} and 500 MHz bandwidth was connected to the BGA2818 outputs. Since several amplitudes were measured from the detector, the oscilloscope's trigger was set to the maximum measured amplitude.

Figure 4.22 shows the captured waveforms of the array's single A-SiPM amplified by the BGA2818 circuit and the reference detector amplified by the Minicircuits ZKL2R5. Although the gain of both amplifiers is the same, a lower amplitude is observed from the BGA2818 because of its lower saturated output power. Additionally, the saturated pulse is differentiated by the RC circuit created by the 50Ω load and C_4 (see Figure 4.14). However, accurate timing relies on the amplification of the beginning of the timing pulse, which is produced by the early photoelectrons, before reaching the saturated output power of the wideband amplifier [30].

Figure 4.23 compares the captured waveforms of the three test circuits of the A-SiPM array (A-SiPM row with Schottky diodes, A-SiPM row without Schottky diodes, and single A-SiPM). In addition, Figure 4.24 compares the captured waveforms of the BGA2818 output that is connected to the Schottky row at several Schottky bias voltages. Differences between peak amplitudes was not observed between the A-SiPM rows with and without Schottky diodes. In the Schottky row circuit, the tail length variations observed in Figure 4.24 are related to the different speeds in which C_5 (in Figure 4.16) is discharged that depends on the Schottky diodes' biasing.

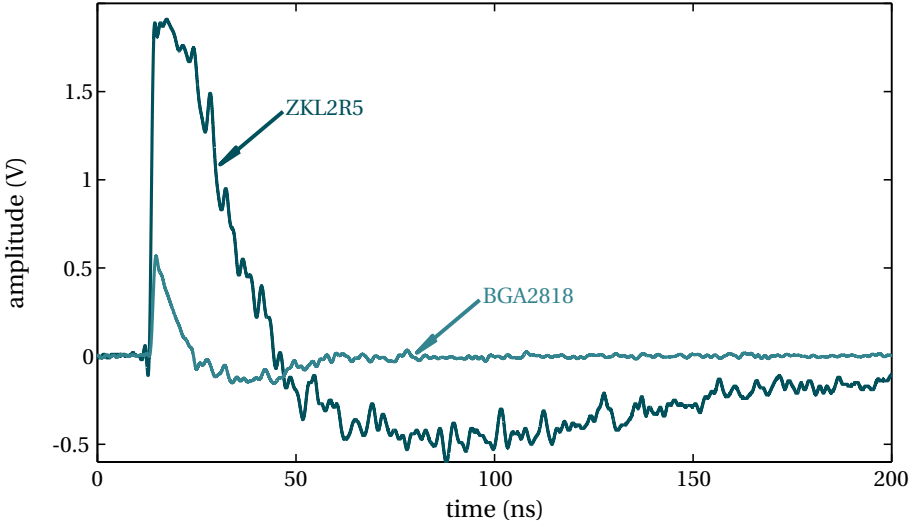


Figure 4.22: FT captured waveforms of single A-SiPMs amplified with BGA2818 and Minicircuits ZKL2R5.

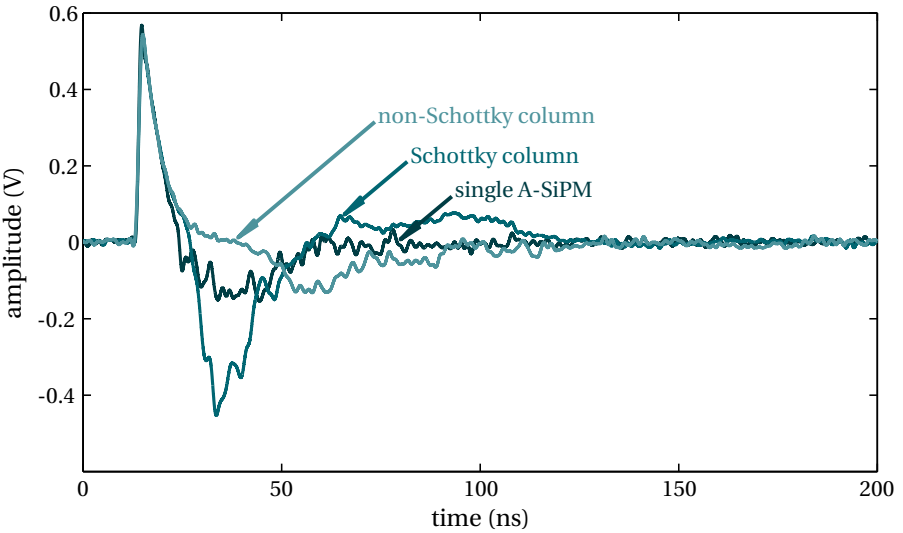


Figure 4.23: FTs captures of the A-SiPM 13, the Schottky row A-SiPM 1, and the non-Schottky row A-SiPM 5, all amplified with BGA2818.

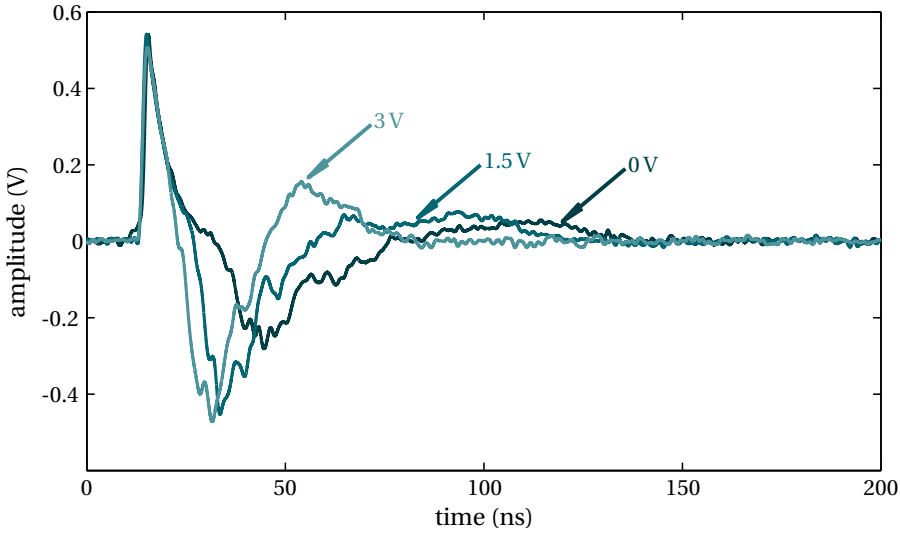


Figure 4.24: FTs captures of the Schottky row A-SiPM 1 amplified with BGA2818 at several Schottky bias voltages.

4.1.6. LYSO PIXEL ENCODING

Since the TIAs' output pulse polarity is negative, a DC voltage was added for connecting the TIAs to the Panther board (see Figure 4.17), which required a positive input voltage. In a full PET module implementation, the DC voltage can be replaced by connecting ST_{IN} (in Figure 4.15) to the A-SiPM cathode, and biasing the anode to negative voltage [31]. The DC voltage causes extra power consumption and R_{dc} produces a slight impedance mismatch.

We glued the $3 \times 3 \times 5$ mm³ LYSO Gen3 scintillator on the A-SiPM 2, place the ²²Na source close to the scintillator, and measured the time difference between ToT_{left} and ToT_{right} (see Figure 4.17) with the Panther board (see Figure 4.6). The measured events were filtered by an energy window that captured the entire 511 keV photopeak. We also performed the same experiment on the A-SiPM 3 in order to verify the LYSO pixel identification. Figure 4.25 shows the histograms that corresponds to the two previously explained experiments.

4.1.7. ENERGY RESOLUTION

In order to calibrate the energy spectrum, we assumed that the A-SiPM output pulse shape follows a single-exponential waveform and the pulse shape is independent of the γ -energy deposited. Consequently, the relationship between the area of the output pulse shape and the ToT can be calculated as follows:

$$A_p = V_{th} \tau_d \exp\left(\frac{t_{tot}}{\tau_d}\right). \quad (4.1)$$

Where A_p represents the area of the pulse, which is proportional to the compressed energy before the A-SiPM's saturation correction, τ_d is the decay constant of the pulse, V_{th}

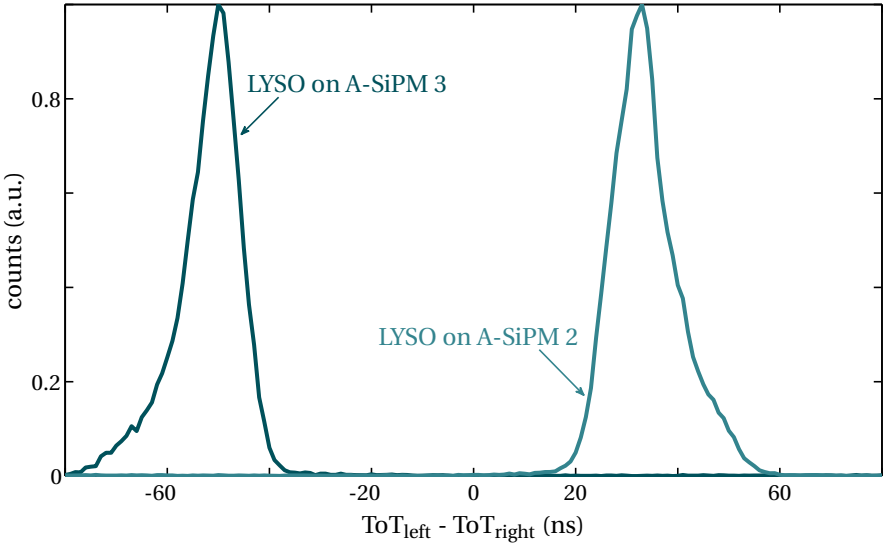


Figure 4.25: Time difference histogram between ToT_{left} and ToT_{right} , when the LYSO scintillator was glued on the A-SiPMs 2 and 3.

is the threshold of the comparator, and t_{tot} is the measured time distance between the falling and rising edges of the comparator output pulse.

The full energy calibration is performed by compensating for the saturation effect produced by the limited number of cells of the A-SiPM, by following

$$E_{\gamma} = -A_{pmax} \log\left(1 - \frac{A_p}{A_{pmax}}\right). \quad (4.2)$$

Where A_{pmax} is the maximum energy that can be measured by the detector and E_{γ} is the calibrated deposited γ -photon energy.

There are three unknown values, which are V_{th} , τ_d , and A_{pmax} ; therefore, we estimated them by measuring the t_{tot} that corresponds to three different known deposited E_{γ} values. This procedure was performed by measuring the uncalibrated ToT spectrum of three different photopeaks (see Figures 4.26a). Later, we used the calibrated constant to convert the ToT values to its corresponding E_{γ} following equations (4.1) and (4.2). The calibrated spectra are shown in Figure 4.26b, where an energy resolution of 14 % is achieved. This energy calibration procedure was performed when the LYSO(ce) scintillator of $3 \times 3 \times 5 \text{ mm}^3$ was glued on the A-SiPM 1, which belongs to the A-SiPM row with Schottky diodes.

4.2. OUTLOOK

We propose to use TDC-on-FPGA in combination with a simple analog front-end based on off-the-shelf components in order to build a PET detector module (see Figure 4.27). The target application of this PET detector module is brain molecular imaging.

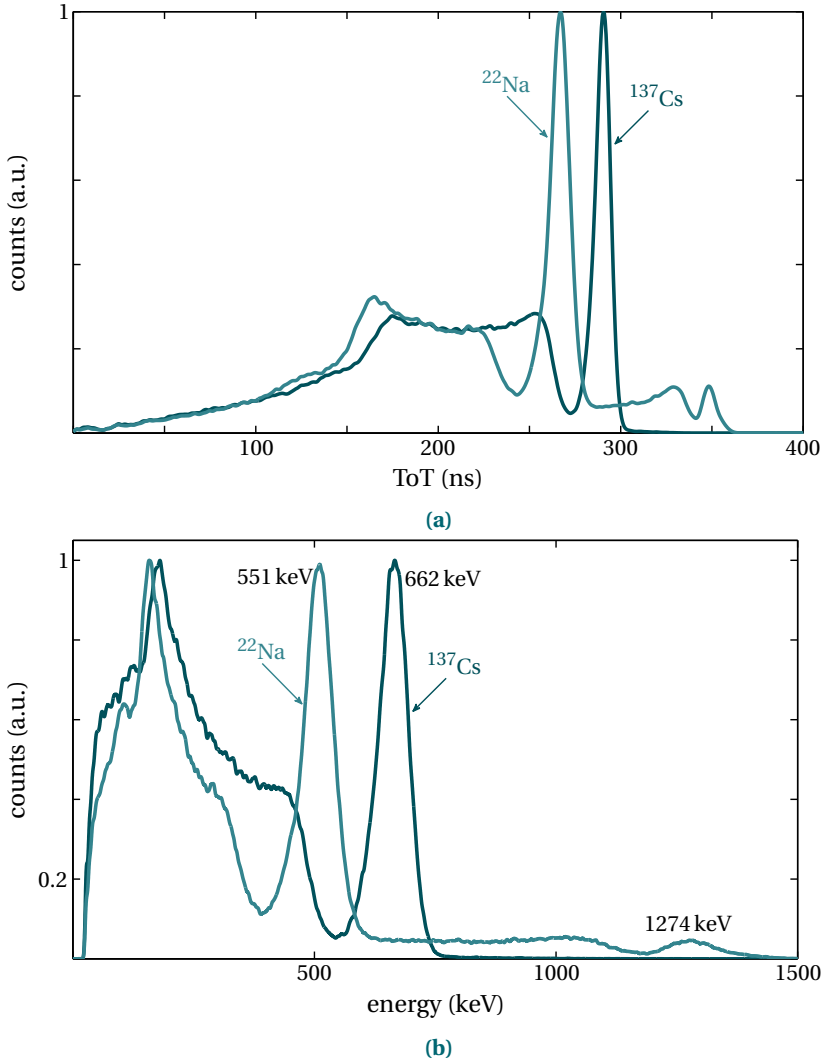


Figure 4.26: Energy calibration result. (a) ToT energy spectra of ^{22}Na and ^{137}Cs sources. (b) Calibrated energy spectra of ^{22}Na and ^{137}Cs sources.

The detector is composed of an 8×8 A-SiPM array of 3 mm pitch and equipped with FTs. The board that allocates on the top layer the A-SiPMs is customized in order to host the small footprint Schottky diodes (SMS7621), in addition to small board-to-board connectors. The analog front-end allocates the fast comparators (ADCMP607), the wide-band amplifiers (BGA2818), and the TIAs circuits based on the LT6230-10. The last board contains a small footprint FPGA (Artix7-100T-CSG324) and all the required circuitry to operate it.

The detector module has independent row circuitries, in order to realize 8 independent measurement channels. Each A-SiPM row also has an independent scintillator's pixel-encoding circuit that also improves the scintillator's identification in order to avoid edge packing effects. The experimental results were measured with four A-SiPM with FTs connected in parallel. However, in the proposed PET detector module, there are eight FTs per column. If the amplitude of the FTs is further reduced, this effect could be mitigated by choosing a wideband amplifier with a larger gain. The total number of required high-accuracy TDCs is 8 (for timemark estimation) and the total number low resolution TDCs is 16 for ToT calculations.

The timing experiments were performed utilizing small scintillation crystals in order to verify that state-of-the-art CRT can be achieved with off-shelf-components [30]. However, in the complete PET detector module thicker scintillation crystals are required for detecting the 511 keV γ -photons with high efficiency. Subsequently, timing deterioration is expected with ticker scintillators due to degrading factors, such as light transport variations [9].

The power consumption estimation and components' area relative to the detector size are shown in Table 4.2. Although we utilized the OPA656 as a transimpedance amplifier, we propose to use the LT6230-10 as a lower power consumption alternative. The Artix SOM expends 2.5 W when is idle and around 4 W when the 16 TDC channels are operating at full capacity (see Table 4.2). In addition, we included the comparator TLV320 for the scintillator's pixel-encoding and energy estimation ToT circuits because it has a lower power consumption than the ADCMP607 (see Table 4.2). We kept the ADCMP607 for the timing channels because of its low jitter and programmable hysteresis feature.

The power consumption of a typical PET ASIC is about 25 mW per channel, which leads to a total power consumption of 1.6 W the 64 channels (8×8 A-SiPM array) [5]. In our design, we observe a power consumption that is around 1 W for the analog front-end in addition to 2.5W-4W for the FPGA and all its required circuitry (see Table 4.2). However, we include an FPGA per detector module for data post-processing and communication [32]. Power consumption becomes critical in PET scanner implementations with reduced space for a cooling system, such as PET/MRI inserts [33]. Table 4.3 compares the proposed detector with respect to state-of-the-art ASICs for TOF-PET.

4.3. SUMMARY

We demonstrated that full-flexible and fast prototyping TOF-PET detector modules can be built with off-the-shelf components, TDC-on-FPGA, and A-SiPMs with FTs. We achieved a sub-120 ps CRT at a single A-SiPM level. A minimum degradation was observed when multiplexing the FTs with Schottky diodes. We obtained an energy resolution of 14 %, which is compatible for the targeted PET applications. In addition, we

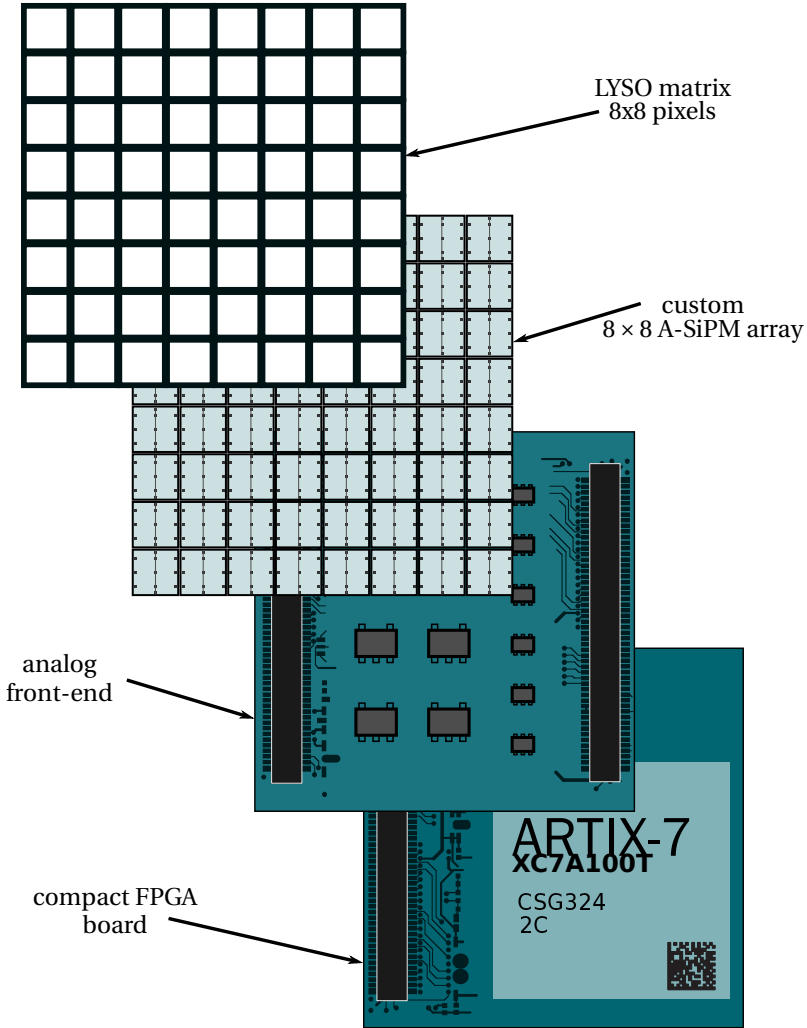


Figure 4.27: Description diagram of the proposed PET detector module.

Table 4.2: Detailed power consumption and area occupation description.

	total devices	power per device (mW)	area per device (%)	total power (mW)	total area (%)
BGA2818	8	65	0.87	520	7
OPA656	16	280	1.01	4400	16
LT6230-10	16	11	1.56	176	25
TLV320	16	1<	0.52	16<	8.36
ADCMP607	8	37.5	1.56	300	25
total analog power ^a				1012	
FPGA-SOM	1	2500-4000	40	2500-4000	40

^aPower calculated with LT6230-10 instead of OPA656.

Table 4.3: ASICs for TOF-PET comparison.

	channels	hit rate (kcps)	TDCs (ps)	energy estimation	total power (W)
STiC3 ^a	64	40	50 LSB	ToT	1.6
FlexTOT ^b	16	>1000	-	ToT	0.16
TOFPET2 ^c	64	600 ^d	31 LSB	ToT	0.524 ^e
Outlook design	8 ^f	> 1000	12 ^g	ToT	1 + (2.5-4) ^h

^aValues according to [5, 34].

^bValues according to [24].

^cValues according to [25].

^dA simultaneous maximum rate in every channel is limited by the data throughput.

^eThis value depends on specific settings.

^fIt includes a scintillator pixel-encoding circuit in order to allocate 64 A-SiPMs.

^gThis value corresponds to the single-shot resolution (σ).

^hThe FPGA power consumption can be reduced further by optimizing the SOM circuitry (see Table 4.2).

verified the LYSO pixel identification of a A-SiPM row composed of 4 elements.

The Schottky diode decoupling circuit avoids the signal amplitude reduction when connecting FTs in parallel. However, we did not observe a significant CRT degradation in the multiplexing circuit without Schottky diodes, which is 135 ± 10.3 ps FWHM with respect to the 128 ± 7.8 ps FWHM achieved with Schottky diodes.

We also concluded that the proposed PET detector module does not lose a significant amount of γ -events when the A-SiPM array shares the same measurement channel row-wise. This requires a measurement channel with a dead time of 1 μ s, which it is already achieved by the Panther board.

REFERENCES

- [1] M. E. Casey and R. Nutt, *A Multicrystal Two Dimensional BGO Detector System for Positron Emission Tomography*, IEEE Transactions on Nuclear Science 33, 460 (1986).
- [2] D. Bailey, D. Townsend, P. Valk, and M. Maisey, *Positron Emission Tomography: Basic Sciences* (Springer London, 2006).
- [3] M. R. Phelps, *PET: Physics, Instrumentation, and Scanners* (Springer Science+Business Media, 2006).
- [4] B. Weissler, P. Gebhardt, C. Lerche, J. Wehner, T. Solf, B. Goldschmidt, J. Mackewn, P. Marsden, F. Kiessling, M. Perkuhn, D. Heberling, and V. Schulz, *MR compatibility aspects of a silicon photomultiplier-based PET/RF insert with integrated digitisation*, Physics in Medicine & Biology 59, 5119 (2014).
- [5] T. Harion, K. Briggel, H. Chen, P. Fischer, A. Gil, V. Kiworra, M. Ritzert, H. C. Schultz-Coulon, W. Shen, and V. Stankova, *STiC — a mixed mode silicon photomultiplier readout ASIC for time-of-flight applications*, Journal of Instrumentation 9, C02003 (2014).
- [6] S. Mandai, V. Jain, and E. Charbon, *A fully-integrated 700x800 μm^2 multi-digital silicon photomultiplier with column-parallel time-to-digital converter*, in *ESSCIRC (ESSCIRC), 2012 Proceedings of the* (2012) pp. 89–92.
- [7] T. Frach, G. Prescher, C. Degenhardt, R. de Gruyter, A. Schmitz, and R. Ballizany, *The digital silicon photomultiplier - Principle of operation and intrinsic detector performance*, in *Nuclear Science Symposium Conference Record (NSS/MIC), 2009 IEEE* (2009) pp. 1959–1965.
- [8] B.-L. Bérubé, V.-P. Rhéaume, A. C. Therrien, S. Parent, L. Maurais, A. Boisvert, G. Carini, S. A. Charlebois, R. Fontaine, and J.-F. Pratte, *Development of a single photon avalanche diode (SPAD) array in high voltage CMOS 0.8 μm dedicated to a 3D integrated circuit (3DIC)*, in *Nuclear Science Symposium and Medical Imaging Conference (NSS/MIC), 2012 IEEE*.

- [9] S. Dolinsky, G. Fu, and A. Ivan, *Timing resolution performance comparison for fast and standard outputs of SensL SiPM*, in *2013 IEEE Nuclear Science Symposium and Medical Imaging Conference (2013 NSS/MIC)* (2013) pp. 1–6.
- [10] E. Venialgo, N. Lusardi, A. Geraci, K. O'Neill, S. Gneccchi, C. Jackson, S. E. Brunner, D. R. Schaart, and E. Charbon, *An order-statistics-inspired, fully-digital readout approach for analog SiPM arrays*, in *2016 IEEE Nuclear Science Symposium, Medical Imaging Conference and Room-Temperature Semiconductor Detector Workshop (NSS/MIC/RTSD)* (2016) pp. 1–5.
- [11] N. Lusardi, A. Palmucci, and A. Geraci, *Fully-migratable TDC architecture for FPGA devices*, in *2016 IEEE Nuclear Science Symposium, Medical Imaging Conference and Room-Temperature Semiconductor Detector Workshop (NSS/MIC/RTSD)* (2016) pp. 1–3.
- [12] N. Lusardi, F. Garzetti, M. Cibin, R. Sury, and A. Geraci, *Hardware and Software Co-Design of a System-of-Chip for Real-Time Bidirectional Transfer and Processing of Data from a Time-to-Digital Converter*, in *2017 IEEE Nuclear Science Symposium and Medical Imaging Conference (NSS/MIC)* (2017).
- [13] N. Lusardi, F. Garzetti, and A. Geraci, *Fully Programmable System for Multi-Channel Experiments Targeting to Time Measurement at High Performance*, in *2017 IEEE Nuclear Science Symposium and Medical Imaging Conference (NSS/MIC)* (2017).
- [14] N. Lusardi and A. Geraci, *Comparison of interpolation techniques for TDCs implementation in FPGA*, in *2015 IEEE Nuclear Science Symposium and Medical Imaging Conference (NSS/MIC)* (2015) pp. 1–2.
- [15] Lusardi, N. and Geraci, Angelo, *8-Channels high-resolution TDC in FPGA*, in *2015 IEEE Nuclear Science Symposium and Medical Imaging Conference (NSS/MIC)* (2015) pp. 1–2.
- [16] S. Jan, D. Benoit, E. Becheva, T. Carlier, F. Cassol, P. Descourt, T. Frisson, L. Grevillot, L. Guigues, L. Maigne, *et al.*, *GATE V6: a major enhancement of the GATE simulation platform enabling modelling of CT and radiotherapy*, *Physics in Medicine & Biology* 56, 881 (2011).
- [17] J. Allison, K. Amako, J. Apostolakis, P. Arce, M. Asai, T. Aso, E. Bagli, A. Bagulya, S. Banerjee, G. Barrant, *et al.*, *Recent developments in Geant4*, *Nuclear Instruments and Methods in Physics Research Section A: Accelerators, Spectrometers, Detectors and Associated Equipment* 835, 186 (2016).
- [18] H.-P. W. Schlemmer, B. J. Pichler, M. Schmand, Z. Burbar, C. Michel, R. Ladebeck, K. Jattke, D. Townsend, C. Nahmias, P. K. Jacob, *et al.*, *Simultaneous MR/PET imaging of the human brain: feasibility study*, *Radiology* 248, 1028 (2008).
- [19] K. Gong, S. Majewski, P. E. Kinahan, R. L. Harrison, B. F. Elston, R. Manjeshwar, S. Dolinsky, A. V. Stolin, J. A. Breczynski-Lewis, and J. Qi, *Designing a compact*

- high performance brain PET scanner—simulation study*, Physics in Medicine & Biology 61, 3681 (2016).
- [20] M. Fishburn, L. H. Menninga, C. Favi, and E. Charbon, *A 19.6 ps, FPGA-based TDC with multiple channels for open source applications*, IEEE transactions on nuclear science 60, 2203 (2013).
- [21] N. Lusardi, F. Garzetti, G. Bulgarini, R. Gourgues, J. Los, and A. Geraci, *Single photon counting through multi-channel TDC in programmable logic*, in *Nuclear Science Symposium, Medical Imaging Conference and Room-Temperature Semiconductor Detector Workshop (NSS/MIC/RTSD), 2016* (IEEE, 2016) pp. 1–4.
- [22] A. Rochas, *Single photon avalanche diodes in CMOS technology*, Tech. Rep. (Citeseer, 2003).
- [23] S. Seifert, H. T. Van Dam, J. Huizenga, R. Vinke, P. Dendooven, H. Lohner, and D. R. Schaart, *Simulation of silicon photomultiplier signals*, IEEE Transactions on Nuclear Science 56, 3726 (2009).
- [24] A. Comerma, D. Gascón, L. Freixas, L. Garrido, R. Graciani, J. Marín, G. Martínez, J. M. Pérez, P. R. Mendes, J. Castilla, J. M. Cela, J. M. Fernández-Varea, and I. Sarasola, *FlexToT - Current mode ASIC for readout of common cathode SiPM arrays*, in *2013 IEEE Nuclear Science Symposium and Medical Imaging Conference (2013 NSS/MIC)* (2013) pp. 1–2.
- [25] P. Electronics, *PETsys Time-of-Flight PET ASIC* ((accessed April 20, 2018)).
- [26] L. SensL Technologies, *High PDE and Timing Resolution SiPM Sensors in a TSV Package* ((accessed April 20, 2018)).
- [27] SensL, *Readout Methods for Arrays of SiPM*, in *Application note [online]* (2015).
- [28] J. Proffitt, *Diode enhanced amplifier circuits and methods thereof*, (2015), uS Patent 9,106,191.
- [29] S. Blahuta, V. Ouspenski, P. Menge, and K. Yang, *Next Generation LYSO:Ce,Ca Single Crystals* ((accessed April 20, 2018)).
- [30] S. Seifert, H. van Dam, and D. Schaart, *The lower bound on the timing resolution of scintillation detectors*, Phys. Med. Biol. 57, 1797 (2012).
- [31] L. SensL Technologies, *C-Series: Low Noise, Fast, Blue-Sensitive Silicon Photomultipliers* ((accessed April 20, 2018)).
- [32] M. Bijwaard, C. Veerappan, C. Bruschini, and E. Charbon, *Fundamentals of a scalable network in SPADnet-based PET systems*, in *2015 IEEE Nuclear Science Symposium and Medical Imaging Conference (NSS/MIC)* (2015) pp. 1–3.
- [33] G. Delso and S. Ziegler, *PET/MRI system design*, European journal of nuclear medicine and molecular imaging 36, 86 (2009).

- [34] R. Becker, C. Casella, S. Corrodi, G. Dissertori, J. Fischer, A. Howard, M. Ito, and W. Lustermann, *Studies of the high rate coincidence timing response of the STiC and TOFPET ASICs for the SAFIR PET scanner*, Journal of Instrumentation 11, P12001 (2016).

5

MD-SiPM METROLOGY AND MEASUREMENT METHODS

Part of this chapter is under preparation for submission as “Esteban Venialgo, Shingo Mandai, and Edoardo Charbon. MD-SiPMs: Individual Building Block and Full-System Comprehensive Analyses. IEEE Journal of Solid-State Circuits, 2019”.

In this chapter, we give a detailed circuit description and analysis of the individual building elements such as the SPAD-cell array, TDCs, event-driven discrimination and readout logic; in addition to their corresponding characterization and performance verification. The SPAD-cell array's PDE, DCR vs. temperature, and masking circuit performance are described. Additionally, we present the evaluation of the 433 TDCs, when they are operated simultaneously, in terms of DNL, INL, timing jitter accumulation, and full photodetector SPTR.

In particular, we give special attention to the measurements methods utilized during the characterization, which are designed for the presented implementation of the MD-SiPM. The objective of this chapter is to describe in detail the MD-SiPM performance evaluation and metrology, in order to establish a basis for future characterization methods utilized in similar D-SiPMs devices.

5.1. ARCHITECTURE

MD-SiPMs are dedicated SOCs designed for low-light level detection and picosecond-precision light-photon timestamping. This type of photodetector integrates SPADs, TDCs, and a readout logic into a monolithic CMOS sensor. The particular implementation of a 18×9 monolithic array of MD-SiPMs comprises 67,392 SPAD cells with a fill factor of 57% and integrated cell-masking circuit, 433 TDCs with an LSB of 59 ps and programmable common voltage-controlled oscillator (VCO), and on-chip event-driven smart-reset and readout logic. This photodetector was implemented on a high-voltage (HV) standard CMOS 0.35 μm process. Figure 5.1 shows the block diagram of the 18×9 array of MD-SiPMs and Figure 5.2 depicts the photodetector's mounted on a chip-on-board assembly.

5.1.1. SPAD CELL ARRAY

In this photodetector implementation a MD-SiPM block is called cluster. There are 26×16 SPAD cells per cluster and 18×9 clusters; therefore, the total size of the array is 468×144 SPAD cells.

The SPAD-cell array of the of 18×9 MD-SiPM includes two pointers: the mask address and the cell-out pointers, which are utilized for individual SPAD-cell masking memory writing and cell memory readout, respectively. The pointers are realized by incremental counters connected to combinational decoders. The masking and readout are performed row-wise; therefore, the pointer's address corresponds to a specific row and the R/W registers have a width of 16×9 bits (see Figure 5.1). In addition, the cell-out pointer controls the ROW<0:467> signals in order to enable and disable the readout of a specific SPAD-cell row (see Figure 5.3).

In order to realize a fast readout and/or counting of the SPAD-cells that have detected a photon, for γ -photon energy estimation and SPAD-camera readout mode, the cell memory of every SPAD cell is connected as shown in Figure 5.3. Every SPAD cell that belongs to the same column shares an input bit of the CELL_OUT register through a high-threshold inverter. Therefore, there are large parasitics in the connecting node of a single input of CELL_OUT. For mitigating the large parasitics, in every readout cycle, in which one complete SPAD-cell row is read out at once, the CELL_IN nodes are

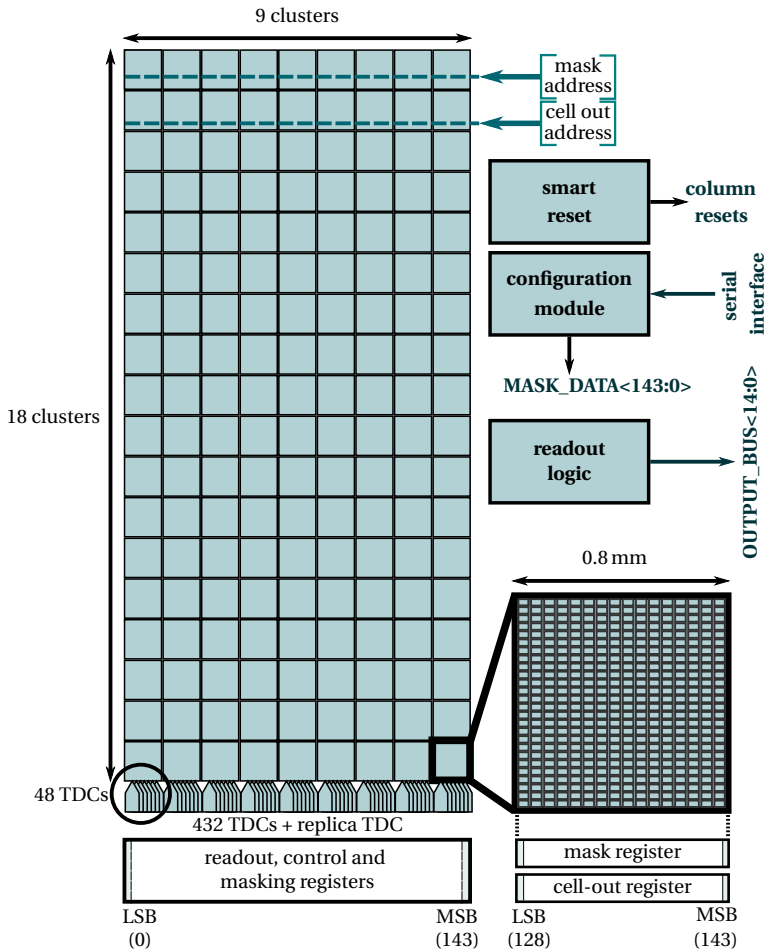


Figure 5.1: Description diagram of the monolithic array of 18 × 9 MD-SiPMs.

pre-charged by activating the ENEPREBIN signal (see Figure 5.3). During the pre-charge phase the cell-out address pointer disconnects all the in-cell output memories. After the line is pre-charged, the cell-out pointer connects the corresponding SPAD-cell row and the SPAD cells pull down the CELL_IN corresponding bit at low speed. Therefore, the connecting node is sampled with a high-threshold inverter, in order to detect in a short clock cycle if the SPAD-cell memory has stored a detection.

The full SPAD-cell's circuit schematic is depicted in Figure 5.4. The LOAD_MASK signal is controlled by the mask address, which enables the memory writing of a complete row of SPAD-cell masking memories at once. A masking register of 144-bit width stores the masking values, which are serially preloaded within a configuration module, and it is connected to MASKDATA (see Figures 5.1 and 5.4). When the SPAD is deactivated by the masking circuit, it is logically disabled through the AND gate formed with NAND₁

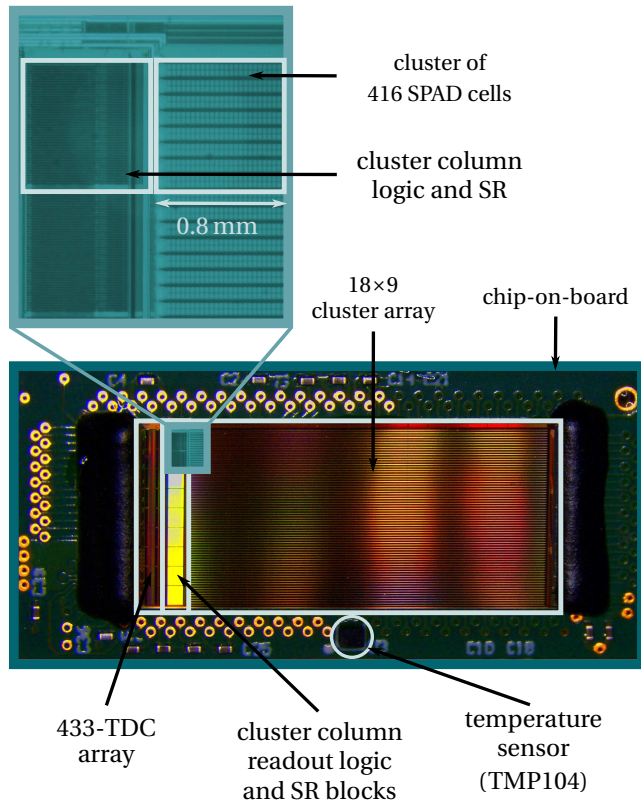


Figure 5.2: Photograph of the 18×9 array of MD-SiPMs' assembly.

and INV_5 . Additionally, it is possible to bias a masked SPAD below its breakdown voltage through M_2 by setting V_E to a voltage higher than the SPAD excess bias voltage (see Figure 5.4).

The SPAD is connected to a passive quenching transistor that is biased with V_{QBIAS} , typically at 0 V. The SPAD is actively recharged through M_4 and the RESET signal is the output of a narrow pulse produced by a monostable circuit. M_3 disconnects the recharge of the masked SPADs.

The AND gate output is divided into two signal branches. The first branch is connected to the cell's memory, which stores the SPAD value when the SET signal is enabled. The second branch is connected to MD-SiPM's timing lines through M_8 and M_7 , which is activated during normal operation with the TIME_ENABLE signal.

5.1.2. 433-TDC ARRAY

There are 48 TDCs per cluster column plus a replica TDC, which has an independent STOP signal (see Figures 5.1 and 5.5). The TDCs share a common VCO, which its frequency is adjusted by an integrated band-gap bias generator. The bias generator is set by the configuration module (see Figures 5.1 and 5.5) [1]. The free-running VCO is com-

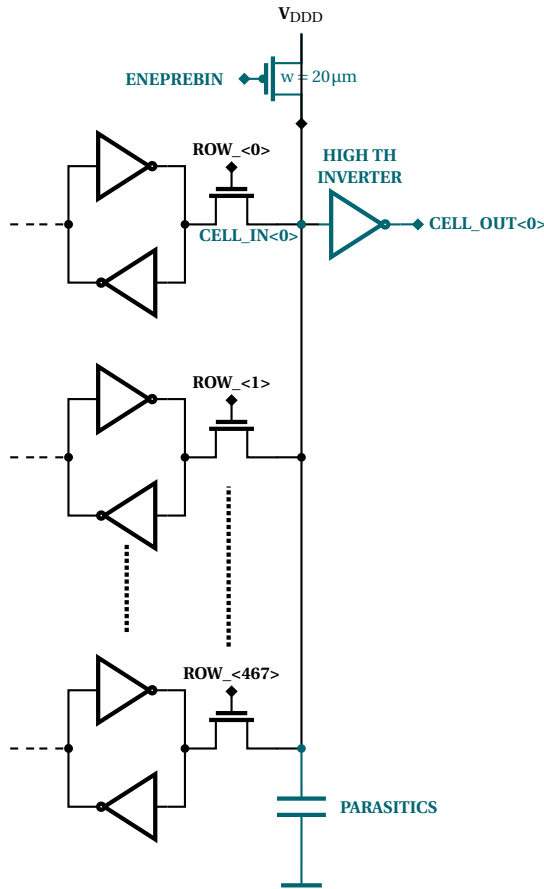


Figure 5.3: Readout structure of the SPAD-cell column.

posed of four symmetric-load delay elements (DEs) that generate eight different phases, which are PH<3:0> and PHB<3:0> (see Figures 5.5 and 5.6) [2, 3]. The phases are distributed along all the TDCs, and two sets of phase repeaters are located every three cluster columns (see Figure 5.5). The default setting of the SWBIASVCO<3:0> runs the VCO at an average frequency of 529.7 MHz.

The TDCs are composed of two sets of eight clocked comparators each (see Figures 5.7a and 5.7b). Each VCO phase is compared by the clocked comparators to an externally-supplied reference voltage (TDC_REF), and 16 different codes are generated that corresponds to a VCO sub-phase [1]. In addition, the latch signals of the clocked comparator sets are controlled by two delayed stop signals, which are τ and $\tau + \Delta T$. This delay is generated by the block STOP delay (see Figure 5.7). In order to obtain an LSB that is 32 times smaller than the VCO period, the two delay STOP signals are shifted by the half of the VCO sub-phase. The delay between the two latch signals is controlled by the VBP_TDC (see Figure 5.7c), which is a voltage provided by the bias generator and

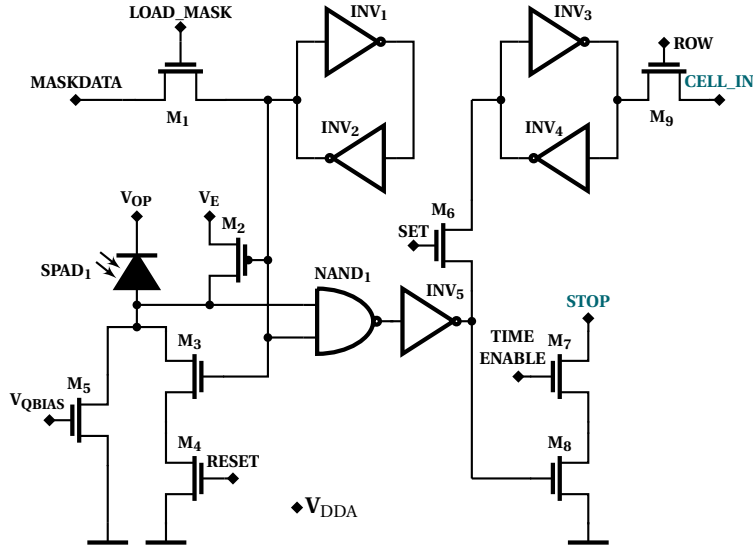


Figure 5.4: SPAD-cell's circuit schematic.

adjusted by setting SWBIAS $TDC<3:0>$ through the configuration module (see Figures 5.5 and 5.7a). In this way, by combining the outputs of the two sets of comparators (D_PH_A and D_PH_B), the VCO frequency is sub-sampled at a resolution that is 32 times smaller than its period. Therefore, the TDC fine-bits are calculated from D_PH_A and D_PH_B, which have a resolution of 5 bits and an LSB of 59 ps.

The last VCO phase (PH_ $<3>$) is injected into a ripple counter of 12-bits in order to extend the TDC range to 7.73 μ s. Additionally, there is synchronizing circuit between the ripple counter and the STOP delay block that is utilized to detect a fixed misalignment between the counter and the clocked comparators (see Figures 5.7a and 5.8). The counter synchronizer block latches the phase of PH $<3>$ when the delayed stop signal arrives. In this way, we can identify what VCO sub-phases are detected when PH $<3>$ is negative or positive. Therefore, we can realign the coarse counter to the VCO sub-phases since we know exactly in what sub-phase the coarse counter is incremented.

After the measurement frame is finished, the outputs of the comparator sets, synchronizing circuit, and coarse counter are memorized into latches by the LATCH_CLK signal before a readout process starts. Figure 5.9 shows the timing diagram of the TDC operation.

The timing line structure is showed in Figure 5.10. This circuit is replicated SPAD-cell column-wise by three times per column (see Figures 2.19 and 5.5). The strength of the pull-up PMOS is externally adjusted by a bias voltage called VPRE (see Figure 5.10). In addition, there is a testing external electrical trigger (E_TRIGGER) that pulls down all the timing lines simultaneously. Also, during the TDC reset phase the timing lines are pre-charged by connecting the gate of pull-up PMOS to ground through an analog multiplexer.

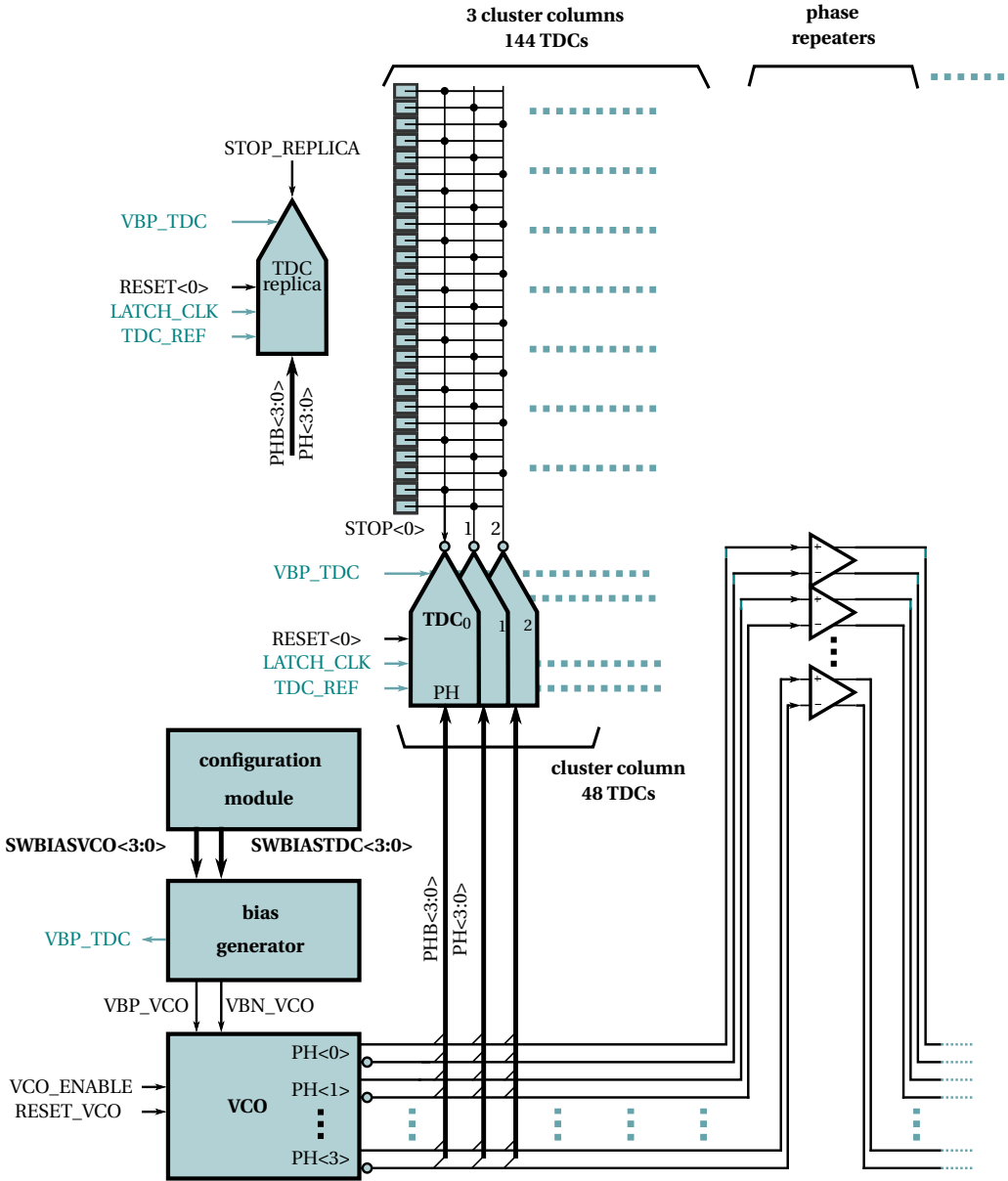


Figure 5.5: Block diagram of the 433-TDC array.

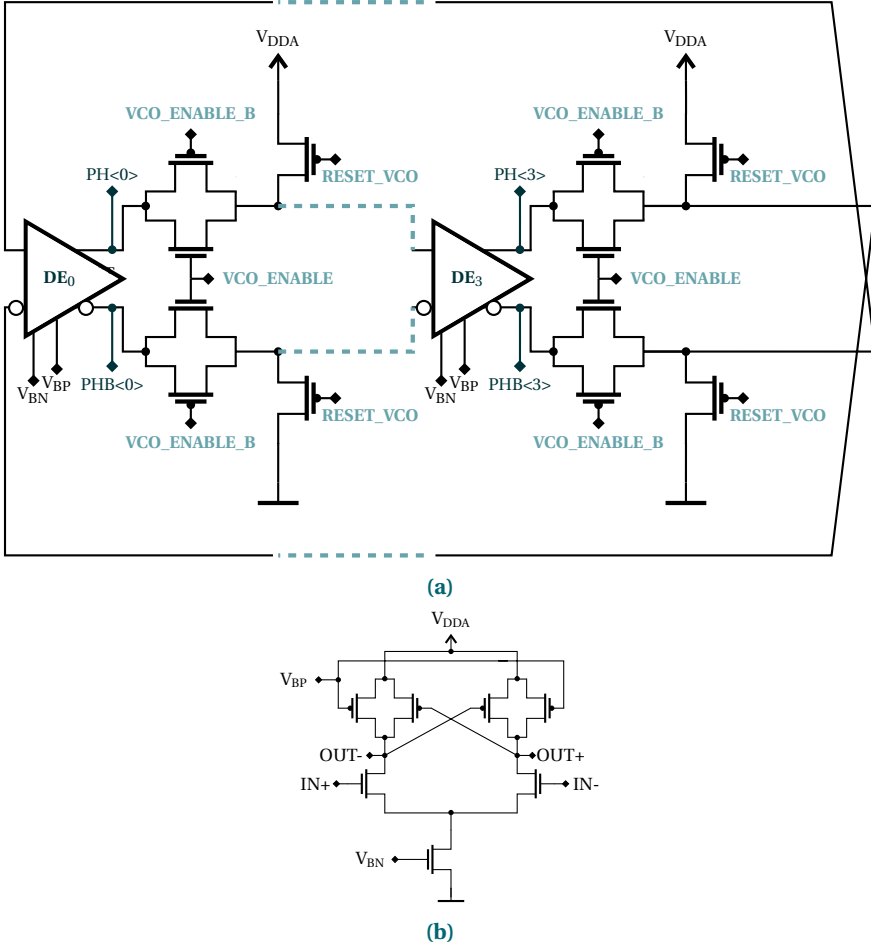


Figure 5.6: Schematic of the free-running common VCO. (a) ring oscillator schematic. (b) symmetric detection element (DE) schematic.

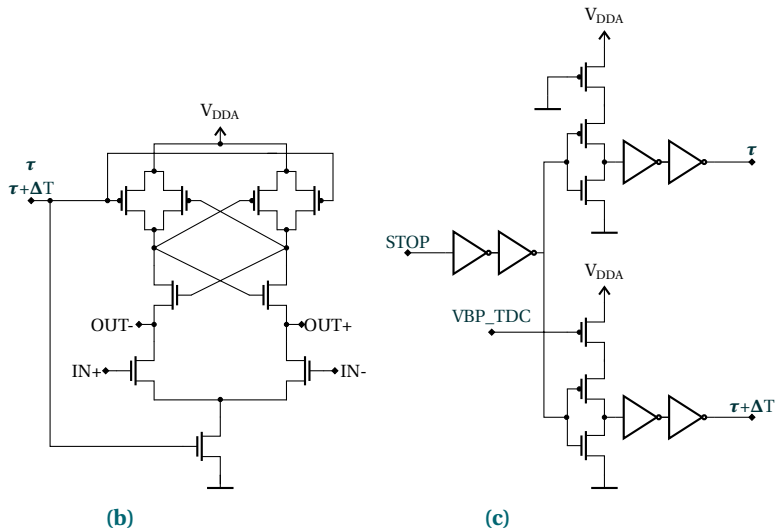
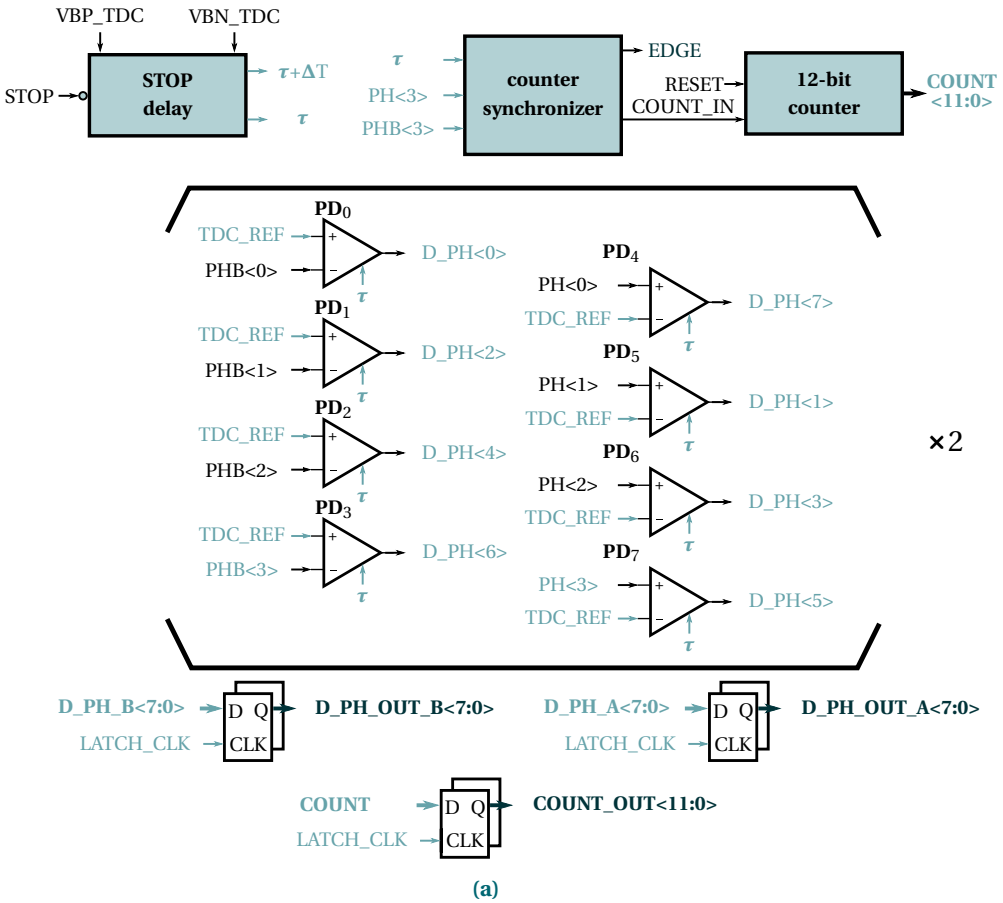


Figure 5.7: TDC block diagram and circuit schematics. (a) TDC block structure. (b) clocked comparator circuit schematic. (c) circuit schematic of the delay stop block.

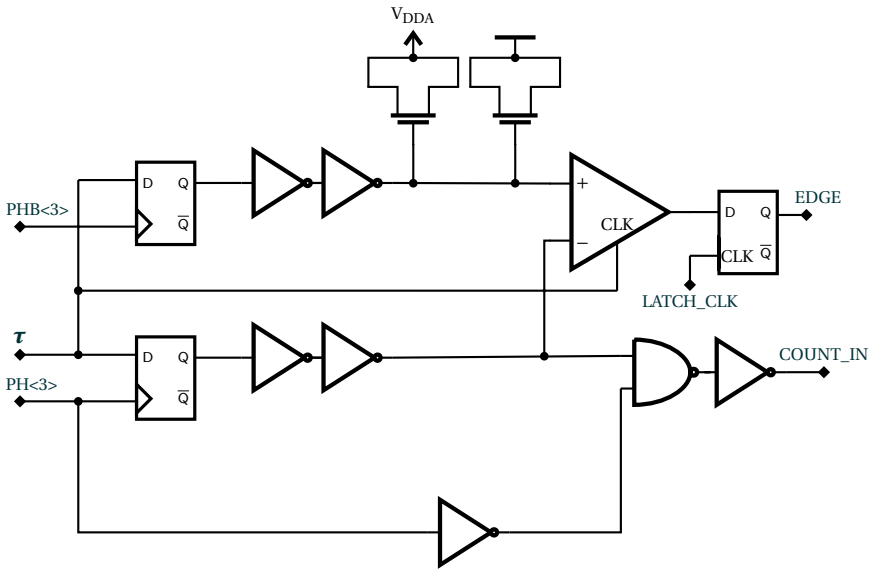


Figure 5.8: Schematic of the counter synchronizer that detects a fixed misalignment between the counter and the clocked comparators.

5.1.3. READOUT

The MD-SiPM has an internal configuration memory of 42-bits that stores several readout settings and operation parameters, such as SWBIASVCO<3:0>, SWBIASTDC<3:0>, etc. This information is loaded through the serial interface at the beginning of the MD-SiPM operation, along with the masking memory information (see Figures 5.1 and 5.11). The CONFSEL signal indicates if the serially loaded information corresponds to the configuration or masking data. 144 masking bits are serially loaded and applied to a complete SPAD-cell row before incrementing the mask address pointer (see Figures 5.1 and 5.11).

There are two ways of operating the MD-SiPM: SPAD camera readout mode and D-SiPM readout mode. In the first mode, there is a fixed VCO enable period that is controlled by an external readout FPGA through the VCO_ENABLE signal (see Figures 5.6a and 5.12a). Before enabling the VCO, the SPADs are recharged with a narrow pulse by utilizing an integrated monostable circuit that is connected to the SPAD-cell RESET signals (see Figure 5.4) and triggered by the external FPGA. Also, the initial VCO phase and TDCs' coarse counters are reset before enabling the VCO. The SPADs' quenching transistors are biased at 0V; therefore, the SPADs that fire during the VCO enable cycle are kept quenched before the beginning of the next VCO measurement cycle. The SPAD-cell memory is enabled by the SET signal after the VCO enable cycles ends (see Figures 5.4 and 5.12a). There is an extra TDC, the replica TDC, which has an independent STOP signal that is controlled by the external FPGA. The purpose of this TDC is to obtain a code that corresponds to the length of the VCO enable cycle, in order to estimate the VCO frequency for every measurement cycle (see Figures 5.5 and 5.12a). After the VCO enable

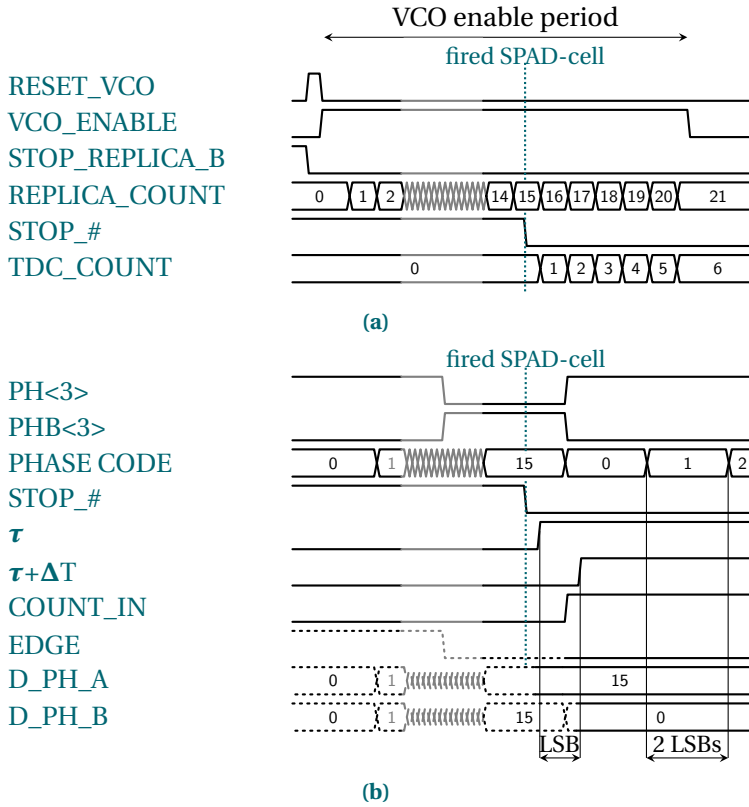


Figure 5.9: TDC's timing diagrams. (a) Replica and cell-array TDCs' timing diagrams. (b) Detailed timing diagrams of the phase detector.

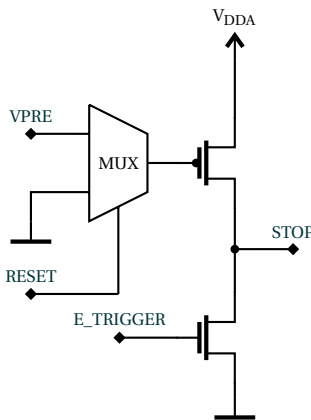


Figure 5.10: Timing line structure.

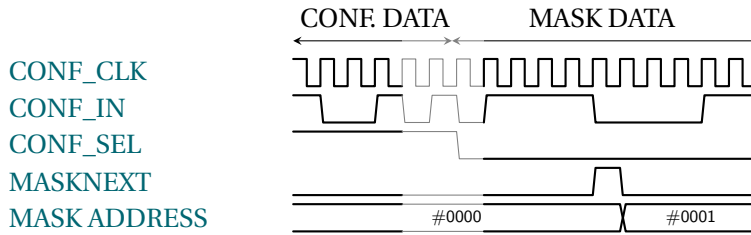


Figure 5.11: Timing diagram of the configuration loading.

period is over, the SPAD-cell state and TDC values are latched before starting a readout phase.

In the D-SiPM readout mode, there is an integrated discrimination logic called smart reset (SR). This module is in charge of monitoring if a γ -photon has interacted with the scintillator, by counting the TDCs that were triggered by subsequent scintillation photons. The SR logic is verifying if the total number of fired TDCs per cluster column is larger than a TDC_TH value, which is preloaded during the configuration phase (see Figure 5.13). Additionally, the SR verification period is also programmable and loaded during the configuration phase. The ENEMONITOR<0:8> register, which stores the result of the comparison at the end of a SR verification period, is transferred to the FPGA through the readout logic module (see Figure 5.1). Each bit of ENEMONITOR corresponds to the comparison result of a particular cluster column. If the result of any comparisons is positive, the external FPGA immediately stops the VCO enable cycle, latch the status of the SPAD-cell array and TDC values before starting the readout phase (see Figure 5.12b). Additionally, the RESET signals of the TDCs and SPAD cells that belong to the same SPAD-cell column are independently controlled by the SR module. Therefore, if the TDC_TH detection condition is not met, only the SPAD cells and TDCs connected to the pulled down timing lines are reset (see RESET_CELL_# and RESET_TDC_# in Figure 5.12b).

In the readout phase, it is possible to read the state of every SPAD cell or a value that corresponds to the addition of the fired SPAD cells of a particular cluster. In addition, it is possible to read only a particular set of 48 TDCs that corresponds to a cluster column in order to optimize the readout speed. The individual SPAD-cell values are externally readable only if the SR logic is disabled. Conversely, the cluster SPAD-cell adds are only enabled if the SR logic is activated. However, it is possible to configure the MD-SiPM with SR enabled, perform a measurement cycle, latch the status of photodetector, quickly re-configure the MD-SiPM memory for disabling the SR, and finally readout individual SPAD-cell values.

Figure 5.14 shows the D-SiPM readout, where the nodes CELL_IN<0:143> are pre-charged with the ENEPREBIN signal before reading the next SPAD-cell row. Also, after all the SPAD cells of that cluster are read out and added, the addition values of a cluster row are transferred to the FPGA during a count readout (CR) cycle. After all the addition values are transferred, the TDC latched outputs are read out by the same output interface (OUTPUT_BUS<14:0>). When reading out individual SPAD-cell values, the procedure is

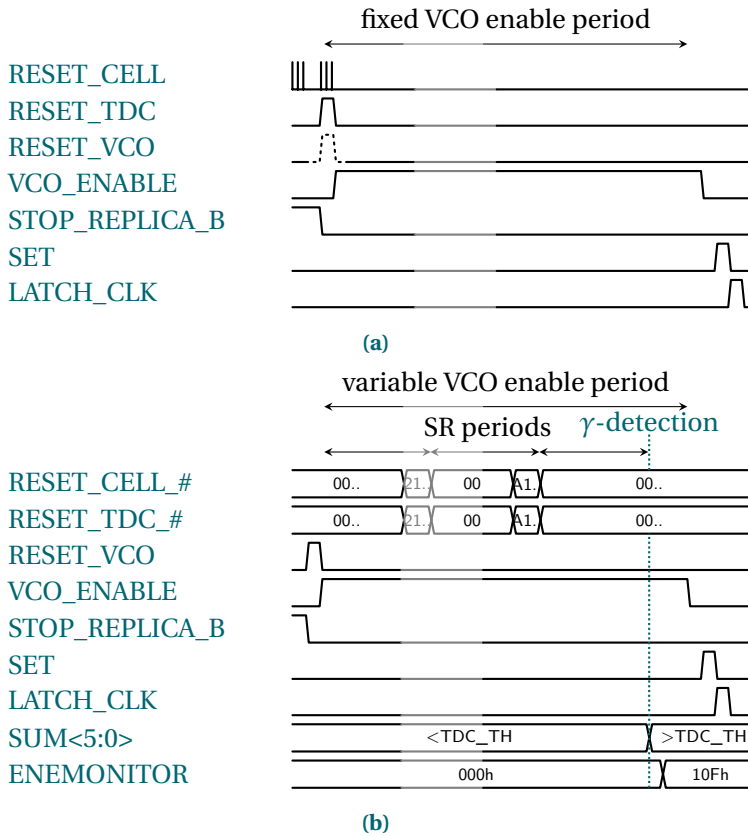


Figure 5.12: MD-SiPM operation's timing diagrams. (a) SPAD camera readout mode. (b) D-SiPM readout mode.

similar; however, a CR cycle is performed in every SPAD-cell row readout in order to transfer the individual values to the FPGA.

5.2. METHODS AND CHARACTERIZATION

The characterization of the 18×9 MD-SiPM is divided into sub-sections that incrementally describe the testing of the individual building blocks. In all the experiments, the SPAD bias voltage (V_{OP}) was 22 V, 20 % of the SPAD-cell with highest DCR were masked, and the measurements were performed at room temperature unless otherwise specified.

5.2.1. SPAD-CELL ARRAY

When disabling all the masking bits, some SPAD cells failed to be reset at the beginning of the measurement frame (see Figure 5.12a). As a result, after acquiring a set of measurement frames in SPAD-camera readout mode, the resulting DCR histogram map showed SPAD-cell that are constantly fired (see Figure 5.15a). The reset failure is related

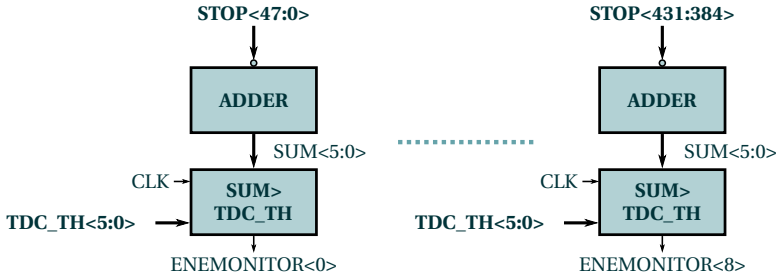


Figure 5.13: SR block diagram.

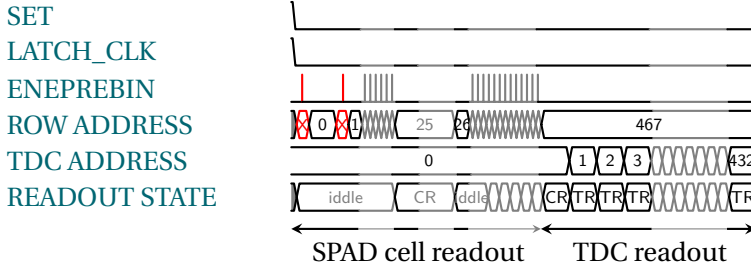


Figure 5.14: MD-SiPM readout's timing diagram.

to the total number of activated SPAD cells since this behavior disappears when a certain amount of SPAD cells are masked.

In order to secure a proper reset when all the SPAD cells are activated, we modify the RESET_CELL signal behavior by producing a modulated RESET_CELL pulse (see Figure 5.12a). The modulation consisted of mixing the RESET_CELL pulse with a clock frequency that is three times higher than the MD-SiPM readout clock frequency. As a result, one SPAD-cell reset-cycle is composed by three consecutive pulses followed by a reset stand-by period. Figure 5.15a shows an obtained DCR histogram map when the readout is configured to perform two consecutive SPAD-cell reset-cycles before the beginning of the VCO enable period. Figure 5.15b depicts an obtained DCR histogram map when the readout is configured to perform five consecutive SPAD-cell reset-cycles, where most of the artifacts are not present.

We also observed that the stand-by period between subsequent reset pulses was mandatory in order to obtain a clean DCR histogram map. Therefore, we concluded that the failure was caused by SPADs that are fired when being recharged by the integrated monostable circuit through M_4 (see Figure 5.4), which causes a local drop of the V_{OP} voltage. This is the reason why a series of pulses effectively reset the SPADs, and the V_{OP} voltage is recovered during the stand-by period. The overhead added by the a sequence of SPAD-cell reset-cycles is negligible with respect to the readout time. Furthermore, during the D-SiPM readout mode operation, the reset-cycles are only required at the beginning of the measurement frame and not during the SR operation, since only few SPAD-cell are reset by the SR module (see Figure 5.12b).

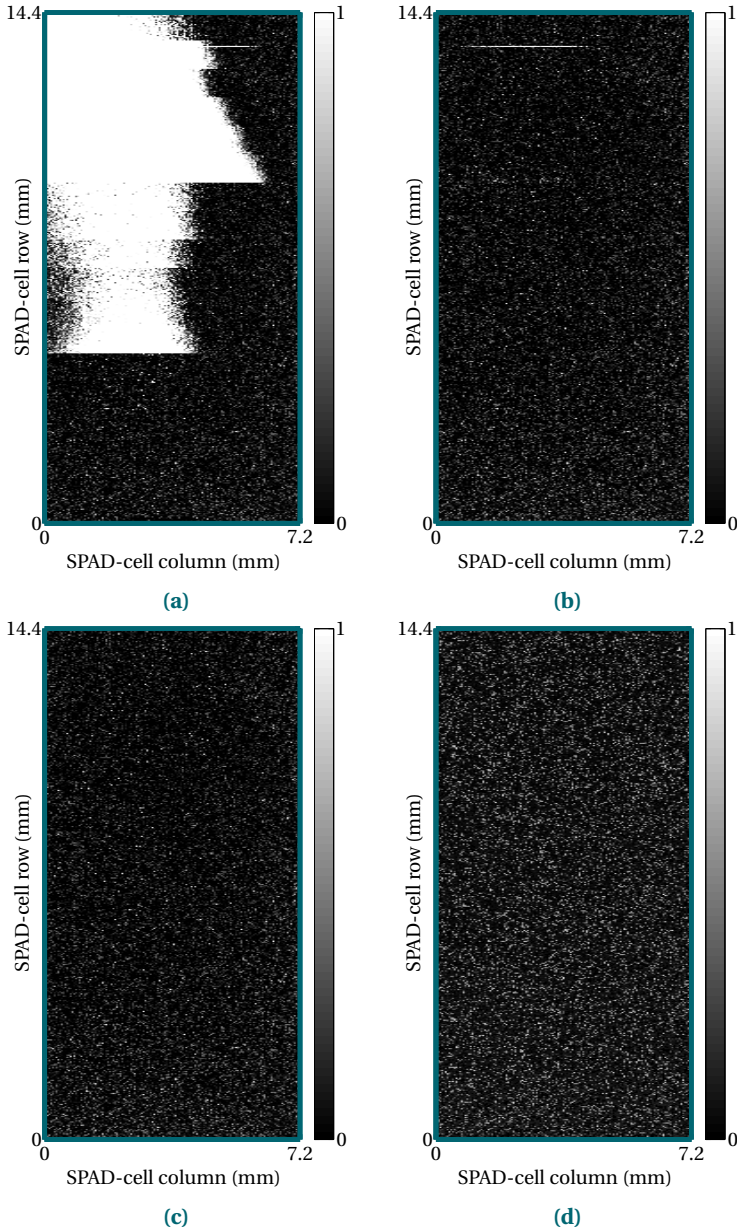


Figure 5.15: DCR histogram map at SPAD-cell level. (a) map obtained with two SPAD-cell reset cycles. (b) map obtained with five SPAD-cell reset cycles. (c) map obtained with five SPAD-cell reset cycles and decreasing V_e to 800 mV. (d) map obtained with five SPAD-cell reset cycles, decreasing V_e to 800 mV, and masking 20% of SPAD-cells.

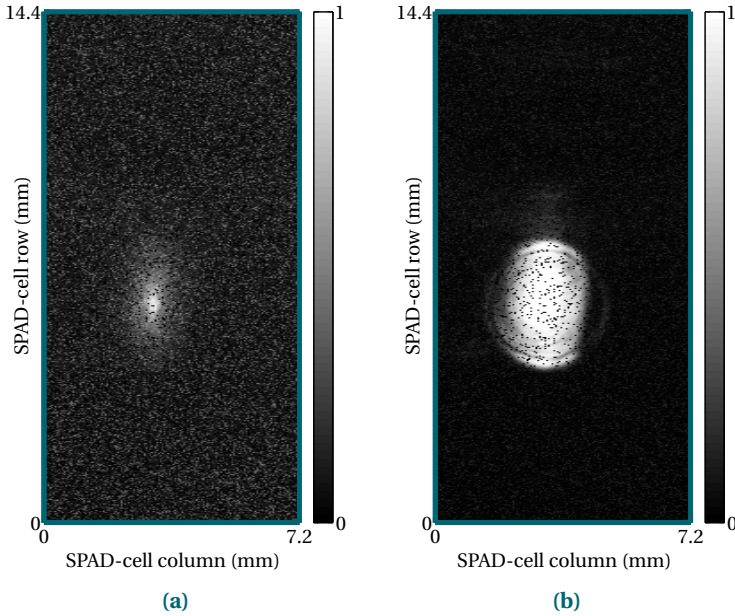


Figure 5.16: DCR histogram map at SPAD-cell level when illuminating the photodetector with a picosecond laser. (a) low laser intensity and a V_{OP} of 22.8 V. (b) high laser intensity and a V_{OP} of 21.5 V.

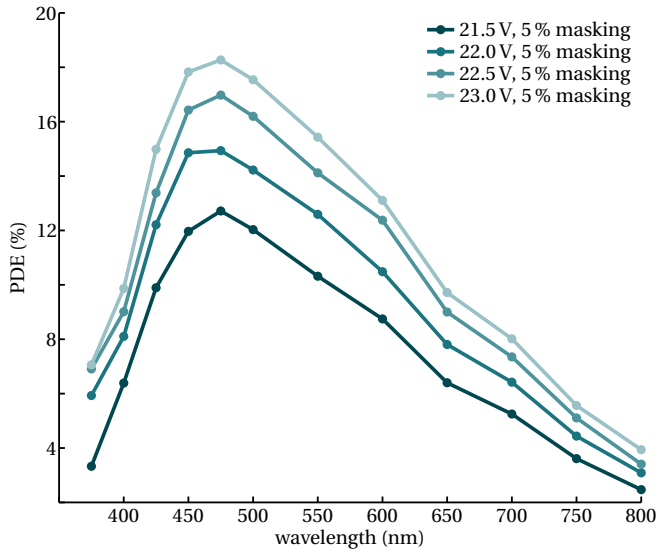


Figure 5.17: PDE as a function of the photon wavelength at several V_{OP} voltages, measured on a central cluster within a 3×3 cluster activation area, with 5% of the SPAD-cell masked.

In addition to the reset failure, we observe a line-type artifact (see Figure 5.15b). This was caused by an improper biasing of the turn-off transistor M_2 (see Figure 5.4). This artifact disappears after reducing V_e from 3.3 V to 800 mV (see Figures 5.15b, and 5.15c). After reducing the voltage of V_e the SPAD turn-off function of M_2 was ineffective since V_e is lower than the SPADs's excess bias voltage. Figure 5.15d shows a more uniform DCR histogram map that corresponds to mask 20 % of the SPAD cells with highest DCR. Typically, the masking process is performed by acquiring two subsequent measurements in SPAD-camera readout. In the first measurement, all the SPAD cells are activated and a DCR histogram map is generated. Before the second readout, the masking memory bits are calculated to disable some percentage of the noisiest SPAD cells and loaded through the configuration module. Then, the second SPAD-camera readout is performed in order to obtain the DCR histogram map that corresponds to mask a SPAD-cell percentage of the array.

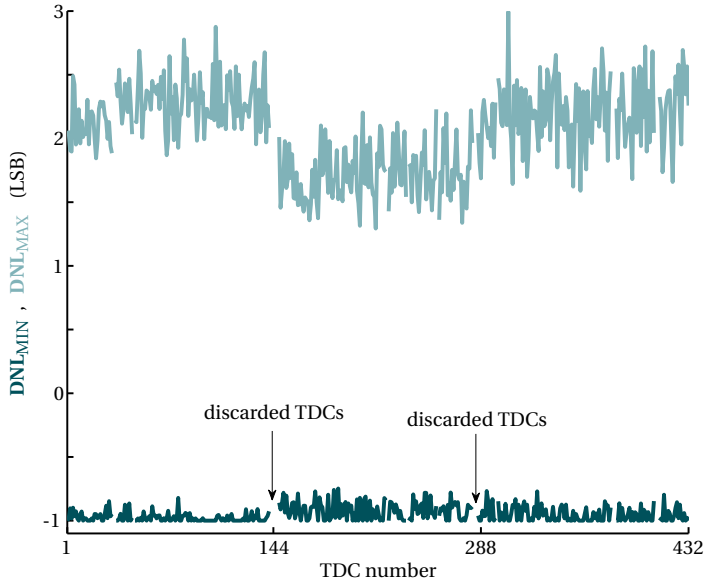
Furthermore, we illuminated the photodetector with a picosecond laser system EIG1000-AF-PiL040F that has a repetition frequency of 40 MHz and a head with a SANYO laser diode DL-5146-152 of 405 nm wavelength. We interposed a neutral-density filter (NDF) between the laser head and the photodetector. The objective of this test was to verify the proper reset of the SPAD cells when the photodetector is illuminated with a transient light pulse. Figure 5.16a shows a DCR map histogram when the laser intensity was set to its minimum value, the V_{OP} voltage was 22.8 V, and 20 % of the array was masked. The DCR map histogram that corresponds to increasing the laser power and reducing the V_{OP} voltage to 21.5 V is shown in Figure 5.16b. When the V_{OP} was not reduced when illuminating the with the higher light power, reset-failure artifacts were observed. Additionally, in Figure 5.16b the black dots observed within the high-intensity area corresponds to the masked SPAD cells.

Finally, we measured the photodetector's PDE as a function of the wavelength. The measurement setup was composed of monochromator (Newport 77250) that was input with an arc-lamp and its output was split by an integrating sphere. One port of the integrating sphere was connected to a reference photodiode (Hamamatsu s1336-18bk) and the other port was illuminating the 18×9 array of MD-SiPMs. During the measurement a subset 3×3 clusters was activated, and the PDE was calculated by considering only the central cluster of the 3×3 subset. The measured SPAD-cell rates were corrected by dark counts. Figure 5.17 shows the PDE as a function of the wavelength for several V_{OP} voltages.

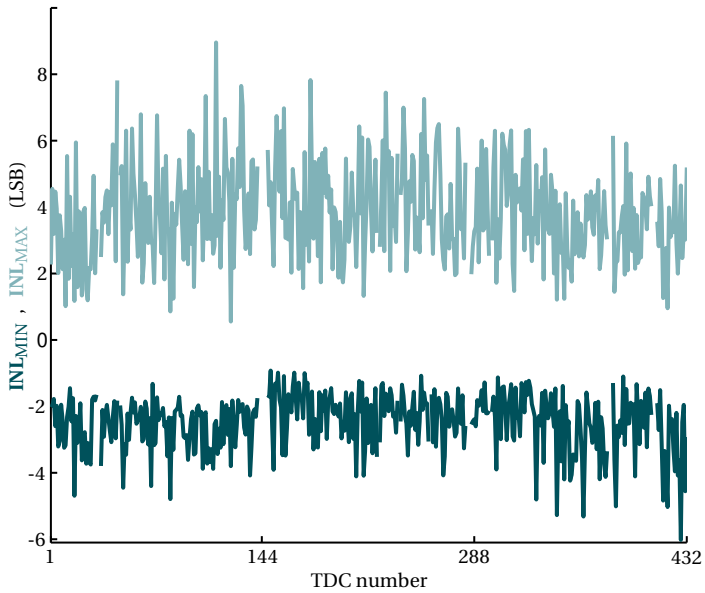
In all of the previous measurements, the V_{DDA} voltage was 3.3 V, which is the supply of the SPAD cells (see Figure 5.4), and the V_{DDD} voltage was 2.8 V, which is the supply of the readout logic and the SPAD-cell column readout structures (see Figures 5.1 and 5.3). In this way we guaranteed a correct readout transfer between the SPAD-cell memory and the high-threshold inverter (see Figure 5.3). If the V_{DDA} and V_{DDD} voltages have the same value, it is not possible to read the SPAD-cell memories.

5.2.2. CHARACTERIZATION OF THE 433-TDC ARRAY

The first step before operating the TDCs was to adjust the VCO frequency and the delayed stop signals, by configuring the values of SWBIASVCO<3:0> and SWBIASTDC<3:0>, respectively. Additionally, the TDC_REF voltage was calibrated to minimize the TDCs'



(a)



(b)

Figure 5.18: Minimum and maximum DNLs and INLs of all the TDCs within a subrange of about 600 TDC bins, when the VCO is reset. (a) minimum and maximum DNLs calculated when the VCO is reset at the beginning of the measurement frame. (b) minimum and maximum INLs calculated when the VCO is reset at the beginning of the measurement frame.

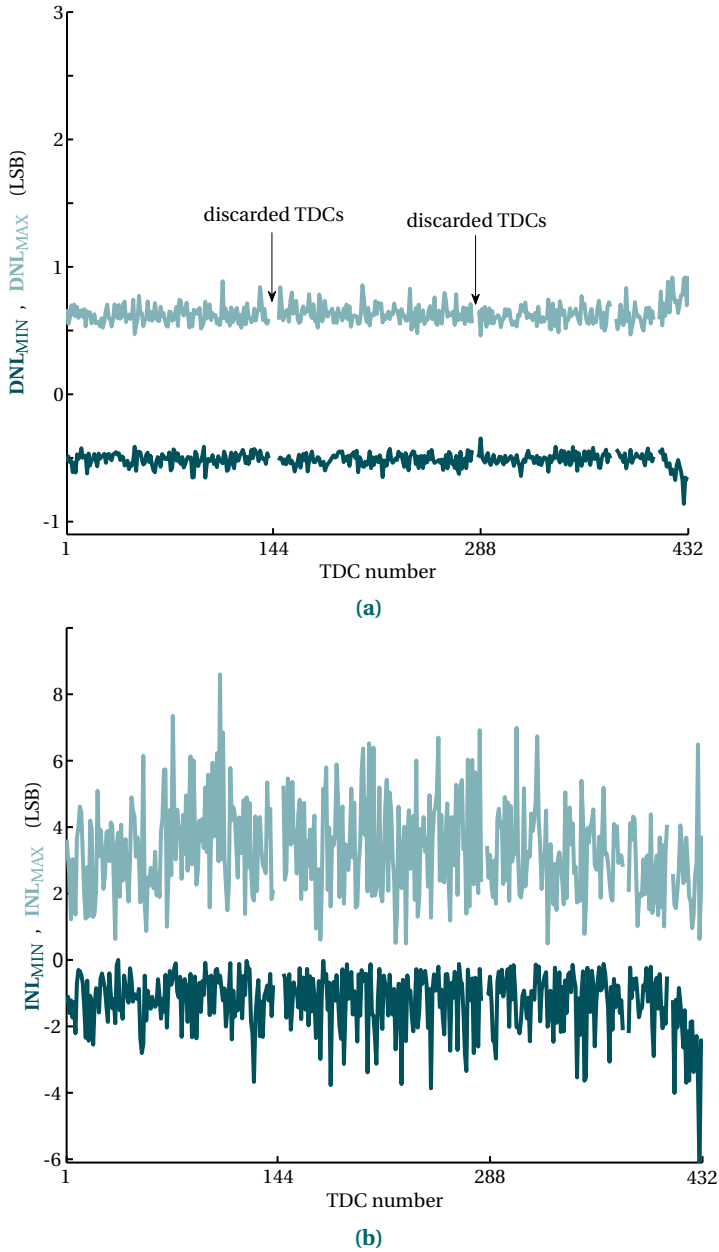


Figure 5.19: Minimum and maximum DNLs and INLs of all the TDCs within a subrange of about 600 TDC bins, with randomized initial VCO phase. (a) minimum and maximum DNLs calculated when the initial VCO's state is randomized. (b) minimum and maximum INLs calculated when the initial VCO's state is randomized.

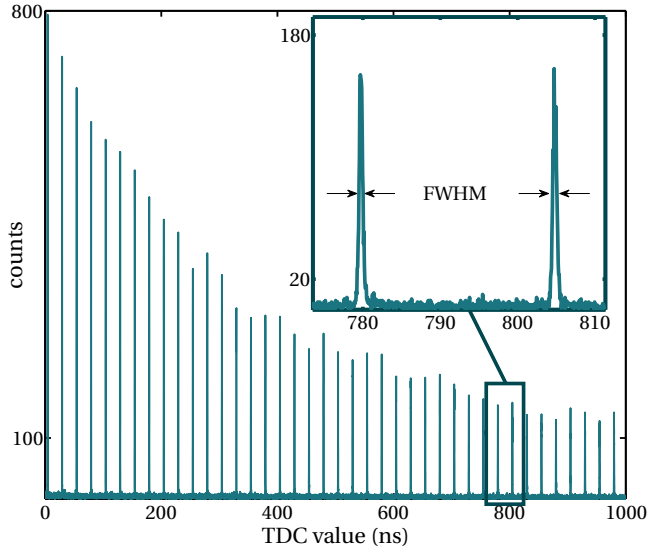


Figure 5.20: TDC timestamp histogram acquired in SPAD-camera readout mode when the photodetector is illuminated with a picosecond laser, which has a repetition rate of 40 MHz. The photodetector was illuminated at single-photon light level. The initial VCO phase was randomized and the VCO enable period was 1 μ s.

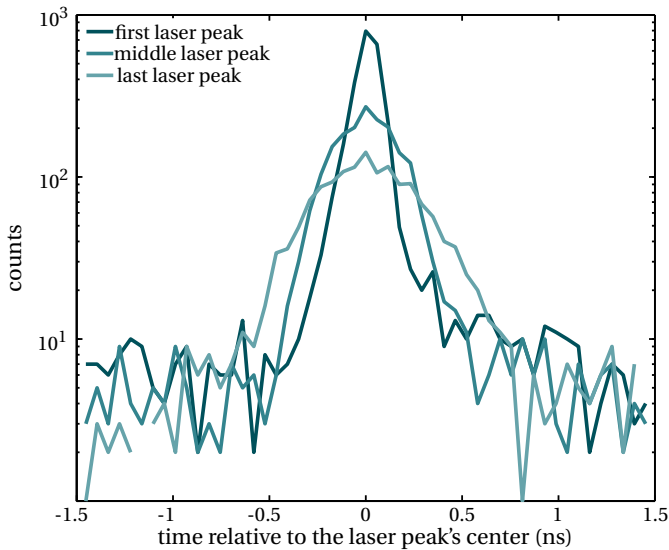


Figure 5.21: First laser peak, middle laser peak, and last laser peak plotted relative to the peak's center within the VCO enable period of 1 μ s.

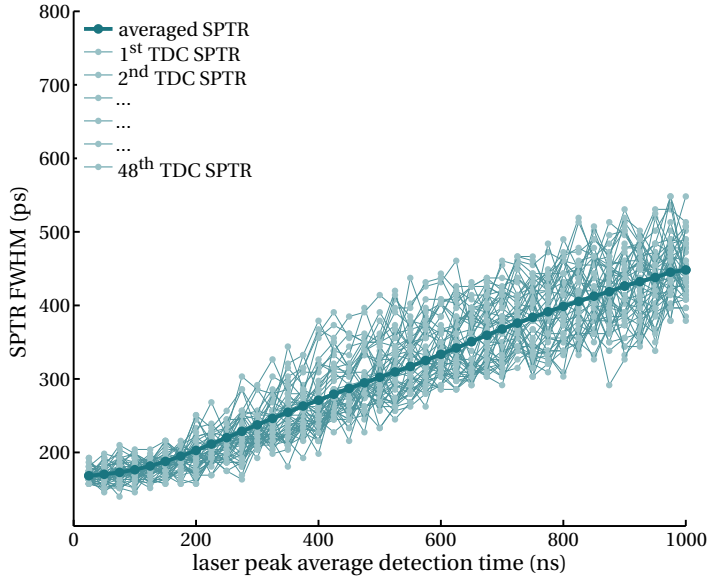
DNL. A calibration script acquired several SPAD-camera readout frames and calculated the DNL between the fine LSBs of all the TDCs. This step was repeated automatically by sweeping the TDC_REF voltage, SWBIASVCO, and SWBIASVCO. After finding the optimum settings for minimizing the DNL between the fine bits, a TDC density test was performed by acquiring several SPAD-camera readout frames that corresponded to dark counts. The histogram of TDC's timestamps of dark counts is not uniform since it follows an exponential behavior. Therefore, the DNL estimation was performed within a subrange of the TDCs' values that had a non-uniformity, due to exponential behavior, below 2 % and a width of about 600 TDC's contiguous values.

Figure 5.18a and Figure 5.18b shows the maximum and minimum measured DNLs and INLs for each TDC, respectively. In the previous measurement, the output of the clocked comparators that belongs to the replica TDC were never utilized in the calculations of the TDCs' value. Since, the STOP_DUM_B signal is already activated before enabling the VCO (see Figure 5.12a). Only, the replica TDC's coarse counter was utilized in order to measure length of the VCO period for estimating the TDCs' LSB size.

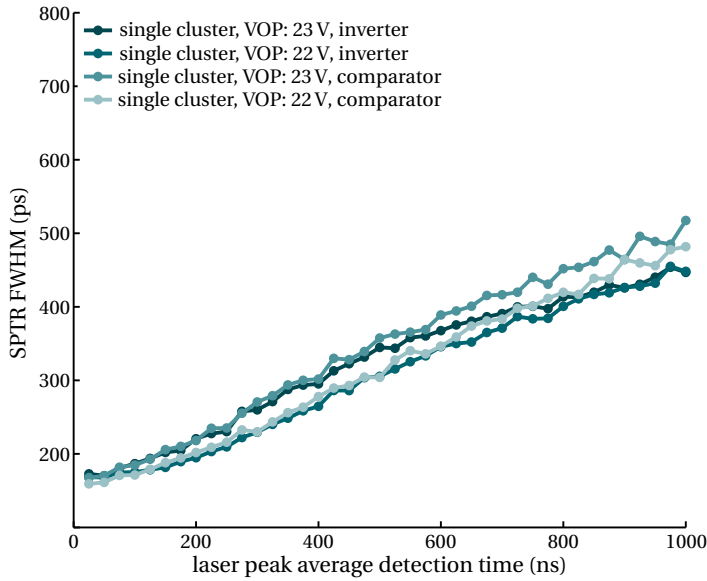
Later, we modified the TDC operation mode by, intentionally, not resetting the VCO at the beginning of the measurement frame (see Figure 5.12a). In addition, we kept the VCO running before enabling the STOP_DUM_B signal; therefore, the replica TDC captured the initial state of the VCO phase, which is randomized with respect to the previous frame. We subtracted the replica TDC's phase to all the TDCs' phases in order to compensate for not resetting the VCO. In this way, for different measurement frames, the same TDC time distance is measured in a different TDC bin. Subsequently, a drastic DNL reduction is achieved by randomizing the initial VCO phase (see Figure 5.19a). In the TDC characterization, some SPAD-cell columns were discarded since the particular utilized photodetector assembly had disconnected masking circuits, due to wire-bonding failure (see Figures 5.18 and 5.19).

By just considering the worst-case TDC, the maximum and minimum DNL was +3 LSB and -1 LSB, respectively, when utilizing a fixed initial VCO phase. In addition, the maximum and minimum DNL was +0.92 LSB and -0.86 LSB, respectively, when utilizing the randomized initial VCO phase. We also calculated the maximum and minimum INLs for all the TDCs, under the two previously explained operation modes (see Figures 5.18b and 5.19b). We did not observe an INL improvement between the two operation methods. However, in a coincident γ -photon detection experiment DNL influences more directly the CRT performance in comparison to INL. Because, the coincident γ -photons are detected within narrow time window in comparison to the total TDC range.

Finally, we performed two sets of SPTR characterizations utilizing the randomized initial VCO-phase method. In the first characterization, we enabled one single cluster and in the second one we enabled one complete cluster row. We exposed the 18×9 array to light pulses generated by the same picosecond laser utilized in the reset characterization. We placed a light diffuser between the NDF and the 18×9 array of MD-SiPMs in order to obtain a uniform light distribution over the photodetector activated area. We verified that the photon rate after subtracting the DCR was below 400 kHz, which is 1 % of the laser repetition rate, for assuring single-photon light level illumination. Figure 5.20 shows timestamp histogram of one TDC, which was acquired in SPAD-camera readout with randomized initial VCO phase, when only one cluster is activated. We opened the

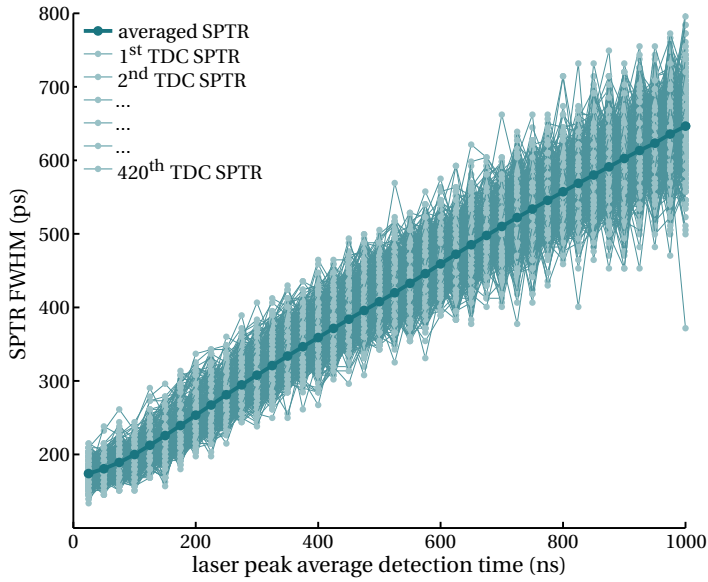


(a)

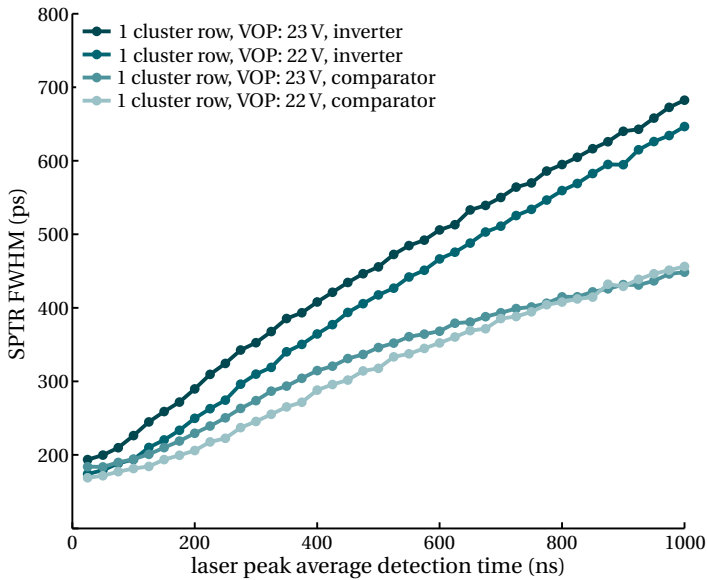


(b)

Figure 5.22: Single cluster's SPTR FWHM as a function of the laser peak average detection time, for several MD-SiPM settings. (a) When a single cluster is activated, the timing lines were sampled by high-threshold inverters and the V_{OP} voltage was set to 22 V. In this measurement 48 TDCs were activated, every light-green curve corresponds to a single TDC and the dark-green curve corresponds to the averaged performance. (b) averaged performance when a single cluster is activated, for several V_{OP} voltages and timing line sampling circuits.



(a)



(b)

Figure 5.23: Cluster row's SPTR FWHM as a function of the laser peak average detection time, for several MD-SiPM settings. (a) SPTR FWHM when a cluster row is activated, the timing lines were sampled by high-threshold inverters and the V_{OP} voltage was set to 22 V. In this measurement 420 TDCs were activated, every light-green curve corresponds to a single TDC and the dark-green curve corresponds to the averaged performance. (b) averaged performance when a cluster row is activated, for several V_{OP} voltages and timing line sampling circuits.

VCO enable period during $1\ \mu\text{s}$ in order to capture several laser peaks. Figure 5.21 shows the overlap of the first measured laser peak, a laser peak measured in the middle of the VCO enable period, and the last measured laser peak, where an increasing SPTR FWHM is observed.

We extracted the SPTR FWHM from the TDCs' histograms of every laser peak captured within the VCO enable period of $1\ \mu\text{s}$ (see Figure 5.20). In the first SPTR characterization only 48 TDCs were enabled since a single cluster was activated. Figure 5.22a shows the SPTR FWHM as a function of the average laser peak detection time. Also, we measured the average performance for several MD-SiPM settings (see Figure 5.22b). We performed the same analysis for the second SPTR characterization, where 420 TDCs were enabled since one complete cluster row was activated (see Figures 5.23a and 5.23b).

The increasing FWHM as a function of the laser peak average detection time is observed in all of the SPTR characterizations (see Figures 5.22 and 5.23). The reason why the SPTR performance degrades is due to timing jitter accumulation in the VCO, which is a free-running oscillator [4]. The best performance was obtained when sampling the timing line with the comparator, in which its reference voltage was set to 3.2 V and timing line pull-up voltage was V_{DDA} set to 3.3 V.

5

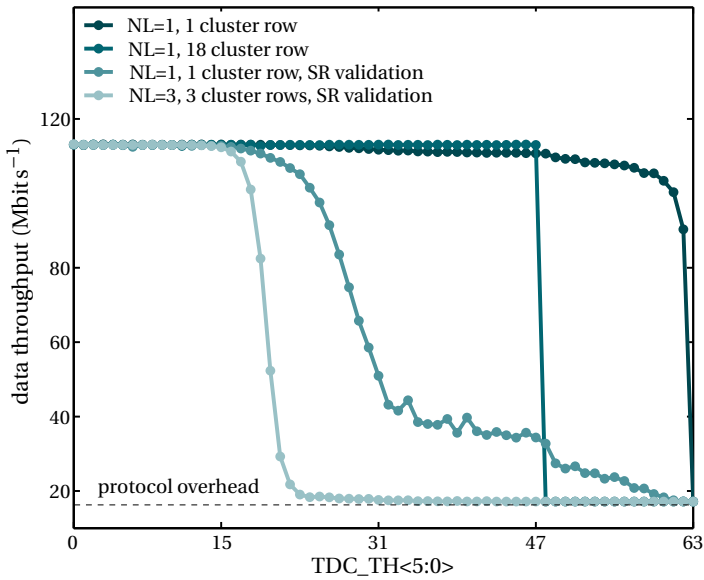
5.2.3. CHARACTERIZATION OF THE SR LOGIC

The SR logic operates in the D-SiPM readout mode in order to detect a minimum number of activated TDCs per cluster column (see Figures 5.12b and 5.13). The adder within the SR module is implemented as a pure combinational circuit, in which its output is sampled by a sequential comparison logic that is synchronous with respect to the readout clock. The detection of a light photon or dark count is an asynchronous event with respect to the readout clock; therefore, the outputs of the SR adder can potentially change within the setup and hold times of the inputs of the sequential comparison logic. In addition, since the adder outputs are not glitch-free logic, they could be sampled when their values are not stable yet.

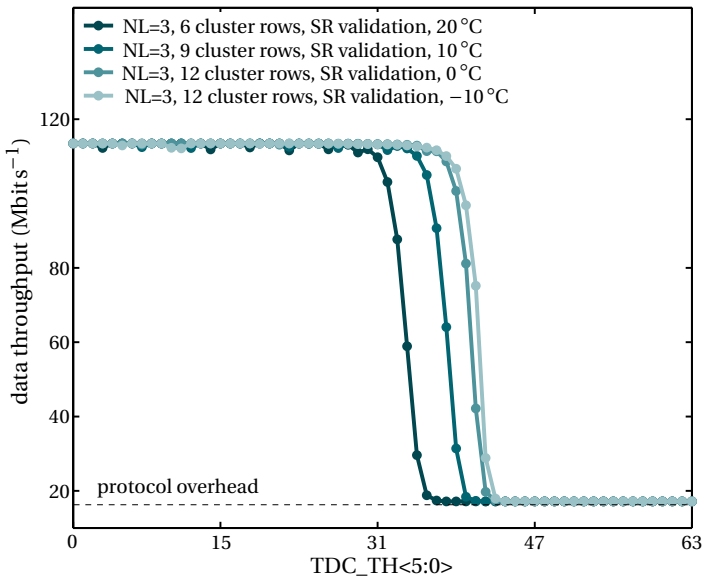
When any of the ENEMONITOR<0:8> bits are activated, the FPGA stops the VCO enable period and starts a readout sequence. If the photodetector is light-shielded the dark counts activates few TDCs that could eventually trigger a readout sequence depending on the preconfigured TDC_TH value. Subsequently, for low values of TDC_TH the readout data throughput increases due to presence of dark counts. If the photodetector is coupled to a scintillator and exposed to radioactivity, when the TDC_TH value is high enough the dark counts cannot trigger a readout anymore. And, only a scintillation event can activate a number of TDCs that is larger than the preconfigured TDC_TH value. In order to study the effects of the asynchronous nature of the STOP signals on the SR logic, we performed a SR characterization by activating different array areas and sweeping the TDC_TH<5:0> value (see Figure 5.13).

In the first test, we activated one complete cluster row and performed one acquisition per configured TDC_TH<5:0> (see Figure 5.24a). Since there are only 48 TDCs per cluster column, the data throughput must drop to its overhead value, which is around $18\ \text{Mbits}^{-1}$, when TDC_TH<5:0> is greater than 47. However, we observed large data throughputs even for TDC_TH values what were larger than 47 (see Figure 5.24a).

Next, we activated all the cluster rows and we observed that the data throughput



(a)



(b)

Figure 5.24: SR characterizations result. Photodetector data throughput as a function of the TDC_TH<5:0> value. (a) for several D-SiPM readout settings. (b) for several temperatures and increasing number of activated cluster rows.

behaved as expected (see Figure 5.24a). Subsequently, we concluded that when we activated all the rows, the DCR count rate was high enough to immediately pull down all the timing lines (see Figure 5.13). Therefore, the SR logic sampled the STOP signals when they were already stable without changing during the setup and hold times of the synchronous comparison logic. However, when we activated only one cluster row, the STOP signals are changing constantly during the VCO enable period. Thus, they are unstable and could be sampled during the metastable window of the synchronous comparison logic. That is the reason why the ENEMONITOR bits had incorrect values, which are failed comparisons since the maximum number of TDCs per cluster column is 48.

Later, we modified the FPGA firmware (FW) in order to perform an ENEMONITOR validation sequence. In the modified FW version, after reading out an ENEMONITOR value that indicated that any cluster rows had more TDCs activated than the TDC_TH value, we reset the SR module and read out again the ENEMONITOR value. Then, we compared the initial ENEMONITOR to the second read out ENEMONITOR, and if they did not match we started a new readout frame without triggering a full photodetector readout. In this way we could detect if the ENEMONITOR value was invalid due to combinational logic' glitches or metastable comparison outputs. Figure 5.24a shows the TDC_TH scan result when the SR validation mechanism is activated, where the ENEMONITOR incorrect values were drastically mitigated.

Later, we performed a second readout addition, which we called it the neighbor logic (NL) validation. We assumed that the photodetector could be coupled to an array of scintillators that are larger than the cluster pitch of 0.8 mm. For instance, the 18×9 array of MD-SiPMs could be coupled to a scintillator array of 6×3 LYSO pixels of 2.4 mm pitch. In this case, if a γ -photon hits one LYSO pixel the scintillation light activates three continuous bits of ENEMONITOR. Subsequently, the readout FPGA triggers a full photodetector readout only if a configurable number of ENEMONITOR's continuous bits is activated. We performed a fourth TDC_TH scan when the NL continuous bits was set to three, in which three cluster rows were activated, and the SR validation was also activated. In this final TDC_TH scan, we observed a correct behavior of the TDC_TH value as a function of the data throughput, which drops to the communication overhead value of about 18 Mbit s⁻¹ (see Figure 5.24a).

Finally, we investigated the maximum number of cluster rows that can be activated that allowed to have free TDCs for γ -photon detection. In this D-SiPM architecture, in which the TDCs are shared column-wise, the DCR at the input of the TDCs depends on how many cluster rows are activated. Therefore, we performed further TDC_TH scans when the photodetector was placed inside a light-shielded temperature chamber (Vörsch VTM-7004). We carried out several acquisition at different chamber temperatures and number of activated cluster rows. During this characterization the NL was set to three continuous bits, the SR validation was also activated, 20 % of the SPAD cells were masked, and the excess bias voltage was 2.5 V. The TDC_TH scans performed at several temperatures are shown in Figure 5.24b. We set the number of activated cluster rows to a limiting value that allowed to have few free TDCs for γ -photon detection. Table 5.1 shows the summary of the previous characterization.

We concluded that the SR validation, which verified two times the ENEMONITOR bits in two consecutive readouts, and the NL, which checks continuous ENEMONITOR

Table 5.1: Temperature chamber measurement summary.

chamber temperature (°C)	+20	+10	0	-10
TMP104 temperature (°C)	+35	+26	+17	+6
SPAD-cell's mean DCR (kcps)	34.15	23.99	16.76	12.38
SPAD-cell's median DCR (kcps)	14.84	11.45	9.30	7.96
V_{OP} (V)	22.03	21.97	21.86	21.74
V_{BD} (V)	19.53	19.47	19.36	19.24
maximum activated cluster rows	6/18	9/18	12/18	12/18

activated bits, are an efficient way to mitigate the effects caused by the asynchronous nature of the STOP signals. In addition, we concluded that the maximum number of cluster rows we could activate was 12, when the photodetector is operated within an environment at 0 °C. Decreasing the environment temperature below 0 °C does not allow to further increase the activated number of rows, since the DCR does not reduce significantly. For SPADs implemented in the same technology, we observed that the DCR triggering mechanism is dominated by quantum tunneling below 10 °C [5].

5.3. CHARACTERIZATION SUMMARY

We presented a comprehensive analysis and characterization performed on the 18×9 array of MD-SiPMs. The SPAD-cell array reset was implemented by a modulated signal, which allowed the proper recharge of a large number of SPADs with a relatively high DCR. We carried out a PDE measurement directly on the SPAD-cell array, in order to verified the achieved 57 % FF [1].

We developed an alternative method to operate the TDCs in order to reduce the DNL drastically. This method befits time-correlated single photon counting (TCSPC) measurements, such as SPTR. However, in γ -photon coincidence measurements the asynchronous nature of the radiation detection performs an intrinsic DNL reduction. We observed a significant timing jitter accumulation within the free-running common VCO, which limits the maximum time in which the reference phase needs to be re-latched. The best SPTR performance was obtained when the timing lines are sampled by the comparator circuit. The full simulations TDC operation was also verified.

The event-driven discrimination circuit is an essential block of D-SiPMs. The γ -event detection circuit, which is called SR, showed unstable behavior when detecting the amount of fired TDCs, due to the asynchronous nature of the timing lines with respect to the readout clock. This effect was corrected by applying a subsequent SR validation cycle and implementing the NL triggering scheme. In the event-driven mode, the maximum number of activated cluster rows, which was 12 at 0 °C with 2.5 V excess bias voltage, was limited by the SPAD-cell dark count rate. Further decrease in temperature did not reduce the DCR since the dominant DCR mechanism below 0 °C was quantum tunneling [5].

REFERENCES

- [1] S. Mandai, *Multichannel Digital Silicon Photomultipliers for Time-of-Flight PET* (Delft University of Technology, 2014).
- [2] S. Mandai, V. Jain, and E. Charbon, *A fully-integrated 700x800 μm^2 multi-digital silicon photomultiplier with column-parallel time-to-digital converter*, in *ESSCIRC (ESSCIRC), 2012 Proceedings of the (2012)* pp. 89–92.
- [3] J. G. Maneatis, *Low-jitter process-independent DLL and PLL based on self-biased techniques*, *IEEE journal of solid-state circuits* 31, 1723 (1996).
- [4] J. A. McNeill, *Jitter in ring oscillators*, *IEEE Journal of Solid-State Circuits* 32, 870 (1997).
- [5] I. M. Antolovic, S. Burri, C. Bruschini, R. Hoebe, and E. Charbon, *Nonuniformity Analysis of a 65-kpixel CMOS SPAD Imager*, *IEEE Transactions on Electron Devices* 63, 57 (2016).

6

MD-SiPM PET SYSTEM INTEGRATION

Part of this chapter is under preparation for submission as “Esteban Venialgo, Shingo Mandai, and Edoardo Charbon. MD-SiPMs: Individual Building Block and Full-System Comprehensive Analyses. IEEE Journal of Solid-State Circuits, 2019”.

This chapter describes the design challenges of integrating MD-SiPMs into real PET detectors. Particularly, it gives a detailed account of detector miniaturization, scintillator's attachment, and D-SiPM readout strategies.

We performed a gradual integration, by starting preliminary tests with MD-SiPMs bonded into CPGA packages. Next, we moved on designing a compact chip-on-board assembly that served as a core for miniaturized PET detector modules. Finally, we implemented two PET modules:

- small-animal PET detector,
- and endoscopic PET detector.

In the first radiation characterization that was ever made with MD-SiPMs, we utilized a 18×9 array of MD-SiPMs that was bonded into a CPGA package (see Figure 6.1) [1]. The CPGA package was placed on a socket that was soldered to a testing board. The testing board had a square hole in order to physically access the photodetector for gluing scintillators. This board was interfaced with a ML-507 FPGA kit, which was connected to a high-speed acquisition board [2, 3].

We glued an LYSO scintillator of $3 \times 3 \times 10 \text{ mm}^3$, which was wrapped with teflon tape, utilizing the LS6257 NuSil glue. In this measurement, we utilized a ^{22}Na radioactive source, which had an activity of $150 \mu\text{Ci}$. We operated the photodetector in SPAD-camera readout mode and off-line calculated the addition of fired SPAD-cells within an area of 4×4 clusters. Figure 6.2 shows the obtained energy spectrum in semi-logarithmic scale, where a large DCR peak is observed, since the SR was disabled. Figure 6.3 depicts the energy spectrum after subtracting the DCR peak mean value, which was about 250 fired SPAD cells. We did not correct for SPAD-cell saturation since the amount of fired cells was about 10 % of the total cells within the area of 4×4 clusters. The obtained energy resolution was 15.7 % at 511 keV.

Next, we designed a miniaturized and cost-effective assembly based on a chip-on-board approach (see Figure 6.4). Besides the wire-bonded photodetector, the assembly contains two temperature sensors TMP104 mounted on the top and bottom layers, power decoupling capacitors, and board-to-board connectors (100-pins Hirose DF40). Also, there is a square hole placed in the assembly's center in order to insert a water-cooling device.

The advantage of building a small assembly was the modular approach that allowed to utilize it in different PET detector implementations. In addition, it was possible to test and verify the individual assemblies before building larger PET detectors. On the contrary, direct bonding of several dies of 18×9 arrays of MD-SiPMs would result into an impractical solution. Because the dies are untested and the module's production yield would be lowered drastically depending on the number of bonded dies.

The intrinsic packing fraction of the 18×9 arrays of MD-SiPMs is 80 % without considering the space for wire-bonding. The chip-on-board assembly has a packing fraction of 35 % because it includes power connection redundancies, extra temperature sensors and a conservative wire-bonding layout. In addition, the larger space allows a safe mechanical handling for insertion and withdrawal operations.

We decided to proceed with this version of the chip-on-board assembly for the testing and characterization phases, before performing a packing fraction optimization

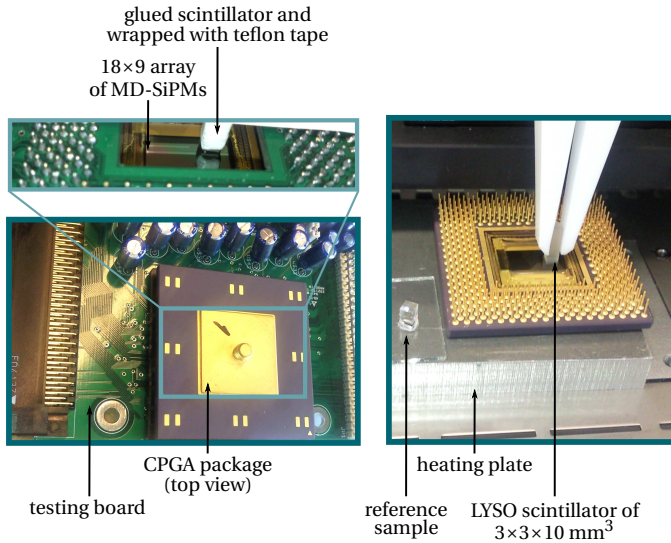


Figure 6.1: Photographs of the first radiation characterization measurement setup utilizing a CPGA-packaged 18×9 array of MD-SiPMs.

phase. When utilizing 80-pins DF40 connectors by eliminating redundant power connections, removing the central square hole, and optimizing the wire-bonding layout, it is possible to increase the packing fraction up to 70 %.

6.1. SMALL ANIMAL PET DETECTOR

The small-animal PET detector was composed of 4×1 monolithic arrays of MD-SiPMs (see Figure 6.5). The 4×1 motherboard can allocate up to four chip-on-board assemblies and includes all the required LDOs, which are adjustable by utilizing digital potentiometers (TPL0501). Additionally, this board has three extra 100-pin board-to-board headers on the back to connect a miniaturized controller FPGA board. This board requires 250 digital inputs/outputs (I/Os) in order to control independently the four monolithic arrays of MD-SiPMs; therefore, a board based on an FPGA packaged in a CSG484 device fulfill all the system requirements [4].

The advantage of having digital potentiometers on board is that we were able to apply automatic bias voltage sweeps for optimizing the photodetector performance, such as a TDC_REF sweep for TDC's DNL reduction (see Figure 5.18). Also, we could adjust the power supplies to reduce power consumption in case of continuous operation. In addition, we could monitor the temperature of each individual monolithic arrays of MD-SiPMs from the FPGA by reading the TMP104 temperature sensors (see Figure 6.4 and Table 5.1).

For the testing and characterization phases, we utilized a standard XCM-206Z-LX75 board, instead of a custom miniaturized board based on a CSG484-FPGA, in order to rely on a tested FPGA device (see Figure 6.6) [5]. We designed a custom FPGA interface

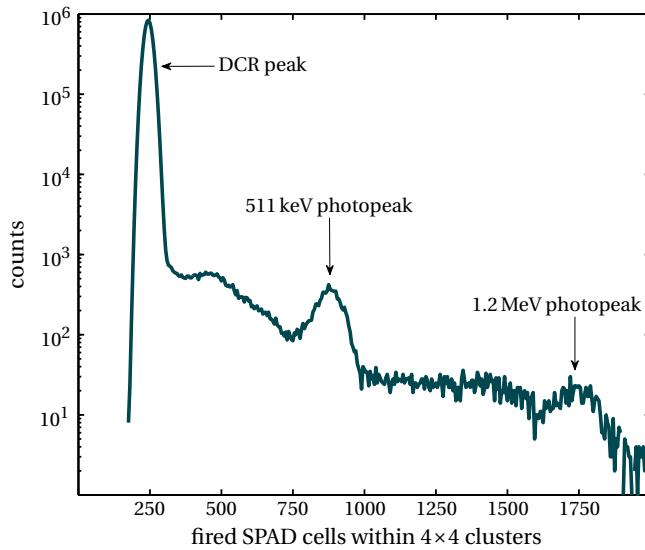


Figure 6.2: First energy characterization of the MD-SiPM, which was acquired in SPAD-camera mode, with a LYSO scintillator of $3 \times 3 \times 10 \text{ mm}^3$ and exposed to a source of ^{22}Na , which had an activity of $150 \mu\text{Ci}$.

6

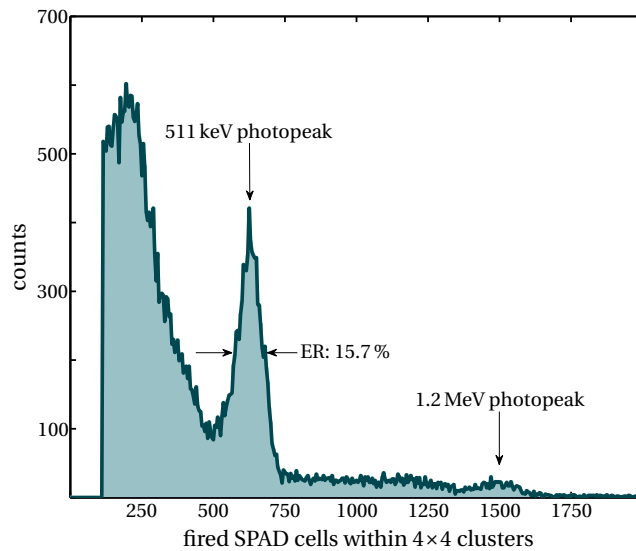


Figure 6.3: Energy spectrum of the MD-SiPM with subtracted DCR peak.

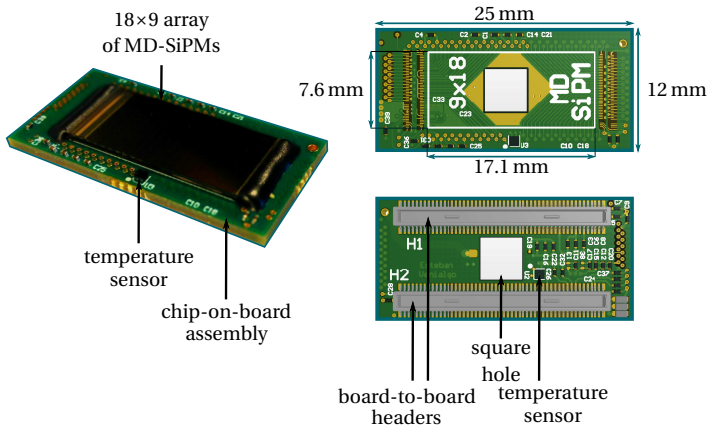


Figure 6.4: Chip-on-board detailed assembly. Assembly photograph (left) and rendered design images (right).

that was placed between the XCM-206Z-LX75 and the 4×1 motherboard. Additionally, the custom FPGA interface also connects a high-speed USB controller board for data acquisition.

A clear advantage of this modular approach based on board-to-board stacking is that a failed part can be replaced immediately. Additionally, the scintillator array attachment was performed independently on each chip-on-board assembly. Furthermore, we tested several scintillator pixel's sizes by just inserting and removing different chip-on-board assemblies, which had a different LYSO matrices attached on them.

Finally, we utilized just a simple fan to cool down the 4×1 monolithic arrays of MD-SiPMs to a stable temperature of about 40°C . If no cooling was provided, we observed a slow positive thermal feedback that could reach a temperature of above 100°C [6]. Also, we tested a water-cooling device based on a 3D-printed frame and its performance was comparable to the simple fan approach [6]. However, for endoscopic-PET applications only liquid-cooling based systems meet the spatial constrains required by the application.

6.1.1. DETAILED FIRMWARE DESCRIPTION

We performed a full FW replacement, in order to operate the 4×1 module, with respect to the previous version [1]. The new FW development followed a design methodology that was based on:

- full synchronous design (including modules' resets and the MD-SiPM interfacing),
- modular design for code re-utilization,
- individual skew adjustment with ODDR2 and ODELAY2 components to assure FW reproducibility,
- and single clock domain except for the USB-FIFO controller and low-speed SPI peripherals.

The FW detailed block diagram is shown in Figure 6.7. The FW is designed to receive

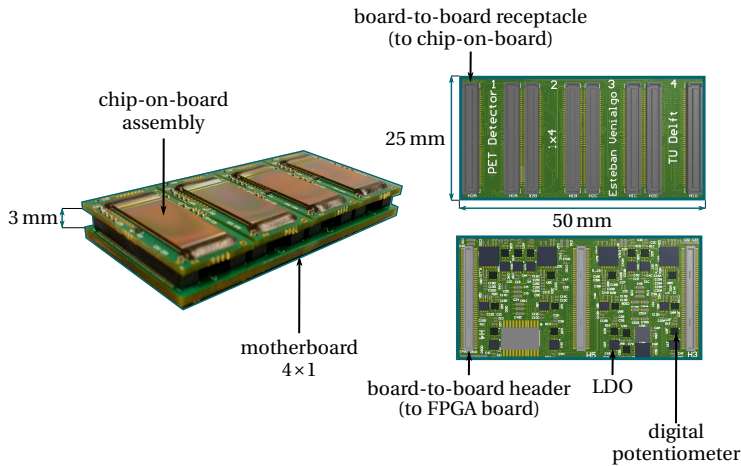


Figure 6.5: Motherboard 4×1 detailed assembly. Assembly photograph (left) and rendered design images (right).

a sequence of commands through the CONF_TX and CONF_RX signals, which connects the FW’s configuration module to an acquisition computer. The commands are generated by a script that produces the corresponding serial-protocol sequence, which is decoded by the configuration module. In this way, the system is highly adaptable to any calibration or acquisition sequences since it is directly programmed from high-level scripting.

The possible commands are the followings:

- send MD-SiPM configuration and masking information to the FPGA,
- load the stored configuration and masking information into the MD-SiPM number N,
- read the temperature sensor daisy chain,
- program a value into a specific power supply or bias voltage,
- read out K SPAD-camera frames from the MD-SiPM number N,
- read out K D-SiPM frames from the MD-SiPM number N,
- and stop the current readout sequence.

The PLL and reset module generates a synchronous reset for all of the FW modules in addition the clock signals. The voltage controller generates the SPI sequence and address to program a specific TPL0501 by utilizing a slower clock (CLK_SLOW); therefore, this module is considered as being in a separated clock domain. The temperature readout module is in charge of reading the daisy chain of TMP104s, and send the temperature values to the acquisition computer through the configuration module.

There is a separated logic to control each array of MD-SiPM that is connected to the motherboard 4 × 1 module (see Figure 6.7). The MD-SiPM controller interprets the decoded commands and their corresponding data, which is relevant to the MD-SiPM operation, and executes them by controlling the MD-SiPM configuration, SPAD-camera readout, and D-SiPM controller modules.

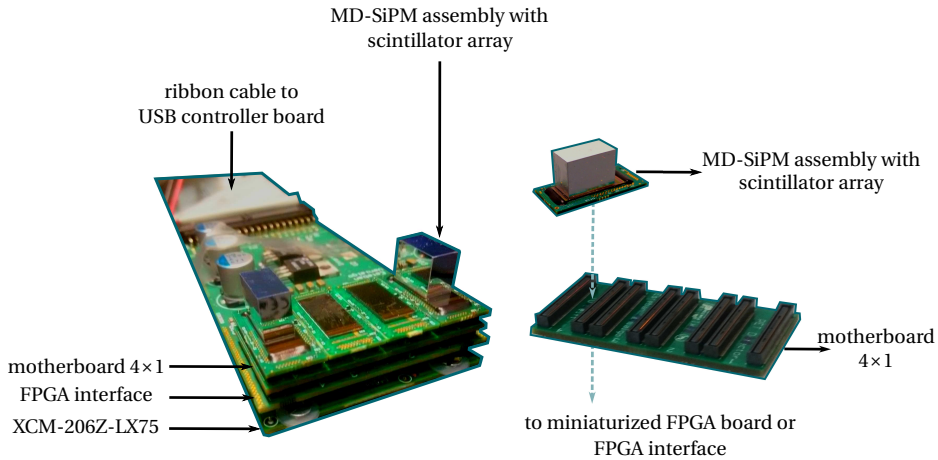


Figure 6.6: Photographs of the full detector setup. Full assembled detector (left) and individual parts (right).

The I/Os, which actually interfaces the array of 18×9 MD-SiPMs, of the individual MD-SiPM controller modules are multiplexed and registered by the I/O controller (see Figure 6.7). Additionally, the I/Os connected to the photodetector are registered by an ODDR2 or IDDR2 FPGA component and their skews is adjusted by an ODELAY2 or IDELAY2 FPGA component [7]. There is a specific skew adjustment for each location of the motherboard 4×1 . In this way, any FW modifications does not change the skews between the MD-SiPM I/O signals. Furthermore, the CLK_FAST signal, which has three times higher frequency than the CLK_GLOBAL signal, is utilized to generate the modulated reset signal (see subsection 5.2.1).

Since the array of 18×9 MD-SiPMs is a prototype design, the digital I/O switching characteristics are not thoughtful measured. Therefore, it is desirable that once the FPGA I/Os skews are adjusted they do not change during subsequent FW placing and routing iterations, which are required during the FW development cycle. It is important to notice that the array of 18×9 MD-SiPMs has four independent clocks to operate the integrated modules, which are the SR, the readout logic, the configuration module, and the cell-out registers (see Figure 6.7). The integrated configuration module of the array of 18×9 MD-SiPMs allows to send testing data that is read out through the readout logic. Therefore, the skews were adjusted by sending and reading out testing data and verifying that the error rate was exactly 0 %.

The individual MD-SiPM controller modules within the FW send the acquired TDC and SPAD-cell information, through the USB controller module, to the acquisition computer (see Figure 6.7). This module is partitioned into two clocks domains since the USB controller board, which contained a USB-FIFO device (FT2232H), generates its own FIFO writing clock [8]. The USB controller's timing requirements are set by FW constraints instead of adjusting skew with ODELAY2 FPGA components, since the switching characterizations are fully reported within its datasheets [8]. Additionally, we input an

FPGA-PLL with the CLK_FTDI signal, which was set with a negative phase in the output clock, in order to meet the timing constraints.

Finally, there is an acquisition mode called master/slave that allows to perform coincidence measurements within the same motherboard 4×1 (see Figures 6.7). For example, the coincidence measurement performed between 18×9 MD-SiPMs placed in the slots 1 and 4 utilized the master/slave acquisition mode (see Figure 6.9).

6.1.2. RADIATION CHARACTERIZATION

We attached three types of LYSO scintillator matrices to the MD-SiPMs, which had a pitch of 2.4 mm, 1.6 mm, and 0.8 mm (see Figure 6.8) [6]. Additionally, the radiation characterization was performed utilizing the motherboard 4×1 (see Figure 6.9) [6].

During the γ -energy and CRT characterizations, the slots 1 and 4 were occupied by the chip-on-board assemblies that were coupled to the scintillator matrices of 2.4 mm pitch. In order to read out the temperature values from the TMP104, all the motherboard 4×1 's slots must be populated with MD-SiPM assemblies. Subsequently, we paced two dummy boards that also had a TMP104 sensor in order to close the daisy chain loop. We placed a fan to circulate an air flow in order to keep the operating MD-SiPMs at a temperature of 38 °C. We utilized a ^{22}Na source during the energy and CRT characterizations that had an activity of 25 μCi .

6

6.1.3. γ -ENERGY CHARACTERIZATION

During the γ -energy characterization, we placed the ^{22}Na on top of one of the 6×3 LYSO scintillator matrices of 2.4 mm pitch, and performed two acquisitions, one with SR disabled and a second one with SR enabled. In both case we read out the individual SPAD-cell values, and performed the energy estimation off-line. Additionally, we captured individual scintillations utilizing the chip-on-board assemblies with attached scintillator matrices of 0.8 mm and 1.6 mm pitch (see Figure 6.10 and 6.11).

When the SR was disabled, we measured 150 GB of data in SPAD-camera mode during 3.65 h, and the VCO enable period was set to 1 μs . Most of the measurement frames contained only dark counts and few frames captured individual scintillations (see Figure 6.12). We estimated for each individual data frame the amount of fired SPAD cells below each LYSO scintillator pixel and calculated the energy histograms (see Figure 6.13a).

Next, we enabled the SR and performed the readout in SPAD-camera mode by reloading the MD-SiPM configuration memory at the beginning and end of each measurement frame. In this characterization, we activated four cluster rows in order to avoid the SR saturation at room temperature (see table 5.1). Figure 6.13b shows the energy spectra that corresponds to three LYSO pixels that are below the activated cluster rows. When SR is enabled the DCR peaks are reduced drastically since only scintillation events are transferred to the FPGA. Additionally, this measurement was performed in 104 s and we acquire 1 GB of data.

6.1.4. CRT CHARACTERIZATION

In the CRT characterization, we placed the ^{22}Na source between the two LYSO scintillator arrays in order to detect coincident γ -photons (see Figure 6.9). In this measurement, we

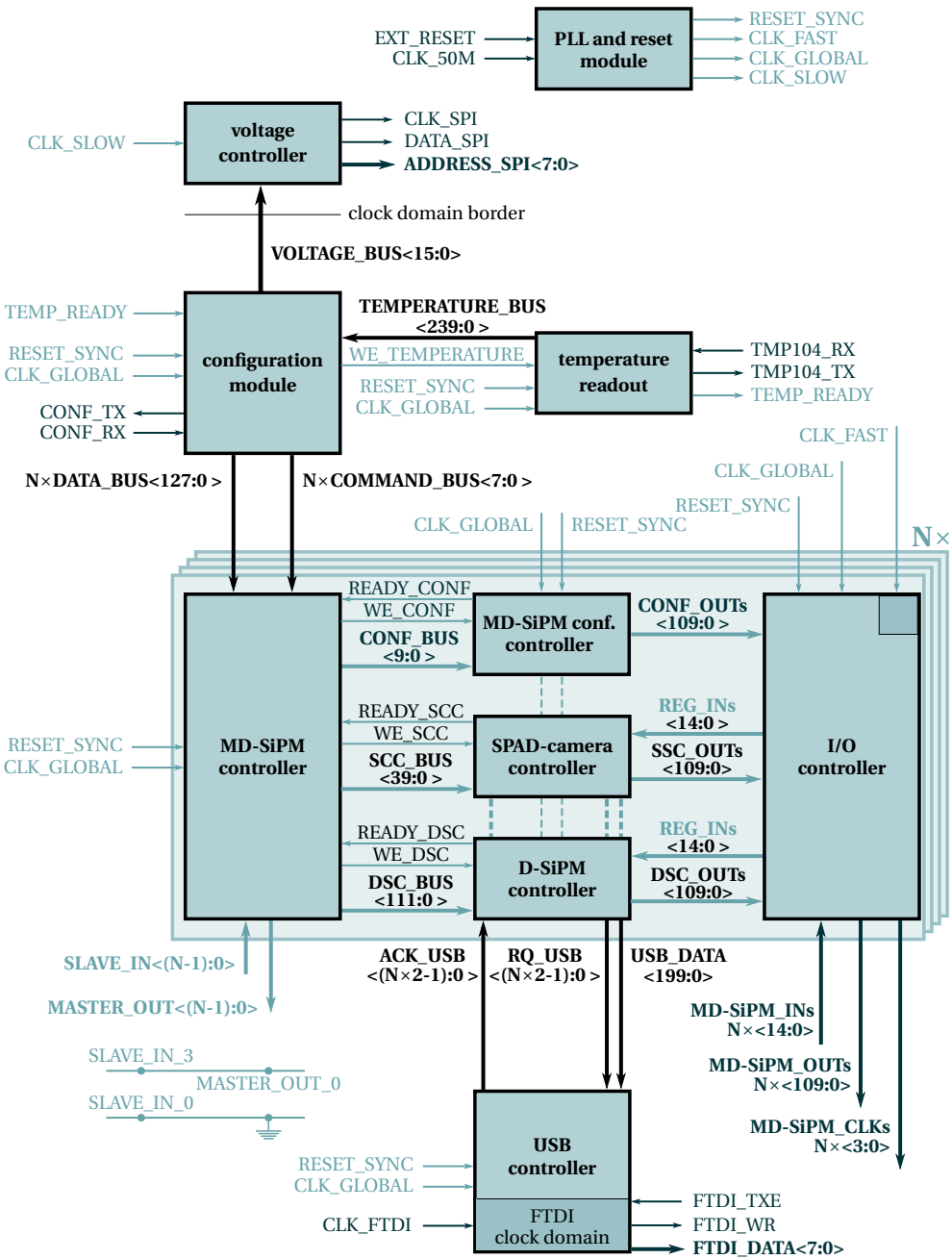


Figure 6.7: Detailed FW block diagram.

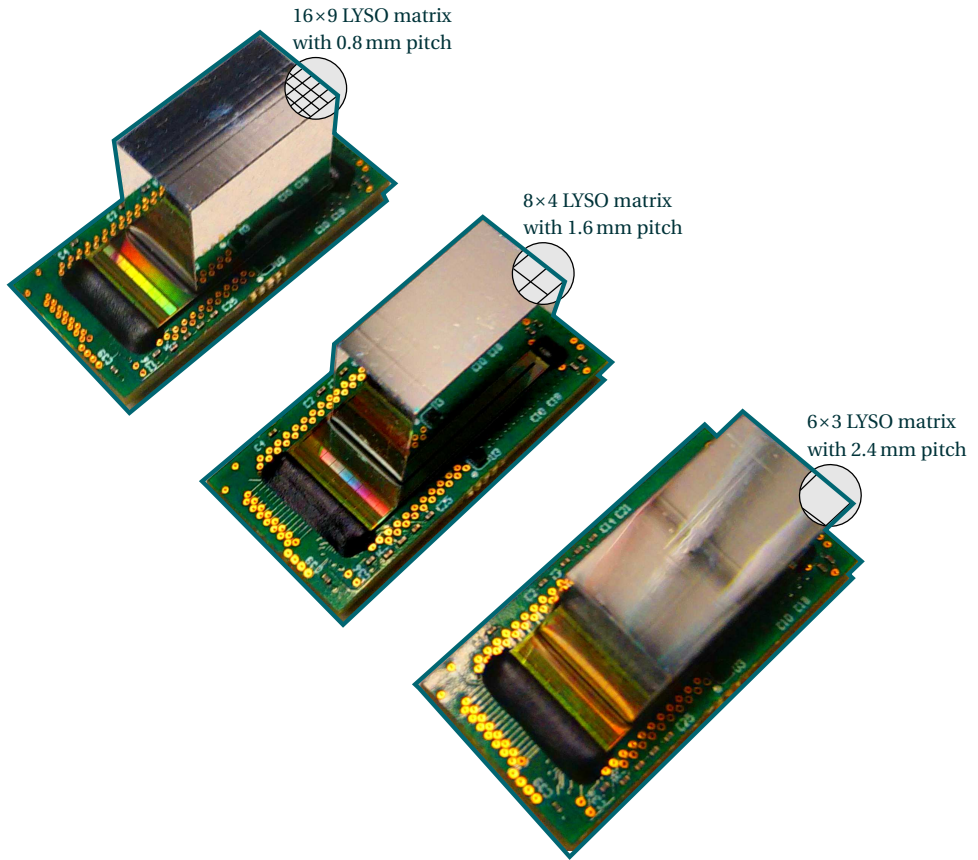


Figure 6.8: Pictures of the scintillator matrices attached to chip-on-board assemblies.

activated 3×3 clusters as indicated in Figure 6.9. The acquisition was performed with SR enabled and SPAD-camera readout mode with the master/slave logic activated.

We calculated the γ -photon energy in the same way as in Figure 6.13b and filtered 511 keV photopeak by an energy window filter. Next, we sorted the timestamps and filtered the dark counts accumulated before the γ -detection took place (see Figure 6.14). The applied DCR filter was a time-distance dark count filter [9]. Later, we calculated the time distance between detectors' timestamps of the γ -events, by selecting the second timestamp as optimum γ -photon timemark. Figure 6.15 depicts the CRT histogram measured as second timestamp distances between the two detectors.

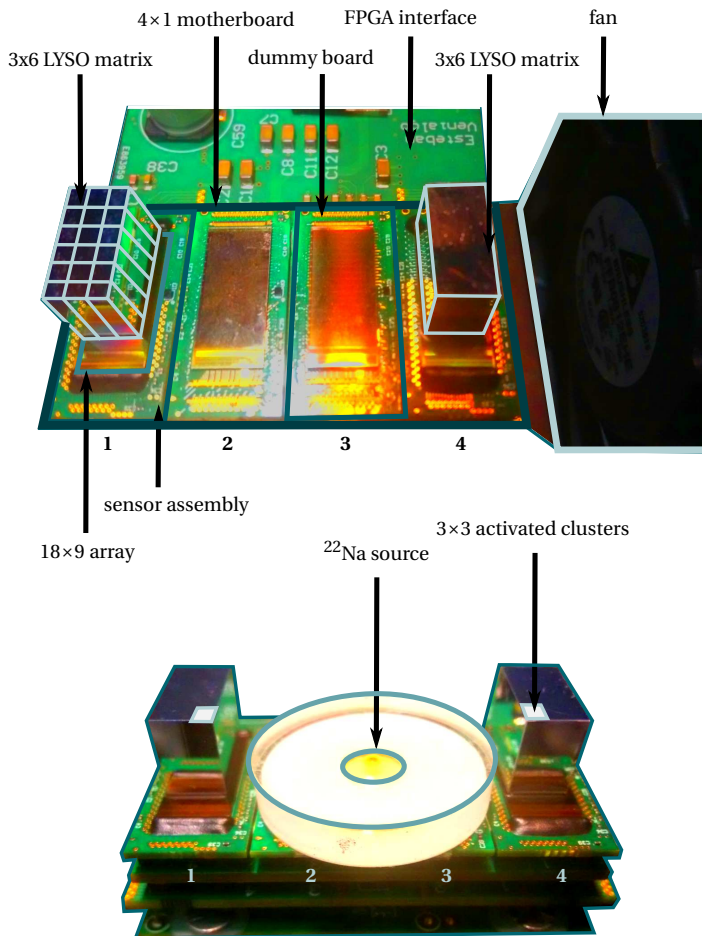


Figure 6.9: Photographs of the radiation characterization measurement setup.

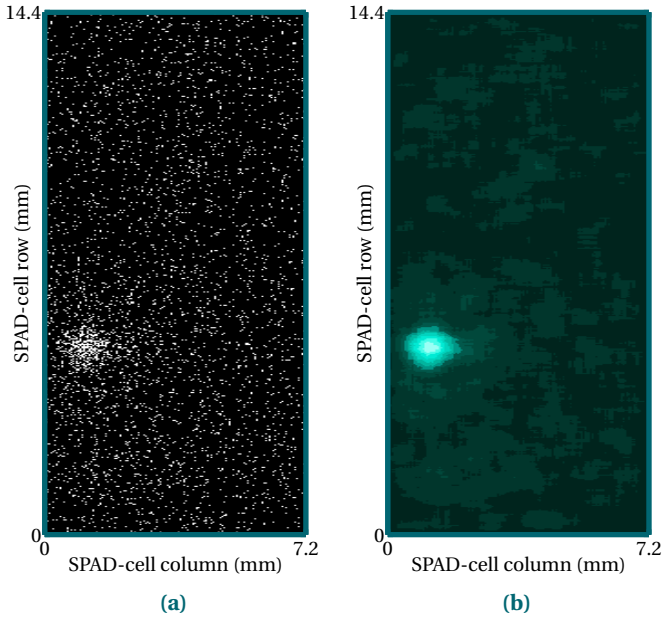


Figure 6.10: Scintillation captured in SPAD-camera mode utilizing the 16×9 LYSO matrix with 0.8 mm pitch. (a) raw data frame. (b) binary imaged post-processed with a 2D mean filter.

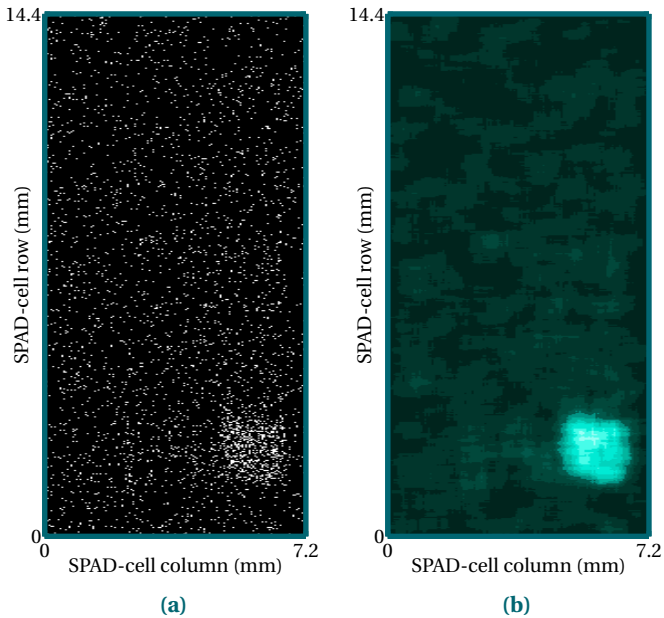


Figure 6.11: Scintillation captured in SPAD-camera mode utilizing the 8×4 LYSO matrix with 1.6 mm pitch. (a) raw data frame. (b) binary imaged post-processed with a 2D mean filter.

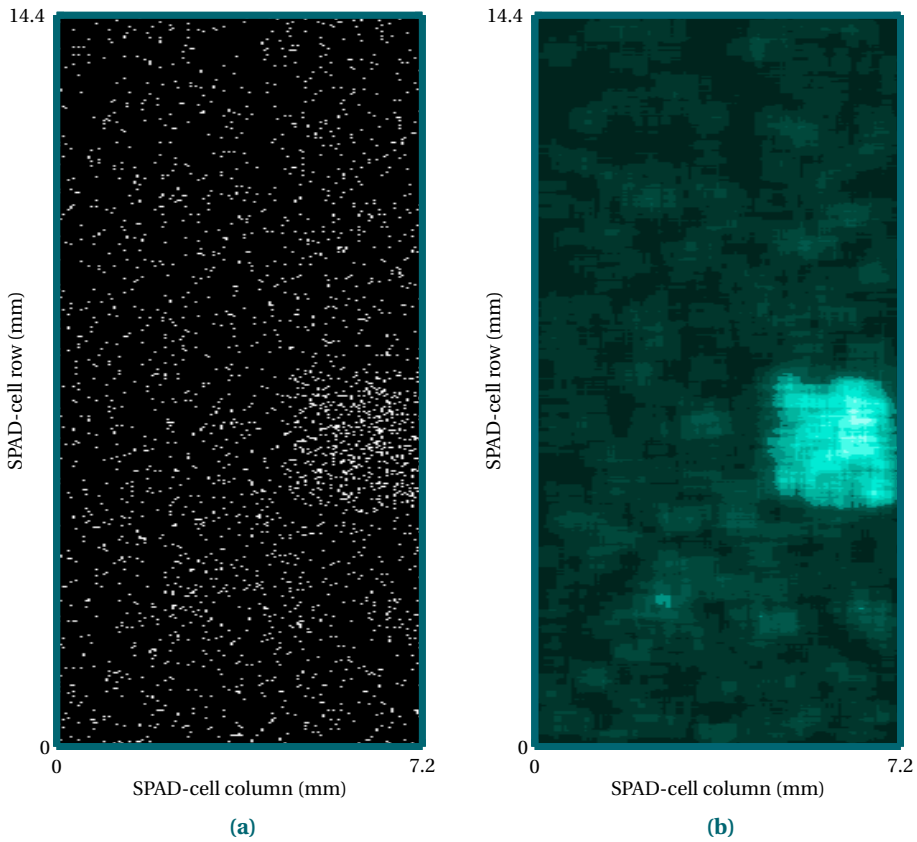
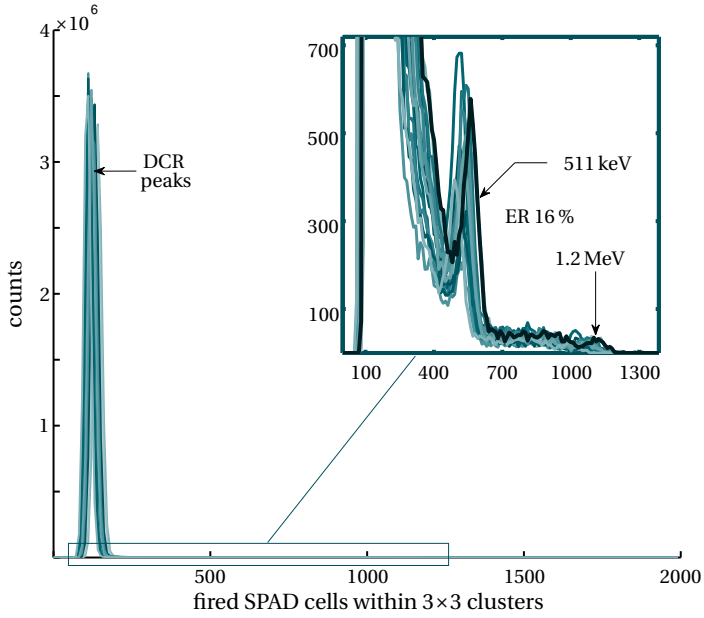
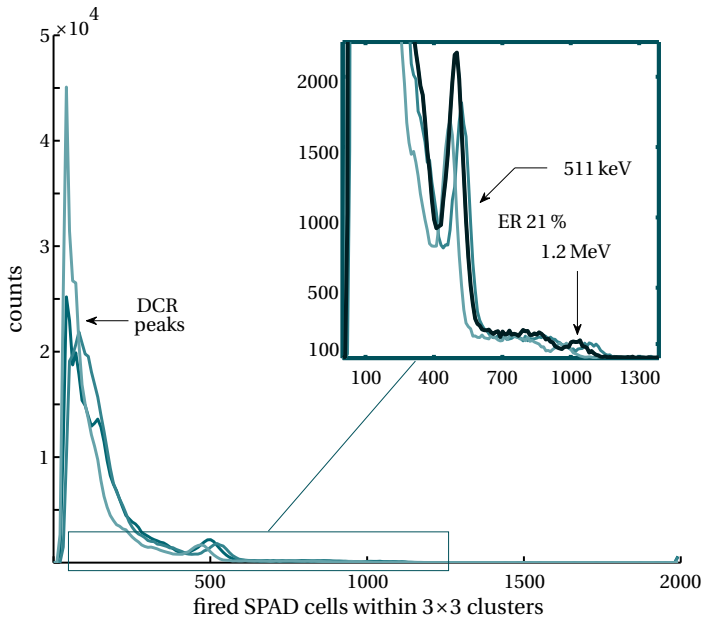


Figure 6.12: Scintillation captured in SPAD-camera mode utilizing the 6×3 LYSO matrix with 2.4 mm pitch. (a) raw data frame. (b) binary imaged post-processed with a 2D mean filter.



(a)



(b)

Figure 6.13: Energy spectra of the individual LYSO scintillator pixels. (a) 18 energy spectra captured with SPAD-camera mode and SR disabled. (b) 3 energy spectra captured with SPAD-camera mode and SR enabled.

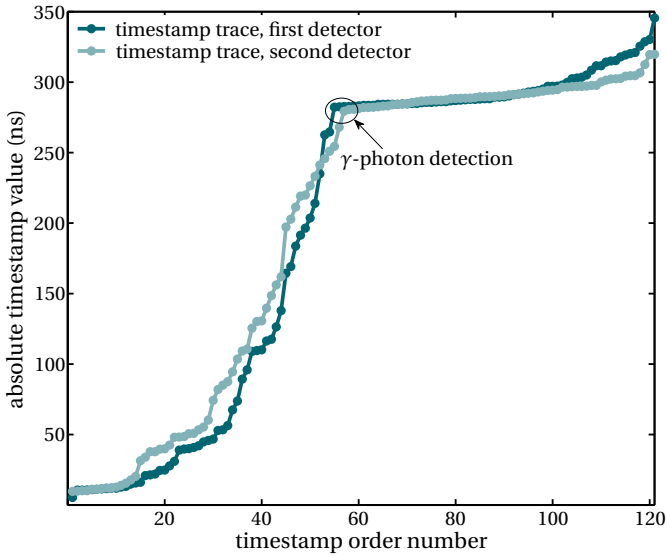


Figure 6.14: Absolute timestamps of a coincident γ -photon detections measured on the detector pair.

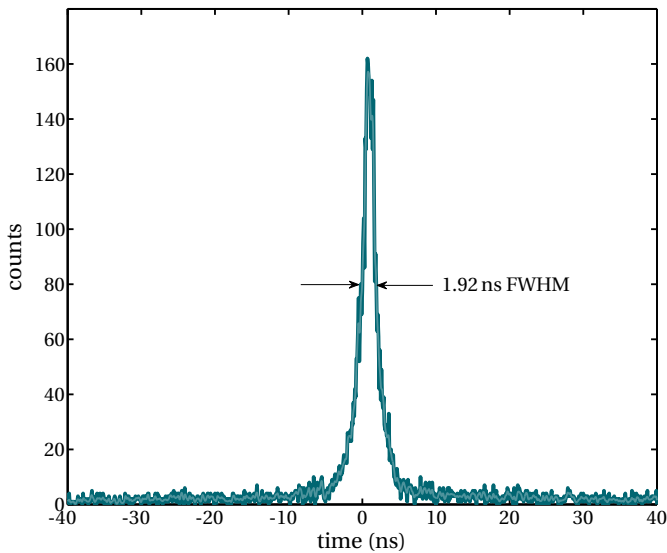
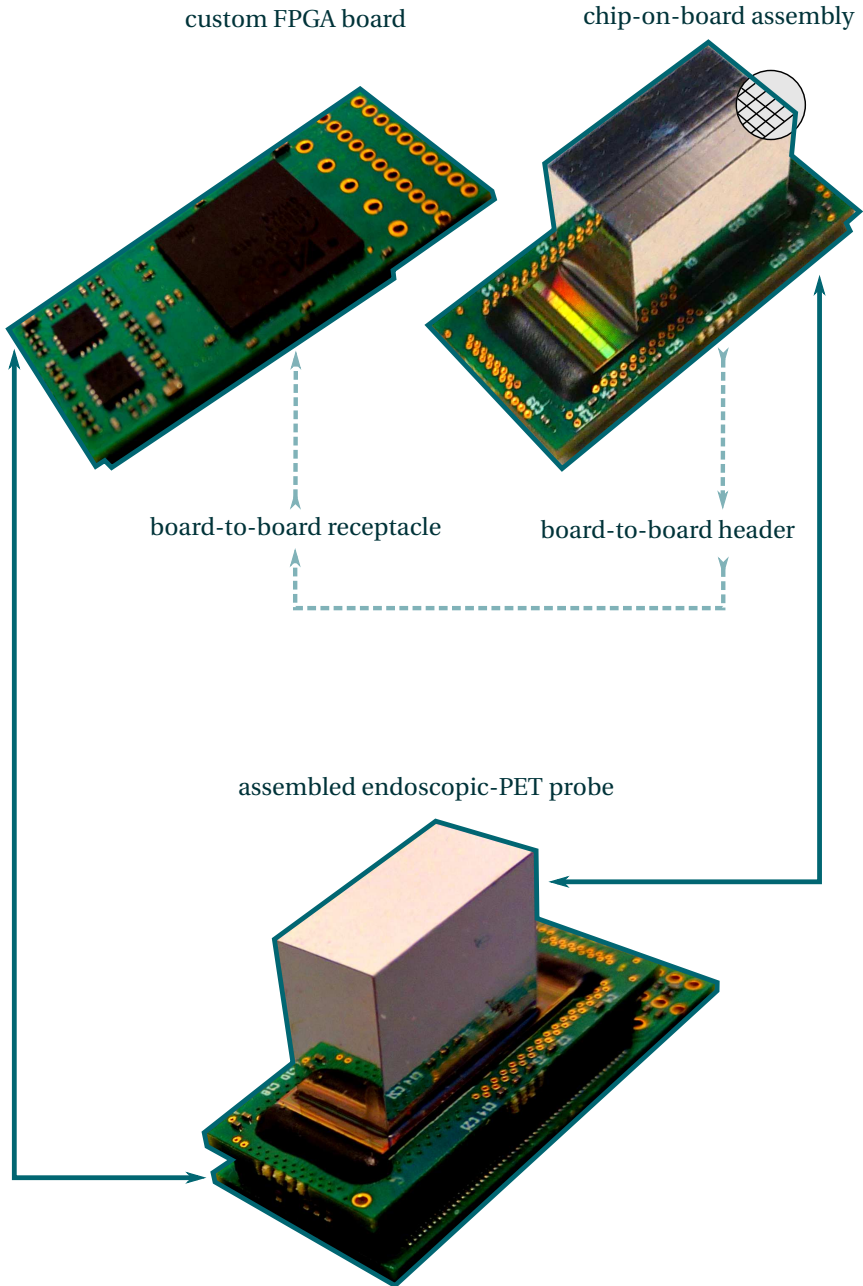


Figure 6.15: CRT histogram. Second timestamp difference histogram, after applying the dark count filter.



6

Figure 6.16: Picture of the assembled endoscopic-PET probe.

6.2. ENDOSCOPIC PET DETECTOR DESIGN

Endoscopic-PET, which is a novel molecular imaging modality, requires a compact and highly-miniaturized PET detector that is integrated into an endoscopic probe [10]. The array of 18×9 MD-SiPMs was designed within the EndoTOFPET-US project's framework, as the custom photodetector for the endoscopic PET probe implementation.

The initial probe design specification were over-constrained in terms of space and PCB requirements, which lead to a challenging design. Therefore, we decided to implement a probe with less constrained specifications that served as an intermediate proof of concept design [6]. In this new design, we re-utilized the chip-on-board assembly along with a custom FPGA board based on a Microsemi FPGA (AGL1000V2-CSG281). Instead of using a flex-rigid PCB approach we separated the design into two boards; therefore, the approach allow the full testing of the individual parts before the full probe was assembled. The full probe was electrically tested successfully and the FW is currently under development (see Figure 6.16). The final probe dimensions are $13.5 \times 30.5 \times 15.8$ mm.

6.3. SUMMARY

The modular design approach allowed to test, fully characterized, and integrate arrays of 18×9 MD-SiPMs for PET applications. We verified the drastic DCR reduction in the energy spectra when SR reset was enabled. The FWHM ER measured at 511 keV was between 16% and 21% for SPAD-camera and D-SiPM readout modes, respectively. We evaluated the CRT performance by carrying out the coincidence experiment between to LYSO pixels of 2.4 mm pitch, which was 1.92 ns FWHM. We found the main design limitations in the SPAD in terms of DCR and PDE, which limited the ER and the CRT.

In conclusion, we verified the functionality and performance of all of the building blocks of 18×9 array of MD-SiPMs, which enables a full-PET detector system that targets PET applications.

REFERENCES

- [1] A. Carimatto, S. Mandai, E. Venialgo, T. Gong, G. Borghi, D. R. Schaart, and E. Charbon, *11.4 A 67,392-SPAD PVTB-compensated multi-channel digital SiPM with 432 column-parallel 48ps 17b TDCs for endoscopic time-of-flight PET*, in *Solid-State Circuits Conference-(ISSCC), 2015 IEEE International*.
- [2] Xilinx, *ML505/ML506/ML507 Evaluation Platform User Guide* ((accessed November 12, 2018)).
- [3] R. Bugalho, C. Gaston, M. Rolo, J. C. Silva, R. Silva, and J. Varela, *Endotofpet-us data acquisition system*, *Journal of Instrumentation* 8, C02049 (2013).
- [4] Xilinx, *Spartan-6 Family Overview* ((accessed November 12, 2018)).
- [5] HUMANDATA, *Xilinx Spartan-6 FGG676 FPGA board* ((accessed November 12, 2018)).
- [6] E. Venialgo, S. Sinha, T. Gong, S. Mandai, A. Carimatto, S. E. Brunner, D. R. Schaart, and E. Charbon, *Small-animal and endoscopic PET detector modules based on*

- multichannel digital silicon photomultipliers*, in *Nuclear Science Symposium, Medical Imaging Conference and Room-Temperature Semiconductor Detector Workshop (NSS/MIC/RTSD)*, 2016 (IEEE, 2016) pp. 1–5.
- [7] Xilinx, *Spartan-6 FPGA SelectIO Resources - User Guide* ((accessed November 12, 2018)).
- [8] F. T. D. I. Ltd., *FT2232H Dual High Speed USB to Multipurpose UART/FIFO IC Datasheet, Version 2.5* ((accessed November 12, 2018)).
- [9] E. Venialgo, S. Mandai, T. Gong, D. R. Schaart, and E. Charbon, *Time estimation with multichannel digital silicon photomultipliers*, *Physics in Medicine & Biology* 60, 2435 (2015).
- [10] N. Aubry, E. Auffray, F. Mimoun, N. Brillouet, R. Bugalho, E. Charbon, O. Charles, D. Cortinovis, P. Courday, A. Cserkaszky, *et al.*, *EndoTOFPET-US: a novel multimodal tool for endoscopy and positron emission tomography*, *Journal of Instrumentation* 8, C04002 (2013).

7

CONCLUSIONS AND OUTLOOK

Improving the performance of molecular imaging instruments allows the observation of molecular and cellular processes in a more precise way. The ultimate timing resolution and positron sensitivity has not been reached by the state-of-the-art detectors yet. Additionally, PET equipment requires the design and implementation of complex readout circuits that limit its availability due to high research and development costs.

Regarding the timing resolution of scintillation-based detectors, extensive work (chapter 3) explained the limitations involved in improving the timing performance [1–5]. We performed a comprehensive work in order to find the missing component that allowed to utilize the complete timing information contained in a scintillation pulse. This missing part were the multiple-timestamp timemark estimators, which approximates the CRLB. Additionally, it appears that standard high-efficiency estimators, such as MLE, cannot reach the CRLB under specific conditions of small number of photoelectrons and low total timing jitter. This finding is relevant to field of Cherenkov-based PET detectors, where the former conditions are the typical case [6]. Furthermore, we found that the regularity conditions for obtaining a valid CRLB are met; therefore, we attributed the divergence between the CRLB and the MLE to asymmetry of the PDFs that corresponds to small number of photons and low total timing jitter. However, a theoretical analysis on the PDF's skewness is required in order to formally verified it.

Next, we experimentally studied the performance of PET detectors based on state-of-the-art photodetector technologies, such as A-SiPMs and D-SiPMs in chapters 4, 5 and 6. Undoubtedly, the performance on A-SiPMs was superior due to the fact that their PDE and DCR are significantly superior than in the case of the $9\times$ array of MD-SiPMs. The limitations of the $9\times$ array of MD-SiPMs in terms of PDE and DCR are related to the utilization of a standard CMOS process for building SPADs. Similar D-SiPM designs achieve a comparable performance to A-SiPMs since they are implemented on a SPAD-customized CMOS process [7]. However, the A-SiPMs, which are fabricated in fully custom technologies, have more degree of freedom for further SPAD optimizations, since they do not have to fulfill with extra constrains related to the CMOS integration.

From the obtained practical experience, we learned the process of creating and analyzing the performance PET instrumentation based on fully digital and partially analog elements. The process of utilizing A-SiPMs for building PET instruments did not require a relatively complex approach, in comparison to D-SiPMs, in order to reach state-of-the-art timing performances (as far as ASIC development is avoided). In this respect, we designed and characterize A-SiPM based instrumentation that full filled with the requirement of being a full-flexible and a fast-prototyping solution. The drawback of the proposed approach, which is explained in chapter 4, is the higher power consumption when comparing it to ASIC solutions. The main purpose of the ASIC-less design was to open the possibility of designing TOF-PET instruments by utilizing standard components and design flows, which are widely available. Subsequently, chapter 4 fulfilled with objective of driving the molecular instrumentation to solutions that are available to a wider public.

PET instruments based on D-SiPMs, where the measurement signals are confined within a CMOS die, and in particular the 18×9 array of MD-SiPMs requires a completely different design flow, in comparison to A-SiPMs. D-SiPMs that are already fully tested and verified, such as the DPC, allows a direct system integration [7]. The advantage of

such an integration is that only digital signaling is required to build a large system based on thousands of measurement channels running synchronously. Subsequently, this approach warrants less degradations when expanding from single modules to full PET scanners. Besides the limited performance of the MD-SiPM in terms of PDE and DCR, once the FW was developed its porting or addition of extra functionalities required only hardware description language (HDL) coding.

Finally, we thoroughly studied the performance of MD-SiPMs and developed metrology methods for their full characterization. We could verify the simultaneous TDC operation and γ -photon multiple timestamping. We developed a new operation methods for TDC's DNL reduction, which did not require the sensor redesign and manufacturing. In addition, for the first time, we fully integrated these devices into PET modules that were characterized in terms of γ -radiation detection performance.

7.1. FUTURE WORK

Inorganic scintillators, which in essence convert γ -energy into light, have a limited conversion efficiency. For instance, LYSO generates approximately 20000 light photons per 511 keV γ -photon, which means that the efficiency is about 11 % [8]. Increasing the light output, as well as reducing the photodetectors SPTR, impacts directly on the scintillators' intrinsic timing resolution [1–5].

However, improving the conversion efficiency is a challenging task since the scintillation materials have to fulfill with many demanding requirements simultaneously, such as light transparency, high γ -detection efficiency, photodetector-matched refractive index and emission wavelength, fast rise and decay times, reduced cost, etc. These simultaneous and strict requirements do not allow a rapid development of improved scintillation materials; subsequently, LYSO, which was developed in the 1990s, has been the material of choice for PET scanners [9].

Since PET detectors based on scintillation materials found its intrinsic limitations in the scintillators themselves, new γ -radiation detection methods has been investigated based on Cherenkov emission [6, 10]. The intrinsic timing resolution of Cherenkov radiators, which is about tens of picoseconds FWHM when utilized to detect 511 keV γ -photons, requires more sophisticated light extraction and detection systems for avoiding further timing degradations. Additionally, the low number of emitted light photons results into a reduced γ -photon detection efficiency and unknown γ -photon energy information. Alternative methods based on hybrid scintillation/Cherenkov emissions has been proposed in order to resolve the pure-Cherenkov detectors limitations [11]. However, the disadvantage of hybrid scintillation/Cherenkov detectors is that some of the requirement for detecting photons emitted by both mechanisms goes into opposite directions, such as the light photon's wavelength [6, 10, 12].

In pure Cherenkov detection, the photodetector's SPTR has a strong influence into the γ -photon timemarking due to the low number of detected photons [13]. Therefore, in this case improving the photodetector's SPTR is a crucial element for further CRT reductions. Additionally, new improved-SPTR photodetectors, which are based on low-threshold electronics are in current development [14]. Furthermore, alternative light-extraction methods that are wavelength-optimized are also under research [15, 16].

We consider that the way to improve the PET technology consist on further reduc-

ing the timing resolution, which has not reached the fundamental limits of the PET technique yet. Additionally, increasing the PET scanner detector coverage by developing cost-effective detectors improves significantly the positron sensitivity [17]. In these regards, pure Cherenkov PET detectors are an interesting option for creating next-generation TOF-PET instruments due to the lower cost and outstanding intrinsic timing resolution of Cherenkov radiators. However, besides the light-extraction and photodetector's PDE and SPTR challenges, there is still a fundamental unanswered question which is: what about the energy estimation?.

REFERENCES

- [1] R. F. Post and L. I. Schiff, *Statistical Limitations on the Resolving Time of a Scintillation Counter*, Phys. Rev. 80, 1113 (1950).
- [2] E. Gatti and V. Svelto, *Review of theories and experiments of resolving time with scintillation counters*, Nuclear Instruments and Methods 43, 248 (1966), proceedings of the Tenth Summer Meeting of Nuclear Physicists.
- [3] M. Fishburn and E. Charbon, *System Tradeoffs in Gamma-Ray Detection Utilizing SPAD Arrays and Scintillators*, Nuclear Science, IEEE Transactions on 57, 2549 (2010).
- [4] S. Seifert, H. van Dam, and D. Schaart, *The lower bound on the timing resolution of scintillation detectors*, Phys. Med. Biol. 57, 1797 (2012).
- [5] E. Venialgo, S. Mandai, T. Gong, D. R. Schaart, and E. Charbon, *Time estimation with multichannel digital silicon photomultipliers*, Physics in Medicine & Biology 60, 2435 (2015).
- [6] S. Brunner, L. Gruber, J. Marton, K. Suzuki, and A. Hirrtl, *Studies on the Cherenkov effect for improved time resolution of TOF-PET*, IEEE Trans. Nucl. Sci 61, 443 (2014).
- [7] T. Frach, G. Prescher, C. Degenhardt, R. de Gruyter, A. Schmitz, and R. Ballizany, *The digital silicon photomultiplier - Principle of operation and intrinsic detector performance*, in *Nuclear Science Symposium Conference Record (NSS/MIC), 2009 IEEE* (2009) pp. 1959–1965.
- [8] S.-G. Crystals, *LYSO Scintillation Material* ((accessed April 20, 2018)).
- [9] C. Melcher and J. Schweitzer, *Cerium-doped lutetium oxyorthosilicate: a fast, efficient new scintillator*, IEEE Transactions on Nuclear Science 39, 502 (1992).
- [10] S. Korpar, R. Dolenc, P. Križan, R. Pestotnik, and A. Stanovnik, *Study of TOF PET using Cherenkov light*, Nuclear Instruments and Methods in Physics Research Section A: Accelerators, Spectrometers, Detectors and Associated Equipment 654, 532 (2011).
- [11] S. Brunner and D. Schaart, *BGO as a hybrid scintillator/Cherenkov radiator for cost-effective time-of-flight PET*, Physics in Medicine & Biology 62, 4421 (2017).

- [12] S.-G. Crystals, *BGO Bismuth Germanate Scintillation Material* ((accessed April 20, 2018)).
- [13] A. Muntean, G. Francesco, E. Venialgo, B. Claudio, and E. Charbon, *Tradeoffs in Cherenkov Detection for Positron Emission Tomography*, in *2017 IEEE Nuclear Science Symposium and Medical Imaging Conference (NSS/MIC)* (IEEE, 2018).
- [14] A. Sachdeva, E. Venialgo, , and E. Charbon, *In-pixel Low-Threshold Comparator for Improved Timing-Resolution Digital SiPM*, in *2018 IEEE Nuclear Science Symposium and Medical Imaging Conference (NSS/MIC)* (IEEE, 2018).
- [15] A. Knapitsch, E. Auffray, C. Fabjan, J.-L. Leclercq, P. Lecoq, X. Letartre, and C. Seassal, *Photonic crystals: A novel approach to enhance the light output of scintillation based detectors*, Nuclear Instruments and Methods in Physics Research Section A: Accelerators, Spectrometers, Detectors and Associated Equipment 628, 385 (2011).
- [16] G. Francesco, N. Descharmes, E. Venialgo, B. Claudio, and E. Charbon, *Light Extraction Enhancement in Scintillation Crystals Using Thin Film Coatings*, in *2018 IEEE Nuclear Science Symposium and Medical Imaging Conference (NSS/MIC)* (IEEE, 2018).
- [17] S. R. Cherry, T. Jones, J. S. Karp, J. Qi, W. W. Moses, and R. D. Badawi, *Total-body PET: Maximizing sensitivity to create new opportunities for clinical research and patient care*, J Nucl Med 59, 3 (2018).

Appendices

A

**PURE STANDARD CMOS
P+/NWELL SINGLE-PHOTON
AVALANCHE DIODES**

Since the implementation of planar SPADs in custom technologies, later CMOS integration, and full-SPAD CMOS sensor implementation, SPADs became the core-component of analog/digital silicon photomultipliers [1–5]. As described in chapters 3, 4, 5, 6, the scintillation-detector timing performance largely depends on the amount of detected photoelectrons. In a second order of priority, the photodetectors' SPTR and overall DCR limits the timing performance.

All the peripheral electronics, which could be inserted on/off chip, influences on the photodetector's research and development complexity, as well as the difficulty of the system-level integration. Therefore, the intrinsic photodetectors' performance depends mainly on the SPAD features, such as PDP, FF, timing jitter, and DCR. Particularly, in the case of utilizing the most common PET scintillator that is the LYSO, the first phase of digital/analog SiPM research and development consist on creating optimized SPAD for NUV photon detection.

A.1. SPADs IN A PURE CMOS 140 nm PROCESS

Implementing SPADs in custom technologies, which are not CMOS, gives more freedom in tuning the doping profiles for creating high-PDE and low-DCR SPADs for A-SiPM implementations. In addition, In custom CMOS technologies that are optimized for SPAD, any doping profiles modification must be compatible with the CMOS doping profiles. Furthermore, creating SPADs in pure CMOS technologies does not allow any doping profile modifications, and the available doping profiles are only optimized for CMOS.

Therefore, the challenging process of creating SPADs with desirable features in pure standard CMOS technologies is based on the clever utilization of the available CMOS doping profiles. Typical available transistor doping profiles are well and contact creation profiles such as deep n-type well (DNW), n-type well (NW), highly doped n-type (N+), etc (see Figure A.1).

When designing epitaxial and circular SPADs, the main challenge remains in engineering a high electric-field region that is compatible with the desired impinging photons' wavelength. For example, NUV detection requires the design a multiplication region that is close to the silicon surface. An additional challenge remains in avoiding premature junction breakdowns outside the engineered multiplication region, such as premature edge breakdown [6].

A.1.1. SPAD TEST STRUCTURE

In order to avoid the premature edge breakdown, a peripheral region with lower doping concentration is placed [6–8]. For example, when creating a junction between a highly doped p-type (P+) and a NW doping regions, the P+ region is extended further by Δ_{P+} over the NW region (see Figure A.1). In this way, the doping gradient is lower at the edges of the central NW region, and the breakdown voltage at the edge is increased with respect to the multiplication region's breakdown voltage.

The SPAD's maximum FF is not only limited by the Δ_{P+} but also by the surrounding NW region that is required for connecting the cathode to its external contact. The minimum distance between the central and surrounding NW regions is Δ_{NW} . This minimum distance depends mainly on the central P+ and surrounding NW lateral diffusions and

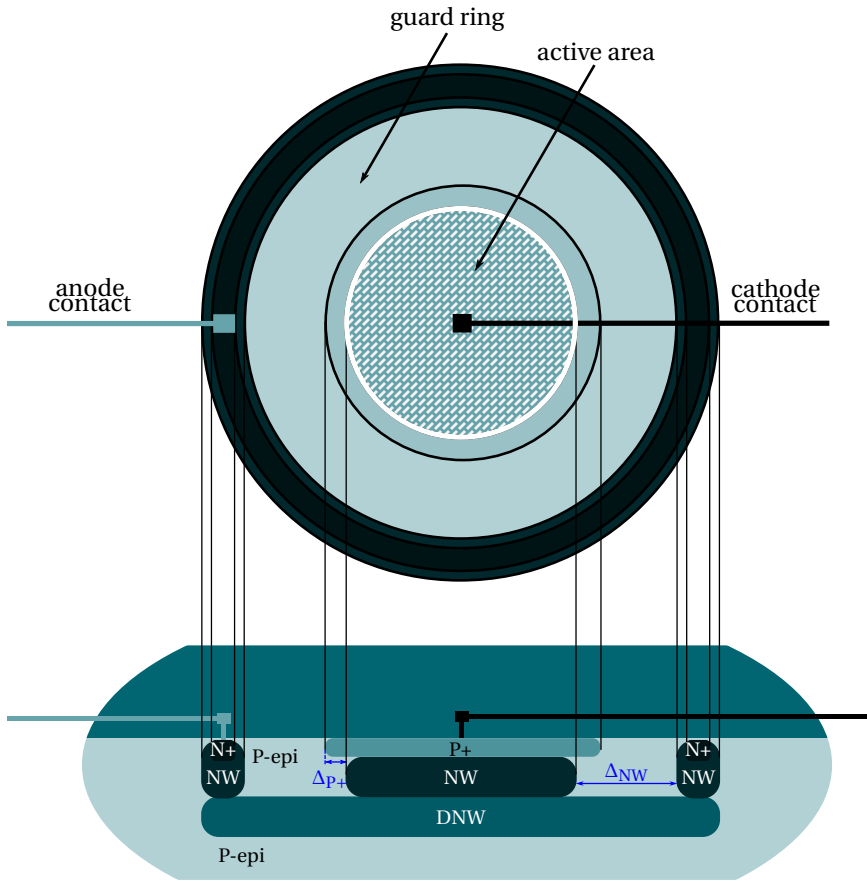


Figure A.1: P+/NWELL CMOS FSI SPAD's structure.

doping concentrations.

Typically, when designing SPADs in pure standard CMOS technologies, the accurate doping information not available to the SPAD designer. Therefore, the SPAD design parameters, such as Δ_{P+} and Δ_{NW} , are empirically determined by designing a so-called "SPAD farm". The SPAD farm consist of implementing repetitions of the same SPAD structure but by sweeping the design parameters. Nevertheless, technology computer-aided design (TCAD) simulations are utilized, with approximated doping information as input data, in order to qualitatively understand the relationship between the SPAD design parameters. Furthermore, when full doping information is available, TCAD becomes powerful calculation tool for SPAD design [9].

A.1.2. TCAD SIMULATION

The electric-field distribution of the SPAD structure of Figure A.1 was simulated utilizing a 2D TCAD simulator [9]. The 2D simulation result of the electric-field magnitude's de-

vice cross section is shown in Figure A.2, where only half of the SPAD was simulated. The SPAD dimensions were optimized to avoid premature breakdowns; therefore, a uniform and high-intensity electric field is observed in the multiplication region.

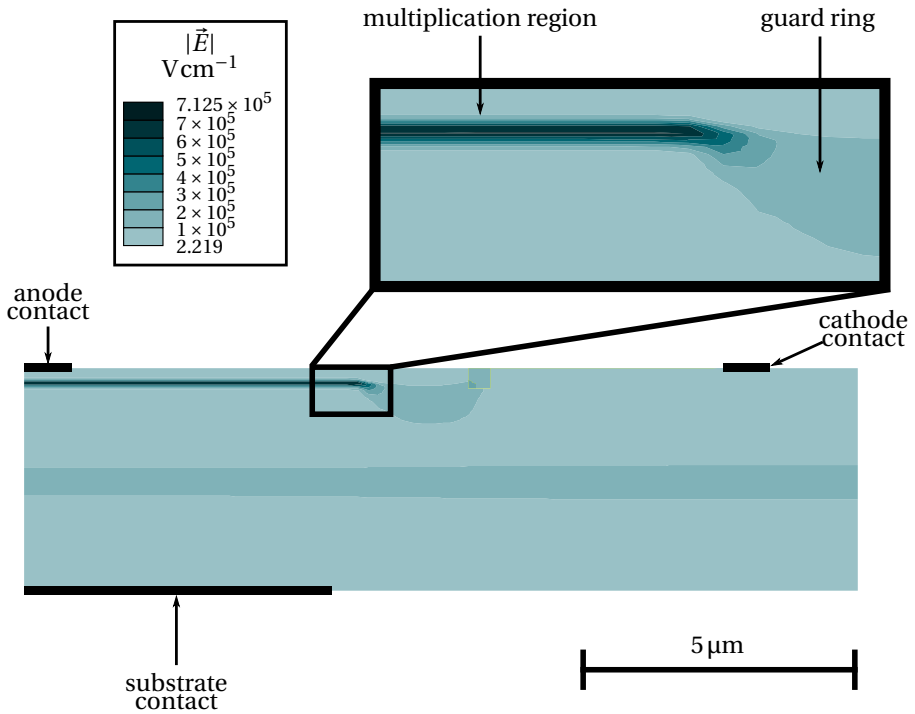


Figure A.2: Result of the cross-sectional TCAD simulation of the P+/NWELL CMOS SPAD.

A.1.3. LIGHT-EMISSION TEST

The observation of infrared light by hot-carrier photon generation, is a measurement technique that allows to investigate the location and uniformity of the multiplication region [6, 7, 10]. A relatively large current flowing into the junction is required in order to observe a significant amount of infrared light through a microscope and a camera device. Typical current values are around few milliamperes. When the diodes is reversed biased and a current of few milliamperes is being injected into the device, a uniform voltage supply across the junction is not guaranteed. Subsequently, the result of this method is considered as an indication of the multiplication region planar distribution [7]. The utilization of high sensitivity camera devices allows to reduce the injection of current and therefore obtaining more accurate results.

Figure A.3 shows the light-emission test result of the implemented SPAD structure (see Figure A.1), where a uniform light distribution is observed in the engineered multiplication region.

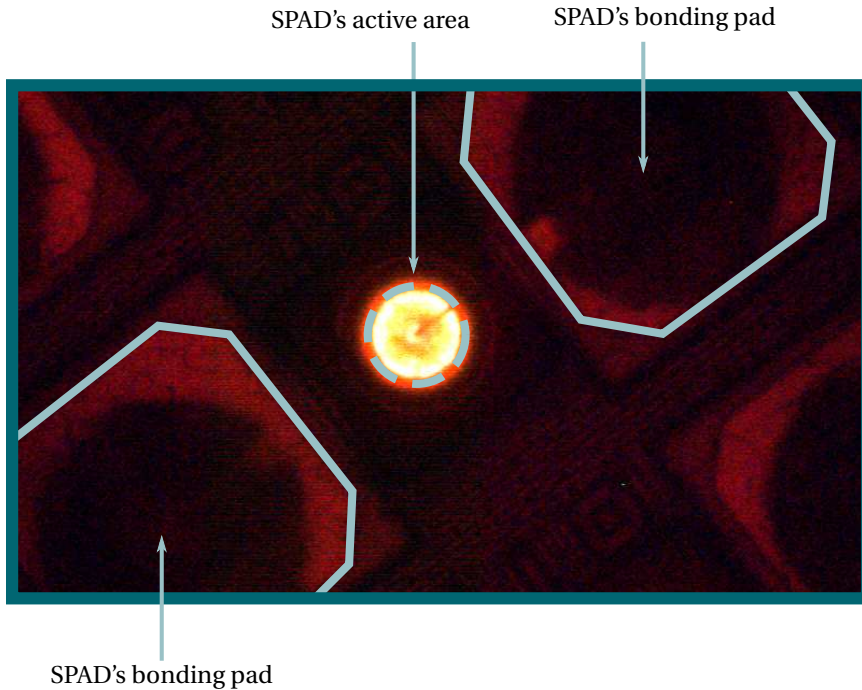


Figure A.3: Light-emission test of the P+/NWELL CMOS SPAD.

A.1.4. PHOTON DETECTION PROBABILITY

The structure depicted in Figure A.1 was implemented with two different diameters: $8\ \mu\text{m}$ and $20\ \mu\text{m}$. The PDP measurements were performed utilizing the same equipment of section 5.2. In the PDP calculations, the active area size was considered as the central NW planar area calculated from the CAD layout tool.

Figure A.4 shows the PDP values that corresponds to the two implemented SPADs as function of the wavelength and for several excess bias voltages. Although the junction structure is the same, higher PDP values are observed for the $20\ \mu\text{m}$ SPAD in comparison to the $8\ \mu\text{m}$ SPAD. These variations are related to the uncertainty in the active area estimation, where the edge effects are less significant as the SPAD diameter increases.

A.1.5. DARK COUNT RATE

The DCR for $8\ \mu\text{m}$ and $20\ \mu\text{m}$ SPADs, and two devices per diameter, was measured at several excess-bias voltages and room temperature (see Figure A.5). During this measurement, and external active quench and recharge circuitry was utilized and the rates were corrected by dead time [7].

A.2. SUMMARY

The design of SPADs in pure standard CMOS technologies are organized in several steps:

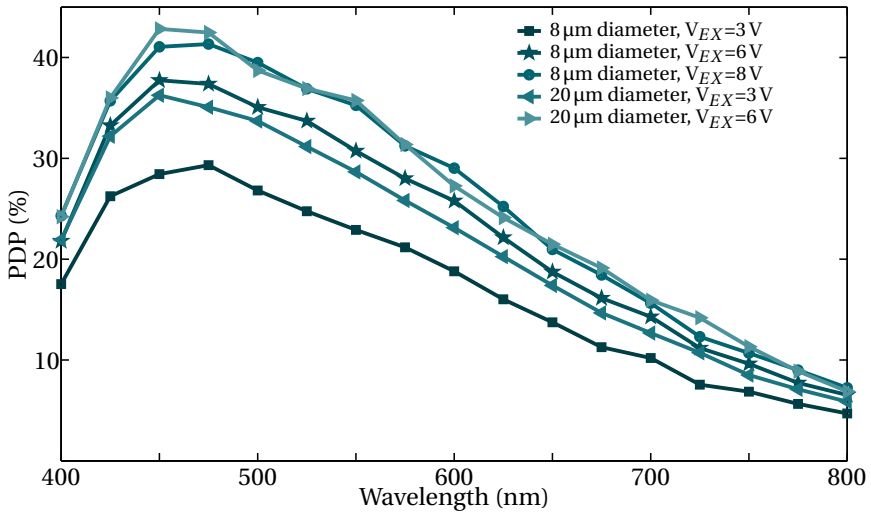


Figure A.4: PDP measurement result for the 20 μm and 8 μm P+/NWELL SPADs at several excess bias voltages.

- technology doping layers study,
- possible SPAD junction analysis,
- TCAD simulations,
- SPAD farm design,
- SPAD implementation,
- and *SPAD farm measurement* and conclusions.

This appendix briefly introduced the designs, tools, method results utilized during the SPAD implementation process. The main performance limitations of the SPAD implementations on a pure standard CMOS technology are the fixed doping profiles, which are not optimized for SPADs.

The SPAD performance parameters are directly linked to the application. For example, in the case of scintillation detection for TOF-PET, high-PDE and low-DCR is a strict requirement. However, other SPAD applications have more relaxed requirements in terms of sensitivity and noise, and the wide availability of pure standard CMOS technologies is always an advantage [11].

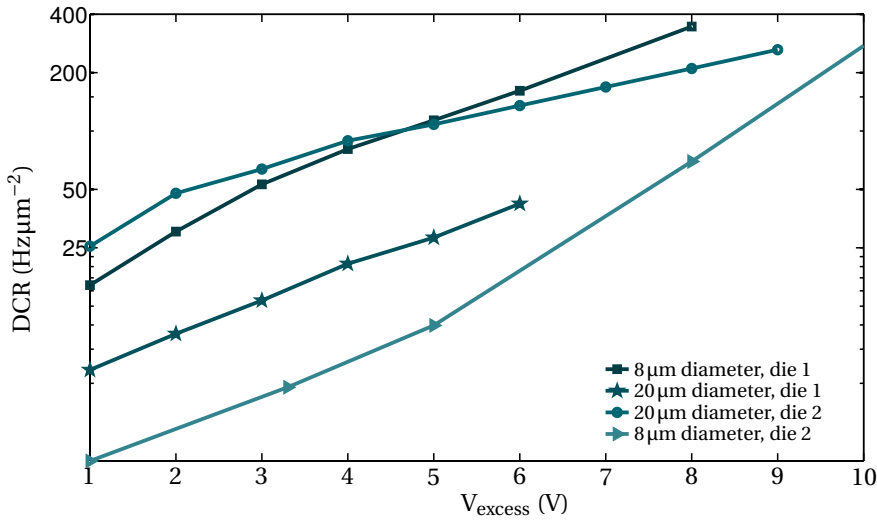


Figure A.5: DCR measurement result for the 20 μm and 8 μm P+/NWELL SPADs at several excess bias voltages.

REFERENCES

- [1] M. Ghioni, S. Cova, A. Lacaita, and G. Ripamonti, *New silicon epitaxial avalanche diode for single-photon timing at room temperature*, *Electronics letters* 24, 1476 (1988).
- [2] A. Rochas, *Single photon avalanche diodes in CMOS technology*, Tech. Rep. (Citeseer, 2003).
- [3] C. Niclass, A. Rochas, P.-A. Besse, and E. Charbon, *Design and characterization of a CMOS 3-D image sensor based on single photon avalanche diodes*, *IEEE Journal of Solid-State Circuits* 40, 1847 (2005).
- [4] T. Frach, G. Prescher, C. Degenhardt, R. de Gruyter, A. Schmitz, and R. Ballizany, *The digital silicon photomultiplier - Principle of operation and intrinsic detector performance*, in *Nuclear Science Symposium Conference Record (NSS/MIC), 2009 IEEE* (2009) pp. 1959–1965.
- [5] S. Mandai and E. Charbon, *Multi-channel digital SiPMs: concept, analysis and implementation*, in *2012 IEEE Nuclear Science Symposium and Medical Imaging Conference Record (NSS/MIC)* (IEEE, 2012) pp. 1840–1844.
- [6] M. W. Fishburn, *Fundamentals of CMOS single-photon avalanche diodes* (fishburn, 2012).
- [7] C. Veerappan, *Single-Photon Avalanche Diodes for Cancer Diagnosis* (Delft University of Technology, 2016).

- [8] E. Kamrani, F. Lesage, and M. Sawan, *Premature edge breakdown prevention techniques in CMOS APD fabrication*, in *New Circuits and Systems Conference (NEWCAS), 2012 IEEE 10th International* (IEEE, 2012) pp. 345–348.
- [9] I. Synopsys, *Taurus Medici, A 2D device simulator* ((accessed May 31, 2018)).
- [10] M. Herzog and F. Koch, *Hot-carrier light emission from silicon metal-oxide-semiconductor devices*, *Applied physics letters* 53, 2620 (1988).
- [11] C. Bruschini, H. Homulle, and E. Charbon, *Ten years of biophotonics single-photon SPAD imager applications: retrospective and outlook*, in *Multiphoton Microscopy in the Biomedical Sciences XVII*, Vol. 10069 (International Society for Optics and Photonics, 2017) p. 100691S.

ACKNOWLEDGEMENTS

When I decided to pursue a PhD abroad, I was looking for an environment where I could learn about the latest molecular imaging technologies, as well as an international working atmosphere. When I was invited for a PhD position interview by Prof. Edoardo Charbon, I had the unique chance to learn about the latest developments in digital SiPMs as well as scintillation and SPAD statistical models. Additionally, the lab's students, who eventually became colleagues and friends of mine, enthusiastically showed me their research work about SPAD-based sensors.

First of all, I would like to thank my supervisor and promotor Prof. Edoardo Charbon for giving me the unique opportunity of participating in the AQUA lab and performing the research work explained within this thesis. He patiently and straightforwardly taught me SPAD and digital SiPM concepts as well as statistical knowledge. Additionally, his research methodologies and management style guided me and improved my scientific quality and skills.

Additionally, I would like to thank Dr. Chockalingam Veerappan who explained to me all the steps involved in SPAD design, from TCAD simulation to actual silicon layout implementations. He always helped me in difficult and fun lab SPAD measurements, as well as advised me about the struggles of the PhD life. Also, I would like to thank Dr. Shingo Mandai who taught about SPAD CMOS sensor design and challenges. We had long discussions about the statistical limitations of MD-SiPMs, which lead into our first journal paper.

Also, I would like to thank Dr. Dennis Schaart and Prof. Geurt Jongbloed for explaining scintillation statistics and detection methods, as well practical details of the Cramér-Rao lower bound. We had long discussions about interesting findings related to the Cramér-Rao lower bound that helped me in strengthening and developing further that concept in the field of scintillation detection. Dennis help and scientific style always provide me an example of high quality research.

The AQUA lab was a synergistic environment where my colleagues: Dr. Pengfei Sun, Dr. Scott Lindner, Dr. Juan Mata Pavia, Dr. Myung-Jae Lee, Dr. Michel Antolović, Chao Zhang, Ting Gong, Claudia Damiani, Dali Zhang, Martijn Bijwaard, Harald Homulle, Dr. Samuel Burri, Andrea Ruffino, Arin Ulku, Augusto Ximenes, Bishnu Patra, Jeroen van Dijk, Preethi Padmanabhan, Rosario Marco Incandela, Ling Song, Bahador Valizadeh Pasha, Junjie Weng, Francesco Gramuglia, Andrada Muntean, and Dr. Claudio Bruschini; always openly and keenly shared technical experience and knowledge as well as personal views about research and technology. In particular, I would like to thank those who joined the soccer table team, which was a fun way to release research stress. Also, I would like to thank Siddharth Sinha for sharing with me the experience of learning FPGA and firmware development and Ashish Sachdeva for for sharing with me the experience of learning analog IC design.

Moreover, I want to thank Dr. Nicola Lusardi, Fabio Garzetti, Prof. Angelo Geraci, Dr. Stefan Brunner, and Giacomo Borghi for their knowledge and support about TDCs on FPGAs and A-SiPM experimentation, which eventually lead into a journal paper. Dr. Nicola Lusardi, Fabio Garzetti shared implementation and remote support hours in order to achieve state-of-the art results with A-SiPMs and scintillator.

In addition, I would like to thank Minaksie Ramsoekh, Joyce van Velzen, Zu-Yao Chang, Lukasz Pakula, and Ron van Puffelen for their support in fixing administrative issues as well as complex assembled boards.

I would also like to take this opportunity to thank all my colleagues from the PicoSEC-MCNet project, whom I shared endless and fun training hours. In particular I would like to thank Etinnette Aufray for building and supervising the PicoSEC-MCNet project, which helped many researchers to develop themselves as professional scientists.

My friends, whom I have shared memorable moments, helped to find Delft as if it were home: Paolo Palmieri, Rodolfo Solera, Constantino García, Andrea Pizzo, Reenu Toodesh, Reyes Menéndez, Pía González, Ana Gallegos, and Accel Abarca.

I do not want to forget my former lab colleagues from Argentina, with whom I learned the first concepts of PET and built several prototype tomography scanners: Andrés Cervantez, Lucio Martinez Garbino, Martín Belzunce, Juan Alarcón, Elías Da Ponte, Daniel Estryk, and Juan Carlos Gómez. In particular, I would like to thank my former advisor: Claudio Verrastro for introducing me to research and scientific world and encouraging me in pursuing my PhD study abroad.

Finally, I would like to thank to all my family for their unconditional love and support: Lucía Venialgo, Mariángeles Venialgo, Ana Venialgo, Nieves Araujo Costoya, Darío Venialgo, María Antonia Romero, Luis Fernando Araujo Costoya, María del Carmen Araujo Costoya, Weiqi Hu, and Hong Liu. In particular, I want to deeply thank my wife: Wenhuan Hu, for her infinite patience, love, and support that were essential for finalizing this thesis.

ABOUT THE AUTHOR



Esteban Venialgo was born in Caseros, Buenos Aires, Argentina. He received the degree of Electrical Technician in 2000 from Instituto Leonardo Murialdo, Villa Bosch, Buenos Aires, Argentina. In 2005-2006 he worked as a undergraduate fellow in the development of artificial neural networks for real-time FPGA-based hardware and light-transport simulation in scintillation detectors at Grupo de Inteligencia Artificial y Robótica (GIAR) at Universidad Tecnológica Nacional Facultad Regional Buenos Aires (UTN-FRBA), Argentina. In 2007-2012 he worked at the Comisión Nacional de Energía Atómica (CNEA) in the design, implementation, and characterization of the AR-PET scanner and AR-TGS. He received the degree of electrical engineer from the UTN-FRBA in 2008. In 2007-

2011, he lectured the class of artificial neural networks within the artificial intelligence course at UTN-FRBA as teacher assistant. In 2013, he joined the Delft University of Technology, where he is currently pursuing the Ph.D. degree in applied quantum architectures under the supervision of Prof. Dr. Edoardo Charbon. Esteban's research interests includes SPAD-based sensors, applied statistics and estimation algorithms, artificial neural networks, system design and integration, molecular imaging instrumentation, GNU/Linux, and FPGAs.

ALUMNI

- Siddharth Sinha (daily supervisor).
Msc. thesis: Small-Animal PET Detector Module Based on Multichannel Digital Silicon Photomultipliers, 2016.
- Ashish Sachdeva (daily supervisor).
Msc. thesis: Design of Low-Threshold Comparator for Improved Timing-Resolution Analog/Digital SiPM, 2018.

LIST OF PUBLICATIONS

JOURNALS

1. Shingo Mandai, Esteban Venialgo, and Edoardo Charbon. Timing optimization utilizing order statistics and multichannel digital silicon photomultipliers. *Optics Letters*, 39(3):552–554, 2014
2. Martin Belzunce, Claudio Verrastro, Lucio Martinez Garbino, Esteban Venialgo, Elias da Ponte, Augusto Carimatto, Juan Alarcon, Daniel Estryk, and Isaac Marcos Cohen. An attenuated projector for iterative reconstruction algorithm of a high sensitivity tomographic gamma scanner. *IEEE Transactions on Nuclear Science*, 61(2):975–984, 2014
3. Esteban Venialgo, Shingo Mandai, Tim Gong, Dennis R Schaart, and Edoardo Charbon. Time estimation with multichannel digital silicon photomultipliers. *Physics in Medicine & Biology*, 60(6):2435, 2015
4. Esteban Venialgo, Nicola Lusardi, Fabio Garzetti, Angelo Geraci, Stefan E Brunner, Dennis R Schaart, and Edoardo Charbon. Towards a Full-Flexible and Fast-Prototyping TOF-PET Block Detector Based on TDC-on-FPGA. *IEEE Transactions on Radiation and Plasma Medical Sciences*, 2018
5. Esteban Venialgo, Shingo Mandai, and Edoardo Charbon. MD-SiPMs: Individual Building Block and Full-System Comprehensive Analyses. **to be submitted to** *IEEE Journal of Solid-State Circuits*, 2019

CONFERENCES

1. Esteban Venialgo, Shingo Mandai, and Edoardo Charbon. Time mark estimators for MD-SiPM and impact of system parameters. In *Nuclear Science Symposium and Medical Imaging Conference (NSS/MIC), 2013 IEEE*, pages 1–2, Oct 2013
2. Shingo Mandai, Esteban Venialgo, and Edoardo Charbon. Energy estimation technique utilizing timing information for TOF-PET application. In *Nuclear Science Symposium and Medical Imaging Conference (NSS/MIC), 2013 IEEE*, pages 1–3. IEEE, 2013
3. Edoardo Charbon, Shingo Mandai, and Esteban Venialgo. Large Format Single-Photon Image Sensors in CMOS Technology. In *Single Photon Workshop*. Oak Ridge National Laboratory, 2013
4. Esteban Venialgo, Shingo Mandai, and Edoardo Charbon. MD-SiPM PET detector module design. In *Nuclear Science Symposium and Medical Imaging Conference (NSS/MIC), 2014 IEEE*, pages 1–4. IEEE, 2014

5. Ting Gong, Shingo Mandai, Esteban Venialgo, Augusto Carimatto, and Edoardo Charbon. FPGA-based fast gamma-ray time mark estimator for ultra-miniature endoscopic PET applications. In *Nuclear Science Symposium and Medical Imaging Conference (NSS/MIC), 2014 IEEE*, pages 1–4. IEEE, 2014
6. Chockalingam Veerappan, Esteban Venialgo, Claudio Bruschini, and Edoardo Charbon. SPADnet network modeling, simulation and emulation. In *Real Time Conference (RT), 2014 19th IEEE-NPSS*, pages 1–2. IEEE, 2014
7. Lucio Martínez Garbino, Esteban Venialgo, Daniel Estryk, Claudio Verrastro, and Martín Belzunce. A pulse modeling tool for PET scanners. In *Nuclear Science Symposium and Medical Imaging Conference (NSS/MIC), 2014 IEEE*, pages 1–2. IEEE, 2014
8. Augusto Carimatto, Shingo Mandai, Esteban Venialgo, Ting Gong, Giacomo Borghi, Dennis R Schaart, and Edoardo Charbon. 11.4 A 67,392-SPAD PVTB-compensated multi-channel digital SiPM with 432 column-parallel 48ps 17b TDCs for endoscopic time-of-flight PET. In *Solid-State Circuits Conference-(ISSCC), 2015 IEEE International*, pages 1–3. IEEE, 2015
9. Esteban Venialgo, Shingo Mandai, Ting Gong, Dennis Schaart, and Edoardo Charbon. Practical time mark estimators for multichannel digital silicon photomultipliers. In *Nuclear Science Symposium and Medical Imaging Conference (NSS/MIC), 2015 IEEE*, pages 1–3. IEEE, 2015
10. Esteban Venialgo, Siddharth Sinha, Ting Gong, Shingo Mandai, Augusto Carimatto, Stefan E Brunner, Dennis R Schaart, and Edoardo Charbon. Small-animal and endoscopic PET detector modules based on multichannel digital silicon photomultipliers. In *Nuclear Science Symposium, Medical Imaging Conference and Room-Temperature Semiconductor Detector Workshop (NSS/MIC/RTSD), 2016*, pages 1–5. IEEE, 2016
11. Esteban Venialgo, Nicola Lusardi, Angelo Geraci, Kevin O'Neill, Salvatore Gnacchi, Carl Jackson, Stefan E Brunner, Dennis R Schaart, and Edoardo Charbon. An order-statistics-inspired, fully-digital readout approach for analog SiPM arrays. In *2016 IEEE Nuclear Science Symposium, Medical Imaging Conference and Room-Temperature Semiconductor Detector Workshop (NSS/MIC/RTSD)*, pages 1–5, Oct 2016
12. Esteban Venialgo, Nicola Lusardi, Fabio Garzetti, Angelo Geraci, and Edoardo Charbon. A Network-Enabled PET Detector Module Based on TDCs on FPGA. In *2017 IEEE Nuclear Science Symposium and Medical Imaging Conference (NSS/MIC)*. IEEE, 2017
13. Esteban Venialgo, Shingo Mandai, and Edoardo Charbon. Design and Characterization of 4x1 MD-SiPM Small-Animal PET Building Block. In *2017 IEEE Nuclear Science Symposium and Medical Imaging Conference (NSS/MIC)*. IEEE, 2017

14. Andrada Muntean, Esteban Venialgo, Salvatore Gnecci, Carl Jackson, and Edoardo Charbon. Towards a fully digital state-of-the-art analog SiPM. In *2017 IEEE Nuclear Science Symposium and Medical Imaging Conference (NSS/MIC)*, pages 1–4. IEEE, 2017
15. Francesco Gramuglia, Myung-Jae Lee, Esteban Venialgo, Claudio Bruschini, and Edoardo Charbon. Towards 10ps SPTR and Ultra-Low DCR in SiPMs Through the Combination of Microlenses and Photonic Crystals. In *2017 IEEE Nuclear Science Symposium and Medical Imaging Conference (NSS/MIC)*, pages 1–3. IEEE, 2017
16. Andrada Muntean, Gramuglia Francesco, Esteban Venialgo, Bruschini Claudio, and Edoardo Charbon. Tradeoffs in Cherenkov Detection for Positron Emission Tomography. In *2017 IEEE Nuclear Science Symposium and Medical Imaging Conference (NSS/MIC)*. IEEE, 2018
17. Ashish Sachdeva, Esteban Venialgo, , and Edoardo Charbon. In-pixel Low-Threshold Comparator for Improved Timing-Resolution Digital SiPM. In *2018 IEEE Nuclear Science Symposium and Medical Imaging Conference (NSS/MIC)*. IEEE, 2018
18. Gramuglia Francesco, Nicolas Descharmes, Esteban Venialgo, Bruschini Claudio, and Edoardo Charbon. Light Extraction Enhancement in Scintillation Crystals Using Thin Film Coatings. In *2018 IEEE Nuclear Science Symposium and Medical Imaging Conference (NSS/MIC)*. IEEE, 2018
19. Esteban Venialgo, Jean-François Pratte, Stefan E Brunner, and Edoardo Charbon. Single-Photon Timing Resolution in Digital Silicon Photomultipliers. In *International Conference on the Advancement of Silicon Photomultipliers*, 2018

